ONSET AND SUBSEQUENT TRANSIENT PHENOMENA OF

LIQUID LOADING IN GAS WELLS: EXPERIMENTAL

INVESTIGATION USING A LARGE SCALE FLOW LOOP

A Dissertation

by

PAULO JOSE WALTRICH

Submitted to the Office of Graduate Studies of
Texas A&M University
in partial fulfillment of the requirements for the degree of

DOCTOR OF PHILOSOPHY

August 2012

Major Subject: Petroleum Engineering

ONSET AND SUBSEQUENT TRANSIENT PHENOMENA OF LIQUID LOADING IN GAS WELLS: EXPERIMENTAL INVESTIGATION USING A LARGE SCALE FLOW LOOP

A Dissertation

by

PAULO JOSE WALTRICH

Submitted to the Office of Graduate Studies of
Texas A&M University
in partial fulfillment of the requirements for the degree of

DOCTOR OF PHILOSOPHY

Approved by:

Co-Chairs of Committee,	Maria A. Barrufet
	Gioia Falcone
Committee Members,	Catalin Teodoriu
	Gerald R. Morrison
	Jader R. Barbosa Jr.
Head of Department,	A. Daniel Hill

August 2012

Major Subject: Petroleum Engineering

ABSTRACT

Onset and Subsequent Transient Phenomena of Liquid Loading in Gas Wells:

Experimental Investigation Using a Large Scale Flow Loop. (August 2012)

Paulo Jose Waltrich, B.S., Federal University of Santa Catarina;

M.S., Federal University of Santa Catarina

Co-Chairs of Advisory Committee: Dr. Maria Barrufet
Dr. Gioia Falcone

Liquid loading in gas wells is generally described as the inability of the well to lift the co-produced liquids up the tubing, which may ultimately kill the well. There is a lack of dedicated models that can mimic the transient features that are typical of liquid loading. Improved characterization of liquid loading in gas wells and enhanced prediction of future well performance can be achieved from the measurements and analyses resulting from this project.

An experimental investigation was carried out to study the onset of liquid loading and the subsequent transient phenomena, using a large scale flow loop to visualize two-phase flow regimes, and to measure pressure and liquid holdup along a 42-m long vertical tube.

From this investigation, it is possible to conclude that liquid loading should not be characterized based on onset criteria alone, and that it may not be a wellbore-only problem, as it would seem that the reservoir also plays a key role in determining if/when/how liquid loading manifests itself.

Additionally, the results from the experimental campaign were used to compare the performance of different wellbore flow simulators. State-of-the-art simulators do not seem to fully capture the nature of liquid loading in vertical tubes. A simplified model is

proposed here to evaluate the liquid transport during the transition from one flow regime to another, during the loading sequence.

DEDICATION

To my parents Paulo (*in memoriam*) and Darci, my bothers Gierri and Maicon, and my wife Ticiana (and family) for their love and support during the course of my life. None of my accomplishments would be possible without them

ACKNOWLEDGEMENTS

To all my friends and everyone who has helped during the difficult times and also making my life more pleasant outside of my work as well, thank you!

NOMENCLATURE

d_T	tube diameter, m
dp/dz	pressure gradient, kPa/m
e_f	liquid entrained fraction
G	acceleration of gravity, m/s^2
h_l	liquid holdup
L/D	length over tube diameter ratio
m_g	gas mass flux, kg/m^2-s
m_w	water mass flux, kg/m^2-s
P	pressure, kPa
PDF	probability density function
Q	volumetric flow rate, m^3/h
T	time, s
T	temperature, K
U_{gs}	superficial gas velocity, m/s
$U_{gs}*$	dimensionless gas velocity
U_{ls}	superficial liquid velocity, m/s
U_C	Turner critical velocity, m/s
v_f	liquid front velocity, m/s
Greek symbols	
A	void fraction
δ_f	liquid film thickness, mm
Δh	height difference, m
Δp	pressure difference, kPa
ρ_c	core density, kg/m^3
ρ_g	gas density, kg/m^3
ρ_l	liquid density, kg/m^3

TABLE OF CONTENTS

LIST OF FIGURES

LIST OF TABLES

1. INTRODUCTION

1.1. Liquid Loading

Liquid loading is a very common problem in mature gas fields, which is estimated to occur in at least 90% of the producing gas wells in the USA (Veeken, Kees et al. 2003). During gas production, liquid (condensate or water) can accumulate at the bottom of the wellbore, increasing downhole pressure and therefore significantly decreasing (or even ending) gas flow. Thus, a fundamental understanding of this phenomenon is extremely important towards the design and optimization of gas wells.

A simplified overview of liquid loading phenomenon during the life of a gas well is illustrated in Figure 1.1.
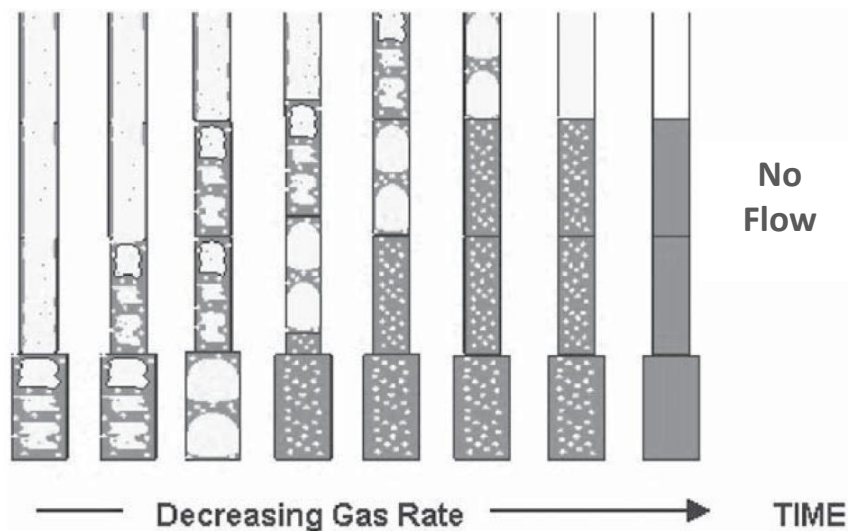
Figure 1.1 – Liquid build up process in a gas well as the gas rate declines (Lea et al. 2003).

_____

This dissertation follows the style of *Society of Petroleum Engineers Journal.*

In the early stages, the well gas rate is generally high, with low liquid content in the wellbore. Due to natural reservoir depletion, the gas production rate decreases over time. The associated lower gas velocity reduces the interfacial friction between the gas and the liquid phases, which in turn slows down the liquid. To honor the liquid mass conservation principle (for a fixed liquid production rate), the cross-sectional area occupied by the liquid must increase with decreasing liquid velocity. The increase in liquid content in the wellbore requires a greater bottomhole pressure to keep the well flowing (due to the associated increase in hydrostatic pressure). This can decrease the gas rate even further, thus initiating a cascade effect which can ultimately kill the well.

1.2. Need for Further Investigation on Liquid Loading

Associated with the liquid build up in the wellbore are common symptoms observed in the field such as liquid slugs arriving at surface, accompanied by erratic and sudden drop in gas production. These symptoms are often used by field operators to recognize wells experiencing liquid loading problems. Such recognition can not only be highly subjective, but may also happen when it is too late to implement remedial solutions. Understanding liquid loading can help develop techniques and tools to predict if/when liquid loading may occur, optimize wells design accordingly, and alleviate its detrimental effects once liquid loading starts manifesting itself.

A considerable amount of studies on liquid loading in gas wells have been carried out over the past 40 years. Many of these studies have relied on surface measurements from the field, with the associated uncertainty that this entails, considering that several key flow parameters cannot be measured in the field, or not with sufficient accuracy. This is perhaps one of the reasons why currently available models cannot predict liquid loading over a wide range of conditions. Additionally, most of the work presented to date is based on the assumption of steady-state or pseudo-steady state flowing conditions, although liquid loading is transient in nature, particularly when considering the time scale for the changes in multiphase flow behavior in the wellbore, which is in the order of magnitude of milliseconds. Thus, transient flow approach to evaluating liquid loading in gas wells appears to be essential.

A more fundamental understanding of the mechanisms behind liquid loading also seems to be required. There is still some inconsistency in the literature regarding the description of the root mechanisms behind liquid loading, including some specific flow regimes (e.g. churn flow) and regime-to-regime transitions, which can possibly be related to the onset of liquid loading.

The evolution of the flow phenomena associated to liquid loading along the wellbore is also poorly understood, due to the limited number of experimental facilities that allow the axial characterization of two-phase flows in long vertical tubes (L/D > 500). In the oil and gas industry, typical wells are in the order of thousand of pipe diameters in length. Pressure varies considerably over the length of a vertical wellbore, leading to varying axial gas velocity, which is in turn associated with varying liquid content along the well. The latter is in essence the liquid loading problem. Thus, being able to characterize the axial variation of pressure, gas velocity and liquid content along the well is essential towards a better understanding of liquid loading.

A better understanding of the physics of liquid loading, together with more reliable models, can lead to enhanced design of deliquification tools which can significantly extend the life of the well, and consequently, increase recovery.

1.3. Objectives

Based on the needs for research presented above, the following objectives were established for the present project:

- *Design and build a dedicated large scale flow loop*: there are a limited number of flow loops around the world which can be used to experimentally characterize the axial behavior of two-phase flows. Since liquid loading is directly related to the liquid build up along the well, the use of a long test section (L/D > 500) is essential to properly investigate liquid loading fundamentals.

- *Axial investigation of flow regimes*: Since flow regime transitions should be related to liquid loading, more studies should be carried out regarding flow development in two-phase flows along vertical tubes. There is a lack of

studies about some flow regimes, particularly for churn flow. Axial flow characterization is extremely important in gas wells because the wellbores are usually long (more than one or two kilometers) and many times local information/models are not comprehensive enough to describe the behavior along the entire pipeline.

- *Experimental investigation of the onset of liquid loading*: the most widely used model to predict the onset of liquid loading cannot accurately evaluate liquid loading over a wide range of conditions. Additionally, some researchers suggest that the onset is directly related to the liquid film flow reversal, which is a feature of particular flow regime transitions. Nevertheless, few experiments have been carried out to investigate this relationship. Thus, an experimental investigation is carried out here to obtain more data and correlate the two-phase flow parameters with the onset criteria models.

- *Experimental investigation of transient flow regime transitions*: only a few works could be found about transient behavior of flow regime transitions. Since the onset of liquid loading can be related to these transitions, understanding the transient behavior of specific flow regimes and their transitions seems to be one of the keys to better understanding liquid loading phenomena.

- *Verification of the performance of state-of-the-art wellbore simulators when predicting two-phase flows under liquid loading conditions*: most times engineers use commercial packages or research codes to predict and evaluate liquid loading. Therefore, a comparison of these models is carried out here to evaluate the results of such simulators when compared to experimental data, and then verify the simulators' accuracy.

1.4. Structure of the Dissertation

Section 2 includes a brief description of flow regimes in vertical tubes, focusing on more details of annular and churn flow patterns and their relations with liquid loading

phenomena. It also discusses the models and correlations generally used for prediction of the onset of liquid loading. Additionally, modeling techniques for evaluation of liquid loading conditions considering both well and reservoir are also included in section 2.

Section 3 discusses the design, instrumentation and capabilities of the large scale flow loop deployed here during the experimental investigations.

Section 4 presents the results for the axial characterization of annular, churn and slug flows. These results are extremely important to understanding how churn flow parameters, such as liquid holdup, behave axially in a long vertical tube. As will be described in section 2, churn flow regime is believed to be directly related to liquid loading. Thus, the conclusions from this experimental investigation can clarify how some flow parameters (pressure and flow rates, for instance) are correlated with the liquid build up along the vertical tube.

Section 5 describes the experimental investigation of the onset of liquid loading. It will present how the liquid accumulation in the vertical test section is related with the associated flow regimes, liquid holdup, pressure, gas and liquid flow rates. The results are then used to evaluate the accuracy of the currently available models to predict the onset of liquid loading.

Section 6 presents a comparison of experimental data with the state-of-the-art commercial simulator for multiphase flow and two research codes. The capabilities of such simulators are verified and suggestions for further improvements in these codes are discussed.

Section 7 gives a summary of the conclusions from this work and suggests future work towards liquid loading studies.

2. LITERATURE REVIEW

Several works have been carried out about liquid loading in the oil and gas industry. However, the understanding and prediction of this phenomenon is still considered weak. A better comprehension of liquid loading fundamentals can lead to more effective production forecasts, design of flowlines and completions, and remediation of wells under liquid loading conditions.

In order to understand the fundamentals of liquid loading we first have to investigate with more details the basic mechanisms that occur during the liquid loading process. Since this process is strongly related to two-phase flows, the objective of this section is first to introduce the basic concepts regarding two-phase flows. Besides these concepts, a review of the techniques available for experimental characterization of two-phase flows is also presented. This section also includes a discussion of the criteria used to predict the onset of liquid loading and its relationship with the two-phase parameters. A brief review of the modeling techniques generally used to evaluate liquid loading are also discussed.

In the end of the section, a summary of the conclusion obtained from this literature review is presented.

2.1. Flow Regimes

Flow regimes (or flow patterns) are defined based on the configuration of the phases (topology) for a given flow. The mechanisms which define the flow regime depend on the force balance in the interior of each phase and its interfaces. The prediction of flow regimes in a given location in a wellbore is extremely important. For instance, correlations and mechanistic models rely on the prediction of flow regimes to properly evaluate the behavior of two-phase flows. Figure 2.1 illustrates the flow regimes which are generally encountered in gas-liquid flows in vertical tubes. These flow regimes can be described as follows (Hewitt 1982):
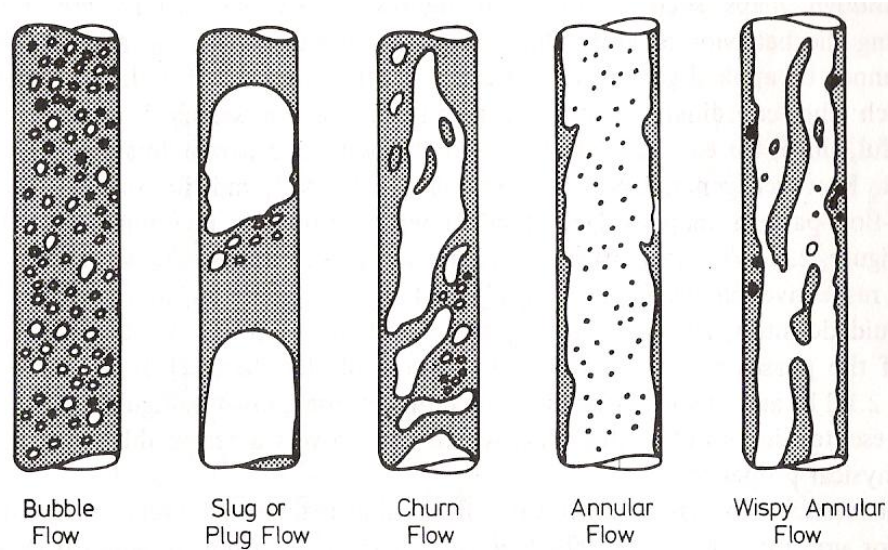
Figure 2.1 – Flow regimes in gas-liquid flow in vertical tubes (Hewitt 1982).

- Bubble flow: Dispersed bubbles flow in a continuous phase of liquid. The size and shape of these bubbles depend on how the gas phase is injected in the liquid phase. This flow regime occurs for high liquid velocities and low gas velocities.

- Slug flow: As the relative gas content is increased, bubble coalescence occurs, and elongated bubbles (Taylor bubbles) are created. The Taylor bubbles flow upward with a liquid film flowing downward around the Taylor bubbles. Separating the Taylor bubbles, liquid slugs flow upwards with dispersed bubbles. Although there is a falling film, the net liquid flow is upward.

- Churn flow: The gas phase flows upward, and the liquid phase presents a chaotic (oscillatory) flow. The gas velocity for this flow regime is not high enough to carry the liquid continuously upward. The liquid is transported upward through large waves. The liquid generally exhibits several gas bubbles entrained in the liquid film. More details about this flow regime are presented later in this section.

- Annular flow: The liquid flows continuously upward as a thin liquid film on the wall of the tube, and the gas flows in the core together with entrained liquid droplets. The gas-liquid interface exhibit disturbance waves, which usually travels faster the liquid substrate. These waves are described in the literature to be one of the sources for the formation of the liquid entrainment as droplets in the gas core, where small droplets are created by the shear process on the tip of the waves. Gas bubbles can also be found trapped in the liquid film, but they are usually in lower levels than encounter in churn flows. More details about this flow regime will also be discussed later in this section.

- Wispy annular flow: As the liquid velocity increases, the liquid film becomes thicker and the droplet coalescence of liquid leads to large lumps or streaks (wispy) of liquid in the gas core.

The occurrence of flow regimes in two-phase flows can be charted in a flow regime map. The flow regimes are represented in the chart as regions, where the coordinates are very often the superficial velocities (meaning the velocity of each phase if they are flowing alone in the tube) or combined parameters which include these velocities. An example of this type of flow regime map was developed by Hewitt and Roberts (1969), as illustrated in Figure 2.2. This map was created with experimental data for air and water at low pressures and for air and steam at high pressures.

It is important to mention here that the flow regime maps are merely a guide to indicate approximate boundaries for the transition between the flow regimes described. The transitions depend upon more complex physical interactions between the phases and thus, specific models have to be developed to determine each transition boundary. These maps should be generally used within the range of pressure and phases velocities in which they were developed.

The flow regimes that can be encountered before and just after the onset of liquid loading are believed in this work to be strongly related to annular and churn flow regimes (as it will be described later in this section). Therefore, an adequate description of both flow regimes should be the first step to develop proper understanding to

investigate liquid loading problems. Barbosa (2001) presented a review of the studies about these regimes and their transitions. In order to point out the major features of annular and churn flows in the literature, a review of the main studies which characterize both flow regimes are presented next.
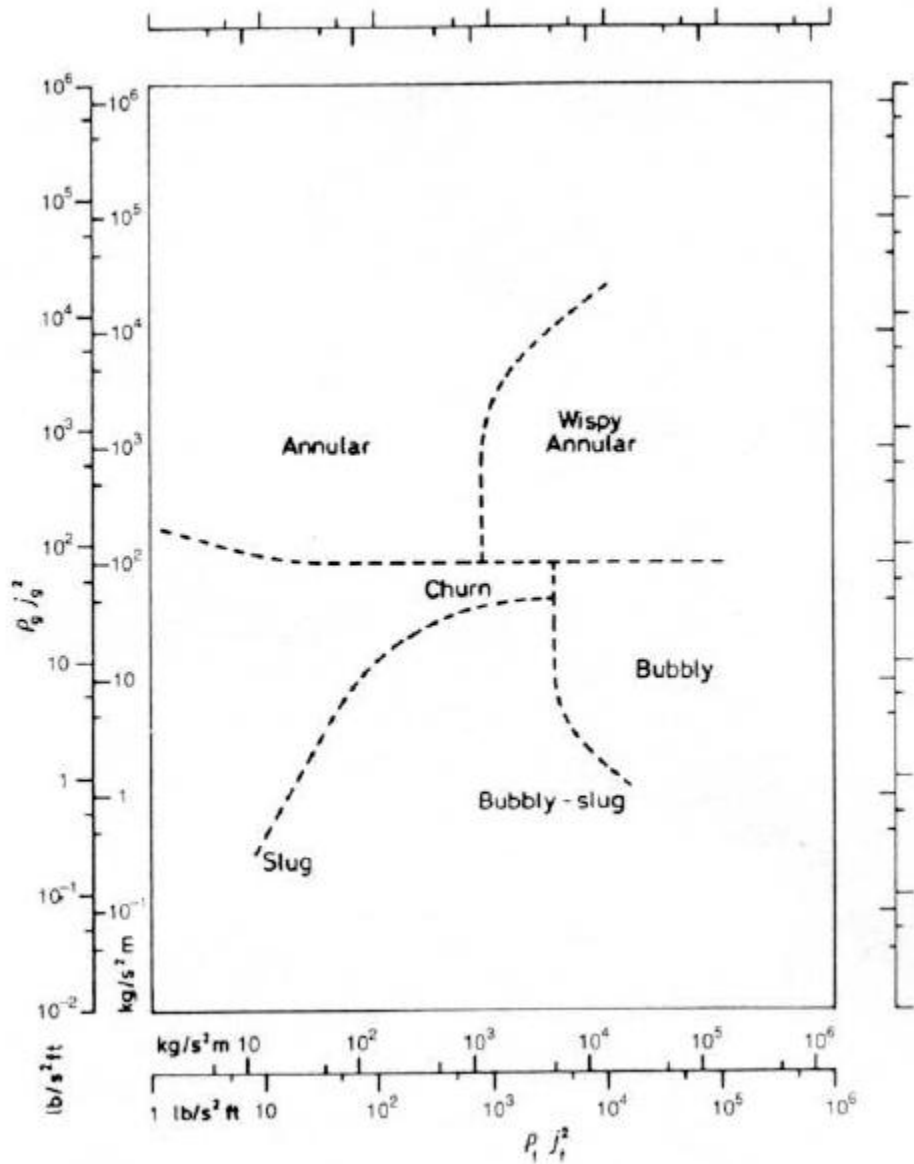
Figure 2.2 – Flow regimes map obtained by Hewitt and Roberts (1969) for vertical upward two-phase flows.

2.2. Annular Flow

Annular flow is described as a gas phase flowing in the core of the pipe, with the liquid phase travelling as droplets within the gas core and a thin liquid film flowing on the wall. A more precise schematic representation of the distribution and interaction mechanisms between the phases in co-current upward annular flow is presented in Figure 2.3.

As can be seen in the figure, the gas phase flows mainly in the core but it is also present in form of bubbles in the liquid film. The entrained gas bubbles are formed from the break-up of the waves of the liquid film and liquid droplet deposition. These trapped gas bubbles can be easily observed in the work of Schubring et al. (2010).

The liquid film can be briefly described as a rough liquid layer next to the pipe wall. The film present waves of different lengths and amplitudes (Azzopardi 1997). The waves are related to the gas core velocity, which act on the interface between the gas core and liquid film through the interfacial shear stress.

In the liquid droplet field, we can identify three main mechanisms:

- *Droplet entrainment mechanism*: liquid droplets are created from the wall film. The action of the gas core can break-up the tip of the waves, creating small droplets.
- *Coalescence*: droplets travelling in the gas core at faster velocities collide with the slower droplets just created from the wall film. The droplets then merge and form bigger droplets.
- *Deposition*: droplets travelling in core can be deposited in the liquid film, once these droplets can have random travel directions and often hit the wall film.

Azzopardi (1997) has done an extensive study regarding drops in annular two-phase flow.
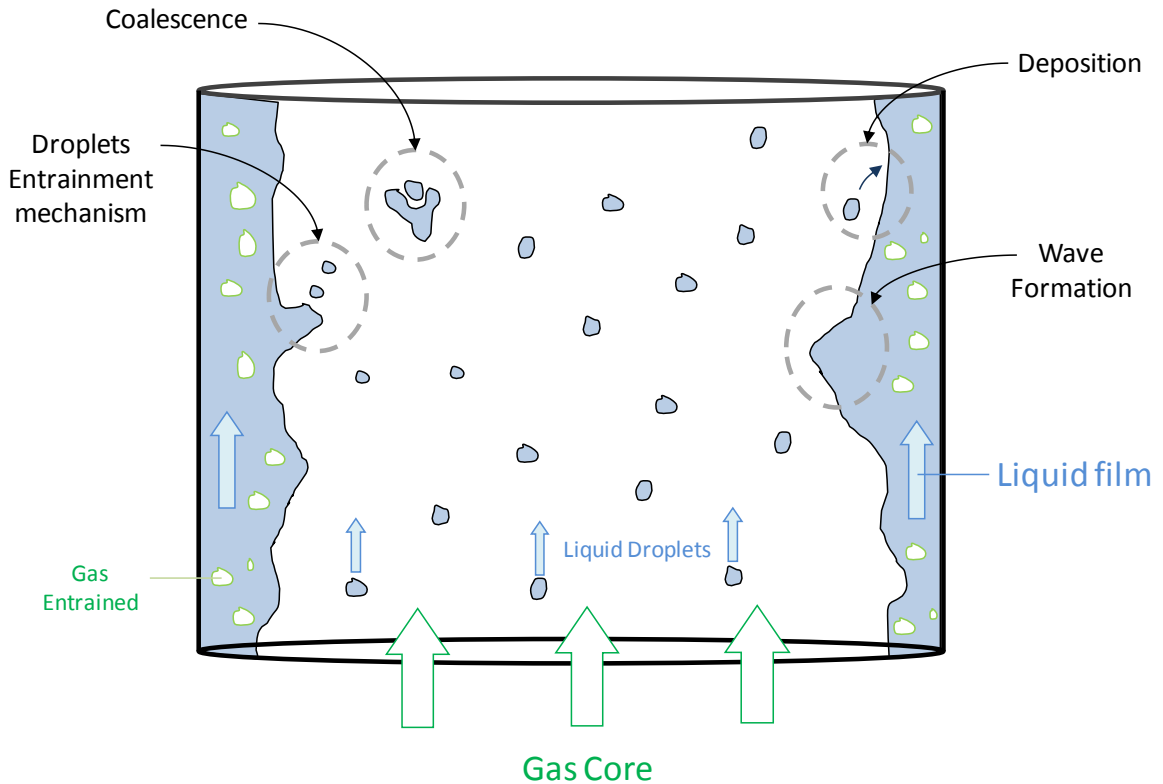
Figure 2.3 – Schematic representation of distribution and mass transfer mechanisms between the phases in annular flow.

2.3. Churn Flow

There is still a considerable disagreement in the literature about the physics and the transition to/from churn flow regime. One of the reasons for this confusion is the similarities in the phase's distribution between churn and annular flow. In churn flow, the distribution of phases is the same as in Figure 2.3 (which is for annular flow). However, the characteristics of the mechanisms in churn flow are considerably different when compared to annular flow. The main differences between these two flow regimes are as follows (Barbosa 2001):

- Hewitt et al. (1985) carried out an experimental investigation for annular flow for the region of minimum pressure drop gradient for the Figure 2.4. From their visualizations, using a dye tracing was possible to establish the mechanisms of churn flow, as shown in Figure 2.5. Liquid is transported

upwards in the film on the wall by large waves. However, behind these waves, there is a thin film that flow downwards. Part of the downward film flow is then picked up by the following large wave. According to the authors, this downward flow (called flow reversal) begins to occur in churn/annular region for $U_{gs}* \approx 1$. The dimensionless gas velocity presented in the figure is given by,

$$U_{GS}{}^{*} = U_{GS}\left[\frac{\rho_G}{gd_T(\rho_L - \rho_G)}\right]^{1/2} \tag{2.1}$$

- A breakdown of the slugs occurs between the transition from slug to churn flow, which intensifies the interfacial friction, increasing consequently the pressure gradient, as shown in Figure 2.4.

  After the dimensionless gas velocity reaches $U_{gs}* = 0.4$, the pressure gradient starts to decrease, due to the decreasing intensity of gas-liquid interaction. The pressure gradient then begins to increase again as annular flow is approached, due to higher levels of friction as consequence of elevated gas velocities.
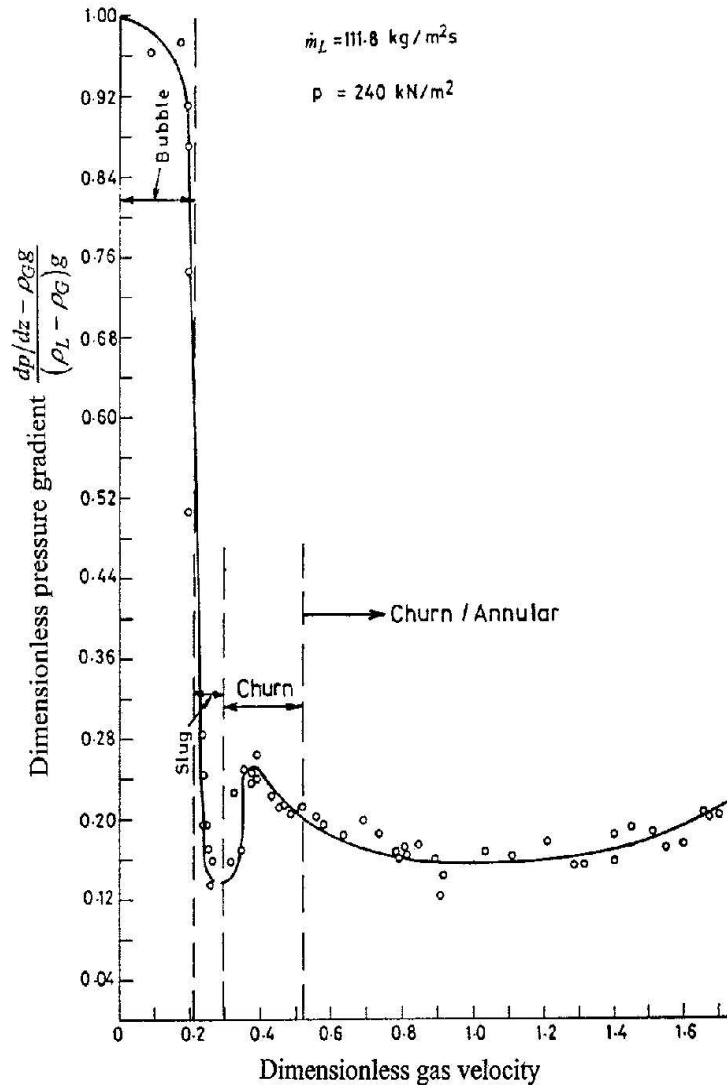
Figure 2.4 – Experimental results for dimensionless pressure gradient as a function of dimensionless air flow rate for different flow regimes (Owen 1986).
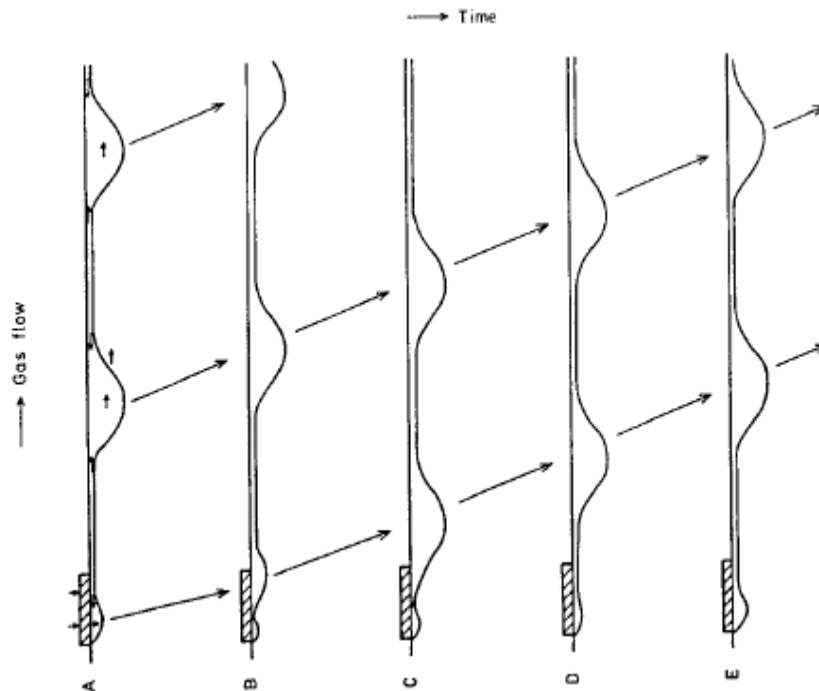
Figure 2.5 – Churn flow mechanism proposed by Hewitt et al. (1985).

- As described earlier, the main droplets creation mechanism is the action of the gas core on the liquid film waves. As large waves are formed in churn flow, higher levels of entrainment are expected to be found in this flow than in annular regime. Therefore, as can be seen in Figure 2.6, the liquid entrainment fraction decreases with the increase of the dimensionless gas velocity ($0.6 < U_{gs}* < 1$ – churn flow). For $U_{gs}* \geq 1$ (e.g., annular flow) the liquid entrainment fraction starts to increase again, but this effect is due to change in mechanism of droplets creation as described by Azzopardi (1997), from 'bag break-up' to 'ligament tearing' of the film waves.

A relatively large amount of work has been done about annular flow but only a few can be found about churn flow mechanisms and modeling (Hewitt et al. (1985); Govan (1990); Barbosa (2001); Da Riva and Del Col (2009)). Once liquid loading may occur within churn flow due to the flow reversal, further studies in this area seems to be needed to a better understanding of liquid loading phenomena.
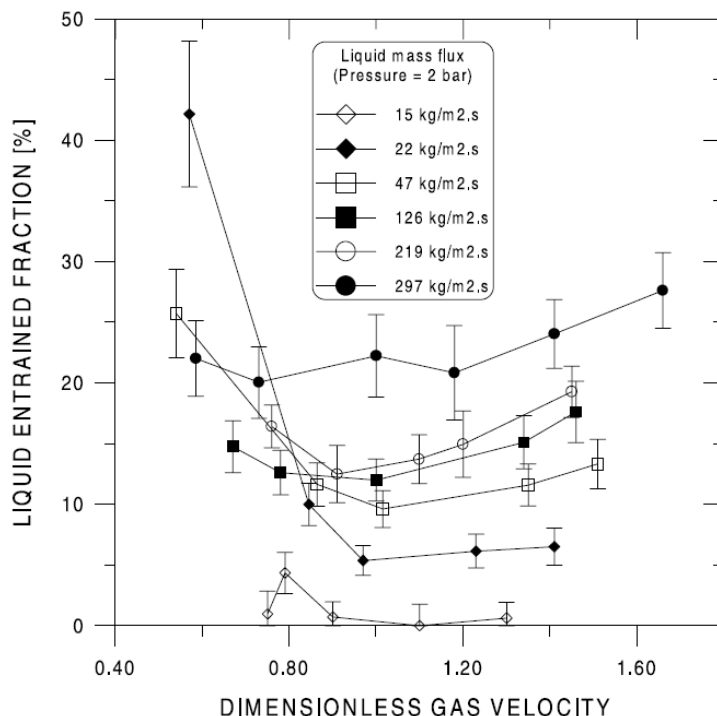
Figure 2.6 – Liquid entrainment fraction as a function of dimensionless gas velocity (Barbosa et al. 2002).

2.4. Experimental Characterization of Annular and Churn Flows

Modeling of annular and churn flows requires prediction of many mechanisms, such as interfacial phase interactions (liquid film velocities and gas entrainment), droplet deposition and entrainment. Very often techniques have to be specifically design to capture the unique features of these two flow regimes. Therefore, the next sections present some of the studies that have been carried out which designed experimental techniques to measure liquid film thickness and liquid entrainment in churn and annular flows.

2.4.1. Liquid film thickness

Most of the mechanisms in annular and churn flow are related to gas-liquid interfacial structure changing with time and space. Therefore, an accurate method to predict and measure liquid film thickness as function of time and space it is crucial for understanding the basic behavior of these flow regimes.

Belt (2007) developed a time and spatially resolved measurement technique of the film thickness in two-phase annular flows. The basic concept of this technique is to measure the electrical potential between two electrodes in contact with a liquid film. As the conductivity changes with the thickness of the liquid film, it is possible to correlate the potential change with the film thickness. This technique has been extensively used in the past (Coney 1973). However, Belt improved the application using a radial and axial distribution of the electrodes. The concept consists of having a series of electrodes flushed to the pipe wall (see Figure 2.7). Using this type of electrodes distribution, an image of the film thickness can be generated, as shown in Figure 2.8.
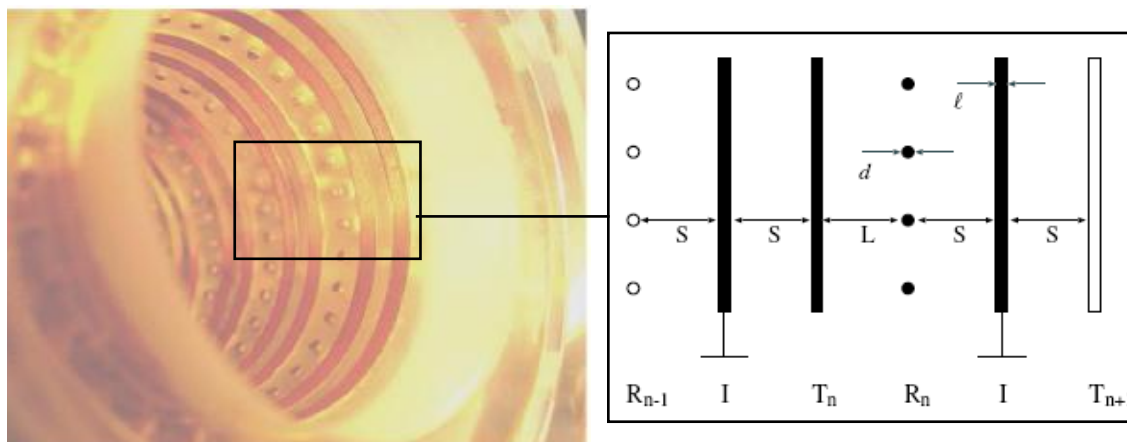
Figure 2.7 – Conductivity probe used by Belt (2007).

(a)

(b)
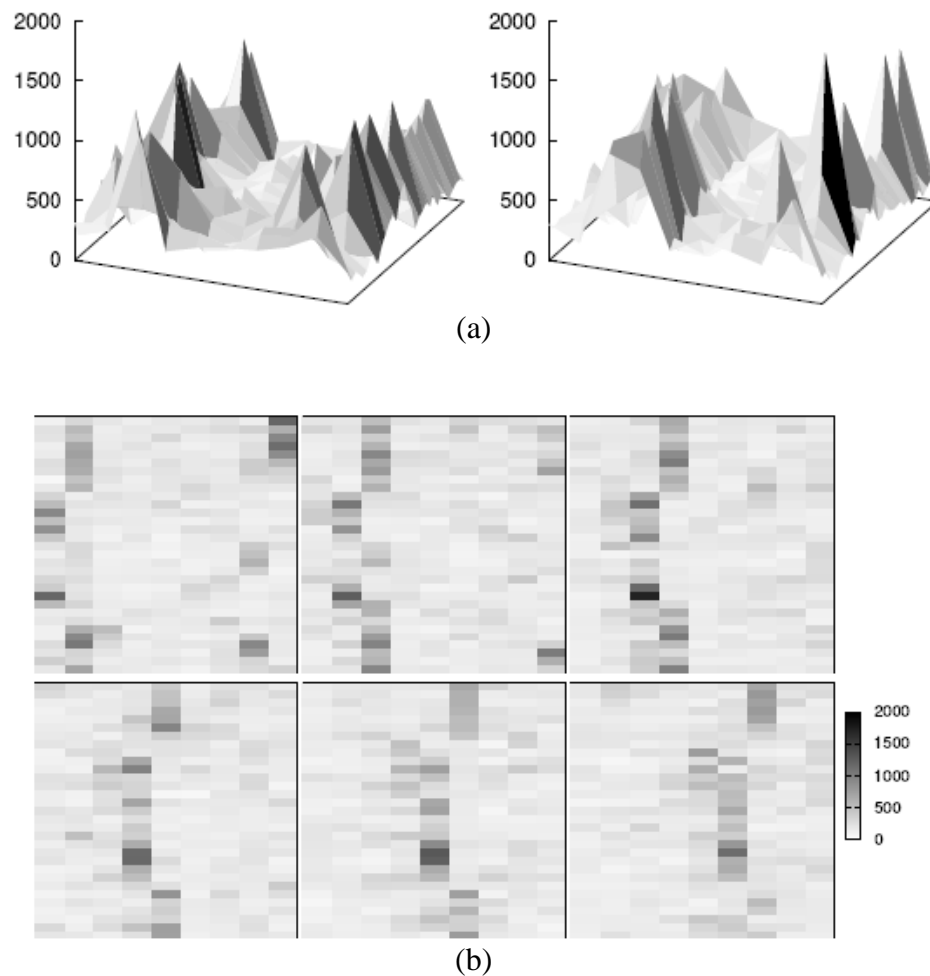
Figure 2.8 – (a) Three dimensional representation of the liquid film. (b) Consecutives snapshots of the liquid thickness measurement, obtained by Belt (2007). The film is flowing from left to right, and the pipe is open (the top and bottom are in contact) for easy visualization.

Although this technique can be used for fast transient and small thickness of the liquid film (200 µm), there is one main disadvantage: the maximum film thickness that can be measured corresponds to the distance between two consecutives electrodes (Coney 1973). Therefore, in order to measure higher levels of film thickness, the electrodes have to be more spaced, hence losing spatial resolution for the measurement. In other words, a single geometry sensor cannot cover wide ranges of gas and liquid flow rates. However, many sensors with different electrodes spacing can be placed in the

pipe to overcome this problem, since this type of sensor does not impose any kind of flow disturbance neither upstream nor downstream to the sensor.

The other problem that may interfere with this technique is the presence of bubbles in the liquid film. According to Belt (2007), the bubbles in the liquid film only become big enough to interfere in the measurement at superficial gas velocities smaller than those at which flow reversal starts.

Nevertheless, some methods which can account for the presence of bubbles in the liquid film measurements can be applied. Schubring et al. (2010) presented an optical technique to measure liquid film thickness in annular flow using Planar Laser-Induced Fluorescence (PLIF). A schematic of the test section used by these authors is presented in Figure 2.9. The authors used a Nd:YAG Laser to generate a sheet of light (allowing investigation of small portion of the flow), and a CCD camera perpendicular to the laser plane to capture the images of the liquid film. A fluorescent material was added to the liquid phase to enhance the contrast between the gas and liquid phases, improving the identification of the gas/liquid interface. In addition, they developed an imaging procedure algorithm to process the images and produce film height distributions.

(a)   (b)
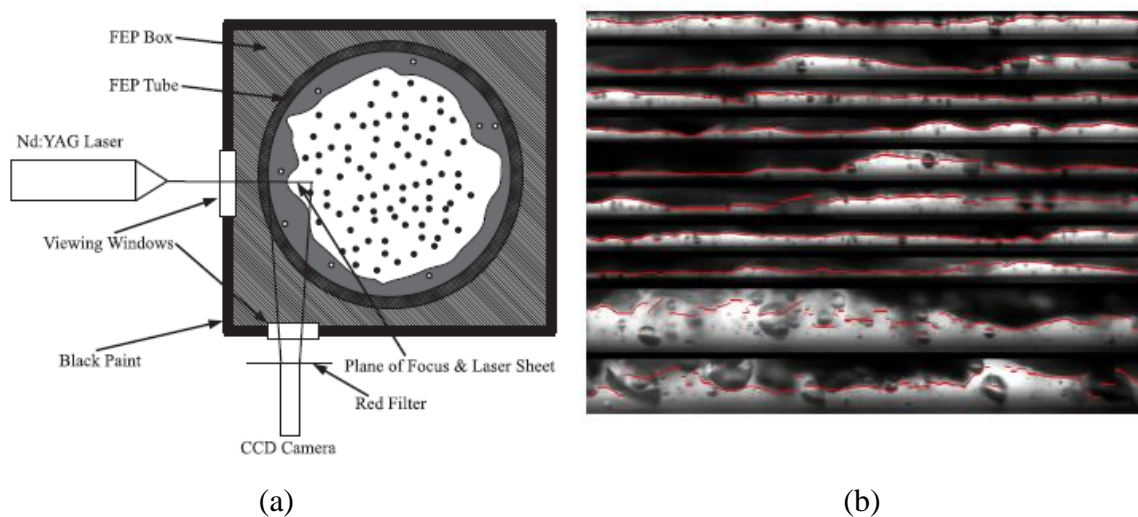
Figure 2.9 – (a) Test section set up for liquid film measurement using PLIF, and (b) images and film thickness distribution. The red lines show the processed film height by a imaging MATLAB code (Schubring et al. 2010).

As can be seen from Figure 2.9b, the images obtained by this technique generate a reasonable picture of the film thickness distribution (red lines in the figure). Also, we can easily see the presence of several bubbles entrained in the liquid film. This technique takes into account the presence of these bubbles in the film thickness measurement.

Although using an optical approach can consider entrained bubbles (which is not possible for conductivity probes), the identification of the gas/liquid interface by PLIF also presents some disadvantages related to the presence of large bubbles in the film. As can be seen in the last two pictures of Figure 2.9b, some blurred bubbles that are probably out of the laser plane make the identification of the interface more difficult. However, the authors carried out an uncertainty analysis and concluded that the total uncertainty for the average film thickness is between 15-25 μm (e.g., around 10-25% relative to the measurements).

To measure the bubbles entrained in the liquid film, Rodríguez and Shedd (2004) used a backlight imaging technique for adiabatic air-water horizontal annular flow. The set up consists of a CCD camera, a light source with a diffuser, and a digital image processing algorithm (NI IMAQ Vision Builder V6.0) to isolate the bubbles in the images, as presented in Figure 2.10.

(a)   (b)
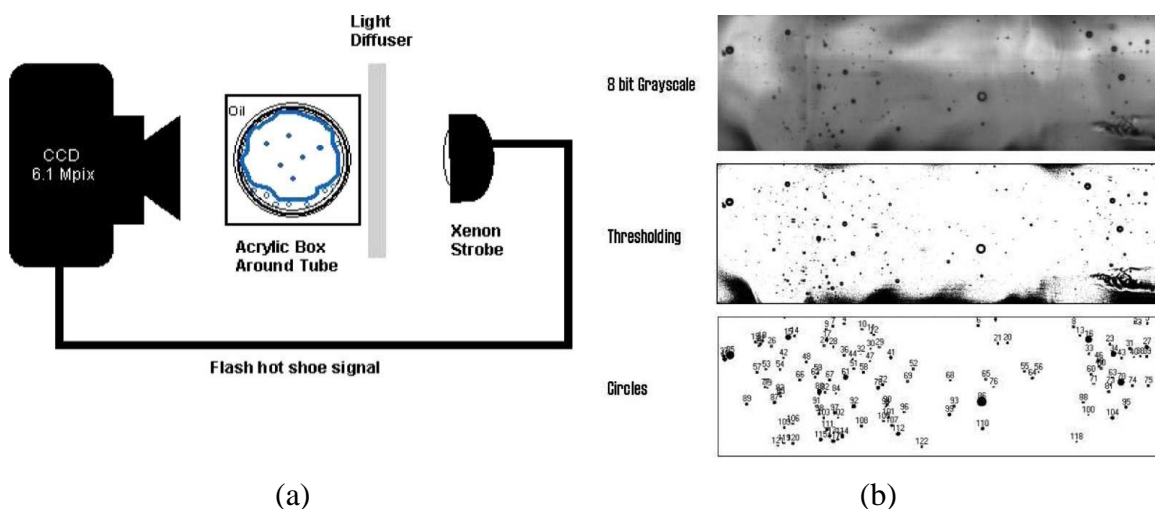
Figure 2.10 – (a) Backlight technique set up, and (b) images processing steps for bubbles identification (Rodríguez and Shedd 2004).

The main disadvantage of this technique is the presence of disturbance waves that are intermittently present in annular flow. When these waves pass through the section being recorded, the images do not provide enough contrast between the liquid film and the bubbles, as shown in Figure 2.11. Therefore, this technique can only evaluate the entrained bubbles for flow conditions that do not have the presence of waves.
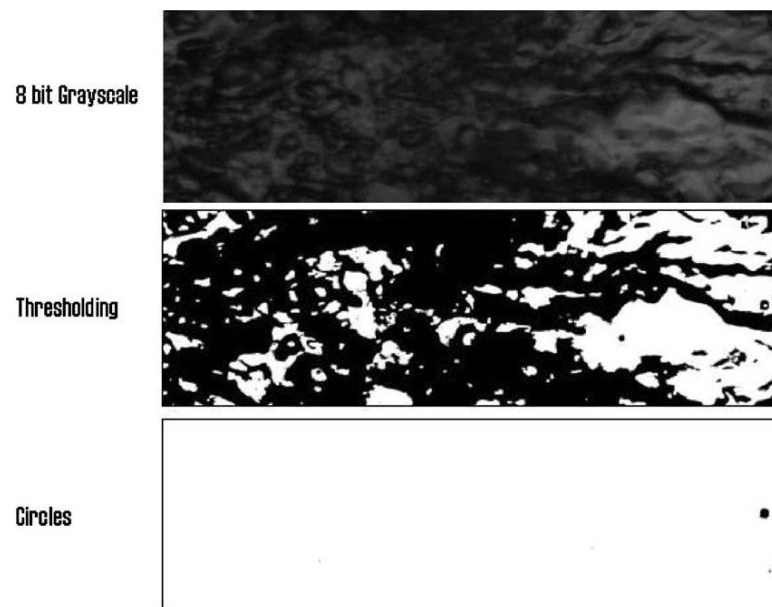
Figure 2.11 – Bubbles being "obscured" by disturbance waves when using backlight technique (Rodríguez and Shedd 2004).

Farias et al. (2012) proposed some enhancements of the technique described by Rodríguez and Shedd (2004). Their technique could obtain longitudinal and cross-sectional measurements of the liquid film. The optical set up for the cross-sectional measurements is shown in Figure 2.12.
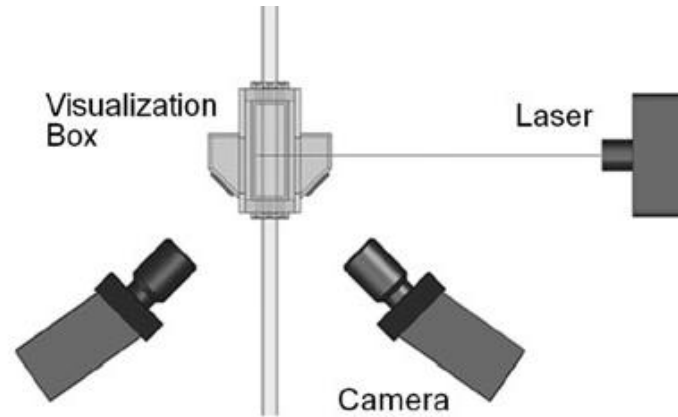
Figure 2.12 – Optical set up developed by Farias et al. (2012) for the cross-sectional measurement of the liquid film in horizontal annular flow.

2.4.2. *Liquid entrainment*

A considerable amount (up to 40% - see Figure 2.6) of liquid mass flux can be found as entrainment in the gas core in churn and annular flows. The entrainment can play an important role in the study and evaluation of two-phase flows. For instance, some mathematical models rely on correlations for the entrained fraction as closure relationship. Neglecting the entrainment on churn and annular flows can imply, for instance, in considerable errors in the pressure drop calculations for these types of flows (Bendiksen et al. 1991). Therefore, investigations regarding the entrained liquid are an essential part in the description of churn and annular flows.

Barbosa et al. (2002) presented an experimental investigation for the liquid entrainment fraction for the transition region between churn and annular flow. The authors used an isokinetic probe to measure the local distribution of gas and liquid mass fluxes. A schematic diagram of this probe is illustrated in Figure 2.13. An empirical correlation was proposed from the experimental results for the fraction of liquid entrainment (in %), which is given by,

$$e_f = 0.95 + 342.55 d_T{}^2 \sqrt{\frac{\rho_L \dot{m}_L}{\rho_G \dot{m}_G}} \tag{2.2}$$

where $\dot{m}_L$ and $\dot{m}_G$ are the liquid and gas mass fluxes, and d_T is the tube diameter. Eq. (2.2) is valid for $0.9 < U_{gs}* < 1.3$, $11 < \dot{m}_L < 334$ (in kg m^{-2} s^{-1}), $1.33 < p < 5.2$ (in bara) and $0.0127 < d_T < 0.0508$ (in m).
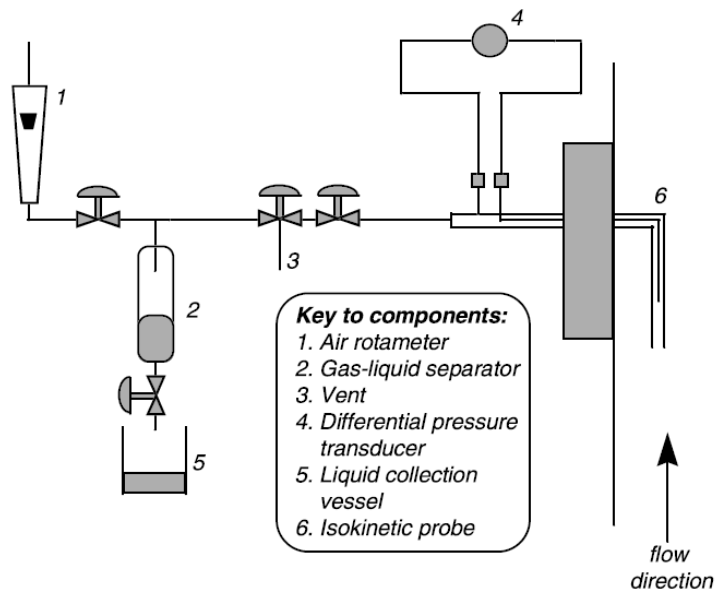
Figure 2.13 – Schematic diagram of the isokinetic probe used by Barbosa et al. (2002) to measure the entrained liquid fraction in churn and annular flow.

Their results also show that the pressure gradient and the liquid entrained fraction exhibit a minimum near $U_{gs}* \approx 1$. They concluded that this behavior should be related to the process of creation of the droplet entrainment (from the break-up of the waves present in churn and annular flows).

Westende et al. (2007) used a Phase Doppler Anemometry (PDA) technique to measure the entrained droplet-size and droplet-velocity at 15 locations in the tube-cross-section for churn and annular flow conditions. The main conclusion from their results was that for churn-to-annular flow conditions, only 0.4% of the droplet were moving at low velocities (< 3 m/s), and the droplet sizes were much smaller than predicted by the Turner et al. (1969) criterion (which is the most widely used model to predict the onset

of liquid loading in the oil and gas industry). According to Turner et al. (1969), at these conditions, most of the droplets would be expected to move to velocities close to zero. Thus, more experimental studies seem to be needed in this area to clarify this inconsistency.

2.5. Phase Fraction Measurement Techniques in Two-Phase Flows

Phase fraction is a dimensionless quantity relating the volume of one of the phases to the total volume occupied by all phases. Commonly, void fraction is the term used to refer to the gas phase, and holdup is the one to refer to the liquid phase. The sum of void fraction and liquid holdup must be equal to unity, hence, if one of these parameters is known the other one can be directly calculated.

The measurement of void fraction is essential in multiphase flow systems. This quantity is the key to determine numerous parameters such as mixture density, effective two-phase flow viscosity, in-situ velocities, prediction of flow regimes, and others. Falcone (2009) presented an extensive review of multiphase flow metering, which includes void fraction transducers. Silva (2008) carried out an extensive review of many types of impedance void fraction measurement techniques applied in multiphase flow systems.

A description of the main type of sensors presented by Falcone (2009) and Silva (2008) are given next.

2.5.1. *Conductivity and capacitance probes*

A common technique to measure void fraction, especially in research because of its low cost and simplicity, are the so-called electrical conductivity and capacitance probes. The basic idea behind both types of probes is to place electrodes in the perimeter of the pipe and measure the impedance between the electrodes, which can be related to the void fraction inside the pipe. For conductivity probes, electrodes are flushed in the inner wall of the pipe (Figure 2.14a) in order to measure the conductivity of the media inside the pipe. Hence, this technique requires a continuous phase which conducts

electricity and is in contact with the wall. The dispersed phase cannot conduct electricity. The capacitance probes do not require conducting phases, then they can be placed in the outer perimeter of the pipe (Figure 2.14b), and be applied, for example, for oil/gas flows. The capacitance probes measure the capacitance between the electrodes, which makes possible to deduce the void fraction in the pipe.

full-ring
electrodes

(a)   (b)
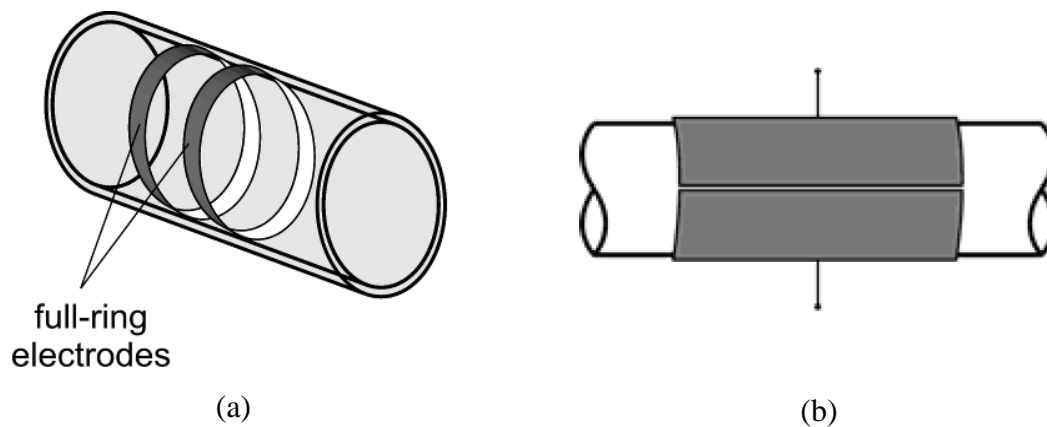
Figure 2.14 – (a) Conductivity and (b) capacitance probes (Silva 2008).

The two techniques described above are relatively easy to implement and have been widely used in research. As shown by Chun and Sung (1986), the accuracy for capacitance transducers technique is within the range of ±10% for different flow regimes. However, as can be shown in Figure 2.15, these authors did not test high levels of void fraction (95% or more). In their experiment the highest tested value for void fraction, α, did not exceed 80%.

The main disadvantage of impedance probes shown in Figure 2.14 is that these sensors can only provide measurements of average void fraction for the cross section area of the pipe, not providing the cross sectional distribution of the phases.
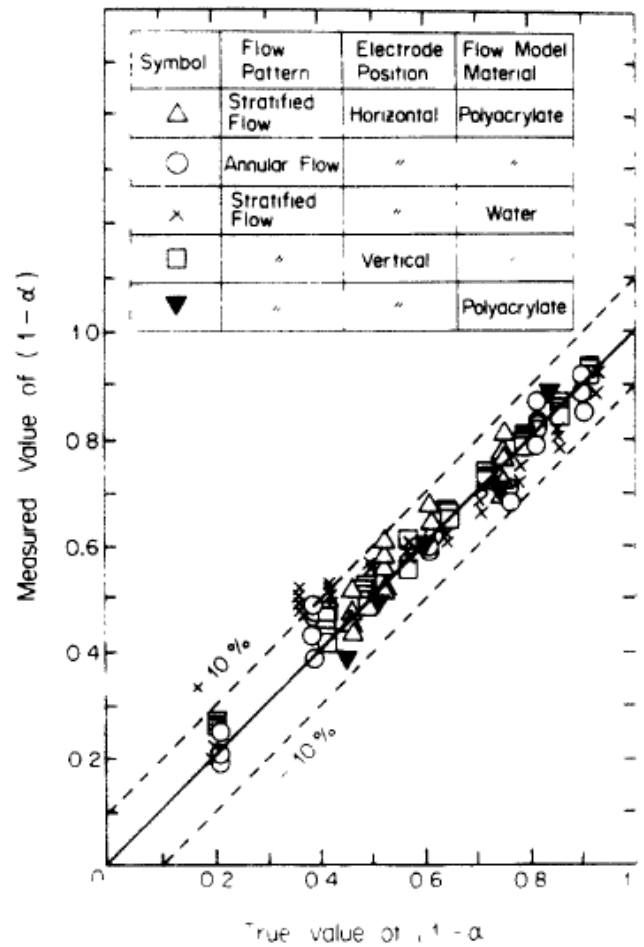
Figure 2.15 – True value against measured value using a capacitance probe for void fraction for different flow regimes and electrode position (Chun and Sung 1986).

The review made by Silva (2008) also included some types of impedance sensors to measure local distribution of void fraction through the cross sectional area of the pipe. More specifically, Silva has paid a special attention to one of them: the so-called wire-mesh sensors.

2.5.2. *Wire-mesh sensors*

Wire-mesh sensors are flow imaging devices that allow flow visualization of multiphase flows with high temporal and spatial resolution. A recent review about these type of sensors have also been carried out by Prasser (2008). The concept and results

examples of this type of sensor are presented in Figure 2.16 and Figure 2.17. Wire-mesh sensors basically consist of two sets of wires spaced axially, which measures the conductivity of the conducting phase. One set is composed by the parallel transmitter electrodes and the other one have parallel receiver electrodes. The sets are placed perpendicular to each other and their planes are also perpendicular to the flow main direction. The sensors electronics measures the local conductivity in the gaps of the crossing points of all transmitter and receiver wires at a high repetition rate. Considering a two-phase flow using air and water, the later is considered the conducting phase and air the non-conducting phase. Hence, the measurement of low conductivity between the transmitter and the receiver grid indicates the presence of the gas phase, which can then give a void fraction distribution along the cross sectional area of the pipe. A more detailed description of wire-mesh sensors principles and measuring techniques can be found in Silva (2008).
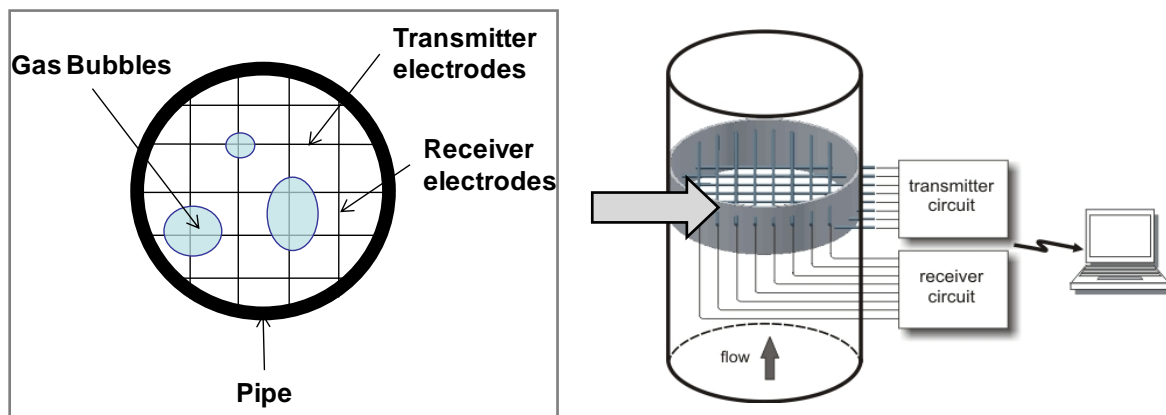
Figure 2.16 – Wire-mesh sensor concept (Silva 2008).
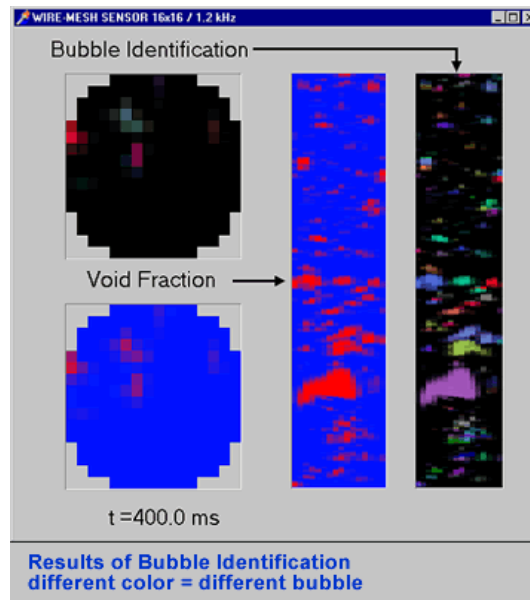
Figure 2.17 – Wire-mesh sensor measurement result example (Silva 2008).

The main advantages of wire-mesh sensors are the low cost and easy installation when compared with other techniques capable of measuring void fraction distributed along the cross section area of the pipe (tomographic flow imaging), such as X-ray and Magnetic resonant imaging (MRI).

The disadvantages of wire-mesh sensors are its intrusiveness, non-tolerance to presence of solid particles in the flow and difficulties to be deployed in flows with high void fraction (for instance, annular flows). The intrusiveness effect was investigated (Silva 2008) and the results have shown that the mesh only affects the flow downstream to the sensors. For industry applications this is a small drawback, once engineers are usually interested in measuring the void fraction, regardless of the disturbance downstream (unless there is an excessive pressure drop, which is not the case). On the other hand, for research purposes, the intrusiveness of wire-mesh sensors can be a considerable disadvantage. Many researches (especially in the present work) are interested to carry out investigations of void fractions in various different locations of the pipe simultaneously. Therefore, once we place one wire-mesh sensor; the flow will be disturbed downstream to the first sensor. This would not be a considerable issue if the investigators could work with only one measurement for each experimental run.

Difficulties regarding flows with high void fraction are more complicated to overcome. For annular flows, (e.g., when the flow exhibits a thin liquid film on the wall of the pipe), the grid of a wire-mesh sensor cannot reach the liquid film close to the wall without being very intrusive. Usually the thickness of the liquid film is from 0.5 to 4 mm (Zabaras et al. 1986) for high gas flow rates. Therefore, an extremely intrusive grid with wires spaced within 0.5 mm would be necessary to capture the entire range of liquid film thickness.

2.5.3. *Electrical capacitance tomography*

Electrical capacitance tomography (ECT) is another very promising tomography flow imaging technique. This technology has the main advantage of being non-invasive and non-intrusive, and it can track fast transients. In addition, it can work with the presence of solids and many different phases, for instance, with oil, water and gas simultaneously. The concept is based on the measurement of the variation of the electrical properties of the flow of the fluids involved, such as capacitance, conduction and inductance. Typical ECT systems consist of an array of several capacitance sensors (Figure 2.18). The measurements of all pairs of sensors are obtained and then combined (based on reconstruction algorithms) to generate a cross-sectional image of the flow. Figure 2.19 shows a representation of the arrangement of a typical ECT image results.
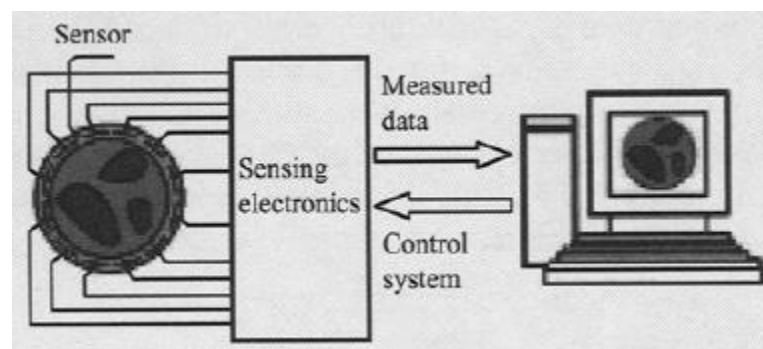
Figure 2.18 – Typical concept for ECT systems (Li et al. 2005).
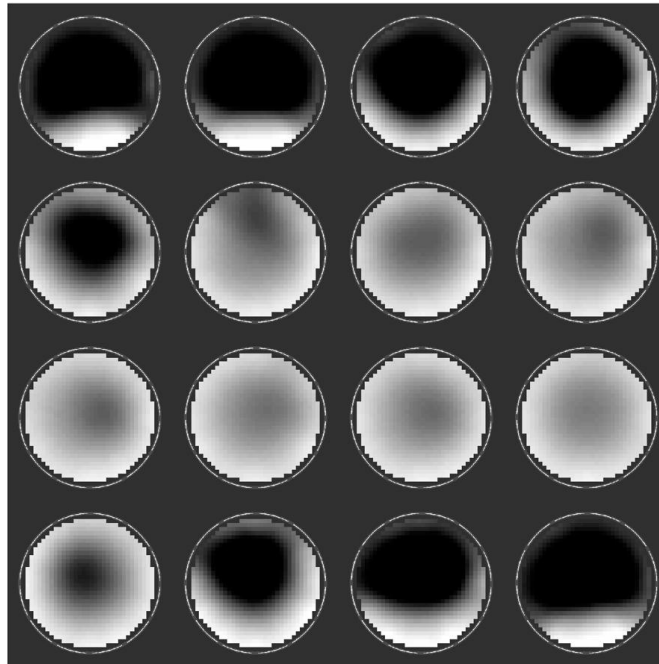
Figure 2.19 – ECT measurement result example for horizontal intermittent flow, with 50 ms between images (Gamio et al. 2005).

The main disadvantage of this system is the low spatial resolution, not exceeding more than 3% of the imaging domain, and the dependence of the reconstruction image algorithm by the flow conditions (Marashdeh 2006). For instance, Li et al. (2005) carried out a measurement of liquid film thickness using ECT technique in a thermosyphon experiment. Their results showed that, for high vapor rates, the ECT reconstruction image algorithms tested was not able to provide resolution high enough for liquid film thickness, where the errors reached up to 50% when compared to an analytical solution. This result also gives a good indication that, up to date, ECT systems might not be appropriate to measure void fraction of flows with high void fractions (e.g., higher than 80%).

2.6. Axial Flow Development in Two-Phase Flows

The characterization of axial flow development leading to transition between flow patterns has important practical applications, particularly for the types of

multiphase flows encountered in the oil and gas industry, where the length of pipelines are of the order of thousands of pipe diameters. State-of-the-art computer codes for the solution of multiphase flows in pipes rely on the identification of two-phase flow regimes (or flow patterns) for a proper selection of mechanistic models and closure relationships. Therefore, some works have been carried out recently to better understand and characterize the axial development of vertical two-phase flows.

For instance, Wolf et al. (2001) carried out an experimental study of the flow development in vertical annular flow. The authors measured local values of the pressure gradient, film thickness, wall shear stress, film flow rate, disturbance wave velocity and frequency for different gas and liquid flow rates. Among all parameters measured, the authors concluded that film flow rate and mean film thickness took a longer axial length to develop. The flow development of film flow rate and mean film thickness took more than 300 diameters, especially for lower air and higher liquid flow rates. Brown et al. (1975) have reported a similar behavior for more than 560 diameters for the same parameters, using a 31.8 mm internal diameter tube. Hazuku et al. (2008) using a laser focus displacement (LFD) meter also concluded that film thickness and wave frequency did not developed completely until the end of a 3 m long and 11 mm ID pipe. As the pipe lengths in the oil and gas industry are essentially much longer than that, the accurate prediction of the development of the flow and its characteristics for long lengths seem to be also critical for a better prediction of liquid loading and other two-phase phenomena.

One of the few studies about axial development of vertical flow regimes which includes churn flow was conducted by Julia et al. (2009). The authors carried out a work about axial development of flow regimes in vertical upward flow in annulus. They identified flow regimes based on more objectives parameters (such as void fraction fluctuations) rather than subjective observations (such as flow visualizations). The development of objective methods for two-phase flow identification is important particularly in axial flow development studies, because of the small axial changes that usually occur in short test sections, which are difficult to capture through visual observation only. The authors' results shows that the increase in the superficial gas

velocity between L/D = 52 and 230 was around 50%, for the churn flow conditions tested. However, only a few runs were carried out for churn/annular flows, since this flow regimes were not the focus of their work.

From the studies regarding axial flow development, it is clear the need of a flow loop with a longer axial length to further investigate the flow development in vertical two-phase flows. Such investigations could provide, for instance, a better understanding of the liquid film behavior, how film thickness and film flow reversal varies axially, and where it occurs. As described previously, a well characterization of the liquid film can be one of the keys to provide proper models for liquid loading phenomena.

2.7. Criteria for the Onset of Liquid Loading

The liquid loading phenomenon in gas wells is mainly related to the accumulation of liquids (condensate or water) downhole. It is believed that this accumulation begins when the gas production rate decreases below a certain level, when the gas cannot drag all the liquids to the surface anymore. The liquid accumulation causes a backpressure in the reservoir, which can significantly decrease the gas production rate.

An accurate prediction of the onset of liquid loading is a very important piece of information for production forecast and well operators. Once the well falls under liquid loading conditions, the production rate decreases sharply and, if no action is taken, the well can die rapidly. Therefore, if liquid loading is not taking into account, unrealistic production forecasts can be obtained, leading to wrong economics and maybe compromising the rate of return of the investments for a particular well.

The most widely used model to predict the onset of liquid loading in the oil and gas industry is the correlation developed by Turner et al. (1969). The main concept of Turner's model is based on a force balance on the largest liquid droplet entrained in the gas core, which considers the drag force exerted by the gas core and the buoyancy force on the liquid droplets. From this force balance, it is possible to calculate the minimum velocity to suspend the largest droplet present in the gas core. Turner's correlation assumes that if the gas velocity decreases below to this minimum, the liquid (in the form

of droplets) will fall in the wellbore and accumulate downhole. Turner et al have compared their model with field data for tubing ID ranging from 1.995 inches (0.05 m) to 7.386 inches (0.19 m), and gas flow rates ranging from 400 Mcf/D (11,000 m^3/D) to 11,767 Mcf/D (333,000 m^3/D). More discussions about Turner's droplet model as presented in section 5.1.

However, as pointed out by some authors such as Coleman et al. (1991a) and Zhou and Yuan (2010), Turner's correlation does not predict the onset of liquid loading in quite a few number of wells, underestimating the triggering of liquid loading. In fact, no direct observation has been found to the assumption that liquid loading occurs due to droplets falling in the wellbore.

Many authors (Coleman et al. (1991a), Guo et al. (2006), Nosseir et al. (2000), Veeken et al. (2009)) have proposed refinements and modifications to Turner's criterion. These several attempts to change Turner's model may indicate that maybe not all physical mechanisms are considered in his model.

With the aim of better understanding the role of the droplets in liquid loading, Westende et al. (2007) carried out an experimental investigation for measuring droplets size and velocity for churn and annular flow conditions. These authors found two reasonable evidences in opposition to Turner's concept.

The first evidence was related to the droplets size. Based on Turner's model, they could calculate that for an air-water system the maximum droplet diameter is about 8.5 mm. From their literature review they observed that, for the same system, the maximum drop diameters are about 2 mm only. Also, the waves in the film wall are in general much smaller than the maximum droplet diameter predicted by Turner's correlation. Therefore, to generate drops of the order of magnitude predicted by Turner, coalescence have to be strong. This is not really expected due to the much dispersed condition of the droplets on the gas core.

The second and stronger evidence against Turner's model is the measurement of the droplets size and velocities. As proposed by Turner, for liquid loading conditions, droplets should start to fall when the gas core goes below the minimum critical velocity. Consequently, velocities smaller or equal to zero are expected to be found under liquid

loading condition. From Westende et al. (2007) observations in churn/annular flows region, only a few droplets (0.4%) were found to have velocities close to zero. In addition to that, the maximum diameter detected was about 350 μm, which is much smaller than the 8.5 mm earlier estimated based on Turner model. Hence, we can expect that the droplets falling in the pipe have a weak or no effect in liquid loading.

Once the accumulation of liquid downhole is not strongly linked to the droplets for churn/annular flows, it has to be mainly caused by the liquid film flow reversal. As described earlier, Hewitt et al. (1985) have observed the flow reversal in churn/annular flow in their experiments, using a dye tracing in the liquid and video records of the flow. Zabaras et al. (1986) confirmed the occurrence of flow reversal in these flow regimes, but using a different technique (measuring the wall shear stress). Using a probe based upon the mass transfer coefficient of a diffusing species, Zabaras et al. were able to measure the wall shear stress, and then, the direction of the flow based on the sign of the measured value. Figure 2.20 presents the results obtained by the authors for average pressure gradient and time fraction for wall shear stress directed downward.

The authors stated that the minimum in the Figure 2.20a corresponds to $U_{gs}^* = 1.06$ ($W_G \approx 5.5 \times 10^{-2}$ kg/s), which goes also in agreement with the studies of Owen (1986) (see Figure 2.4). We can clearly see from Figure 2.20b that we have downward film flow for $W_G < 5.5 \times 10^{-2}$ kg/s. In addition, we can conclude that above the point of minimum pressure gradient, the flow reversal ceases.

The works of Govan et al. (1991) and Barbosa et al. (2001) can illustrate even further that liquid downward flow should occur due to the falling of the liquid film. Govan et al. and Barbosa et al., through experimental measurements and visualization of the downward falling film, could confirm that below a certain gas flow rate level, there is a reasonable amount of liquid that falls into the pipe in the form of a wall film. The work of Veeken and Belfroid (2010) also revisited the root causes of liquid loading and concluded that, based on experimental observations and in multiphase flow simulations, flow reversal seems to be the major cause of liquid loading.

(a)   (b)
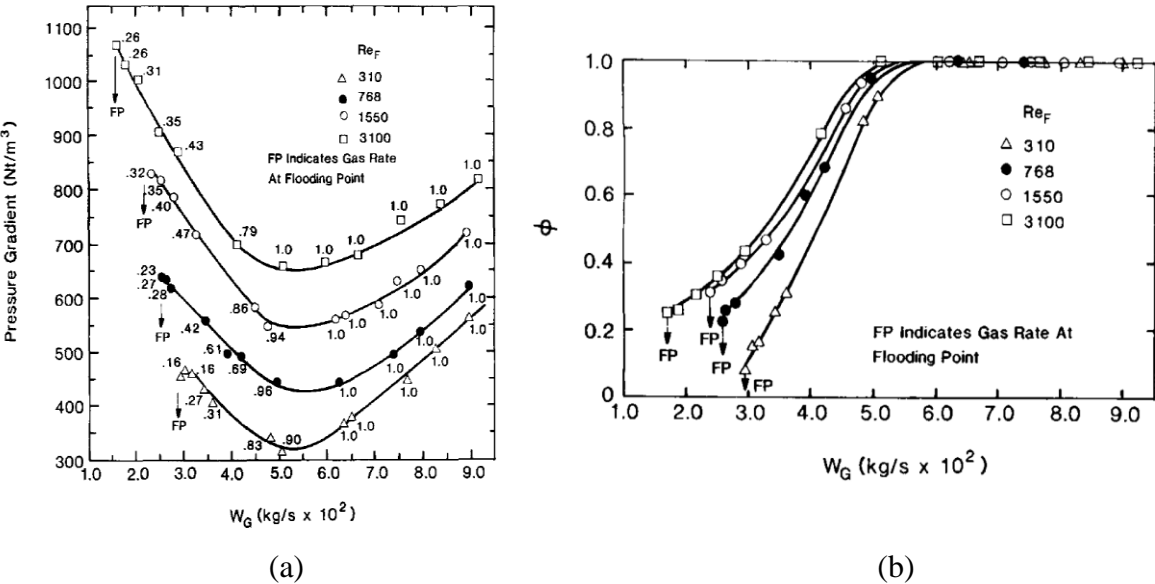
Figure 2.20 – (a) Average pressure gradient, and (b) Time fraction, Φ, of wall shear stress directed downward (Zabaras et al. 1986).

2.8. Modeling Reservoir/Wellbore Interaction During Liquid Loading

The previous sections described some of the correlations available in the literature that can be used to indicate the onset of liquid loading. However, these correlations rely only in the fluid flow in the wellbore without considering the inflow behavior from the reservoir. The reservoir inflow behavior is the one which dictates the fluid flow (e.g., the gas velocity) in the wellbore, and thus, should be taken into account for properly modeling of liquid loading.

The most used technique to predict liquid loading (considering the reservoir inflow) is the so-called nodal analysis (Lea et al. 2003). This model consists of plotting the reservoir inflow performance relationship (IPR) with the wellbore curve. The point of intersection between these two curves gives the operating point, indicating the gas rate and flowing bottomhole pressure at which the well will operate, as illustrated in Figure 2.21. If the operating point is to the right of the minimum pressure in the wellbore curve, the well is under stable conditions and no liquid loading symptoms should be observed. If this point is to the left of the minimum, it is considered as unstable condition and liquid loading problems should be expected. A brief explanation about the

stable and unstable operating point in nodal analysis is presented in section 5.1. A detailed description of the behavior of the stable and unstable operating point can be obtained from Lea et al. (2003).
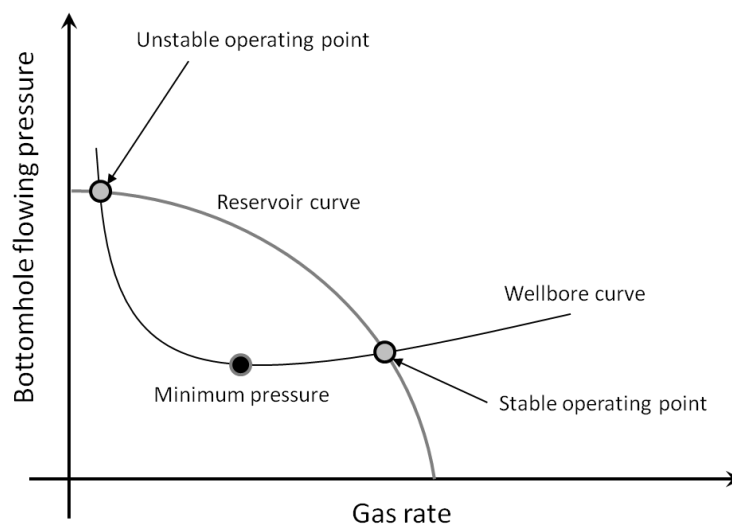
Figure 2.21 – Nodal analysis technique used to predict liquid loading in gas wells. The intersection between the reservoir and wellbore curve defines the operating gas rate and bottom hole flowing pressure for a particular production system.

However, nodal analysis is a steady state approach, while liquid loading phenomena is transient in nature. Nodal analysis considers pseudo-steady steady conditions for the flow in the wellbore and steady-state conditions for the inflow performance for the reservoir. Solomon et al. (2008) made a critical review of some of the liquid loading models, evaluating transient models for either wellbore and reservoir flow. The authors indicated that most of the models still remain missing the possible re-injection of heavy fluids back into the formation, which is expected to occur under transient conditions.

In order to capture some of the liquid loading transient characteristics, Belfroid et al. (2008) used a commercial transient multiphase flow simulator (Bendiksen et al. 1991) for the wellbore and a steady-steady inflow performance relationship for the reservoir.

Their study had the objective of evaluating the onset prediction and dynamic behavior of liquid loading in gas wells. In this study they investigated the effect of tube inclination and reservoir parameters such as permeability, Darcy and non-Darcy resistance parameters on liquid loading predictions. Using actual production data, the authors could verify that reservoirs with higher permeability are more prone to liquid loading issues than the ones with lower permeability. The system with higher permeability cannot cope with small changes in liquid content and became unstable earlier in the well life. Figure 2.22 shows an example of this behavior. The parameter "*A*" (called Forcheimer Darcy inflow resistance) in the figure is directly proportional to the reservoir permeability. The larger the *A*, the higher the permeability. The figure shows that, if LGR changes from 500 to 750 when $Q_{gas} = 4$ and A = 0.1, the well stop producing. However, when the same analysis is made for A = 4, the well will still flow in a stable condition for the same change in LGR.
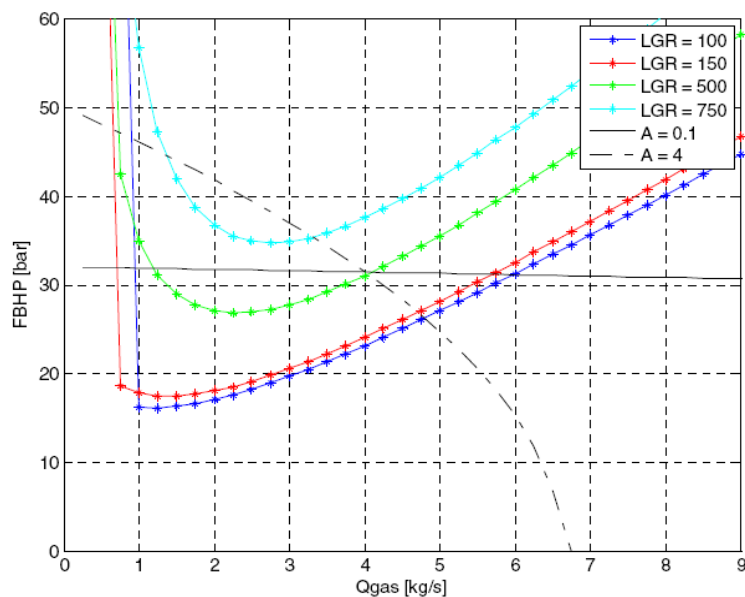
Figure 2.22 – Reservoir inflow performance relationship and wellbore performance curves for different liquid gas ratios (LGR) and reservoirs resistance parameters (A) presented by Belfroid et al. (2008).

Veeken et al. (2009) also applied the same commercial package to investigate the onset of liquid loading using the transient model for the wellbore and a steady-steady model for the reservoir. The authors defined the onset of liquid loading as the point when a rapid decline in the gas flow rate occurs. Then, at this condition, they plotted a profile of some parameters as a function of wellbore length, as shown in Figure 2.23. As can be seen in the figure, the onset of liquid loading is followed by a flow reversal (indicated by the point where water film velocity is equal to zero). It is also indicated in the figure that the flow reversal starts at the wellhead. Curiously, the result of flow reversal provided by simulator is obtained for annular flow, which goes against the studies on flow reversal (Hewitt et al. (1985); Govan et al. (1991); Barbosa et al. (2001)) which says that this mechanism starts on churn flow. This is probably because this commercial package still does not consider a model for churn flow regime.
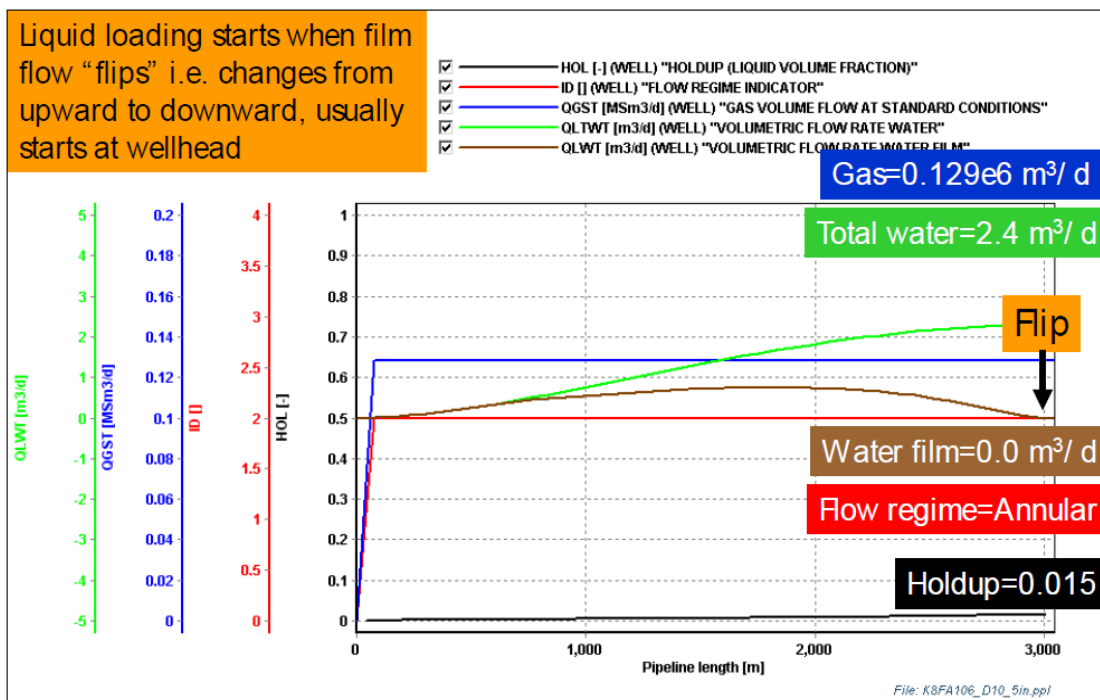
Figure 2.23 – Simulation results for onset of liquid loading in a vertical well obtained by Veeken et al. (2009).

To understand the transient behavior in the reservoir related to liquid loading phenomena, Zhang et al. (2010) developed a model to capture the transient fluid flow behavior in the near-wellbore reservoir region. The authors showed that bottomhole pressure oscillations create a "U-shaped" curve in the pressure profile around the near-wellbore region, as illustrated in Figure 2.24. The reason for this profile is the difference in time scale between the pressure variation in the wellbore and reservoir. While the pressure oscillations in the wellbore vary in the order of milliseconds, the pressure waves in the reservoir travel in the order of minutes or hours. The "U-shaped" pressure profile indicates that re-injection of heavier fluids into the formation is likely to occur. The simulation results obtained from the fully transient model developed Zhang et al. confirmed the backflow into the reservoir.
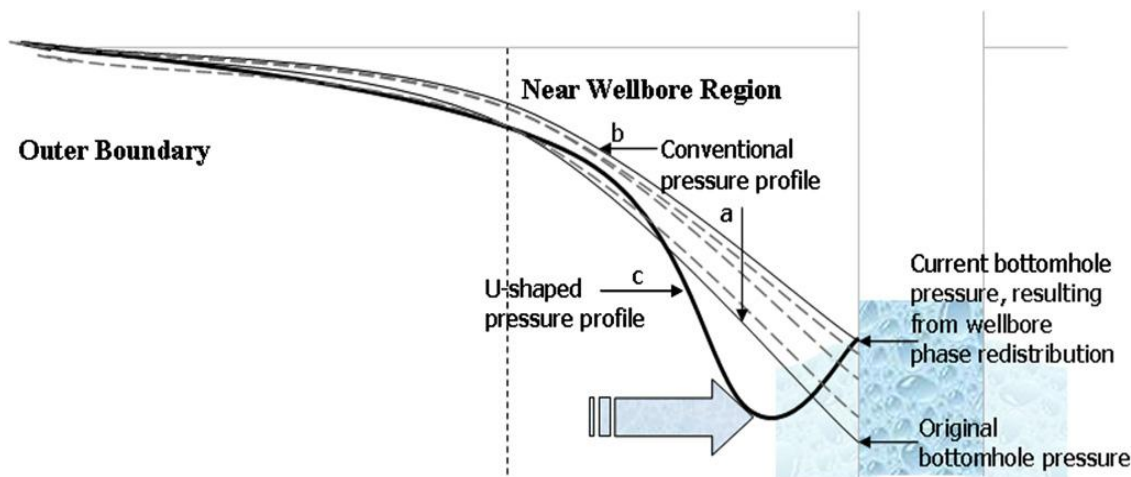
Figure 2.24 – Schematic diagram of the "U-shaped" curve obtained in the pressure profile around the wellbore for the simulation model developed by Zhang et al. (2010).

However, one of the main limitations of the model of Zhang et al. (2010) is that the wellbore pressure oscillations used as boundary conditions were created artificially, without the use of a coupled transient model for the wellbore.

Sagen et al. (2007) have developed a transient coupled near-wellbore reservoir and pipeline model, to study the dynamic interaction between wellbore and reservoir.

Their results showed that there are considerable differences when using a near-wellbore reservoir model and a steady-state performance inflow model approach. However, the simulation results could not be experimentally validated at that time.

Hu et al. (2010) used the wellbore-reservoir integrated dynamic model developed by Sagen et al. (2007) to evaluate well cycling performance with the objective of enhancing production of wells prone to liquid loading conditions. Hu et al. presented simulation results showing that the model could be used to predict the time before excessive liquid loading can take place. Then, having the information about this time, the authors suggest that the well operators could start cycling the well and avoid liquid loading. It was concluded from the results that the use of such a model would be essential to properly estimate the right time to start cycling the well. However, no experimental or field data where used for verification of these results.

Sagen et al. (2011) used the same reservoir integrated model to analyze chemical placement into the formation and start-up scenarios. To investigate this type of procedure, dynamic simulations are believed to be essential due to transients occurring in these operations either in the wellbore and near-wellbore region. From their results they concluded that the dynamic coupled model could be used successfully to simulate such operations. To confirm their conclusions, they included comparison with filed data measurements for the chemical placement operation, which showed reasonable agreement with the simulation results.

2.9. Summary

From the literature review presented here, is clear to see that there still some inconsistency in the understanding of churn flow behavior. One of the main reasons for that is related to the lack of studies regarding the experimental characterization of churn flow regime. Thus, more experimental investigation is recommended in this area. Besides the few studies regarding churn flow, only a small number of works were found discussing axial characterization of two-phase flows in general. Since the length of pipelines are of the order of thousands of pipe diameters in the oil and gas industry, a detailed understanding of the behavior of two-phase flows in the space and time is

essential for the development of models to be used in the evaluation of well performance.

In order to measure liquid holdup (one of the main parameters to experimentally characterize two-phase flows), the most suitable type of sensor was found to be the conductance probes, because of its low cost and simplicity. Also, the average liquid holdup can be obtained with a relatively good accuracy (around 5-10%) using conductance probes. Further description about the type of conductance probe deployed in this work will be discussed in more details in the next section.

There are different criteria available in the literature which indicates the onset of liquid loading. However, there is a clear inconsistency in the root mechanism related to these models. Therefore, further investigation should be carried out to understand further the key mechanisms and parameters involved in the liquid loading onset.

Nodal analysis is widely used as a model technique to evaluate liquid loading. However, liquid loading is a transient phenomenon in nature. Thus, nodal analysis cannot be used to advanced investigations about liquid loading, but only for preliminary evaluations. It is clear to see from the works of Zhang et al. (2010), Hu et al. (2010) and Sagen et al. (2011) that fully transient models for both wellbore and near-wellbore reservoir region should be deployed to predict and study liquid loading, especially to capture the transient nature of the liquids being produced from the wellbore and re-injected back into the reservoir.

3. LARGE SCALE FLOW LOOP - TOWERLAB

3.1. Introduction

In actual oil and gas systems, the wellbores are usually more than one thousand meters long. In the study of multiphase flows in wellbores, the importance of the tube length can be related to the development of the flow regimes throughout the pipeline. In short tubes (L/D < 300), fully-developed flow is usually difficult to obtain. Measurements of the axial behavior of two-phase flows would be even more complicated in such short tubes. There are only a few facilities available for research around the world that features long vertical tubes (L/D > 500). As a consequence, the experimental axial characterization of two-phase flows is very limited in the literature. Therefore, a large scale flow loop was designed and built in this work, which is called TowerLAB.

From the literature review carried out by Fernandez et al. (2010), it was concluded that TowerLAB is one of the longest research flow loop around the world, as illustrated in Figure 3.1. This feature provides an attractive and unique opportunity to study the fundamentals of liquid loading and flow development in two-phase flows, since the longest flow loops presented in Figure 3.1 are from private institutions. Generally private flow loops are more focused in applied studies, such as calibrating and validating flow models or testing new tools for the industry. The limited number of long vertical flow loops is believed here to be one of the reasons for the lack of studies regarding axial characterization of two-phase flows.

Overall, the higher the vertical test section, the closer the experimental results can be compared with the real field scenario for the oil and gas industry. An active length of approximately 43 m was selected to be used as a test section in the TowerLAB, since this is the total length available in the building.

The vertical layout for the test section in TowerLAB has the main objective of reproducing and analyzing liquid loading in vertical wellbores. In other words, the aim of the flow loop design is to visualize the liquid transport along the vertical tube and

measure the associated changes in flow regimes, pressure and liquid holdup during steady-state and transient conditions, and correlate the measurements with the predictions from models available in the literature.
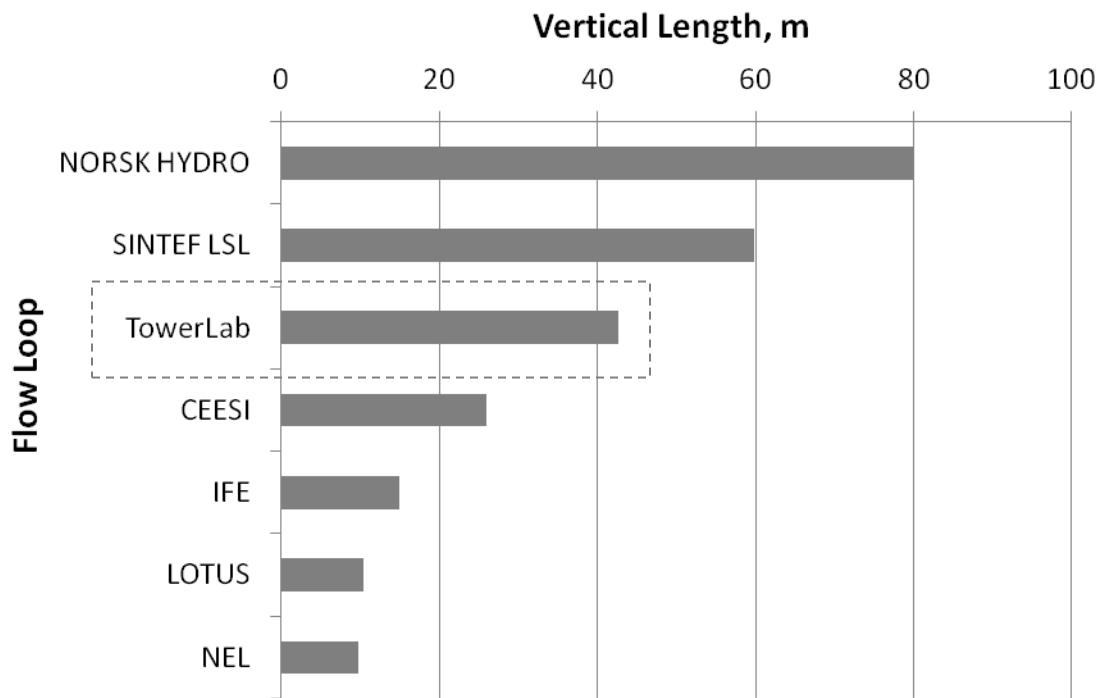
Figure 3.1 – Comparison of vertical test section length for research flow loops around the world (Fernandez et al. 2010).

Several challenges were faced to downscale the flow conditions and facilities dimensions from the field to the lab, particularly regarding the field fluids (oil and natural gas), high pressures (from 2,000 to 50,000 kPa), downhole completions and reservoir characteristics.

Previously to this study, Fernandez et al. (2010) carried out a preliminary design for a new configuration for TowerLAB which included a high-pressure air compressor (with a delivery pressure of approximately 3,000 kPa) and a porous medium to be attached to the bottom of the vertical test section. The design proposed by Fernandez et

al. would allow the experimental investigation of the dynamics between vertical two-phase flows and a porous-media reservoir at high pressures. As previously described, there are strong evidences that the liquid loading symptoms observed in the field are mainly consequences of the interaction of the multiphase flow in the wellbore with the fluid flow in the reservoir.

However, the funds available for the current research project did not allow the purchase of the air compressor and the vessel for the porous medium design by Fernandez et al. The design including a more powerful air compressor and a porous-media vessel should be considered as future research, when more funds should be available to upgrade TowerLAB. Additionally, the use of high pressure would limit the visualization of the flow to observation windows only. The use of continuous transparent tubes is only allowed for lower pressures, since the working pressures for the tube material currently available in the market can only support up to 1,000 kPa.

The use of real fluids such as oil and natural gas can significantly increase complexity of the results analysis, because of the complex interaction between the phases and the many different components present in petroleum fluids. Also, the use of such fluids is limited because of the constant risk of fires and blowouts, since oil and natural gas an extremely flammable. Thus, the use of simpler fluids such as water and air is recommended for fundamental investigations, which is the case of the present study. These simpler fluids can make the results analysis less complex and the basic mechanism of liquid loading – such as film flow reversal and flow regime transitions- can be analyzed with improved accuracy. Of course, more advanced studies should be carried out as future work to understand the impact of the multi-component fluid on liquid loading.

The inclination of the of the tube has also a considerable effect in the liquid loading behavior (Belfroid et al. 2008). Therefore, different tube inclinations such vertically inclined, horizontal and undulated wells should also be considered in the study of liquid loading. However, in the present investigation only a vertical test section was considered, since the fundamental mechanisms and models for vertical wells still seemed

to be weakly understood. Future upgrades in TowerLAB should then consider different test section inclinations to further investigate liquid loading phenomena.

The main idea behind the concept of TowerLAB for this work is a vertical flow loop designed to carry out experimental investigations on vertical two-phase flows for a range of pressures and air/water flow rates in a long vertical tube. The flow loop design consisted of three basic parts:

- Boosting system: is located in the basement and consist of two air compressors and a centrifugal pump, which control the pressure and flow rates of the working fluids.

- Test section: vertical transparent tubing (see Figure 3.2) that goes throughout the tower and has a total vertical length of 43 m, which is instrumented for the measurement of pressure, temperature and liquid holdup. Video cameras also allow the visualization of the two-phase flow in four different positions of the test section.

- Separator: is located at the 10th floor (top of the flow loop) and consist of a 0.57 m^3 capacity separator, which separates the air from the water, venting the air to the atmosphere and returning the water to the water tank located in the basement.

The TowerLAB is located at the Joe C. Richardson building in the Petroleum Engineering Department and starts from the basement and goes up to 43 m, covering the entire height of the building (Figure 3.3). In the past, there was a previous facility built in the TowerLAB. However, this new investigation completely re-designed and enhanced the operating conditions in terms of working pressures, flow rates, instrumentation and layout, enabling to evaluate multiphase flow conditions which were not possible with the previous configuration.

TowerLAB has an available surface area of 4.8 m^2/floor for piping and instrumentation (Figure 3.4). All these features of the facility present an attractive opportunity to conduct innovative research in areas related to integrated oil and gas production systems.
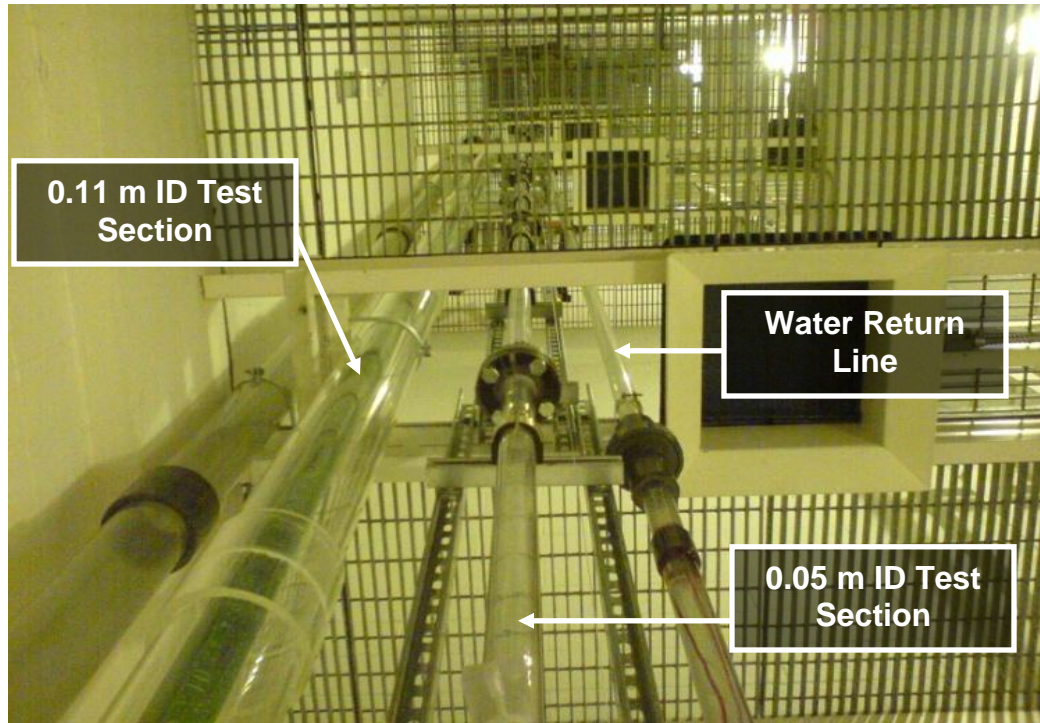
Figure 3.2 – Picture showing the different test sections available in TowerLAB. This picture was taken looking from bottom to top.
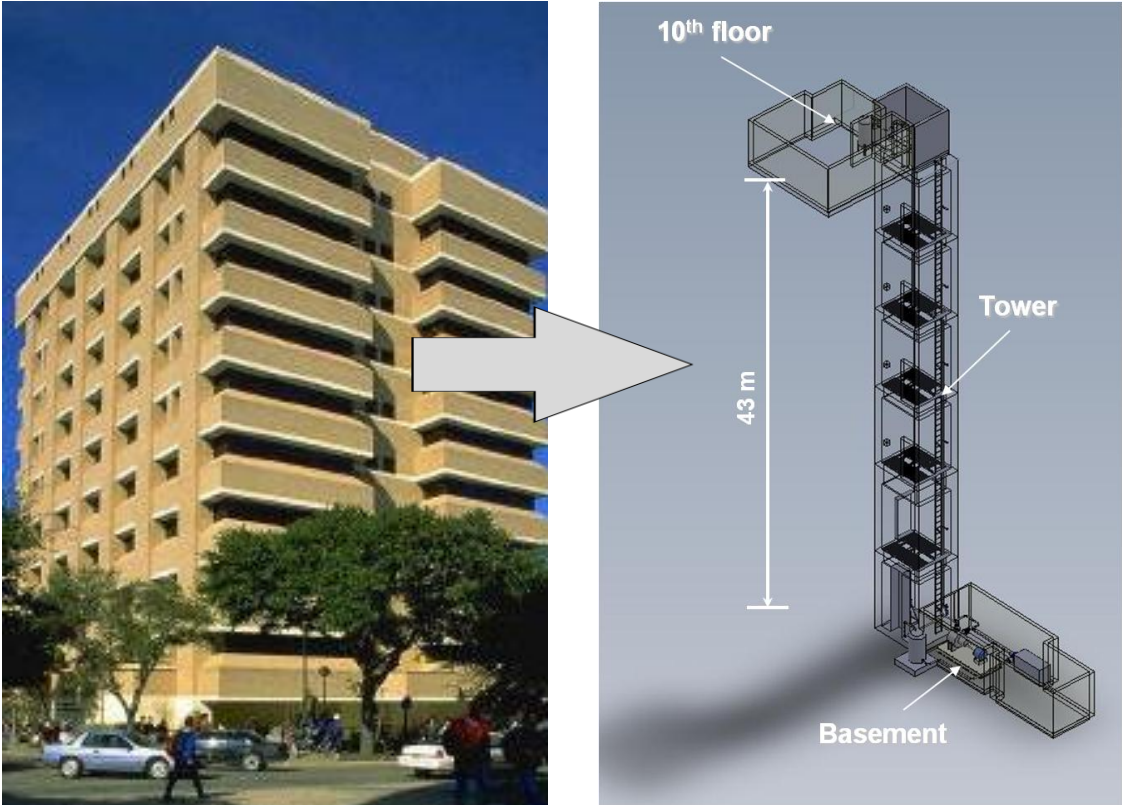
Figure 3.3 – TowerLAB Schematic Overview.
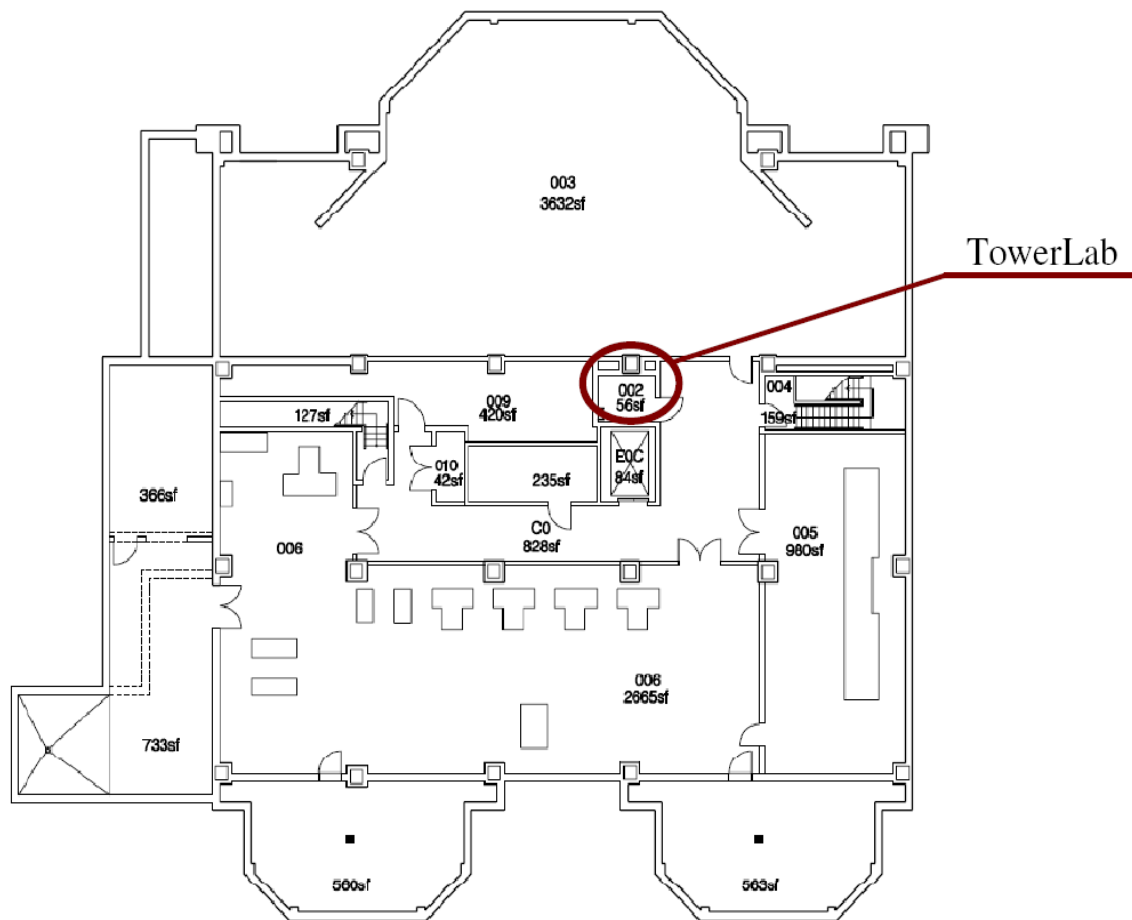
Figure 3.4 – First floor level plan showing the location of the TowerLAB inside the Joe C. Richardson building (Fernandez et al. 2010).

Figure 3.5 presents an overview of TowerLAB, which shows how the different parts of the flow loop are interconnected. The currently working fluids that can be used in the flow loop are air and water.
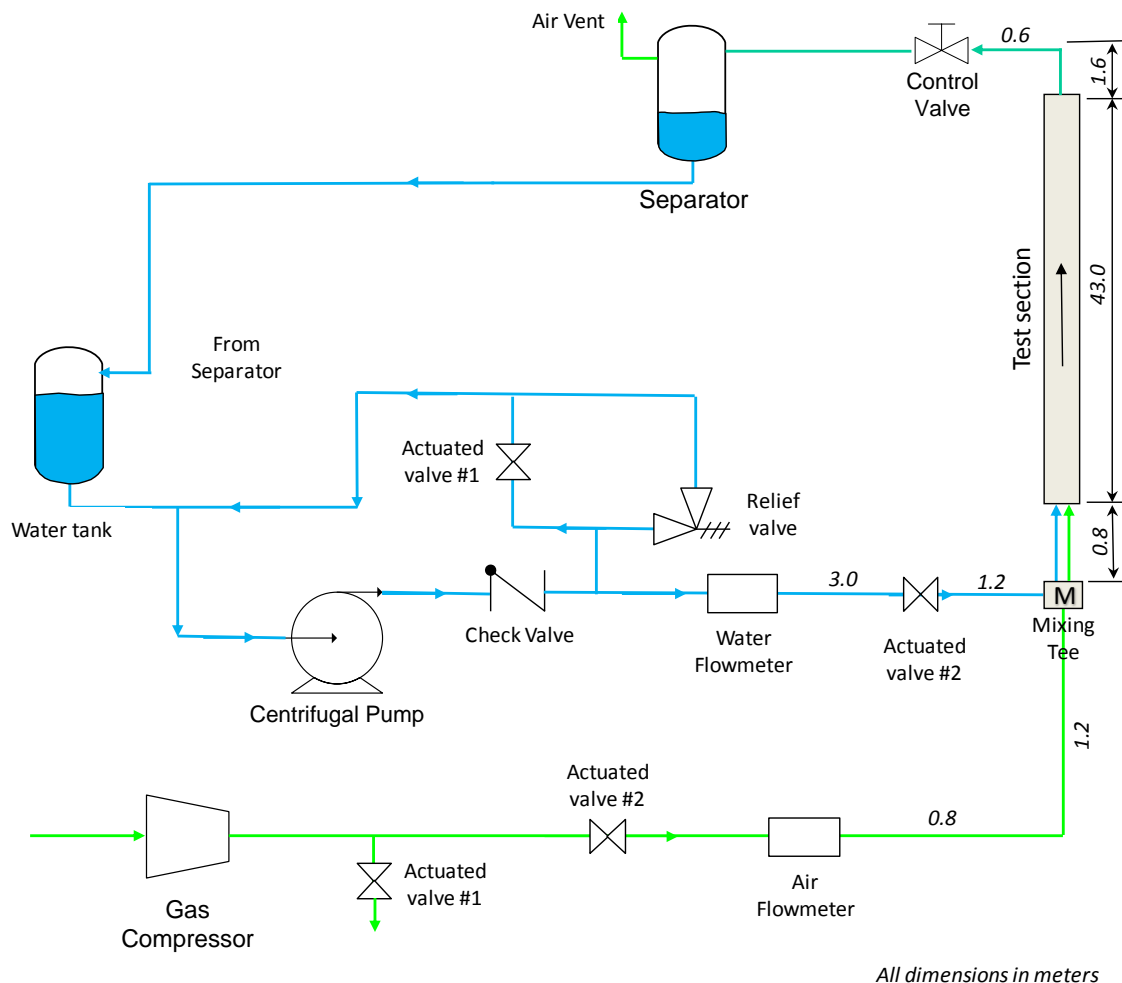
Figure 3.5 – Schematic diagram of the TowerLAB flow loop.

A centrifugal pump (Dayton 2PC38) is used to pump water from a 662 liters water tank to the test section. The water flow rate is controlled using a variable speed driver and an electronically-actuated valve downstream to the water pump. The water mass flow rate is measured using a 0.025 m (1 inch) Coriolis mass flow meter (Micro Motion F100). A water filter, with a 10 μm porous filter element, is also connected just upstream to the mixing tee to keep the water free of particles and impurities.

Compressed air is provided using a screw compressor (Ingersoll Rand 75H-SP), and the flow rate is measured using a 0.038 m (1-1/2 inch) vortex meter (Rosemount 8800D) and a 0.0127 m (½ inch) Coriolis meter (Elite Micro Motion CMF050). The

combination of two actuated valves in the air line (see Figure 3.5) with a control valve (0.05 m ball actuated valve) at the outlet of the test section provides the control of pressure and flow rate for the test section.

Air and water are mixed in a mixing tee, which consists of a 0.05 m perforated nipple (with 45 holes of 3 mm diameters) inserted in a 0.078 m ID tee. Figure 3.6 shows a diagram describing the assembly and the fluids flow through the mixing tee.

The main function of the mixing tee is to allow a smooth entrance of water when it is mixing with air. As explained in the work of Govan et al. (1991), the inlet device can significantly affect the two-phase flow behavior, especially in the flow developing region (between 100 to 300 diameter downstream to the inlet device). The selection of the configuration presented in Figure 3.6 was preferred because this configuration is believed to facilitate the development of annular and churn flow regimes (which are the focus of the present work), and also it is similar to perforated completions encountered in the field for oil and gas wells.

A description of the main features of the design of the test section, instrumentation, boosting system, visualization and data acquisition/control system will be presented next.

3.2. Test Section Design

The selection of the tubing material is the first step regarding the design of the test section. In order to allow visualization of the two-phase flow, four different types of transparent tubes were considered: glass, acrylic, polycarbonate and PVC (polyvinyl chloride). Because of the long vertical length (which makes the inspection more difficult) and high concern about safety (once the facility would operate close to class rooms and offices) glass was initially discarded as an option, due to its hazardous properties in case of a blowout. Hence, between the three options left, polycarbonate seemed to be the most indicated one, since this material can work at higher pressures than the other two and has good transparency.
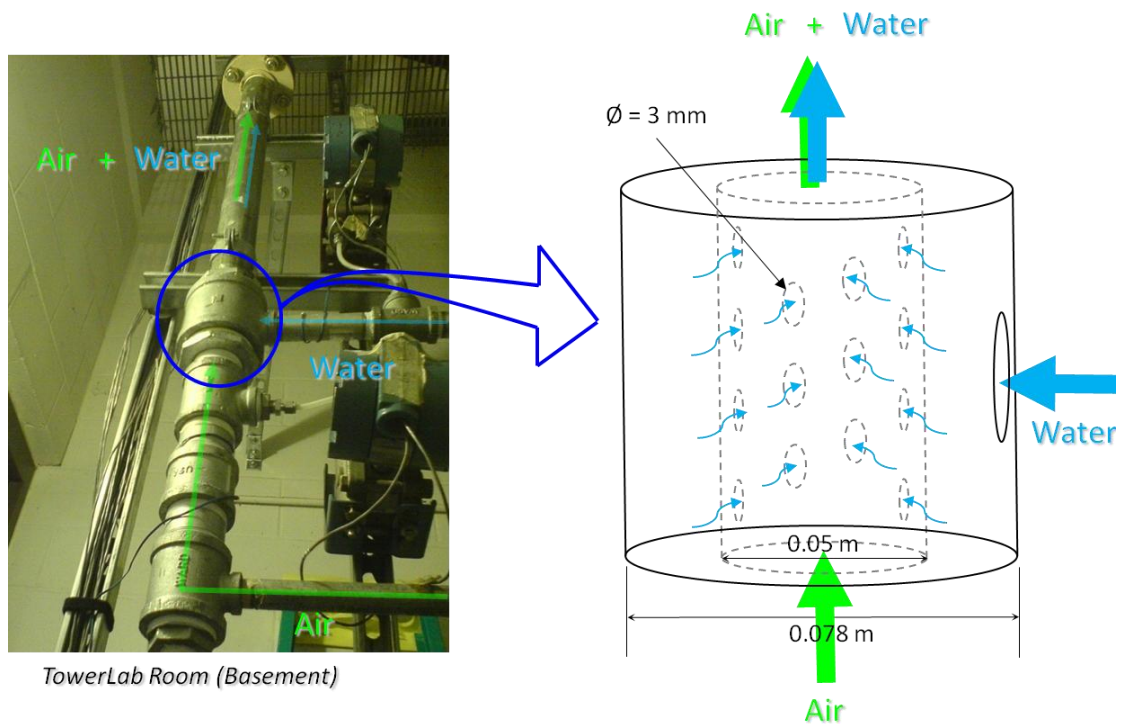
Figure 3.6 – Picture and schematic diagram of the mixing tee.

The tubes made of polycarbonate were designed and installed as a test section in TowerLAB. Two months after the installation, cracks started to grow spontaneously in most tubes, even before start flowing or having pressurized the pipes. The cracks characteristics can be seen in Figure 3.7. The main reason for the occurrence of these cracks is believed to be related to the so-called environmental stress cracking (Al-Saidi et al. 2003), which is a common phenomena in polycarbonate materials. Some of the mechanism that can cause environmental stress cracking can be related to bad fabrication practices (which create micro cracks due to high stress levels) and/or contact of the polycarbonate material with chemicals such as insecticides or certain oils and alcohols.
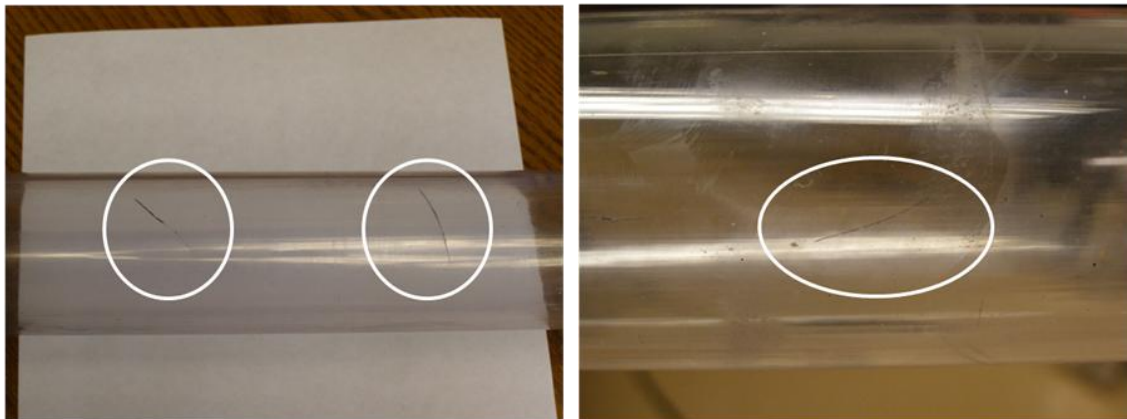
Figure 3.7 – Cracks which stared to grow spontaneously in the polycarbonate test sections.

Because of the occurrence of these cracks, the mechanical integrity of the tubes was compromised, and hence, the polycarbonate tubes were removed from TowerLAB and this option was discarded.

At this point, only acrylic and PVC were left in the initial list of materials suggested. Since an unexpected bad occurrence was experienced with the use of uncommon material for tubes, the clear PVC was then selected as best option, due to its wide application in the plumbing industry and the easy access to fitting and manufactures who work with PVC. One would say that acrylic would be a better option, because of its better transparency and similar working pressures. However, the number of manufactures that work with acrylic is limited and its use in the plumbing industry is not as usual as PVC. Then, the use of acrylic would likely create more unexpected scenarios in terms of damaging the tubes during the fittings fabrication, installation and experimental runs.

In addition, the application of acrylic tube in TowerLAB as part of the test section would still be available in case a more transparent test section is needed. For instance, some acrylic sections could be replaced in certain points to allow better visualization of the flow, since the design of the connections between the tube strings allow the replacement of tubes at each 2 m in the test section (as will be described later).

After having selected the tube material, the next important task was to design the tube diameter (pipe size). The pipe size of production tubing used in gas well

completions within the US, in most cases, range from 0.06 m (2-3/8 inches) to 0.114 m (4-1/2 inches), as reviewed by Fernandez et al. (2010). Hence, the selection of the pipe diameter for the test section should be preferably within this range.

As described earlier, clear PVC was selected as the material for the tubes of the test section. However, PVC tubes have working pressures considerably smaller than steel pipes used in the field. As can be seen from Figure 3.8, for the pipe size range between 2 and 4 inches the maximum working pressure range from 160 to 200 psig (1,100 kPa to 1,380 kPa). As the pressure rating for this type of pipe is low for all pipe ranges, the pipe size of 2 inches (0.05 m) was selected based on the maximum working pressure available.

DIMENSIONS AND PRESSURE RATINGS

Schedule 80

Nominal Pipe Size (In.)	O.D.	Average I.D.	Minimum Wall	Nominal Weight Lbs./ft.	Maximum W.P. PSI*
1/4	.540	.282	.119	.105	570
3/8	.675	.403	.126	.146	460
1/2	.840	.526	.147	.213	420
3/4	1.050	.722	.154	.289	340
1	1.315	.936	.179	.424	320
1-1/4	1.660	1.255	.191	.586	260
1-1/2	1.900	1.476	.200	.711	240
2	2.375	1.913	.218	.984	200
2-1/2	2.875	2.290	.276	1.500	210
3	3.500	2.864	.300	2.010	190
3-1/2	4.000	–	–	–	–
4	4.500	3.786	.337	2.938	160
6	6.625	5.709	.432	5.610	140
6x1/8*	6.625	–	–	–	–
8	8.625	–	–	–	–
10	10.750	–	–	–	–
12	12.750	–	–	–	–

CRITICAL COLLAPSE PRESSURE PSI @ 73°F

Pipe Size (In.)	Sch 40	Sch 80
1/4	7504	22172
3/8	3714	11869
1/2	3255	9370
3/4	1722	4985
1	1399	3841
1-1/4	767	2158
1-1/2	554	1599
2	327	1014
2-1/2	431	1176
3	279	809
3-1/2	211	-
4	169	521
6	84	333
8	57	-
10	43	-
12	35	-

DE-RATING FACTOR

Operating Temp. (°F)	De-rating Factor
73	1.00
80	0.88
90	0.75
100	0.62
110	0.51
120	0.40
130	0.31
140	0.22

Figure 3.8 – Pressure ratings and de-rating factors as a function of temperature for clear PVC pipes (Harvel Plastic, Inc.).

Another relevant parameter that should be taken into account in the test section design is the De-rating factor presented in Figure 3.8. This factor relates the working pressure with the PVC pipe temperature. For a certain working temperature, the working

pressure in the table has to be multiplied by the De-rating factor. The flow temperature in the inlet of the test section is expected to be around 75 ^{o}F. Nevertheless, this is an important parameter that has to be carefully monitored by the control/data acquisition system, in order to assure the mechanical integrity of the test section.

The test section was assembled using strings of 0.05 m ID, 2-m long sections of transparent PVC pipe. The sections are joined together using PVC flanges (see Figure 3.9) to produce a total height of 43 m. The flange connections between pipes allow the assembling and disassembling of new sections in any position of the test section.
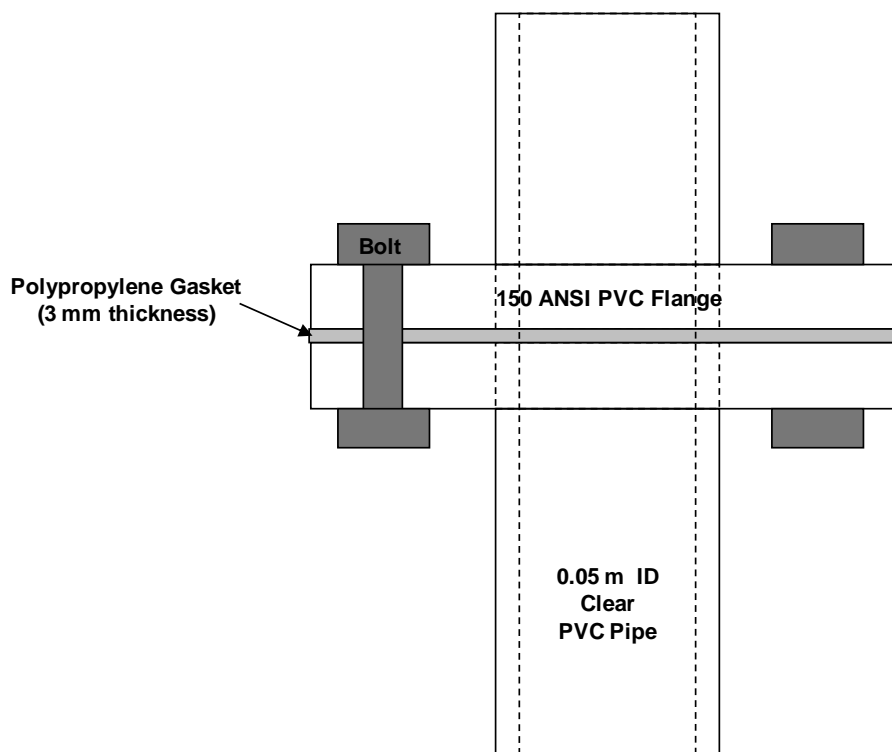
Figure 3.9 – Schematic diagram of the flanges used to connect the test section strings in TowerLAB.

3.3. Test Section Instrumentation

A good strategy to measure the required experimental parameters is as essential as the proper selection of equipments for the facility. The general objective of modeling

gas-liquid flows is to estimate the pressure gradient, or in other words, the change of pressure per unit length of pipe (Falcone, 2006). The pressure gradient, *(dp/dz)*, is often considered to consist of three components, namely gravitational pressure gradient, *(dp/dz)$_g$*, frictional pressure gradient, *(dp/dz)$_f$*, and accelerational pressure gradient, *(dp/dz)$_a$*. In the classical separated flow model for vertical tube steady-state flow in a constant cross-sectional area, these terms are given as (Hewitt 1982),

$$-\frac{dp}{dz}\bigg|_g = \left[(1-\varepsilon_g)\rho_L + \varepsilon_G\rho_G\right]g \tag{3.1}$$

$$-\frac{dp}{dz}\bigg|_f = \frac{\tau_o P}{A} \tag{3.2}$$

$$-\frac{dp}{dz}\bigg|_a = \dot{m}^2 \frac{d}{dz}\left[\frac{x^2}{\rho_G\varepsilon_G} + \frac{(1-x)^2}{\rho_L(1-\varepsilon_G)}\right] \tag{3.3}$$

where *g* is the acceleration due to gravity, ε_G the volume fraction of the gas phase in-situ in the channel, ρ_L and ρ_G the gas and liquid densities, τ_0 the wall shear stress, *P* the channel periphery and *A* the channel cross-sectional area. $\dot{m}$ is the total mass flux and *x* the quality (fraction of the mass flux which is gas).

. Therefore, based on Eqs. (3.1)-(3.3), the primary parameters that should be measured throughout the test section to characterize two-phase flows are:

- Pressure and temperature – to calculate the densities and provide the total pressure drop
- Gas volume fraction (ε_g) or liquid holdup (h_l) – to calculate the gravitational and accelerational pressure gradient
- Gas and liquid flow rates – to calculate the accelerational pressure gradient and correlate the pressure gradient with each corresponding flow rate and flow regime;
- Wall shear stress - to calculate the frictional pressure gradient.

As described earlier, the identification of the flow regimes is also an important parameter regarding two-phase flows. All the parameters described above have a strong

dependence with the flow regimes, and the measurement of these parameters should be related to the corresponding flow regime which is being observed during the measurements. Therefore, a technique which allows the recognition of the flow regimes (such as visual observation) is also an important part of the experimental characterization of two-phase flows.

Figure 3.10 shows a schematic overview of the instrumentation implemented in TowerLAB and the position of each instrument. From all the key parameters described above as part of a proper characterization of two-phase flows, only the wall shear stress was not included as part of the instrumentation. The main reason for not including the wall shear stress was the time constraint. The availability of wall shear stress sensors is still very limited, since it is not widely available in the market and in-house design and fabrication requires extra research efforts in the instrumentation field, which was not the focus on the current work.

The next section includes a detailed description of the main instrumentation implemented in TowerLAB.

3.3.1. *Pressure and temperature measurement*

Pressure taps are inserted in various points (at every 1 m) throughout the test section (see Figure 3.11). However, only five points of interest to measure pressure were added due to the constraint in the number of pressure transducers and channels available in the data acquisition system.

The pressure taps were designed as shown on Figure 3.11. Chue (1975) made an extensive review about static pressure measurement and suggested that the size of the static holes is not of great importance, provided that they are not too large. Although, Shaw (1960) recommended a maximum diameter of about $D/d = 10$ (where D is the tube diameter and d is the tap diameter), and point out that drill burr should be avoided because it can generate a considerable impact on the measurement of static pressure.
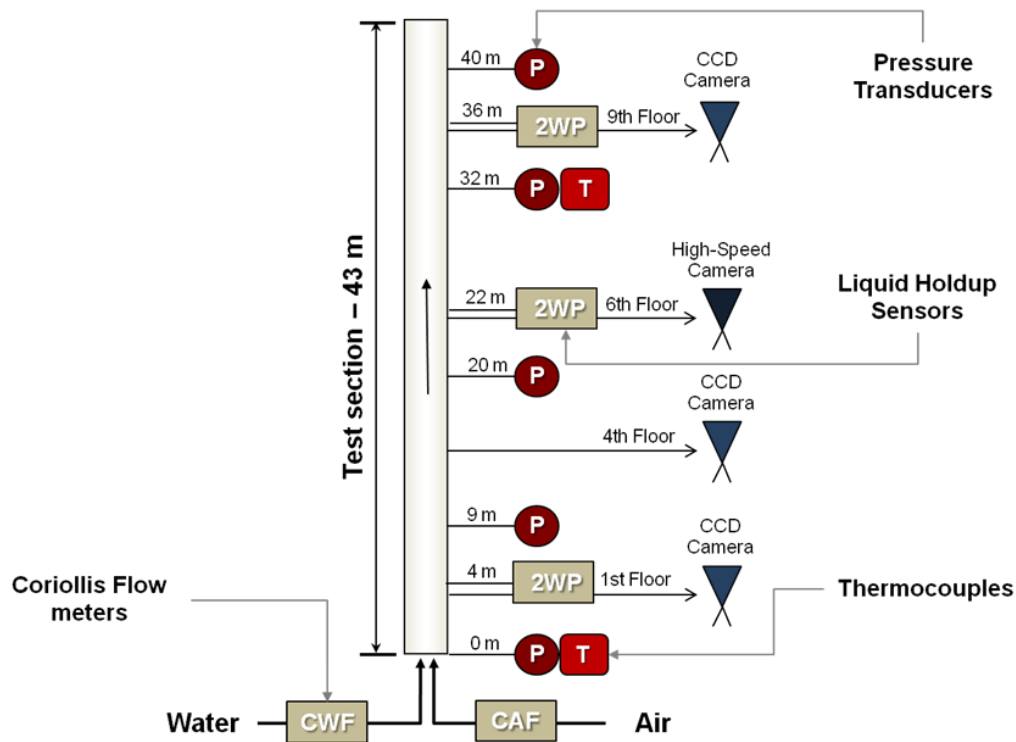
Figure 3.10 – Schematic diagram of the instrumentation implemented in the test section. This diagram provides an overview of the instrumentation installed and position of each instrument.

Therefore, based on the work of Chue and Shaw and on some recommendations from LOTUS rig design (Falcone 2006), the pressure taps were selected to have a hole size of 6.25 mm (1/4"), which is $D/d \approx 4$. The pressure transducers were connected to the taps using 6.25 mm (1/4") nylon lines, which were kept filled with liquid to avoid that bubbles trapped in the nylon lines could damp the pressure signal.

The pressure measurements were performed using absolute pressure transducers, which would be used to obtain the pressure gradient and the absolute pressure in five different points as shown in Figure 3.10.

Rousemount (model 1151) pressure transducers were used for the pressure measurements. Each pressure transducer was calibrated individually and showed very good linearity, as presented in Figure 3.12.
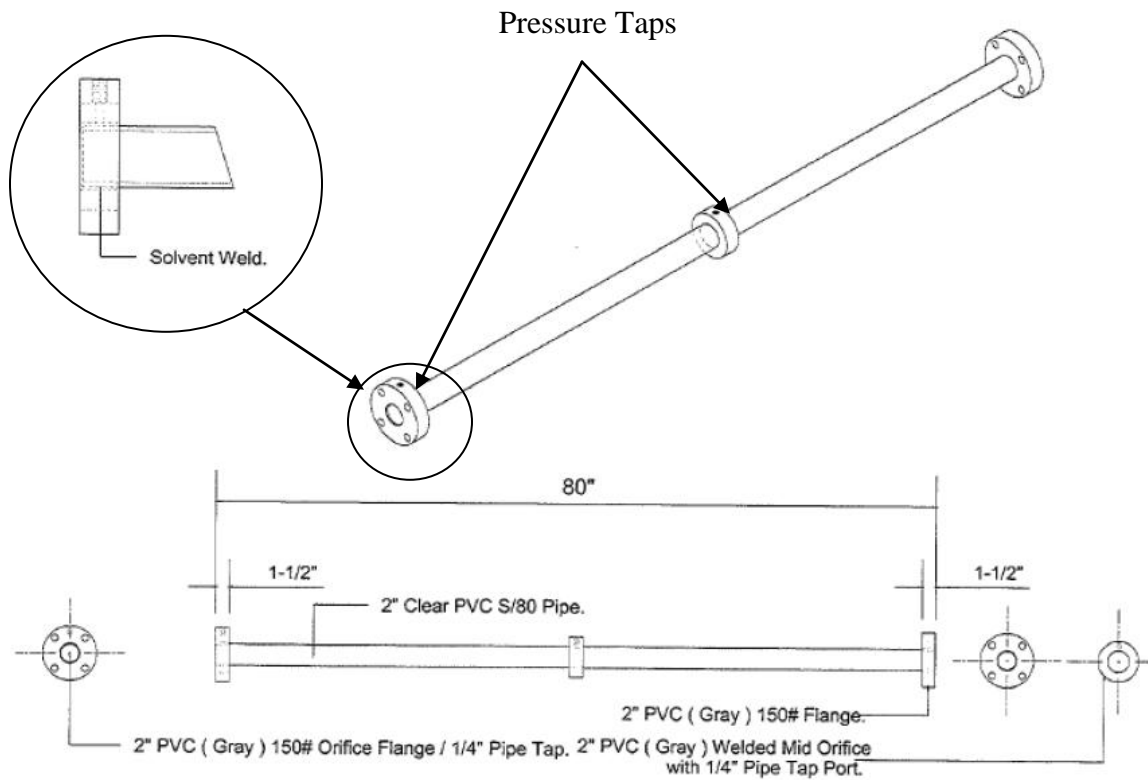
Pressure Taps

Figure 3.11 – Pressure taps dimensions description and position on the test section strings.

$$y = 52089.42911x - 115.32357$$
$$R^2 = 1.00000$$
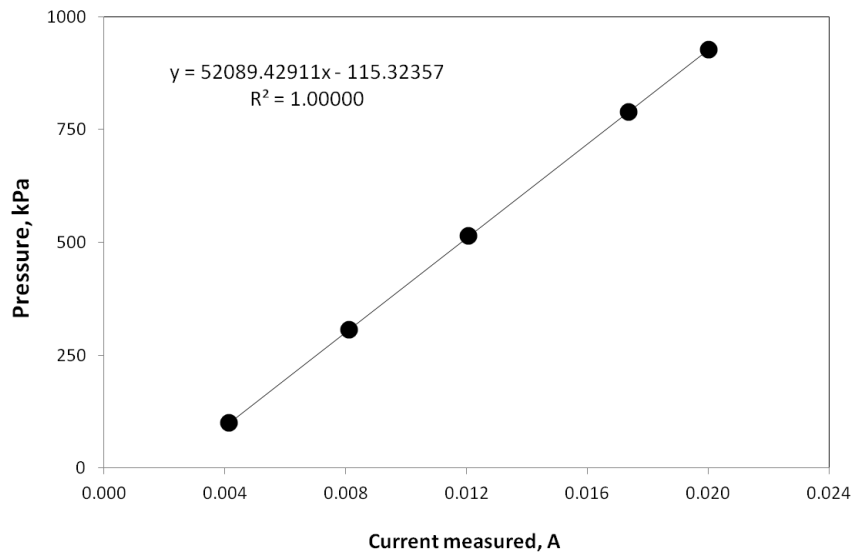
Figure 3.12 – Example of the calibration results for one of the pressure transducers. The results showed the same good linearity for all pressure transducers calibrated.

Besides the individual calibration of each pressure transducer, daily verifications were performed for all transducers in the test section. The objective of this daily verification was to confirm that the transducers would not lose calibration over time. The verification methodology consists of filling the vertical test section with water and then calculate the hydrostatic pressure at each point using the following equation,

$$p_{\Delta h} = p_{atm} + \rho_{H2O} g \Delta h \qquad (3.4)$$

where p_{atm} is the atmospheric pressure, ρ_{H2O} is the water density, g is the acceleration of gravity and Δh is the height of the water column above each corresponding pressure transducer. Figure 3.13 shows an example of the daily verification results. As can be seen, all pressure transducers presented an excellent match with the hydrostatic calculated pressure.
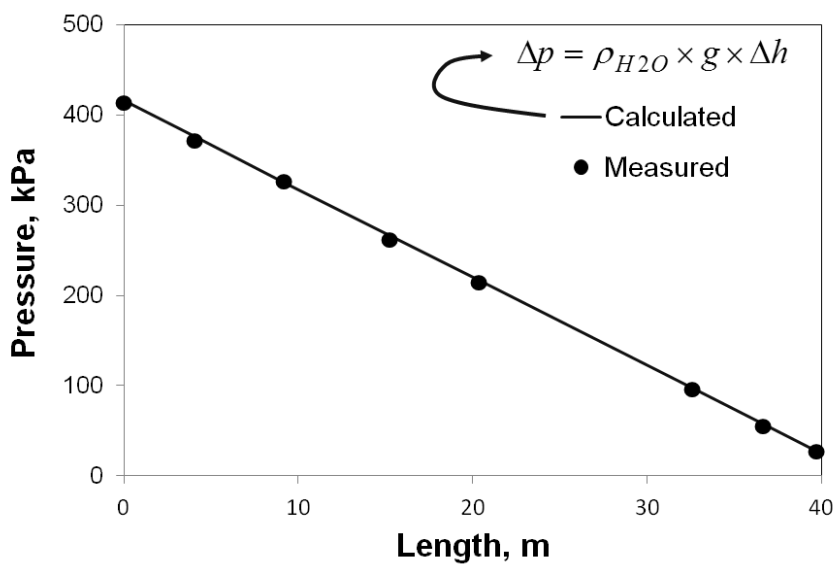
Figure 3.13 – Example of daily calibration verification results for the pressure transducers. The results showed an excellent match for all pressure transducers.

The temperature measurements were obtained using thermocouple probes (type T). The probes were inserted in the same type of nylon lines filled with liquid as used for the pressure transducers, as presented in Figure 3.14.
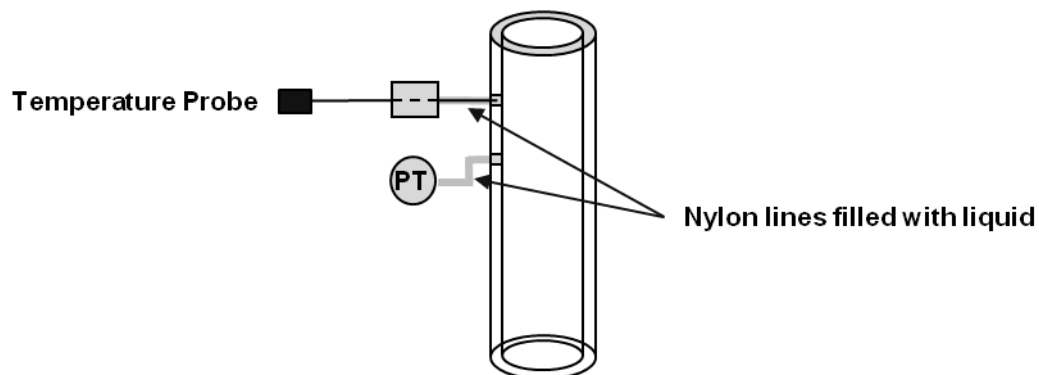
Figure 3.14 –Schematic diagram of the temperature probe connection to the test section.

3.3.2. *Liquid holdup measurement*

The liquid holdup was measured using two-wire conductivity type sensor. The concept of this sensor is based on the work of Zabaras et al. (1986). The main reasons for the selection of conductance probes in the present work were the simplicity to design/fabricate, low cost and reasonable accuracy (in the range of $\pm 5\%$ to $\pm 10\%$). Another reason was the good linearity and accuracy for this type of sensor for the entire range of liquid holdup values. As described in section 2.4. , capacitance and ECT techniques do not provide reasonable accuracy for low levels of liquid holdup ($h_l < 0.1$) and usually do not have a linear relationship for entire range of liquid holdup. The linearity of the sensor was found in this work to be essential to obtain a good accuracy of the measurement. A daily calibration of the liquid holdup sensor was necessary, and the calibration would only be achieved (in a practical way) if the sensor has a good linear relationship between the output signal and liquid holdup over the entire range of possible values (e.g., between 0 and 1). The water conductance changed over time due to

impurities coming from the air compressor. More details about the daily calibration are given later in this section after the calibration procedure is described.

The conductance sensor used in the present work consists of two wires crossing the tubing perpendicularly to the flow direction (see Figure 3.15). The electrical conductance between the wires is proportional to the thickness of liquid between them. Wires of stainless steel with 0.05 mm diameter and coated with a Teflon electrical insulation were used to fabricate the sensors (see Figure 3.16). The insulation was removed for one half of the wires, thus the film is measured in only one side of the tube. The cross-sectional liquid holdup is calculated assuming that the film thickness is uniform in the radial direction, since this probe can only measures the local film thickness.

To ensure a good linearity between the excitation and output signal, an electronic circuit was design and fabricated to generate an excitation signal, demodulate and amplify the output signal. The excitation signal consists of a square wave with a frequency of 100 kHz. The design of this circuit was carry out in collaboration with the Federal Technological University of Parana from Brazil.

To take into account the entrainment of liquid droplets present in annular and churn flows, an empirical correlation proposed by Barbosa et al. (2002) was used here to calculate the entrained liquid and correct the liquid holdup measured by the two-wire sensor. This sensor can only measure the liquid film and not the entrained droplets. Barbosa et al correlation is given by Eq. (2.2).
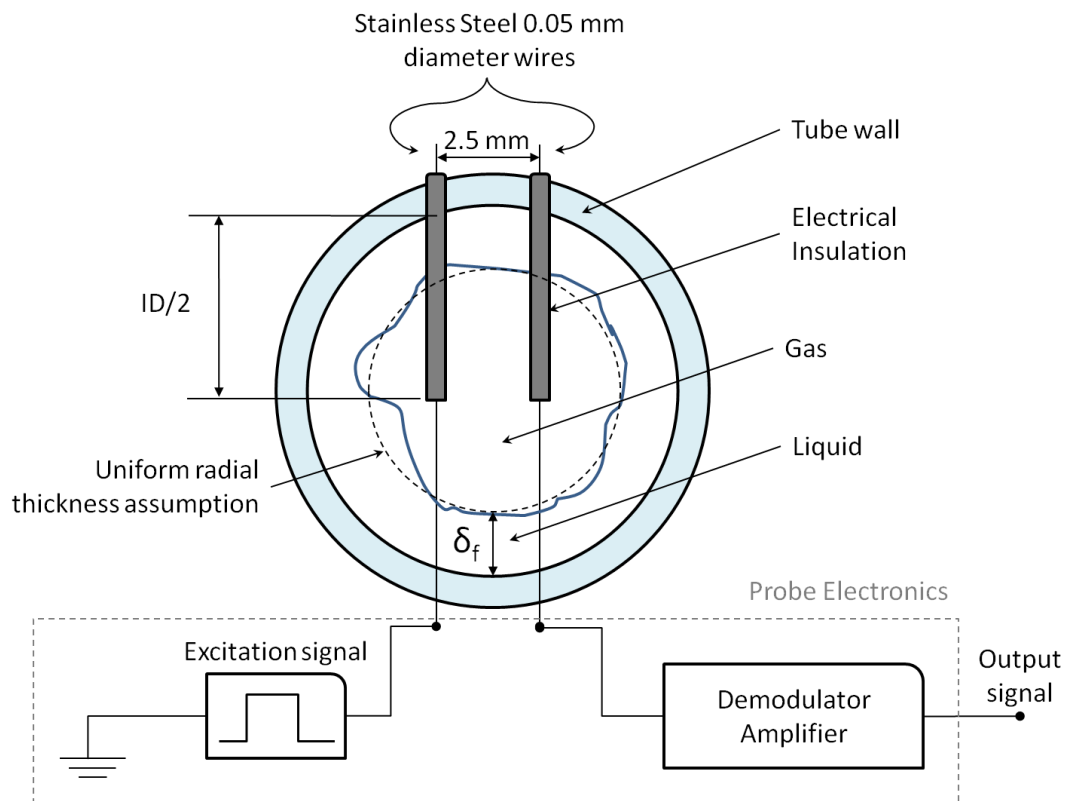
Figure 3.15 – Two-wire sensor concept used to measured liquid holdup
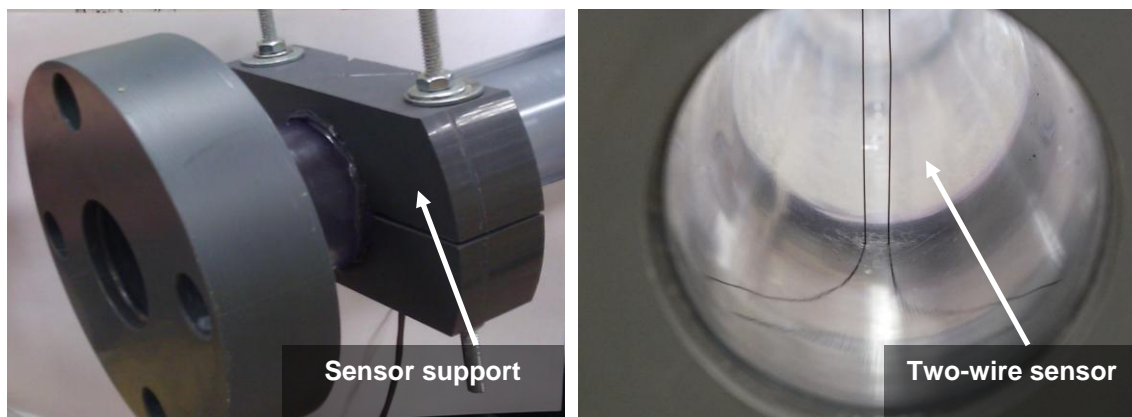
Figure 3.16 – Picture of the actual sensor installed in one of the test section tubes.

The calibration procedure used here was also based on the work of Zabaras et al. (1986). However, their technique was adapted to provide better accuracy. The adapted calibration procedure consists of creating levels of liquid heights in the tube which has

the two-wire sensor is installed. The test section tube is oriented horizontally (but slightly inclined), with one of its ends closed by a transparent window (Figure 3.17). Thus, the different levels of liquid heights are captured by a digital camera placed in front of the transparent window.
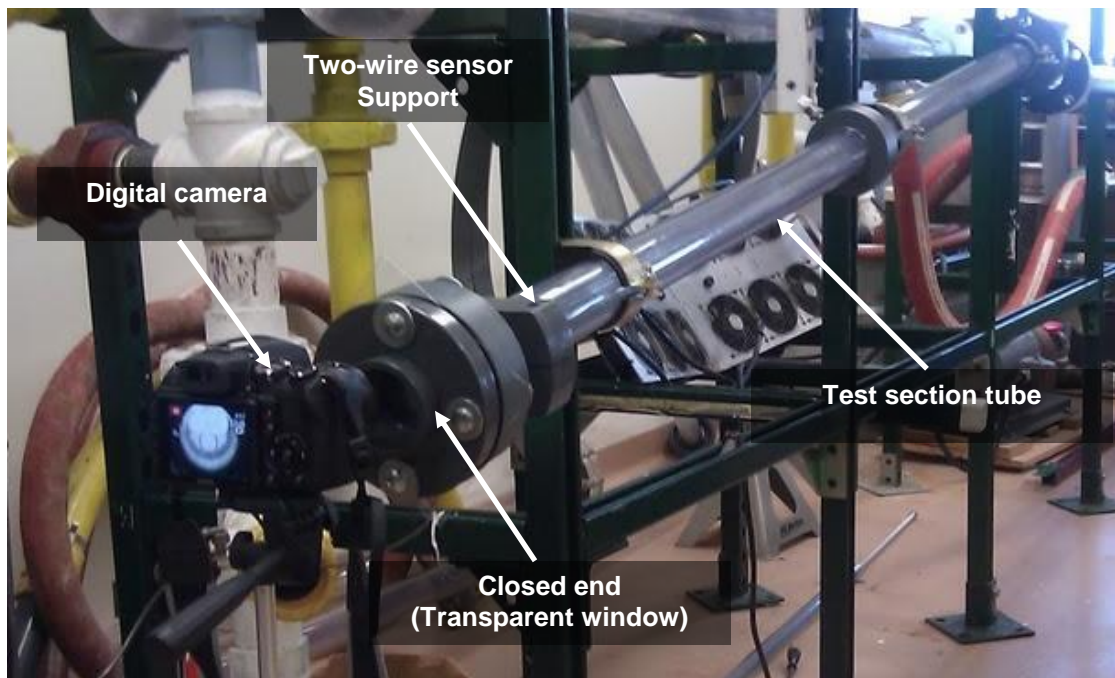
Figure 3.17 – Set up used to calibrate the two-wire sensors. The calibration set up consists of orienting the test section tube in the horizontal, filling it with different levels of liquid film and capturing the film heights via digital pictures.

The digital pictures are stored in a computer and an image processing software (Photron Fastcam Viewer 2006) is used to measure the liquid levels, as shown in Figure 3.18. The measuring concept using this software consists of having a known distance present in the image, which can be used to calibrate the pixels size. After the size of the pixels is calibrated, the software provides the distance in the picture between any two points indicated by the user.

The known distance in our case is the diameter of the wires, which is previously measured using a micrometer. The liquid level is then obtained indicating in the picture

the distance between the bottom of the wire and the liquid level surface. The indication of the bottom of the wire is easily found when the wire image start distorting (losing linearity), while the liquid level is recognized looking at the meniscus formed between the wire and the liquid surface, as shown in Figure 3.18.
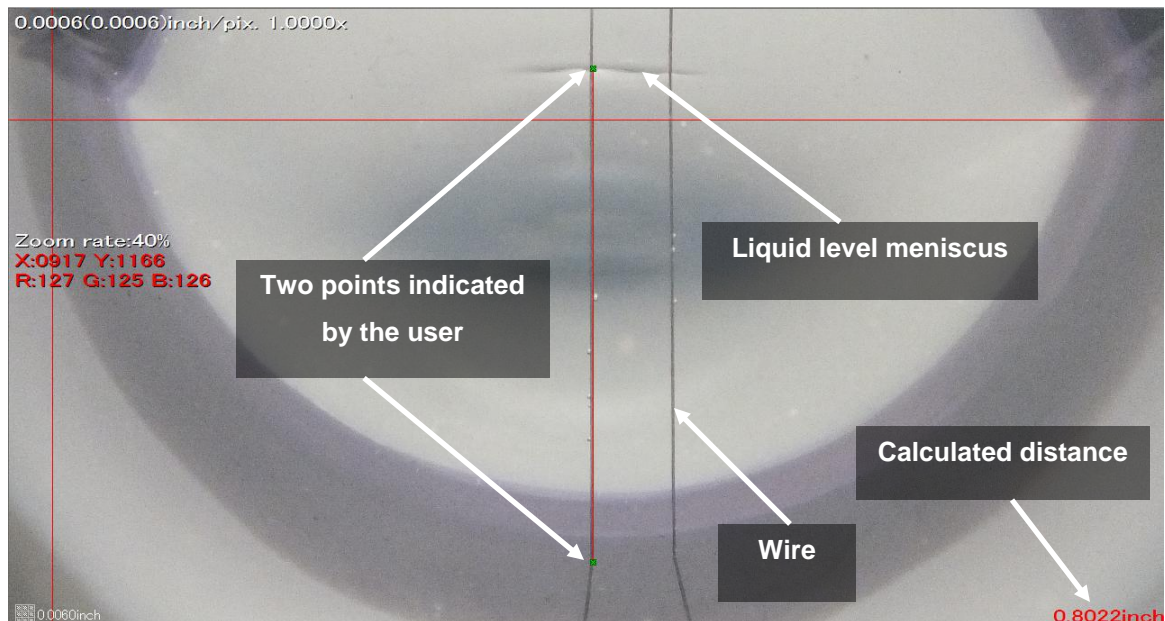
Figure 3.18 – Example of a picture used in the image processing software for the calibration of the two-wire sensors. The picture indicates the main features used on the determination of the liquid film height.

The calibration results of one of the sensors installed in TowerLAB are presented in Figure 3.19. As can be seen, the results showed an excellent linearity between the output signal (in volts) and the full range of liquid height. The linear relationship obtained here by this sensor is important because of two main factors:

- *Extrapolation of the calibration results* between "zero" and minimum liquid height: as can be seen in Figure 3.19, the minimum liquid height value (after zero) in the calibration was around 3 mm. During the procedure, it was extremely difficult to obtain values lower than 3 mm, because at this stage the liquid (water) tend to have a shape of a droplet, which make the

visualization of the wire though the droplet very difficult. However, values between zero and 3 mm would be expected for some conditions (especially in annular flow) during the experimental campaign. Therefore, having a good linearity between the liquid heights and the output signal would give us more accuracy if the calibration results need to be extrapolated between zero and the minimum calibrated value.
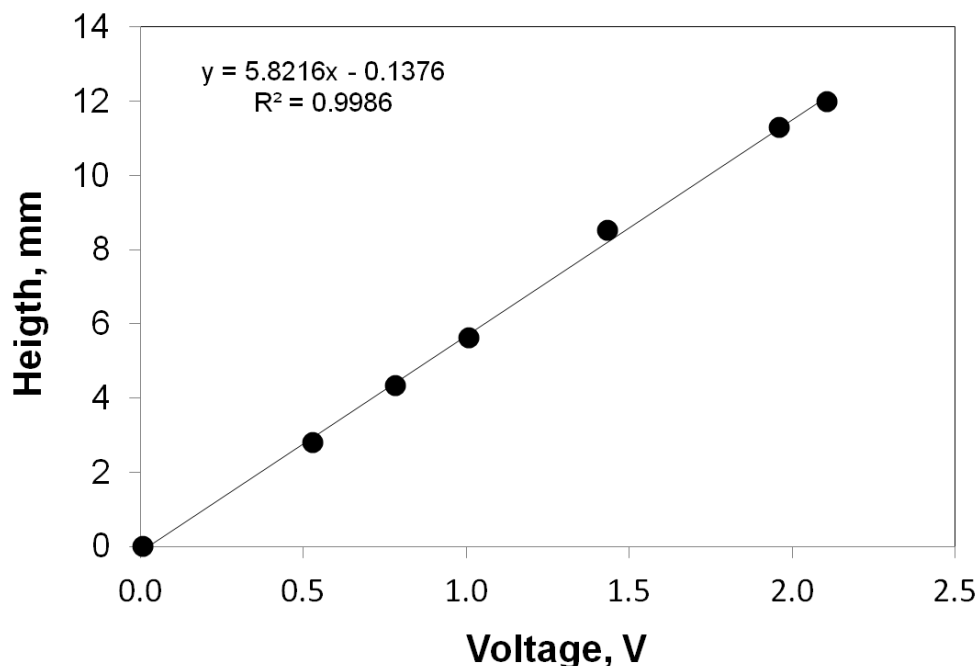
Figure 3.19 – Calibration results for one of the two-wire sensors used for the measurement of liquid holdup. The results showed a very good linearity for the full range of liquid heights.

- *Daily calibration*: the basic principle behind the concept of the two-wire sensor is the measurement of the water conductance between the wires. Thus, if the water conductance varies for any reason (for instance, change in temperature, impurities or concentration of dissolved salts) the calibration results would be affected. After some preliminary tests, it was observed that the conductance of the water of the flow loop changed considerably between two consecutive days. Therefore, more than one calibration during the day

should be performed to assure that the calibration is still valid. However, the standard calibration consists of removing the test section tube from the flow loop, perform the calibration in the horizontal, and then re-install the tube in the vertical flow loop. The execution of this procedure every day would be impractical because of the time constraint. Nevertheless, since the two-wire sensor has a good linearity between the liquid heights and the output signal, an in-situ calibration is possible. The in-situ calibration consists of only measuring the output signal for the test section completely empty and full of water. Since a linear relationship can be obtain using only two points, an in-situ calibration is possible without the need of removing the tube from the flow loop and it can be quickly executed.

3.3.3. Measurement Uncertainties

After the calibration procedures have been established for the main measurement instruments, the uncertainty of the measurements was estimated. The uncertainty calculation procedure was obtained following the recommendations described in ISO (1998). The calculations are based in the average ($\bar{q}$) and standard deviation (*DP*). The definition of these parameters are given by,

$$\bar{q} = \frac{1}{n}\sum_{i=1}^{n} q_i \tag{3.5}$$

$$DP = \sqrt{\frac{\sum(q_i - \bar{q})^2}{n-1}} \tag{3.6}$$

$$U = k\sqrt{u_o^2 + u_s^2} \tag{3.7}$$

where *n* is the total number of measurements, *k* is the Student coefficient (assuming equal to 2 for 95% probability for all calculations), u_s is the uncertainty from the measurement device (for instance, the uncertainty provided by the manufacture or

calibration) and u_o is the standard uncertainty from the measurements. U is the expanded uncertainty.

The standard uncertainty, u_o, can be sub-divided in two groups:

- *Direct measurement variables*: these are measurements obtained directly from an instrument, without the use of any calibration for the measurement procedure. The standard uncertainty is yet classified into two subgroups: a) time independent and b) time dependent variables. Figure 3.20 illustrates the typical behavior of both subgroups.

For time *independent* variables, the standard uncertainty is obtained as follow,

$$u_o = \frac{DP}{\sqrt{n}} \tag{3.8}$$

For the time *dependent* variables, the standard uncertainty is given by,

$$u_o = DP \tag{3.9}$$

- *Indirect measurement variables*: these are variables that require one or more experimental measurement to determine another parameter. For instance, in the measurement of pressure gradient, which depends on the distance between the pressure taps and on the differential pressure measurement. On the calculation for this type of uncertainty the so-called law of uncertainty propagation is used, which is given by,

$$y = f(x_1, x_2, ..., x_N) \rightarrow u_m(y) = \sqrt{\sum_{i=1}^{N} \left(\frac{\partial y}{\partial x_i} u(x_i) \right)^2} \tag{3.10}$$
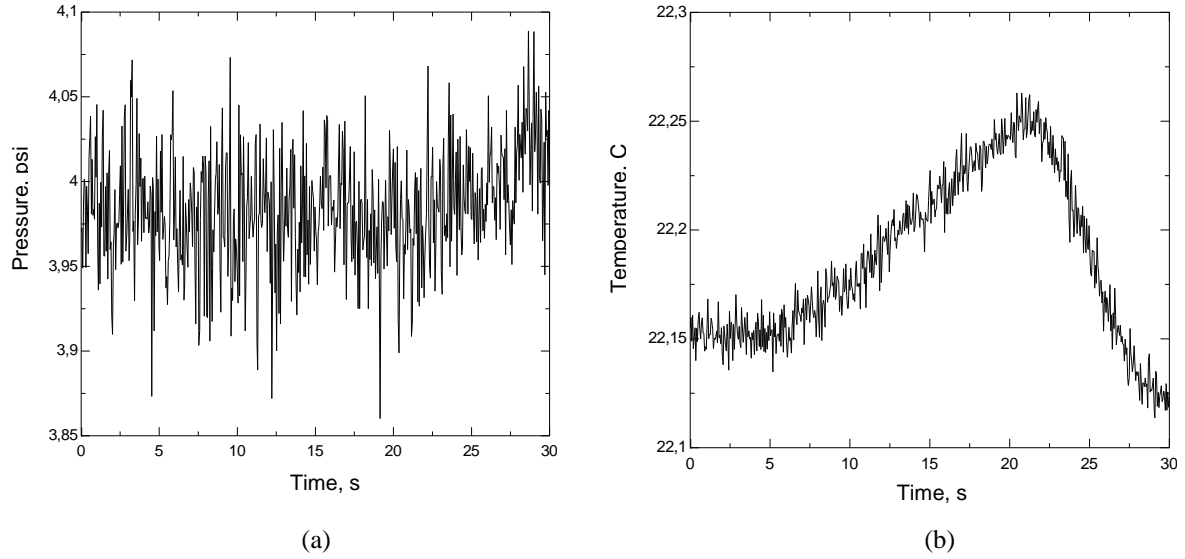
Figure 3.20 – Example of the behavior of measurement which are: (a) time independent and (b) time dependent.

If the variables for the previous equation exhibit a cross-correlation (e.g., if the variation in one variables implies in the change of another) the standard uncertainty is calculated as follow,

$$u_o(y) = \sqrt{\sum_{i=1}^{N}\left(\frac{\partial y}{\partial x_i}u(x_i)\right)^2 + 2\sum_{i=1}^{N-1}\sum_{j=i+1}^{N}\frac{\partial y}{\partial x_i}\frac{\partial y}{\partial x_j}u(x_i)u(x_j)\cdot r(x_i,x_j)} \qquad (3.11)$$

where $r(x_i,x_j)$ is the cross-correlation coefficient for the associated measurements x_i and x_j.

The uncertainty associated to the calibration process is estimated from the following expression,

$$u_{cal} = \sqrt{u_o^2 + u_a^2} \qquad (3.12)$$

where u_o is the measurement standard uncertainty, which is obtained from the maximum standard deviation calculated during the calibration process for one given point.

u_a is the uncertainty related to the curve fit obtained from the calibration process, which is given by,

$$u_a = \sqrt{\frac{\sum(x_o - x_{fit})^2}{N - (1 + PD)}}$$ (3.13)

where x_o is the measured value for every calibration point, x_{fit} is the point in the curve fit associated to x_o, N is total number of point for the calibration, PD polynomial degree of the calibration curve fit.

Using the methodology described above, Table 3.1 presents the calculation of the estimative for the average expanded uncertainty for the experimental measurements obtained for the instrumentation deployed in the present work.

Table 3.1- Average uncertainties for experimental measurements associated to TowerLAB instrumentation

p (kPa)	Δp/Δz (kPa/m)	T (K)	δ_f (mm)	h_l (-)	m_a (kg/h)	m_w (kg/h)
0.3	0.1	1	0.05	0.02	2.5	2

3.4. Boosting System

There are three main parameters that should be taken into account when selecting the boosting system: working fluids, maximum flow rates and working pressures.

The air and water flow rates selection is related to the flow regimes that can be reproduced in the flow loop. In addition, is also relevant to select flow rates which are encountered in the gas wells in the field. Nevertheless, a downscaling using Reynolds number can also be performed to compare the experimental results with field data.

As previously described in the section 2.7. , the onset of liquid loading is expected to occur between annular and churn flow regime. Therefore, the boosting

system should be capable of pumping the working fluids at pressure and flow rates which can reproduce at least annular and churn flows.

In terms of pressure, the boosting system had the primary constraint of the maximum working pressure of 1,380 kPa (200 psi), which is defined by the maximum working pressure for the 0.05 m ID clear PVC pipe (as described in the previous section).

3.4.1. Operational envelope

Based on the selected working fluids (air and water), pressures and combining the air compressor and the water pump, the operational envelope for TowerLAB is presented in Figure 3.21.
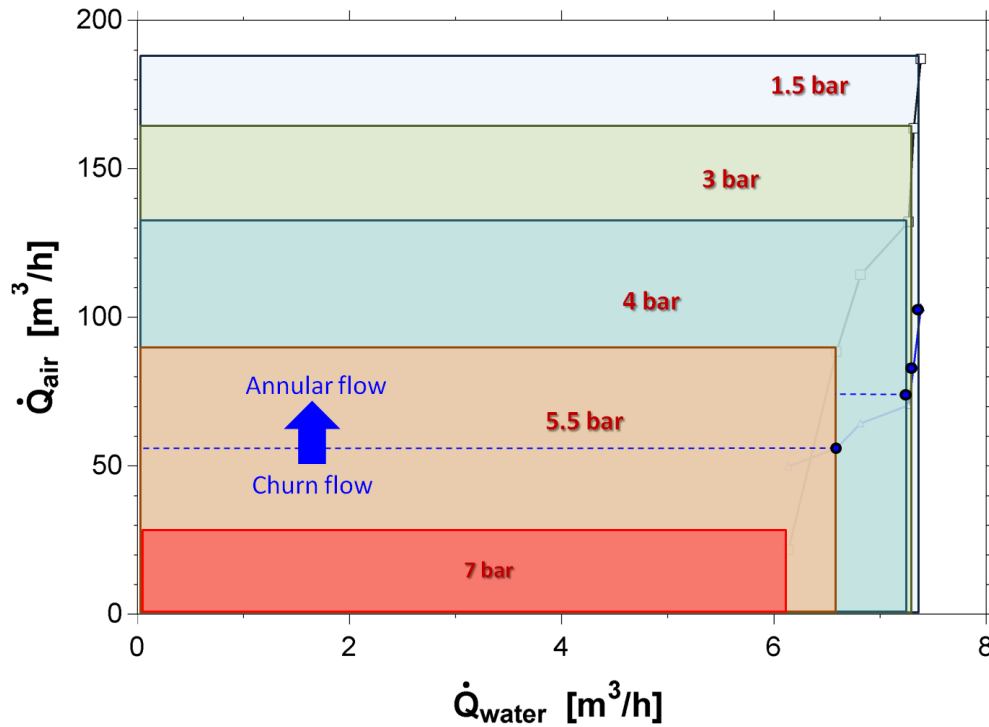
Figure 3.21 – Operational envelope for TowerLAB facility. The blue dashed line show at which gas flow rates and pressures the transition from annular to churn flow is expected to occur.

The blue dashed line in Figure 3.21 shows the expected gas flow rate and pressure at which the transition from annular to churn flow is expected to occur for TowerLAB flow loop.

3.5. Visualization System

In order to recognize the flow regimes and other characteristics of the flow such as liquid flow reversal and wave frequency, a set up with four cameras was implemented in TowerLAB. These cameras were positioned in four different positions along the test section (see Figure 3.10). With this configuration it is possible to capture synchronized videos to investigate the axial behavior of the flow. For instance, the Figure 3.22 presents a snapshot of a video captured during a experimental run. From this video is possible to estimate the speed of the front of the Taylor bubble and the frequency of these bubbles for each of the four axial positions in the test section.

The illumination needed to capture the video was configured similarly to the backlight approach used by Rodríguez and Shedd (2004). However, in the present study a continuous light was used rather than a strobe light. The videos were also taken without the use of the acrylic square box. The use of a flat surface (using a square box) can make the videos more clear. However, after preliminary tests, it was concluded that the clarity of the video was good enough to capture the characteristics of the flow needed, such as recognition of the flow regimes and wave frequency.

Figure 3.22 – Snapshot of a video captured during a experimental run. The videos are used to recognize the flow regime and analyze the axial development of the flow.

However, for higher gas velocities (which is the case of churn and annular flows), the flow exhibit a high wave frequency and velocities, and the visualization using standard cameras became difficult. For these types of flow the use of high speed cameras is essential. Therefore, in these cases, the high speed camera installed in the middle of the test section is used to analyze the characteristics of high frequency flows. A snapshot of the high speed video is shown in Figure 3.23. The high-speed camera can be configured to capture videos up to 10,000 frames per second, and can be positioned in any position along the test section.

Figure 3.23 – Snapshot of a high-speed video captured during an experimental run. The high-speed videos are used to visualize fast change in the flow, which are difficult to capture with standard cameras.

3.6. Data Acquisition and Control System

The signals for all measurements were recorded using a data-acquisition system. The system consists of a National Instruments SCXII-1000 chassis with 4 modules (SCXI -1102, 1102B, 1161, 1124) and a PCI board (NI PCI-6259), which provides a maximum sampling rate of 0.1 ms per channel.

To monitor the facility and carry out the experimental runs, 32 channels are used to measure pressure, 10 channels for temperature, 4 channels for flow rates and 3 channels for liquid holdup sensors. The channels used to measure pressure and flow rates have a resistor built-in, with a known value for each channel. For the temperature channels, there is a built-in thermistor in the terminal block, since the use of thermocouples requires a know value of temperature to use as cold-junction reference temperature.

Besides the measurement of the parameters of interest in the test section, a control system had to be developed for TowerLAB. Since the facility goes across different rooms and floor in the building, controlling the opening of the valves and monitoring pressures gauges around the facility would be extremely difficult without a central monitoring system. Therefore, a central control system was developed with the objective of monitor and control the entire experimental set up from one single station. Figure 3.24 shows a snapshot of the control panel designed to monitor and control TowerLAB. The control panel was developed in LabView environment (Labview 2004).

In this control panel the user has access to the opening of the valves, on/off buttons for the pump and compressors, varying the speed of the pumps, monitor the level of the separator and water tank.

Four electronically actuated valves were used in the facility. These valves respond linearly to the output voltage signal sent by the analog output module installed in the data acquisition system.

The data acquisition and control system can be remotely controlled from any place with a computer where access to internet is available. This provides a real-time technology capability to this system, which can be useful to run and monitor the experimental runs remotely.

Besides the fact that the control system makes the operation of the facility easier, it also improves the safety of the experimental facility. Using the LabView environment, it is possible to program an algorithm to continuous monitor the pressure and flow rates in the key points around the facility, and then take proactive actions in case of abnormal behavior. For instance, if the pressure in the inlet of the test section crosses a safety threshold value, the programmed algorithm would turn off the pump and compressors in a safe sequence to protect personnel and equipment
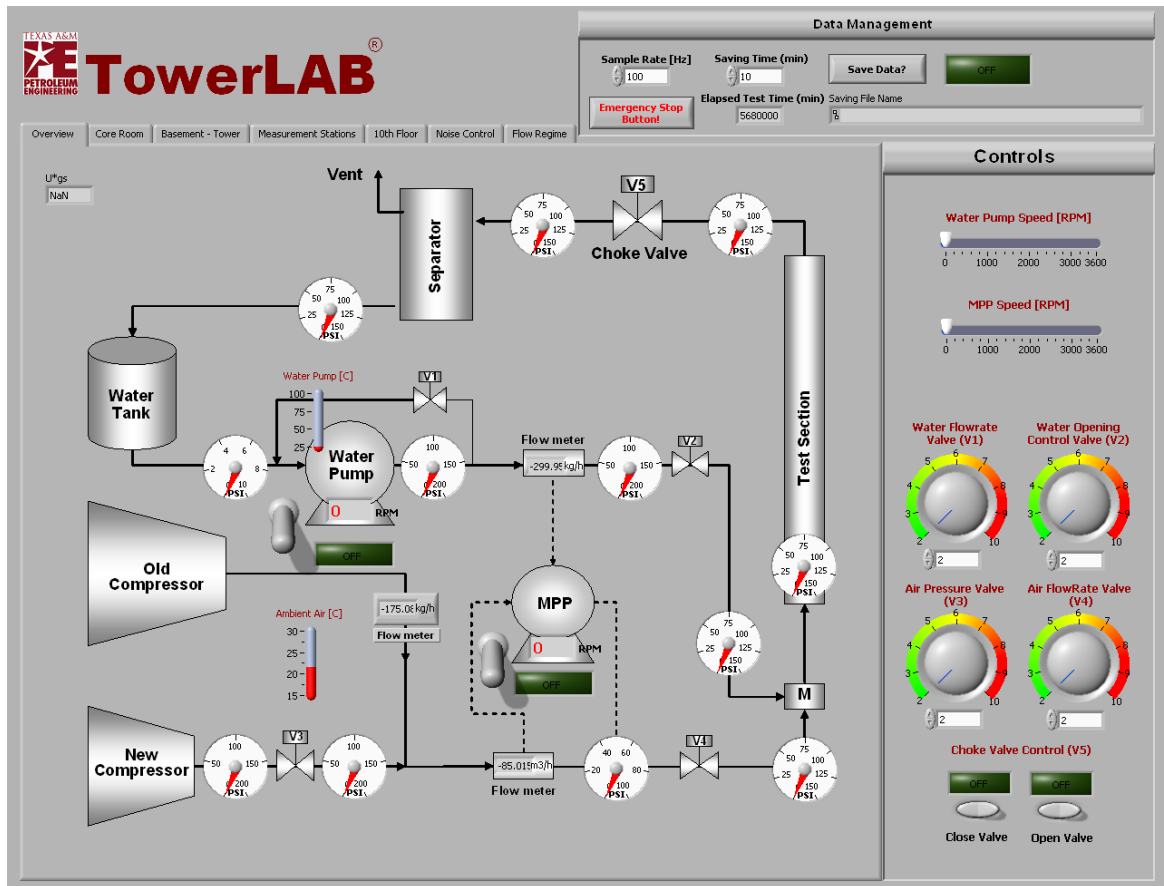
Figure 3.24 – Snapshot of the control panel used to monitor and control TowerLAB facility.

4. AXIAL DEVELOPMENT OF CHURN AND SLUG FLOWS IN A LONG VERTICAL TUBE

4.1. Introduction

The characterization of axial flow development leading to transition between flow patterns has important practical applications, particularly for the types of multiphase flows encountered in the oil and gas industry, where the length of pipelines are of the order of thousands of pipe diameters. State-of-the-art computer codes for the solution of multiphase flows in pipes rely on the identification of two-phase flow regimes (or flow patterns) for a proper selection of mechanistic models and closure relationships. Despite the large body of work available in the literature on flow regime prediction (Hewitt and Roberts (1969); Taitel et al. (1980); (Kaichiro and Ishii 1984)), there is still a lack of studies addressing the axial development of flow regimes in pipes longer than 500 diameters. The number of studies is even scarcer if one considers the particular case of axial development of the slug and churn flow regimes in long pipes. Barbosa et al. (2001) and Da Riva and Del Col (2009) investigated the flow development and wave behavior near the entrance region for churn flow. However, both analyses were limited to the inlet region and a couple of diameters downstream of it.

Although some researchers confirmed the existence of churn flow as a separate flow regime (Hewitt and Jayanti (1993); Jayanti et al. (1993); Azzopardi and Wren (2004)), some confusion has been generated in the past due to the association of the term "churn flow" with a type of developing slug flow (Mao and Dukler 1993). Therefore, the aim of this section is to evaluate experimentally the axial development of gas-liquid flows in a long vertical tube (42-m long, 0.048-m ID) at conditions where a bi-directional (oscillatory) flow of the liquid is observed. In this way, confirmatory quantitative evidence of the existence of both slug and churn flow regimes as independent two-phase flow patterns in a very long tube will be revealed.

More specifically, data will be presented on the behavior of the liquid holdup as a function of distance for conditions at which the slug and churn flow regimes are expected to occur according to well-established models available in the literature (Brauner and Barnea (1986); Jayanti and Hewitt (1992)). The prediction of the transition to churn flow according to the models of Brauner and Barnea (1986) and Jayanti and Hewitt (1992), which were developed based on data for shorter flow loops (L/D < 300), will be assessed in a long tube system for pressures up to 4.2 bara. Additionally, data on churn flow wave frequency calculated from the experimental measurement of liquid holdup at different positions along the test section will be utilized to analyze the flow development of churn flow in a long pipe.

4.2. Results and Discussions

Figure 4.1 presents the Probability Density Functions (PDF) of the liquid holdup for three axial positions for gas and liquid mass fluxes of 4 and 155 kg/m^2-s, at an outlet pressure of approximately 2 bara. The gas and liquid superficial velocities at L/D = 800 are 1.68 and 0.11 m/s, respectively. The PDF of the liquid holdup is obtained using the following equation,

$$PDF_{i,j} = \frac{n_{i,j}}{N} \tag{4.1}$$

where i and j are the lower and upper limits for a particular range of liquid holdup, n is the number of times a liquid holdup measurement falls within this range, and N is the total number of liquid holdup measurements.

As can be seen, the PDF results for L/D = 500 and 800 show two distinct peaks at high and low liquid holdup levels, which agrees well with the expected structure of developed slug flow (high liquid holdup in the liquid slug and low liquid holdup in the Taylor bubble). On the other hand, the absence of a clear PDF peak at L/D = 85 leads to

the conclusion that the slug flow is still undeveloped near the inlet. In fact, the correlation for the length of the slug flow entrance region of Dukler and Taitel (1986) for the condition of Figure 4.1 gives a value of $(L/D)_e = 83$, which corroborates this observation.

Figure 4.2 shows the holdup PDF results for gas and liquid mass fluxes of 16 and 155 kg/m^2-s, at an outlet pressure of approximately 3.8 bara. At this condition, the gas and liquid superficial velocities at $L/D = 800$ are 3.48 and 0.15 m/s, respectively. Only one PDF peak appears at this condition, which becomes more pronounced as L/D increases and the gas expands. Visual observation of the two-phase flow indicated that the flow pattern for this condition was indeed churn flow, as can be seen in Figure 4.2. However, it should be mentioned that there is some similarity between the liquid holdup PDFs of undeveloped slug flow and churn flow (especially at $L/D = 85$), which explains the confusion generated in the literature.
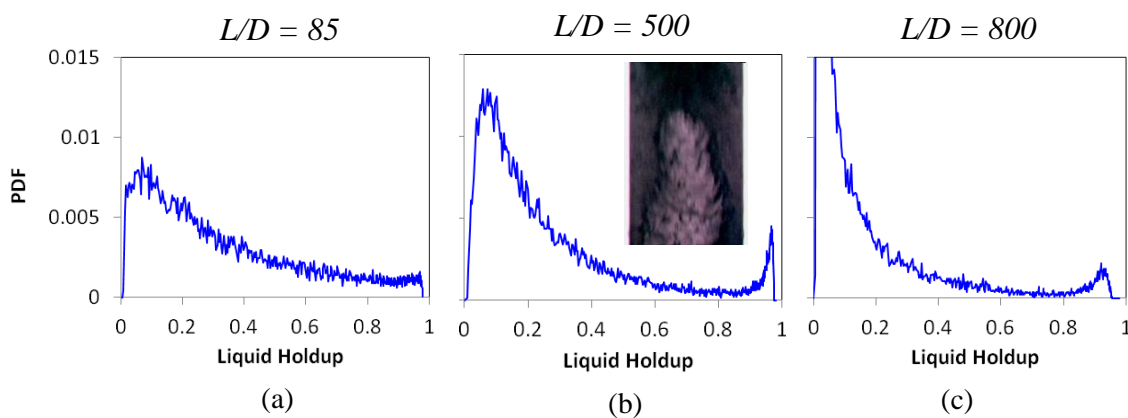
Figure 4.1 – Probability density function (PDF) of liquid holdup measurements at three different axial positions for slug flow conditions (outlet ṁ$_g$ = 4 kg m-2 s-1, ṁ$_w$ = 110 kg m-2 s-1 and at 2 bar pressure).
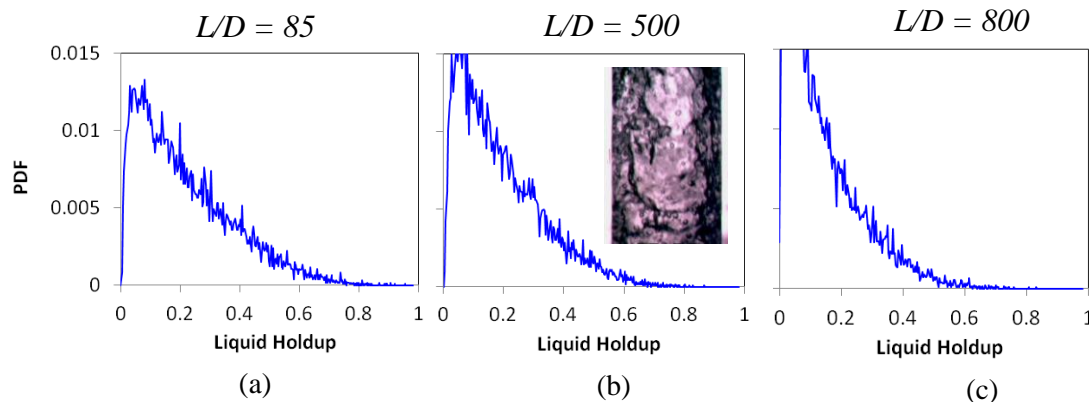
Figure 4.2 – Probability density function (PDF) of liquid holdup measurements at three different axial positions for churn flow conditions (outlet $\dot{m}_g$ = 16 kg m-2 s-1, $\dot{m}_w$ = 155 kg m-2 s-1 and at 3.8 bar pressure).

Another way to discard the possibility of having undeveloped slug flow in the test presented in Figure 4.2 is looking at the criteria of maximum void fraction to collapse the bubbles in the liquid slug for slug flows. Based on the maximum bubble packing used by Brauner and Barnea (1986), the transition from slug to churn flow should occur when the void fraction in the liquid slug reaches a value of ε_{max} = 0.52 (e.g., minimum liquid holdup $h_{l,min}$ = 0.48). From the PDFs for the liquid holdup showed in Figure 4.2 it is possible to see that there is almost no measurements of liquid holdup higher than 0.48, for the axial location L/D = 800. In other words, one can say that the majority of the liquid slugs should have collapsed at this point and we should have churn flow for this position.

When the percentage of the total number of times of which the liquid holdup is higher than 0.48 are calculated for the first liquid holdup measurements in Figure 4.2, we obtain 15.1% and 7.8% for positions L/D = 85 and 500, respectively. Therefore, there is a higher uncertainty of the presence of liquid slugs for these first two points than for L/D = 800. However, using the correlation for the length of entrance region for slug flow proposed by Dukler and Taitel (1986), the entrance region was calculated as $(L/D)_e$ = 204. Hence, the presence of greater number of liquid holdup measurements higher than $h_{l,min}$ = 0.48 could be explained as developing region as observed by Dukler and Taitel for the length of L/D = 85.

Figure 4.3 presents a comparison between experimental data and models that were developed for predicting the slug-to-churn and churn-to-annular transition. The data are presented as a function of the liquid and gas superficial velocities. The local superficial gas velocities were determined based on the inlet gas flow rate (kept fixed) and the local pressure at L/D = 500. Visual observations of the flow configuration, using the high-speed camera, were performed for each experimental run. Additionally, liquid holdup PDFs were used to make the characterization of flow regimes less subjective. As can be seen from Figure 4.3, the occurrence of slug flow at positions far from the liquid inlet (L/D = 500) is in reasonable agreement with the transition models of Brauner and Barnea (1986) and Jayanti and Hewitt (1992) for lower pressures (1.4 bara) and superficial liquid velocities (< 0.3 m/s). However, these models do not have a good match with the data for a higher pressure (4.2 bara), as shown in Figure 4.4. On the other hand, the model of Hewitt and Roberts (1969) presented a better match for higher rather than for lower pressures. The results at L/D = 800 are very similar as observed for L/D = 500.

An important correlation parameter associated with the uni-directional (churn-to-annular) flow transition is the Wallis (1969) criterion, for which the dimensionless gas velocity (U_{gs}*) is equal to unit. The dimensionless gas velocity is given by Eq. (2.1). As can be seen from Figure 4.4, Wallis criterion presents an excellent match with the experimental results. Turner criterion shows a good agreement for the annular-to-churn flow transition for high superficial liquid velocities
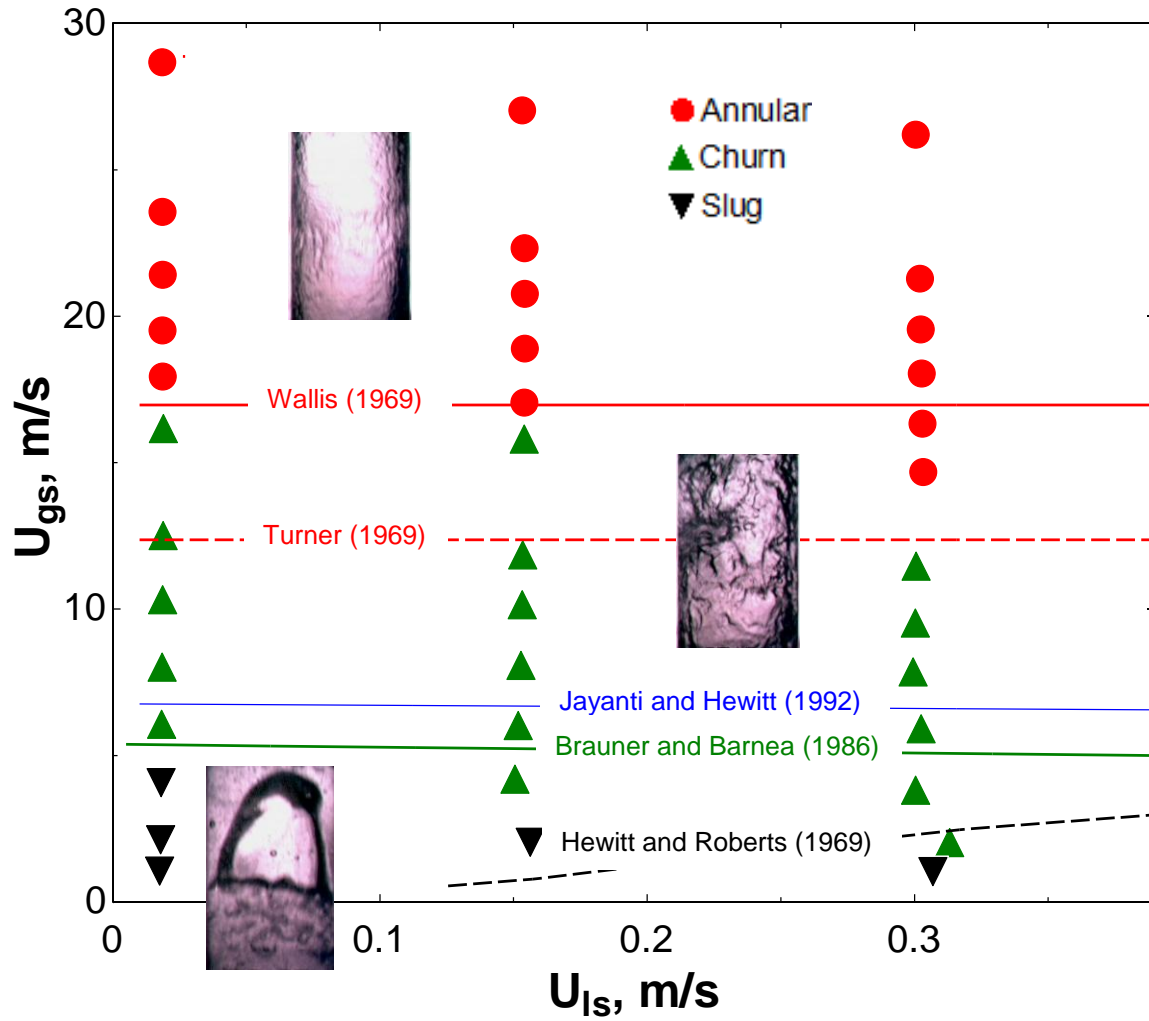
Figure 4.3 – Comparison between flow regime transition models and experimental observations at 1.4 bar.
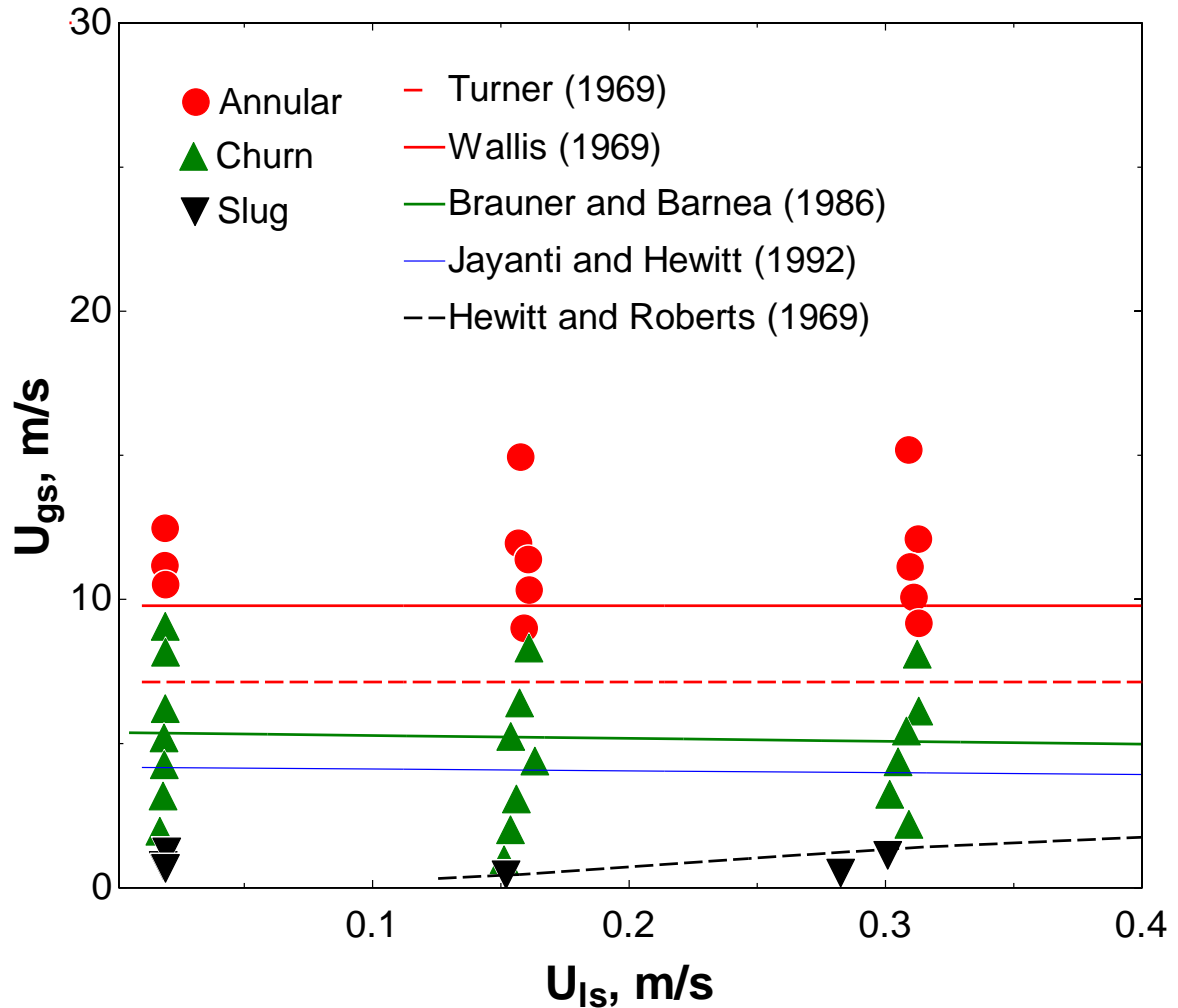
Figure 4.4 – Comparison between flow regime transition models and experimental observations at 4.2 bar pressure.

Figure 4.5 presents experimental results of time-averaged liquid holdup as a function of the dimensionless gas velocity, U_{gs}*, for different axial positions and for pressures between 1.4 and 4.2 bar. As can be seen from the figure, the liquid holdup decreases exponentially with U_{gs}*. The liquid holdup also increases with the liquid mass flux, as shown between the dashed and continuous line. These lines are linear interpolations of the measured liquid holdups points for the mass flux of 19 and 310 kg/m^2-s. The figure also shows that, for U_{gs}* higher than 0.6, there is only a small difference for the liquid holdup between the dimensionless axial position L/D = 500 and 800.
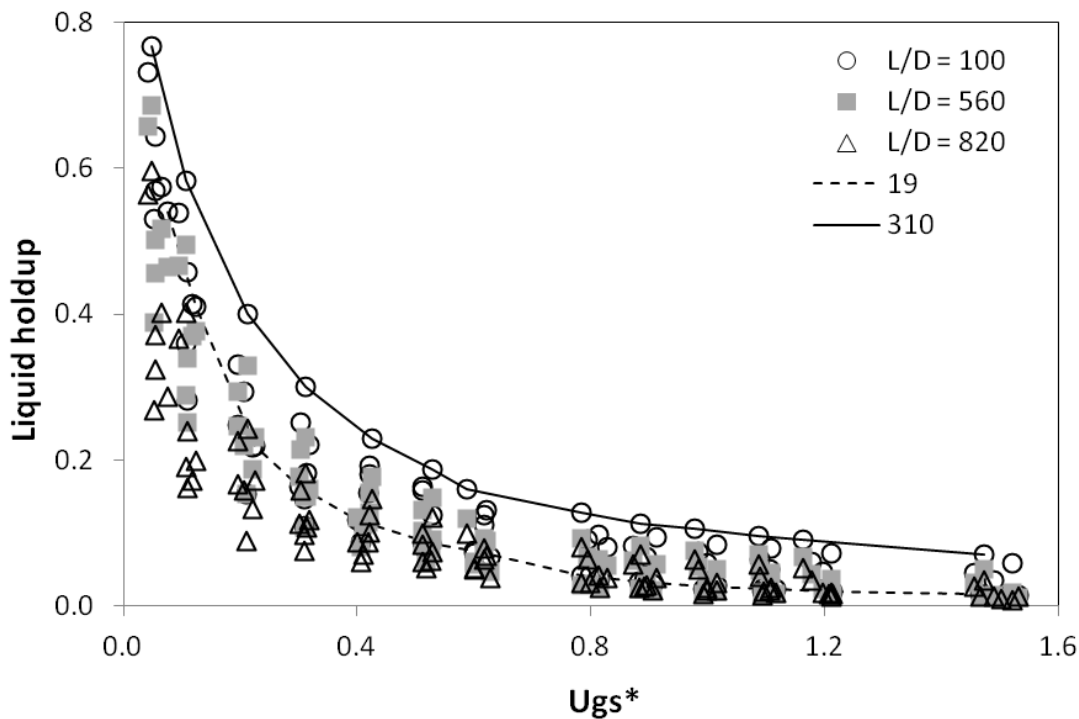
Figure 4.5 – Liquid holdup as function of Ugs* for different axial positions and liquid mass flux, for pressure between 1.4 and 4.2 bar.

The variation of the time-averaged liquid holdup with dimensionless axial position (L/D) is presented in Figure 4.6.

As can be seen from the figure, the liquid holdup varies significantly between all axial positions for the liquid mass flux of 310 kg/m^2-s, while for 19 kg/m^2-s it seems to reach some sort of developed flow for all conditions presented, except for U_{gs}* = 0.3. One could argue that, for the same liquid rate, the axial change in liquid holdup should be a consequence of the axial change of U_{gs}* (due to the axial pressure change). At high gas velocities (churn and annular flows), the holdup variation with distance, for a fixed liquid flow rate, is more important than that of the gas velocity itself (i.e. pressure).
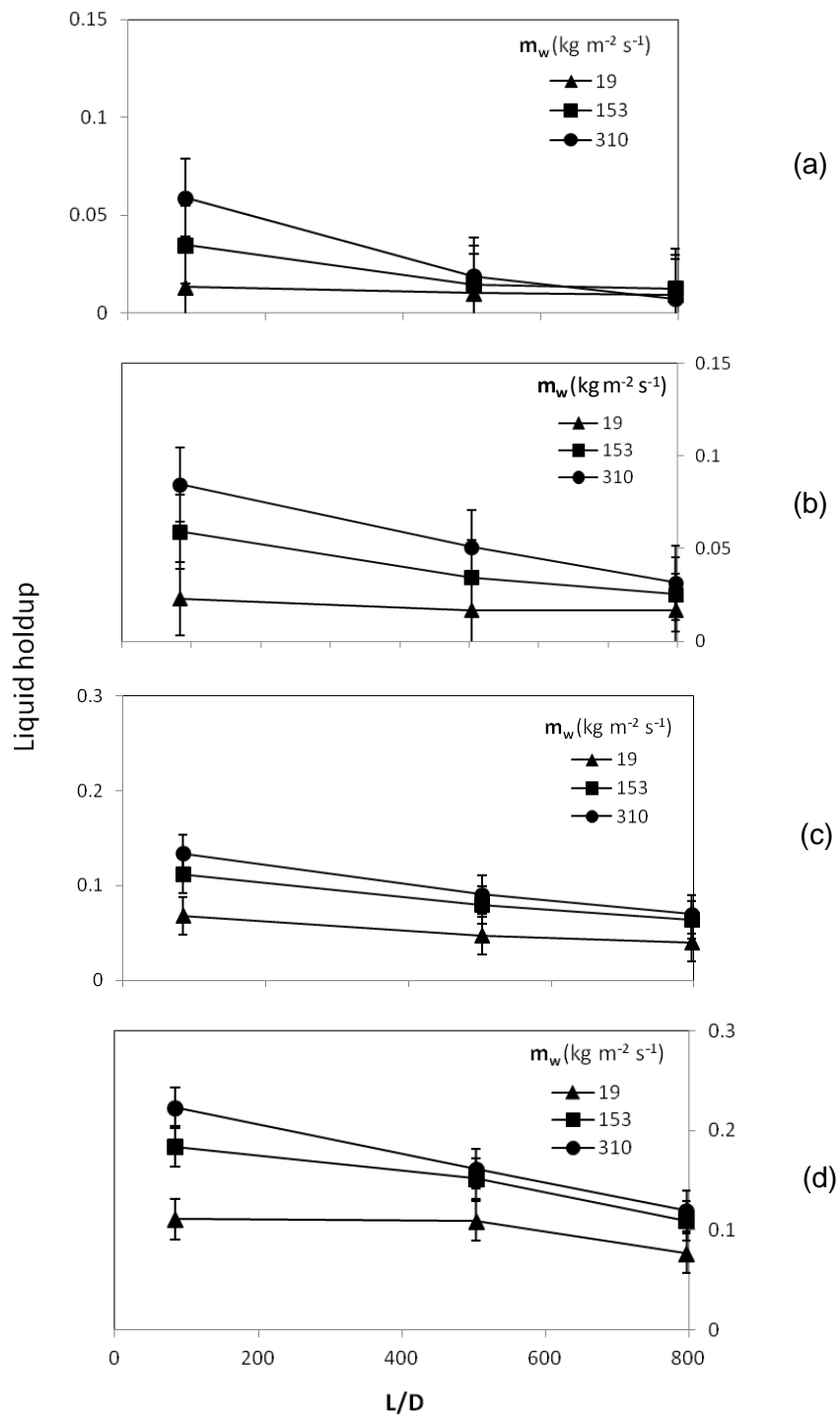
Figure 4.6 – Liquid holdup as function of axial positions for an Ugs* of (a) 1.5, (b) 1.0, (c) 0.6 and (d) 0.3, at 1.4 bar pressure.

This means that the addition to the expansion of the gas, phase redistribution (flow development) is contributing to the axial change in liquid holdup. Also, the maximum axial variation observed in $U_{gs}*$ among all tests was only 40%, while the liquid holdup between the positions L/D = 500 and 800 have changed as much as 200% (see Figure 4.6a) for liquid mass flux of 310 kg/m^2-s. Therefore, the present authors suggest that the flow hasn't reached fully development flow for liquid mass flux of 310 kg/m^2-s in all cases in Figure 4.6.

Figure 4.7 shows the variation of the time-averaged dimensionless liquid holdup with $U_{gs}*$ for the axial position L/D = 500 at 1.4 bar pressure. The liquid holdup in the figure is made dimensionless dividing the liquid holdup at L/D = 500 by the values at L/D = 800 for the same $U_{gs}*$ and liquid mass flux.

As can be seen from the figure, for liquid mass flux of 19 and 153 kg/m^2-s, it seems that the flow is fully developed at L/D = 500, since the dimensionless liquid holdup at this position have values close to the unit for the entire $U_{gs}*$ range. However, for the $U_{gs}* > 1.0$ and liquid mass flux of 310 kg/m^2-s, the fully developed flow region does not seem to be reached, since the dimensionless liquid holdup goes away from the unit. Figure 4.8 present the same analysis of Figure 4.7, however, it shows the effect of pressure. Figure 4.8 shows that the dimensionless liquid holdup only goes away from the unit only for the low pressure curve.
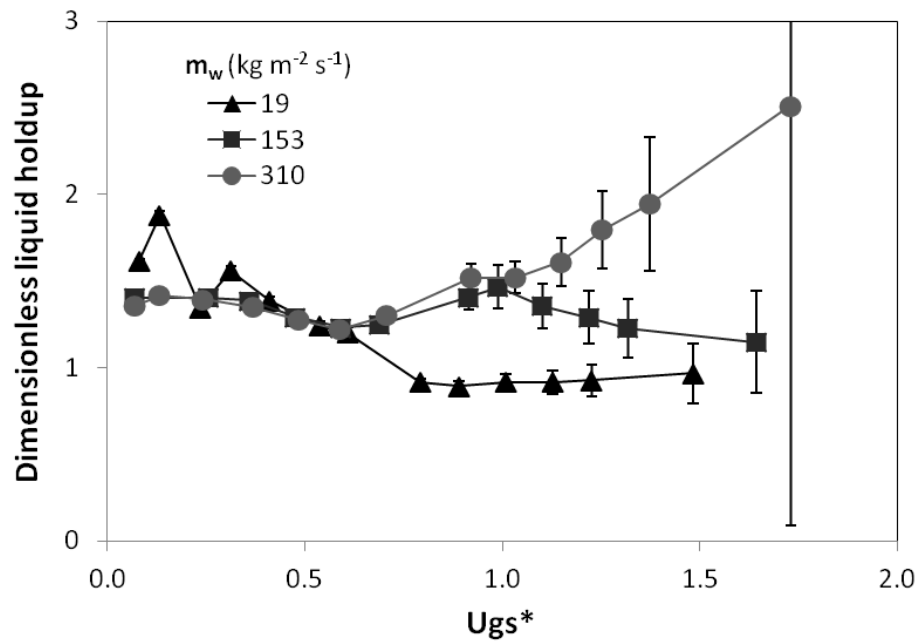
Figure 4.7 – Dimensionless liquid holdup for position L/D = 500 as function of Ugs* for different liquid rates at 1.4 bar pressure.
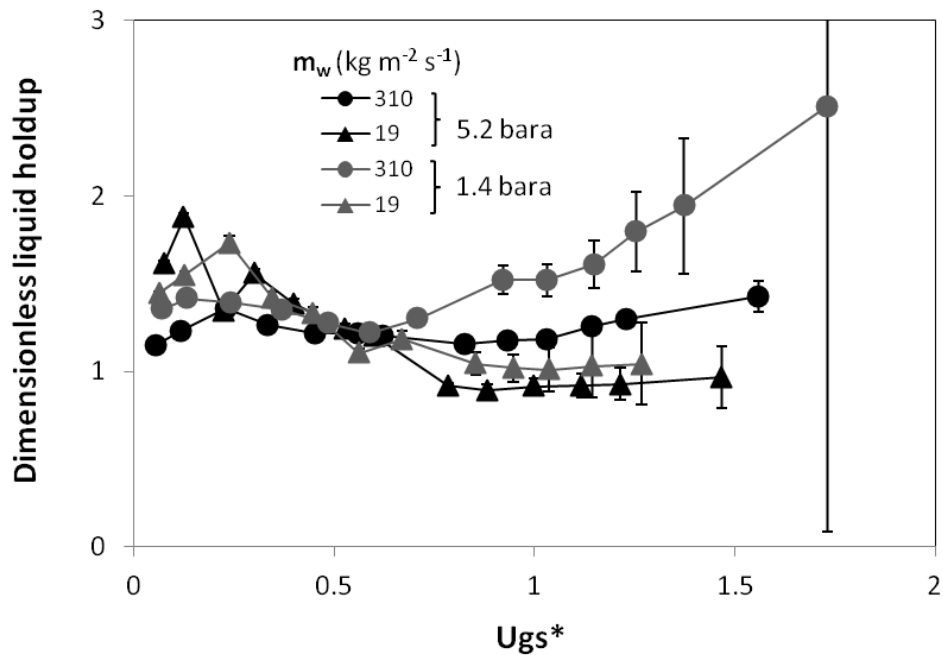
Figure 4.8 – Dimensionless liquid holdup for position L/D = 500 as function of Ugs* for different liquid mass flux and for pressures.

Figure 4.9 presents the wave frequency as a function of U_{gs}* for three different axial positions, liquid mass rates varying from 19 to 310 kg/m²-s, and at pressures ranging from 1.4 to 5.2 bara. The wave frequency was calculated here using an approach similar to the methodology developed by Hazuku et al. (2008) for annular flow. In the present work, this methodology was extrapolated for churn flow conditions as well.

As stated by Hazuku et al. (2008), at the present date there is no consensus of a clear definition about the disturbance waves in annular and churn flows. Therefore, a disturbance wave is defined here (similarly as in Hazuku et al) as a wave whose the thickness peak is higher than the upper wave layer and both ends are lower than the average film thickness (see Figure 4.10). The upper wave layer is defined as (Hazuku et al. 2008):

$$\bar{\delta}_u = \frac{1}{n}\sum_{k=1}^{n}\delta_k, \quad (\delta_k > \bar{\delta}) \tag{4.2}$$

The wave frequency results have a good agreement with the values reported by Barbosa et al. (2001). However, the later authors did not include the axial effect on their wave frequency analysis. As can be seen from Figure 4.9, the wave frequency does not show any significant axial change. Wolf et al. (2001) have also reported that the wave frequency does not change after L/D = 150. However, their observations were only limited to annular flow conditions (U_{gs}* > 1.0).
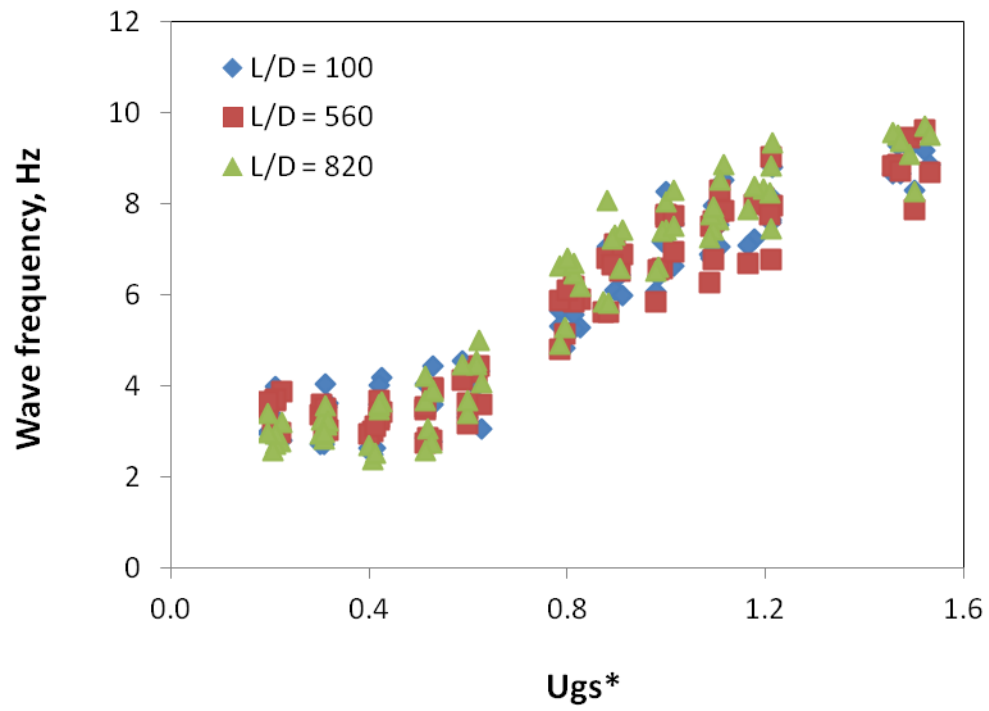
Figure 4.9 – Disturbance waves frequency as function of Ugs* for different axial positions and liquid rates.
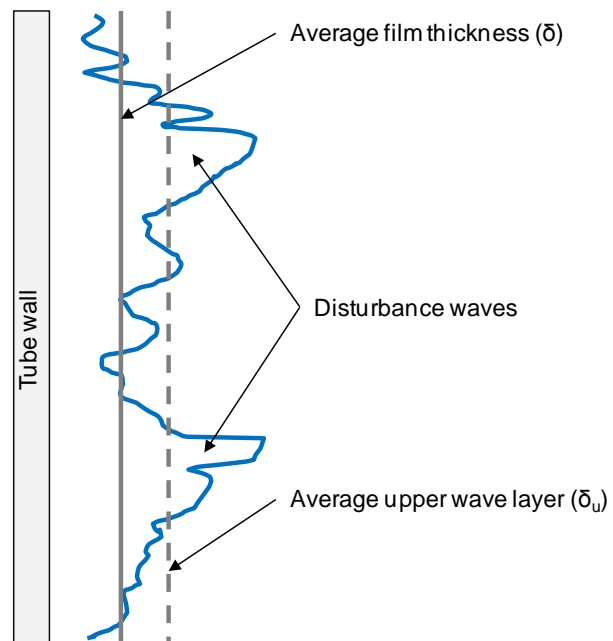
Figure 4.10 – Classification of the disturbance waves used in the calculation of the wave frequency.

The methodology developed by Hazuku et al. (2008) for annular flow was also applied to calculate the slug frequency for the tests with Ugs* = 0.05, and the results are presented in Figure 4.11. The accuracy of this method was confirmed using some of the visual observations. However, using the visual observations to process all experimental runs would be extremely tedious and time consuming.

For U_{gs}* = 0.05, a significant axial change can be observed in the slug frequency, which would be expected due to the coalescence of the Taylor bubbles as a consequence of the axial change in gas velocity. The axial change in gas velocity is caused in turn for elevated pressure gradient levels that are created for higher values of liquid holdup. As presented in Figure 4.5, the liquid holdup increases more severely for U_{gs}* < 0.1.
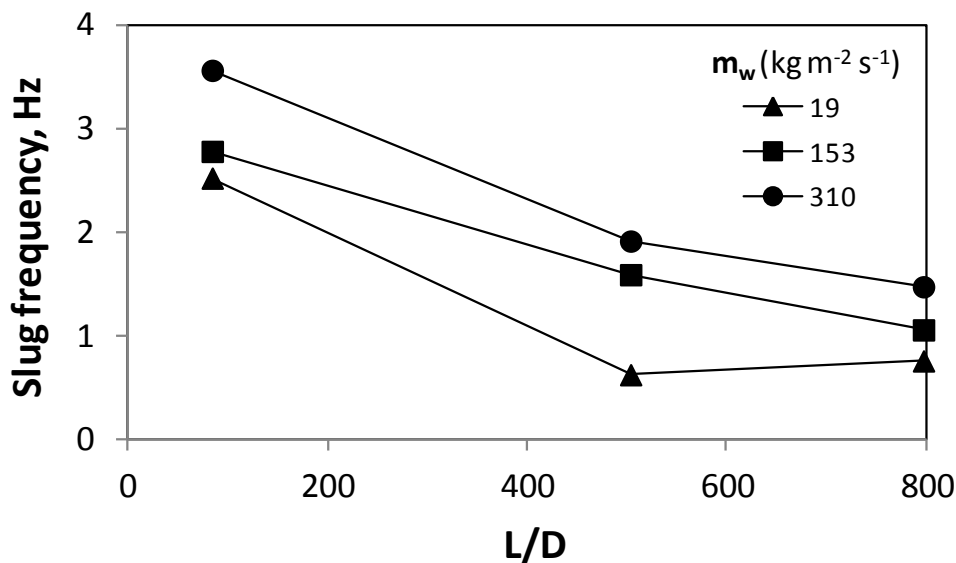
Figure 4.11 – Slug frequency as function of axial positions for an Ugs* of 0.05, at 1.4 bar pressure.

4.3. Conclusions

The axial development of churn and slug flows using a long vertical tube flow loop have been experimentally investigated here. From the experimental results the following conclusions are inferred:

- Using video recordings and PDF analysis for liquid holdup for three different axial positions (L/D = 85, 500 and 800), it was possible to show the similarities between the slug flow entrance region of Dukler and Taitel (1986) and churn flow, which has generate some confusion in the literature about the existence of churn flow as a separate flow regime. Additionally the video recordings and PDF results also confirmed the verification of churn flow for all three axial positions.

- Occurrence of slug flow at positions far from the liquid inlet (L/D = 500) is in reasonable agreement with the transition models of Brauner and Barnea (1986) and Jayanti and Hewitt (1992) for lower pressures (1.4 bara) and superficial liquid velocities. However, these models do not have a good match with the data for a higher pressure (4.2 bara). On the other hand, the model of Hewitt and Roberts (1969) presented a better match for higher rather than for lower pressures.

- The Wallis criterion ($U_{gs}{}^* \sim 1$) for the churn-to-annular flow transition show an excellent agreement with the experimental results for L/D = 500 for pressures of 1.4 and 4.2 bara.

- The liquid holdup varies significantly between all three axial positions (L/D = 85, 500 and 800) for the liquid mass flux of 310 kg/m^2-s, while for 19 kg/m^2-s it seems to reach developed flow for most conditions tested. However, the axial variation of liquid holdup seems to be more significant only for low pressure levels (1.4 bara).

- The disturbance wave frequency did not present a significant axial variation for $U_{gs}{}^*$ between 0.2 and 1.6. However, for slug flow conditions ($U_{gs}{}^* < 0.2$), the slug frequency changes considerably in the axial direction. This axial change in the slug frequency is related axial variation in gas velocity.

5. EXPERIMENTAL INVESTIGATION OF THE ONSET OF LIQUID LOADING

5.1. Introduction

Liquid loading in gas wells is generally defined as the inability of the produced gas to lift the co-produced liquid up the tubing, resulting in liquid accumulation at the bottom of the wellbore (Lea et al. 2003). Thus, the later statement will be preferably used to indicate the definition of the term "liquid loading" in following discussion on this dissertation.

The characterization of liquid loading is often based on field monitoring, with limited measurements of pressure and liquid holdup profiles and usually without visual observations of the phenomenon. Nevertheless, symptoms such as a sharp drop in the production decline curve, liquid slugs arriving at surface and increasing in liquid level in the wellbore are observed in the field (Lea and Nickens 2004), suggesting that liquid loading in gas wells is indeed associated with liquid accumulation at the bottom of the wellbore.

The most widely accepted concept that is used to predict the onset of liquid loading is the droplet model developed by Turner et al. (1969). The model provides the minimum gas velocity required to lift the largest liquid droplet based on a balance between the drag force (exerted by the gas flow) and the droplet weight. The critical gas velocity (in m/s) developed by Turner et al. is given by,

$$U_c = 5.46 \left[\frac{(\rho_L - \rho_G)}{\rho_G{}^2} \sigma \right]^{1/4} \tag{5.1}$$

where σ (in N/m) is the surface tension, ρ_G and ρ_L (in kg/m^3) are gas and liquid densities, respectively.

Turner et al. used only surface measurements from the field to verify the accuracy of this model. In other words, no downhole measurements were made by the later authors to verify the behavior of the flow for liquid loading conditions. The determination if the wells were under liquid loading conditions were made only from the liquid loading surface symptoms as described by Lea and Nickens (2004).

As described in section 2, there are some experimental evidences in opposition to Turner droplet model. Also, some experimental work was carried out showing that liquid can flow downs in vertical two-phase flow in the form a liquid film when the film flow reversal exists, or in other others, after the transition between churn-to-annular flows.

Several mechanisms are associated with the transition from annular to churn flow, which can lead to different ways of define such transition. The most common one is the flow reversal criterion (Wallis 1969), which can be easily observed experimentally and can be correlated by a simple relationship. The flow reversal criterion uses the flooding correlation and states that the transition between churn to annular flow occur when the dimensionless gas velocity $U_{gs}^{*} \approx 1$.

If we make a comparison between Turner et al. (1969) and Wallis (1969) for the liquid loading onset criteria, the superficial gas velocities is around 40% higher for Wallis criterion (e.g., $U_{gs}^{*} = 1$) than for Turner criterion for Eq. (5.1). In other words, for a continuous decline in the production gas rate, the flow reversal criterion would occur earlier than Turner criterion in the life of a gas well.

Another way that is suggested in the literature to predict the onset of liquid loading is to use the so-called nodal analysis (Lea et al. 2003). This technique consists of splitting the production systems into two parts: reservoir and wellbore (plus surface facilities). When plotting the bottomhole flowing pressure as a function of the gas flow rate for these two parts of the system, one can obtain a chart as shown in Figure 5.1. The intersection between these two curves indicates the operating bottomhole flowing pressure and production gas rate. However, as presented in Figure 5.1, there are unstable and stable operating conditions in which the well can flow. These two operating conditions are indentified considering the minimum pressure region that occurs in the wellbore curve. If the intersection between the reservoir and wellbore curves are to the

right of the minimum pressure point, the operating point is considered stable. If the intersection is to the left of the minimum pressure point, it is an unstable operating condition.

In the stable condition, a small increase in wellbore bottomhole pressure requires a higher pressure support from the reservoir, which is in turn obtained with a reduction of the gas rate from the reservoir, readjusting the system back to the operating point. Similarly, the readjustment occurs for a small decrease in wellbore bottomhole pressure. For the unstable operating point, an increase in wellbore bottomhole pressure would require a higher pressure support from the reservoir. Then, in order to sustain the flow, the reservoir would have to decrease the gas rate to obtain a higher pressure support. However, in this region of the wellbore curve, a further decrease of the gas rate causes an increase in the wellbore bottomhole pressure, which in turn creates a cascade effect until the reservoir stop flowing.
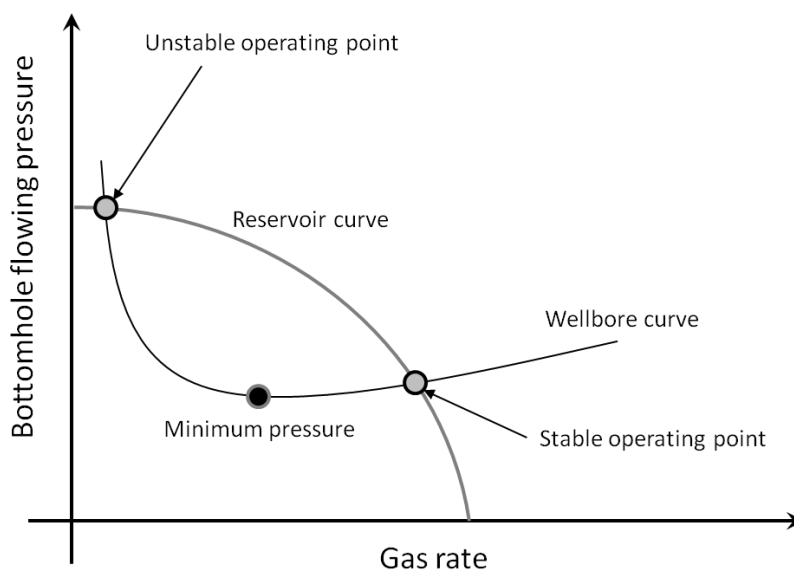
Figure 5.1 – Nodal analysis technique used to predict liquid loading in gas wells. The intersection between the reservoir and wellbore curve defines the operating gas rate and bottom hole flowing pressure for a particular production system.

In overall, the prediction of liquid loading conditions using nodal analysis suggests that if the operating point is to the left of the minimum pressure point, liquid loading problems are expected to occur.

As can be seen, there are still some inconsistencies in the physics behind liquid loading and in the criteria to predict its onset. One of the reasons that should be taken into account for the still weak understanding of liquid loading phenomena is the few studies available about churn flow. There is a lack of information about churn flow in the literature, and the studies are even scarcer when we consider churn flow in transient conditions. As previously described, churn flow is considered here to be the flow regime directly related to the liquid loading phenomena because of the liquid film flow reversal characteristic. Even when considering the other two approaches (Turner criterion and nodal analysis) used to predict the onset of liquid loading, the flow regime estimated to occur for these approaches are also in churn flow conditions (or at least close to its transition). Thus, there is a strong confidence in the present work that more investigation should be carry out about two-phase flows under churn flow conditions, in order to enhance the understanding of fundamentals of liquid loading.

The next section will present an experimental investigation using TowerLAB facility to study the onset and the flow characteristics related to liquid loading conditions. This investigation will try to correlate the flow regimes, pressures, liquid holdup, and gas/liquid flow rates with two-phase flow conditions which are believed to be under liquid loading. Because of the reasons previously explained, the current work will focus most of the experimental campaign in churn flow cases.

5.2. Results and Discussions

The classical definition of liquid loading that can be found in the literature states that this phenomenon is the inability of the produced gas to lift the co-produced liquid up the tubing, resulting in liquid accumulation at the bottom of the wellbore. Some studies such as Sutton et al. (2003) and Coleman et al. (1991b) have even tried to develop methodologies to predict the height of the liquid level as a consequence of the downhole

liquid accumulation. Thus, experimental runs using a large scale flow loop were carried out with the objective of measuring and observing the bottomhole liquid accumulation.

Table 5.1 shows the range of conditions for the experimental runs which were performed for the tests on liquid loading onset.

Table 5.1- Summary of the conditions used in the experimental runs for the tests on liquid loading onset.

Flow Regimes	Inlet pressure, kPa	Outlet pressure, kPa	Air mass flux kg/m^2-s	Water mass flux kg/m^2-s
Annular/Churn/Slug	110-520	110-500	2-80	0-360

Figure 5.2 illustrates the inflow performance relationship for the air compressor for its maximum and minimum capacity used during the tests. Also, the figure shows examples of the tubing performance relationship (TPR - for some conditions tested), which gives a general idea of how the air compressor behaves as a reservoir in the tests carried out in this work.

5.2.1. Liquid loading onset tests

The procedure for this first test consists of initially flowing air through the mixing tee at the entrance of the test section (see Figure 3.5). Next, water is also injected in the mixing tee for a fixed water mass rate, and the pressure is regulated using the choke valve in the end of the test section.
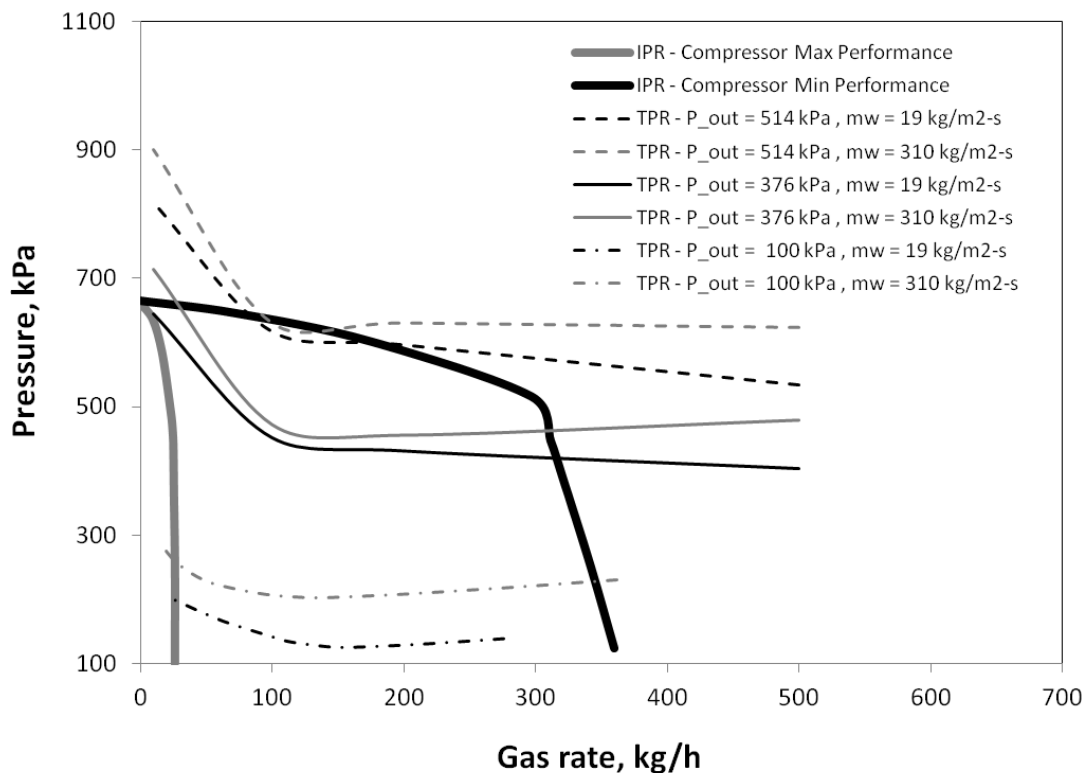
Figure 5.2 – Nodal analysis using the air compressor performance curve and examples of two-phase tubing performance relationship for some of the conditions tested.

For the first test, air and water rates were kept constant during the test, as shown in Figure 5.3. The total test time was approximately five hours (18,000 s) and the data sample rate was 1 Hz.

The average pressure profile for this 5 hours test is shown in Figure 5.4. It is possible to calculate the liquid loading onset criterion of Turner (U_c) and Wallis ($U_{gs}*$), using Eq. (5.1) and Eq. (2.1), water surface tension (0.071 N/m), the air superficial velocity calculated from the average air mass rate from Figure 5.3, and the pressure from the last point (length = 40 m) in Figure 5.4. The calculation results for both criteria for this test was U_c = 7.28 m/s and $U_{gs}*$ = 0.28. Since the superficial gas velocity at the last point is U_{gs} = 2.84 m/s (which is far below the Turner critical velocity) and $U_{gs}*$ = 0.28 is considerably lower than the unit, this test should be considered to be under liquid loading conditions, according to Turner and Wallis criteria.
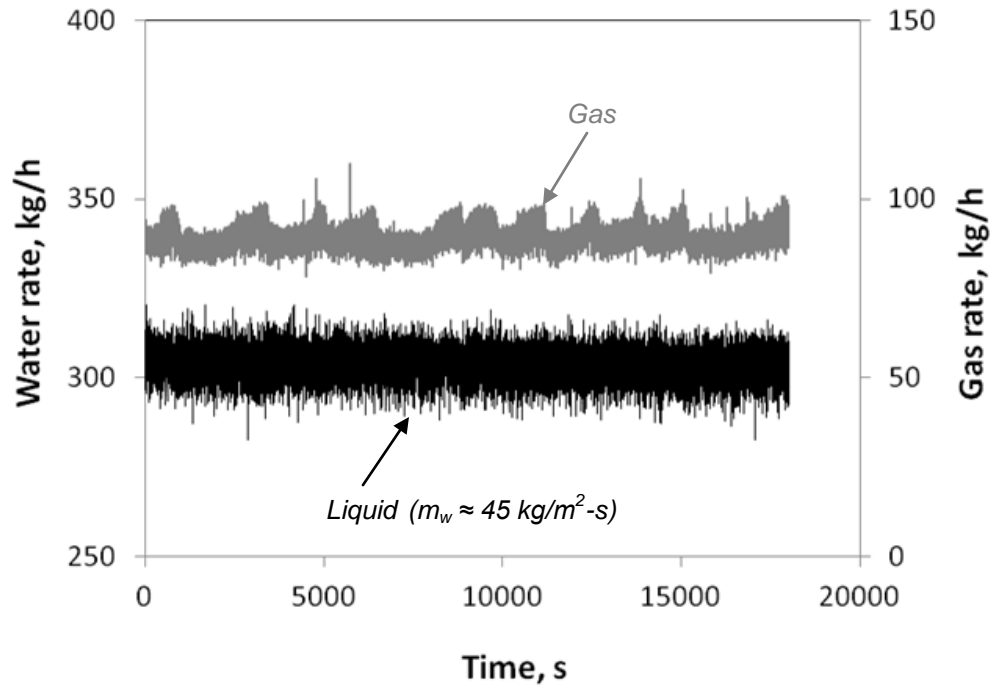
Figure 5.3 – Constant air and water mass rate for the first test (higher gas rate) for liquid loading onset investigation.
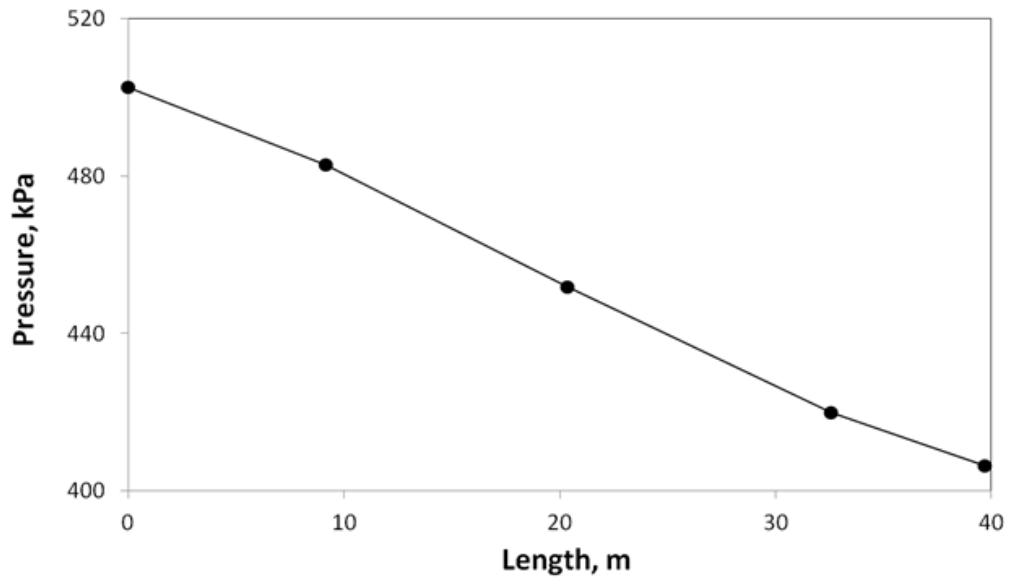
Figure 5.4 – Average pressure profile for the first test (higher gas rate) for liquid loading onset investigation.

However, after running the test for five hours, no increasing in bottomhole pressure or liquid holdup was observed over time, as shown in Figure 5.5. As the outlet pressure and the air/water rates were kept constant, increasing in total pressure drop (differential pressure between the bottom and top) would be expected to occur due to liquid build up in the vertical tube as consequence of liquid loading phenomena (based on the classical definition).
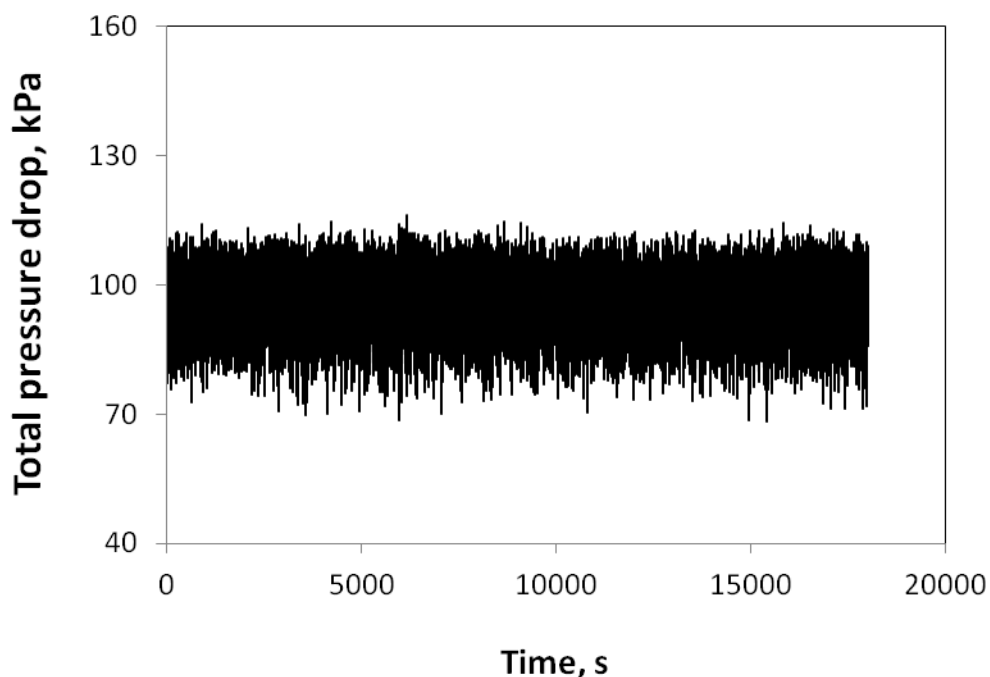
Figure 5.5 – Total pressure drop in the 40 m vertical test section for a five hours test. No increasing in total pressure drop was observed over time under liquid loading conditions and churn flow.

Additionally, visual observations using the visualization system confirmed that there was no liquid building up in any part of the test section. From the flow visualization, it was also possible to determine churn flow regime during the entire experimental run, where the film flow reversal (film oscillatory motion - see Figure 5.6) was identified from bottom to top of the test section.

To confirm even further the non-occurrence of liquid accumulation, another similar test was carried out, but now for an even lower gas rate. The air and water mass rates were kept constant as shown in Figure 5.7. The averaged pressure profile for this new test is presented in Figure 5.8. Using the same approach as the previous test to calculate the liquid loading onset criteria, the results for Turner and Wallis criteria are U_c = 14.53 m/s and $U_{gs}{}^* = 0.11$, respectively. The superficial gas velocity for the top point of the test section is $U_{gs} = 2.16$ m/s, which is almost one order of magnitude lower than the Turner critical velocity and $U_{gs}{}^* = 0.11$ is approximately one order of magnitude lower than the unit. Thus, this test is expected to be under even stronger liquid loading conditions than the first test.
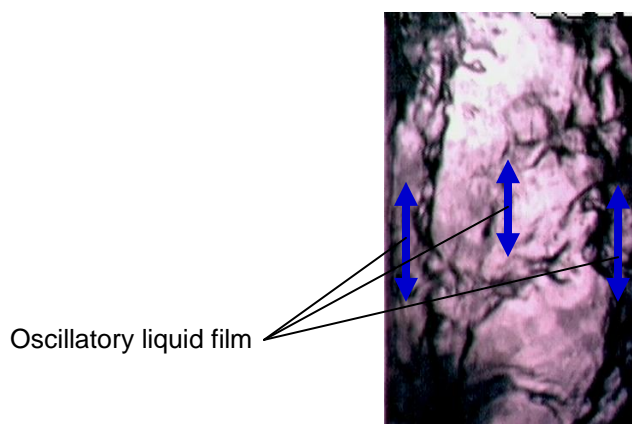
Figure 5.6 – Snapshot from the high speed camera video recordings for churn flow. The picture shows the oscillatory motion of the liquid film when in churn flow conditions.
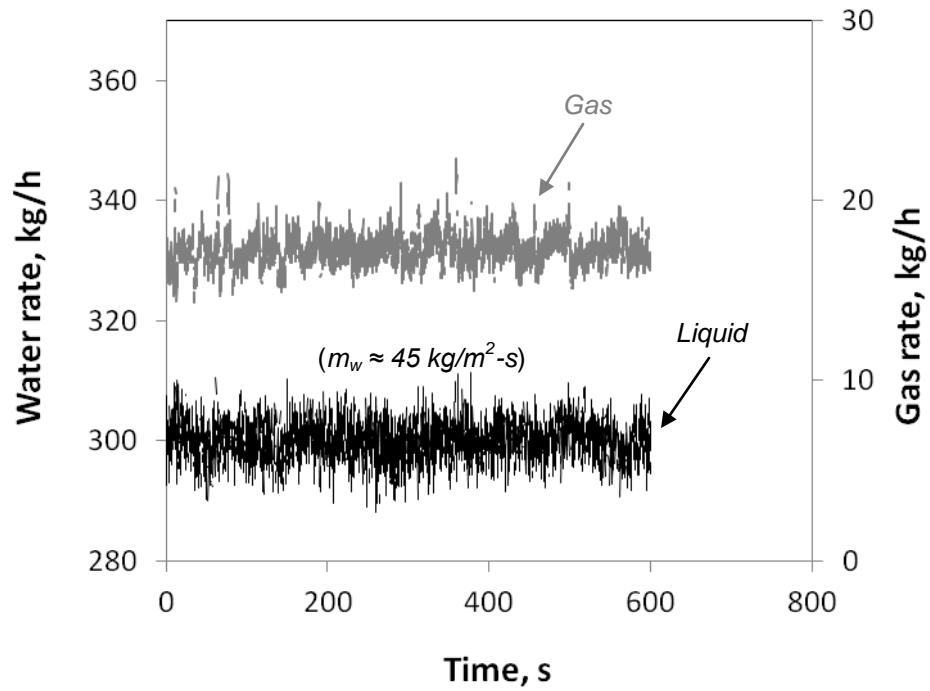
Figure 5.7 – Constant air and water mass rate for the second test (lower gas rate) for liquid loading onset investigation.
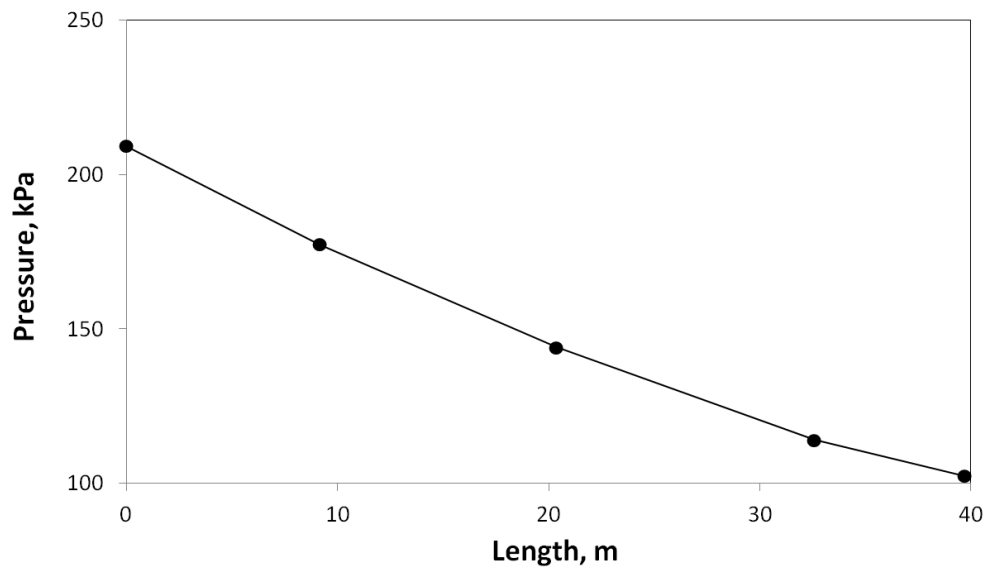
Figure 5.8 – Average pressure profile for the second test (lower gas rate) for liquid loading onset investigation.

Not even for such low gas rate the expected liquid accumulation was observed, as can be seen in Figure 5.9. The results for the total pressure drop show some oscillations, but not an increasing trend due to the liquid build up. These oscillations are only side effects of the liquid slugs flowing through the test section. As presented in Figure 5.10, visualization of the flow throughout the test section confirmed slug flow conditions (i.e., long Taylor bubbles surrounded by a falling liquid film, separated by aerated slugs of liquid).
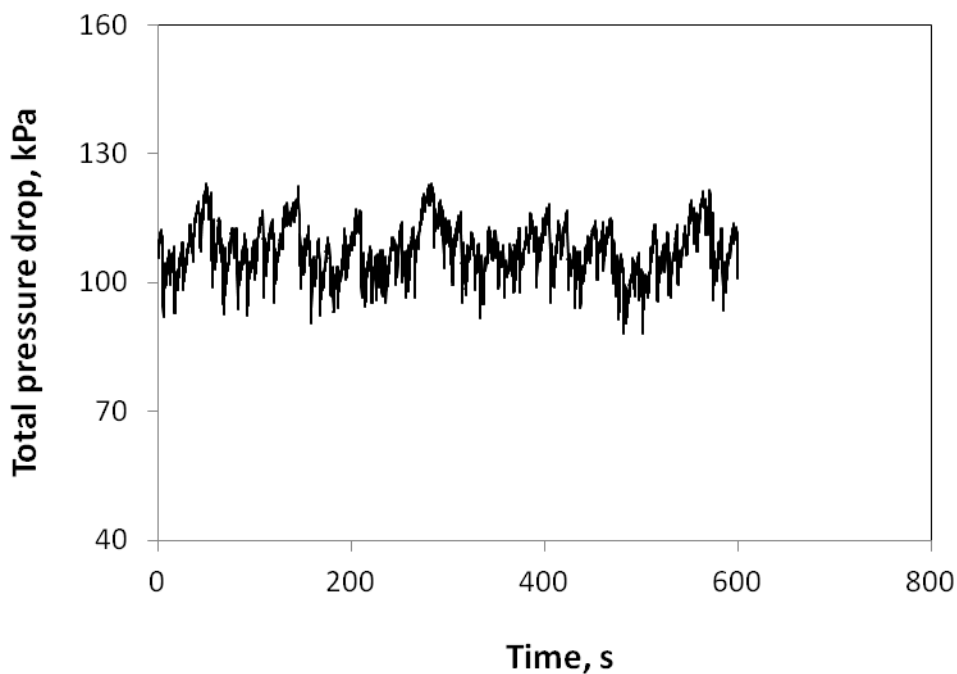
Figure 5.9 – Total pressure drop for the 40 m vertical test section for the low gas rate test. No increasing in total pressure drop was observed over time under liquid loading conditions and slug flow.
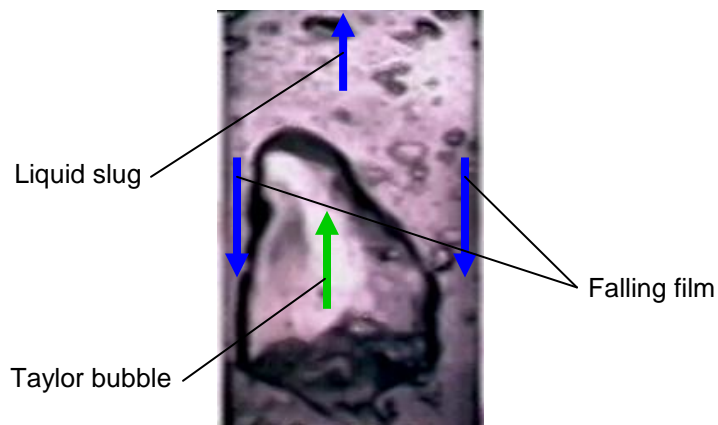
Figure 5.10 – Snapshot from the high speed camera video recordings for slug flow. The picture shows the Taylor bubble in the center with a liquid film flowing downwards and the liquid slug flowing upwards in the top.

One could argue that it would be obvious that for churn and slug flow under steady-state conditions no change in bottomhole pressure should occur, as long as the inflow of gas and liquid is in steady-state condition. However, if one considers Turner's model, the main objective of this model is to indicate if liquid loading is taking place, based only on constant gas flow rate, fluid properties and tube geometry. Thus, the purpose of these tests was to show that Turner criteria alone is not enough to indicate if a particular well will experience the onset of liquid loading.

Since none of the previous two tests showed increase in the total pressure drop or in liquid holdup over time, a series of other similar tests were carried out for different gas rates. The test procedure is similar to the first two tests previously described. However, now the gas rate is kept constant for one hour, and then the gas rate is decreased for the next gas rate point. The procedure here tried to reproduce a pseudo-steady state process regarding the gas flow rate decline that would occur in an actual gas well. The test were carried out beginning from the highest (U_{gs}* = 1.6) to the lowest (U_{gs}* = 0.05) gas flow rate tested. For a fixed outlet pressure and liquid mass flux, the gas rate is reduced in a continuous way from one test to another, keeping the gas flow rate constant for one hour for each test point. These tests were run for liquid mass flux of 153 kg-m^{-2}-s^{-1} and at 4.8 bara outlet pressure.

Again, no increase in total pressure drop or liquid holdup was observed during the one hour when the gas rates were kept constant for each test run. To confirm that most tests were expected to show liquid loading behavior, Figure 5.11 presents a comparison of the conditions of these tests with Turner and Wallis criteria.

The figure shows the superficial gas velocity for each test as a function of $U_{gs}*$ and Turner critical velocity for each corresponding test. Then, based on Turner and Wallis onset criteria, the highlighted region in the plot indicates which tests (squares) should be under liquid loading conditions. As can be seen from the figure, most tests are in the liquid loading region.
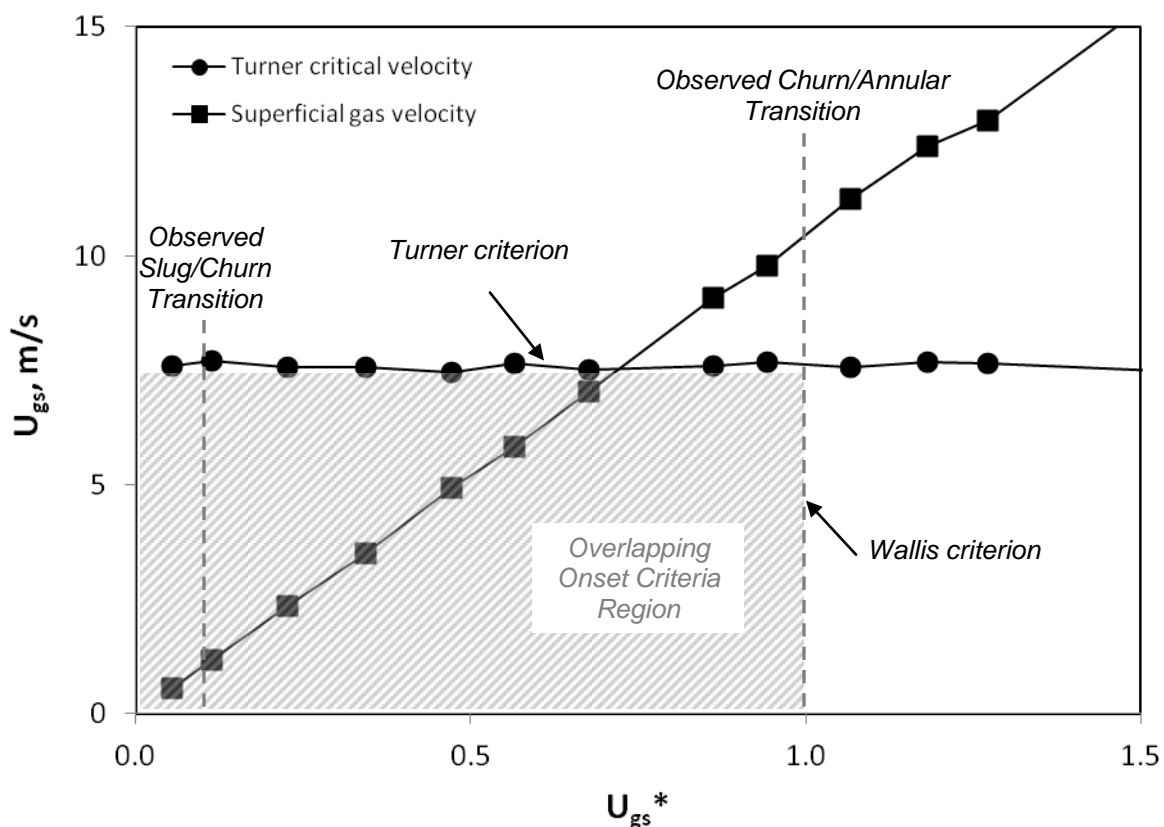
Figure 5.11 – Comparison between tests gas velocities with Turner and Wallis onset criteria for liquid mass flux of 153 kg/m^2-s and at 4.8 bara pressure. The squares show the superficial gas velocity for each test and the circles show Turner critical velocity for each corresponding test.

Since no onset of bottomhole liquid accumulation over time was observed for each constant gas rate test, one could argue that liquid loading can be related to the increase in liquid content due to gas flow rate decline. Figure 5.12 shows the liquid holdup at the bottom of the test section (L/D = 85) as a function of U_{gs}* for three water mass fluxes (m_w = 310, 153 and 19 kg-m^{-2}-s^{-1}) and at 4.8 bara outlet pressure. As can be seen from the figure, the liquid holdup increases exponentially and continuously (without a sudden increase) as U_{gs}* decreases. To confirm that this measurement pattern observed here is not a consequence of the type of sensor used in this study, the same trend in liquid holdup is observed using other types of sensors (such as wire mesh sensors and γ-ray densitometer) as presented by Prasser et al. (1998).

Thus, if we consider Figure 5.12, it is difficult to establish a point in the dimensionless gas velocity (or gas rate) at which the liquid holdup suddenly starts rising. One could say that Turner criterion is the beginning of severe liquid holdup levels. Other could say that the onset is the Wallis criterion, or another could even say that it is a point in the beginning of the liquid holdup curve. The axial liquid holdup profile throughout the test section was also observed as constant over time for all tests. An example of how the liquid holdup changes axially was presented in section 4.

Since there is always an increase and no sudden change in liquid holdup as the gas flow rate declines, the onset of liquid loading could be seen as the point when the well start producing any amount of liquid, with no regard to the gas flow rate. The later statement is based on the no observation of liquid accumulation for all the conditions tested, the continuous increase of liquid holdup for the entire range of gas rates tested, and considering only a vertical tube and not taking the reservoir behavior into account

It is important to mention that one of the reasons that can be attributed to the non-observation of the field liquid loading symptoms (such as liquid slugs arriving at the surface and erratic gas production) is the absence of the reservoir attached to the bottom of the test section. Changes in the flow rates provided by the reservoir as a function of the pressure behavior in the bottom of the wellbore is believed to be an important part of the system dynamics, as described earlier in the nodal analysis method. However,

Turner's model is the most widely used approach to predict liquid loading onset and it does not consider the reservoir behavior
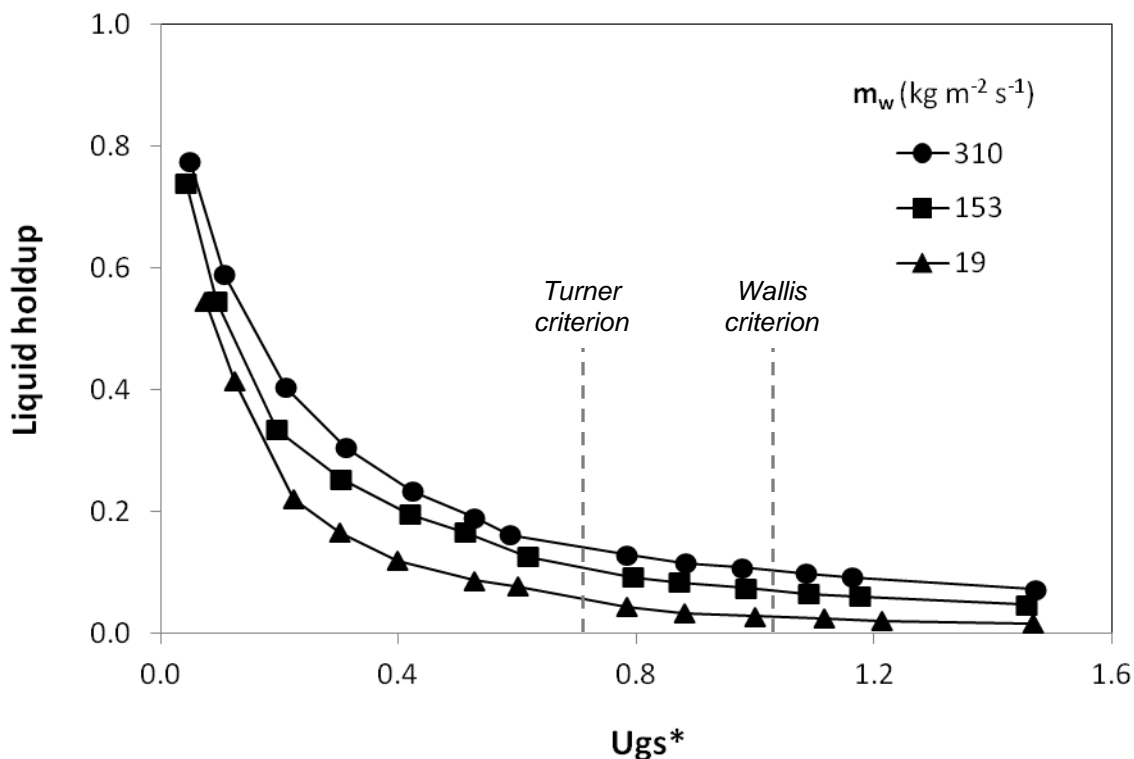
Figure 5.12 – Liquid holdup as function of dimensionless gas velocity. The figure shows a continuous and exponential increase of liquid holdup with dimensionless gas velocity.

Also, the current flow loop does not have the larger casing diameter (very often 2 to 5 times larger than the producing tubing diameter) connected to the bottom of the test section. The downhole casing can act as liquid-storage compartment, which can trap liquid over time due to pressure oscillations in the vertical wellbore, and could potentially also generate the liquid loading symptoms observed in the field.

Pressure oscillations during the tests were also evaluated using the standard deviation calculation from the pressure measurements. Figure 5.13 presents the percentage of the standard deviation for the bottom pressure measurements as a function U_{gs}^*. These results include tests for water mass fluxes between 19 and 353 kg-m^{-2}-s^{-1},

and pressures between 1.4 and 4.2 bara. As can be seen from the figure, there is no sudden transition for the bottomhole pressure oscillations (or pressure standard deviation) as the dimensionless gas velocity is decreased. Thus, it is clear to see that the utilization of either Wallis or Turner criteria is significantly subjective to predict the onset of high levels of pressure oscillations in a vertical two-phase flow. Elevated levels of pressure oscillations could be argued as one of the sources of liquid loading symptoms, since these oscillations can consequently create gas/liquid production variation and creation of liquid slugs.
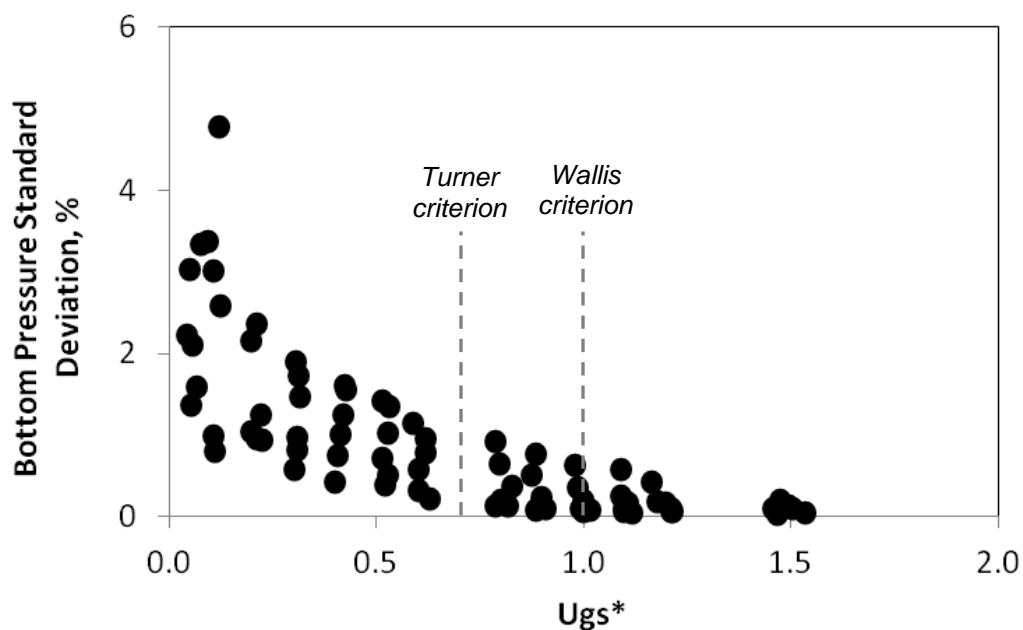
Figure 5.13 – Percentage of the standard deviation for bottomhole pressure measurements as function of Ugs* for different liquid mass fluxes and pressures between 1.4 and 4.2 bar.

When considering a gas rate decline, another important way to analyze the effects of the increase in the liquid content in a vertical tube is to look at the pressure gradient. Figure 5.14 shows the pressure gradient as a function of $U_{gs}*$ for a water mass flux of m_w = 153 kg-m^{-2}-s^{-1} and at 4.2 bara pressure. As can be seen, it is not clear how to establish

the criteria at which point the pressure gradient suddenly starts rising more severely, leaving a wide range of uncertainty to define at which gas flow rate can be related to the onset of severe increasing in the pressure gradient. However, as described by Zabaras et al. (1986), Jayanti and Hewitt (1992) and Barbosa et al. (2002), the minimum in the pressure gradient curve occur near to Wallis criterion ($U_{gs}^{*} \approx 1$), for all tests and axial positions. Thus, if one considers the inflow reservoir performance (IPR) and the instability created if the intersection between IPR and pressure gradient curve are to the left of the minimum point (as previously described in nodal analysis), Wallis criterion seems to be the most recommended to be used in nodal analysis, rather than Turner's criterion.
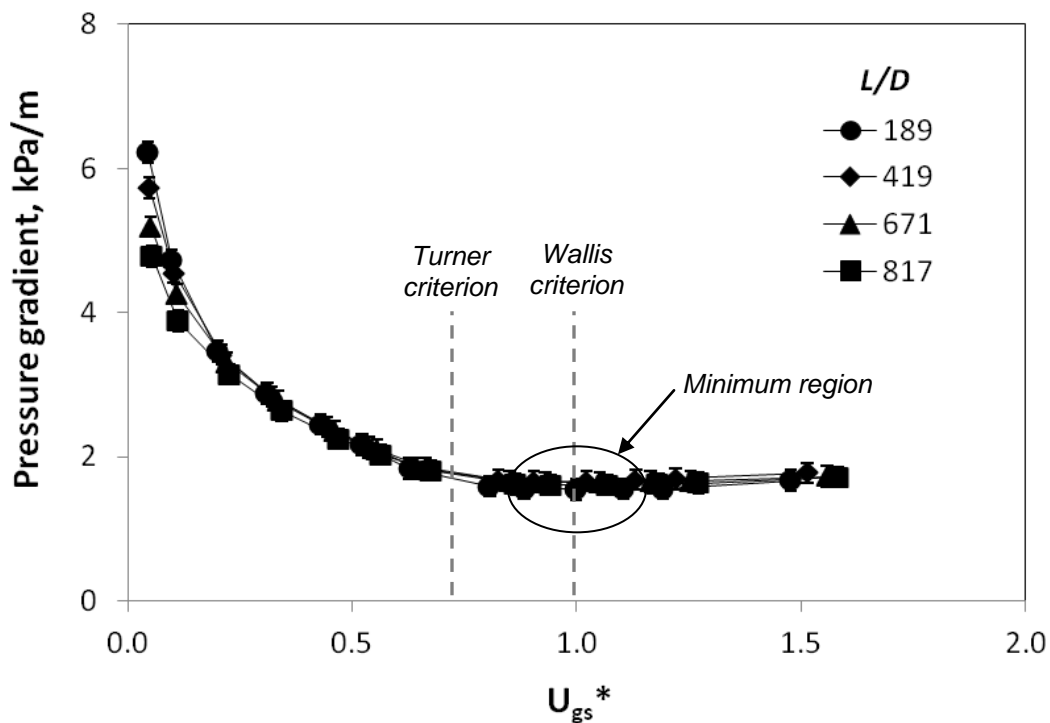
Figure 5.14 – Pressure gradient as function of dimensionless gas velocity for four axial positions. The tests were performed for $m_w = 153$ kg-m^{-2}-s^{-1} and at 4.2 bara pressure.

Another example of the importance of the results presented in Figure 5.14 is to analyze the pressure gradient along the tube. One could consider that it is possible to calculate the liquid level in the wellbore looking for a change in the pressure gradient in a particular point along the vertical wellbore. Some authors (Coleman et al. (1991b); Sutton et al. (2009)) have tried to calculate the pressure gradient along the wellbore and then determine the height of a static liquid column based on a change in the pressure gradient curve. They have also correlated the occurrence of this change with Turner critical velocity.

From the results presented here, no liquid height was observed accumulating in the bottom of the tube, even when running the experiment for hours. Then, looking at the pressure gradient from Figure 5.14, there is virtually no difference in the pressure gradient between bottom and top of the test section, even for gas rates considerably lower than the liquid loading onset criteria of Turner and Wallis. Thus, based on the on the non-observation of axial change in pressure gradient, we could say that there is no liquid loading for this test. Therefore, it is clear to see here that there is an inconsistence in using Turner's criterion and the axial variation on pressure gradient to evaluate liquid loading conditions.

5.2.2. Start-up and shutdown tests

Since no liquid buildup was observed in the previous tests (when the test procedure consisted of first flowing only gas and then start injecting liquid), the test procedure was re-designed to try to produce a more severe scenario where the liquid accumulation as described by the classical liquid loading definition could take place. The procedure of the subsequent tests consists of the following steps:

1. Fill completely the test section from bottom to top with water;
2. After the entire vertical tube is full of water, the valve in the gas and water inlet lines are open until the valve opening reaches a specific value (for instance, 50% opening), releasing a specific flow rate of gas and water;
3. The valves opening are kept constant for 15 minutes and then they are closed;

4. The valves are kept closed until there are no more variation in the test section inlet pressure and total pressure drop (pressure difference between bottom and top);

5. After there is no more variation in the pressure measurements, the valves are reopened to the previous opening values as in step 2;

6. The valve opening is kept constant for more 15 min and the valves are closed again;

7. The valves are kept closed and the measurements are then recorded until there are no more variation in the test section inlet pressure and total pressure drop.

The objective of these tests is to create what is believed to be a severe scenario (start-up and shutdown) in terms of liquid loading, to push harder the observation of liquid accumulation. The liquid accumulation is expected to be verified looking at the period when the air and water valves are closed, and then compare the hydrostatic pressure between the first and second shutdowns. If the hydrostatic pressure for the second shutdown period is higher than for the first one, it means liquid accumulation in the tube (e.g., liquid loading).

The first test (high gas rate) was performed for a gas rate above the critical gas velocity of Turner and Wallis. Figure 5.15 shows the air and water rate during the entire first test.
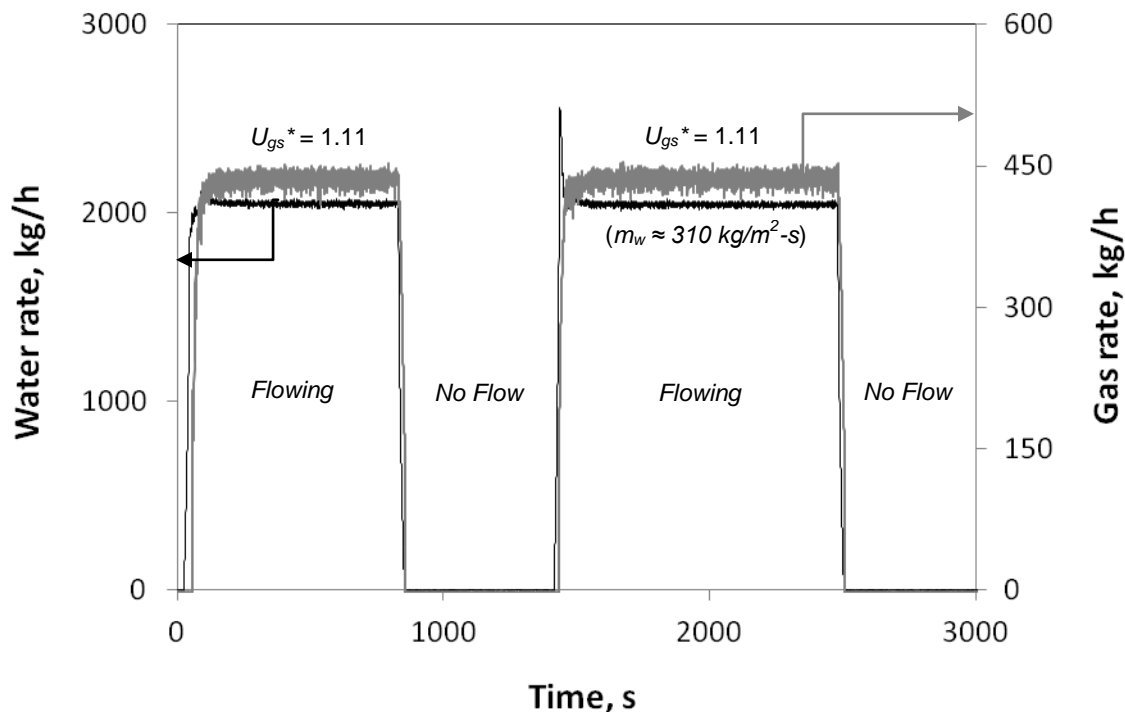
Figure 5.15 – Air and water mass rate for the first test (high gas rate) for start-up/shutdown scenario investigation. The outlet pressure during the stable period is 4.8 bara.

The dimensionless gas velocity during the flowing period of the test was calculated as $U_{gs}^* = 1.11$, which indicates that the gas velocity is above the critical velocity of Wallis ($U_{gs}^* = 1$). The outlet superficial gas velocity was calculated as 12.2 m/s, which is also significantly higher than the calculated Turner critical velocity ($U_c = 8.0$ m/s). The time-averaged pressure profile for the flowing period is shown in Figure 5.16. The bottom (inlet) gauge pressure is presented in Figure 5.17 for the entire test.
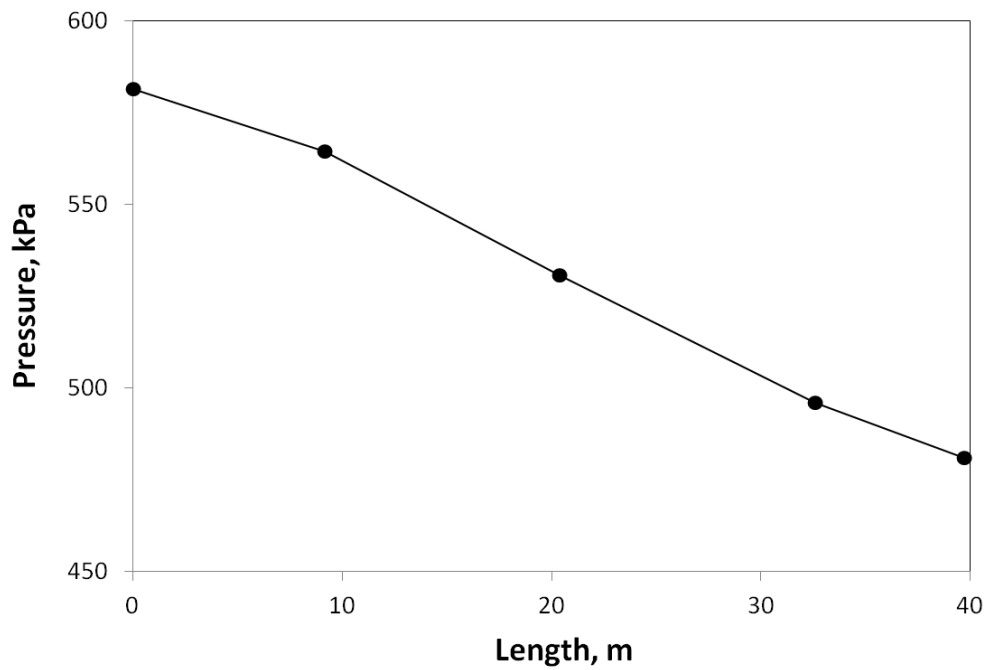
Figure 5.16 – Average pressure profile for the first test (high gas rate) during the flowing period for the start-up/shutdown scenario investigation.
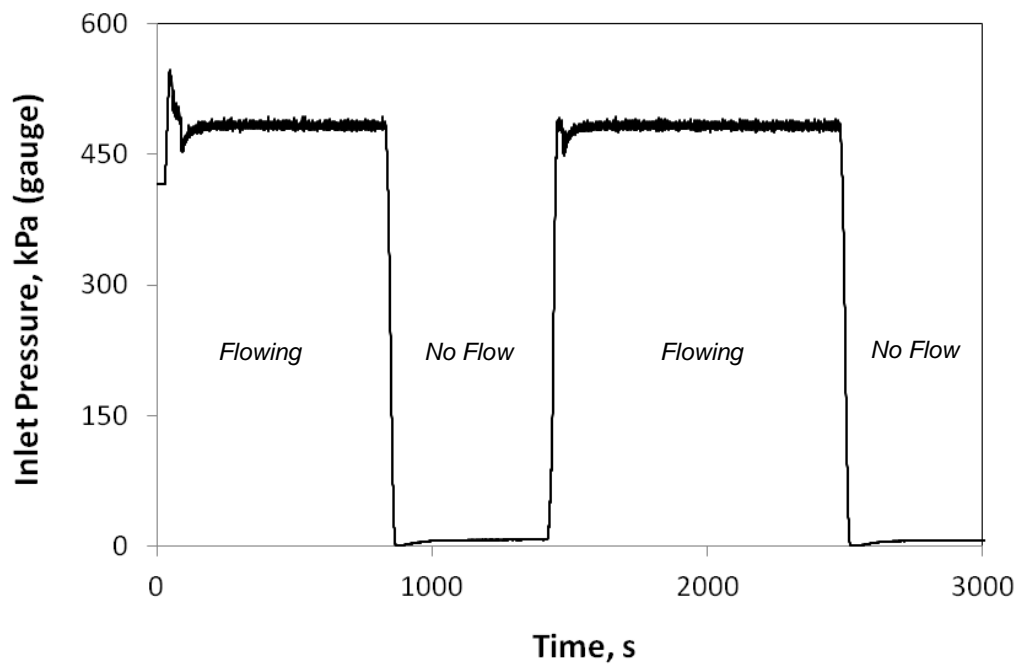
Figure 5.17 – Inlet (bottom) pressure (gauge) for the first test (high gas rate) for start-up/shutdown scenario investigation.

As can be seen from Figure 5.17, the inlet pressure reaches steady-state after only 180 seconds (3 minutes), and stay constant for 15 minutes until the air and water valves are closed. During the no-flow period, is easy to see that there is no significant liquid build up above the inlet pressure transducer, since the inlet pressure is approximately zero for the first and second no-flow periods. The no-presence of liquid column in the bottom of the test section can be also confirmed observing the inlet liquid holdup, as presented in Figure 5.18.
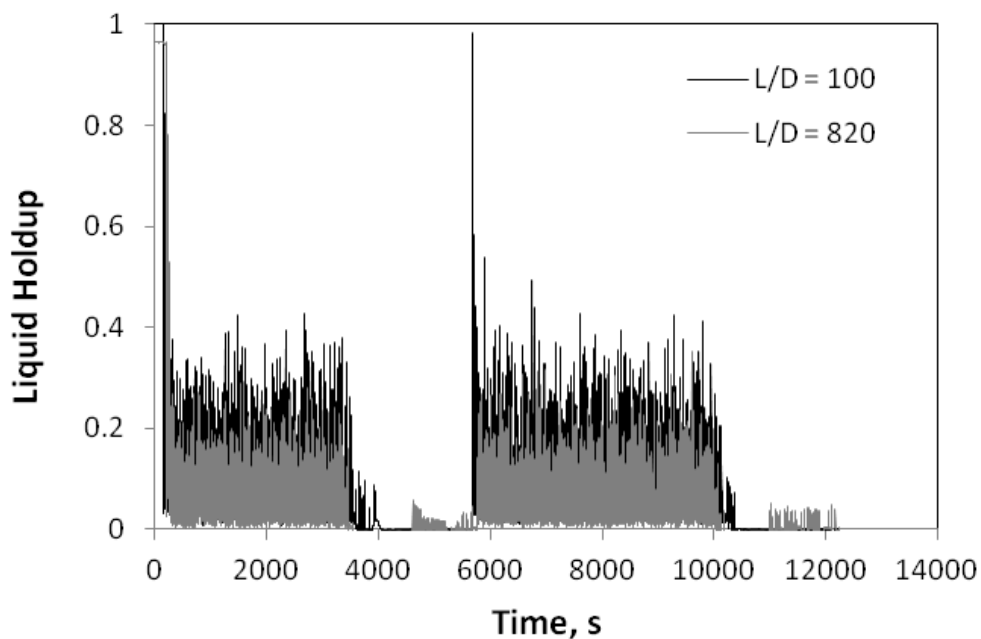
Figure 5.18 – Inlet and outlet liquid holdup for the first test (high gas rate) for start-up/shutdown scenario investigation.

The non-accumulation and small content of liquid in the test section during the no-flow periods was already expected, since the gas velocity was higher than critical velocities of Turner and Wallis. However, even for high gas flow rates, there is still some amount of liquid that builds up in the bottom of the tube after the valves are closed. The small content of liquid accumulates in the bottom part of the test section between the mixing tee and the first pressure transducer (which is positioned at L/D = 40

downstream to the mixing tee). As can be seen from Figure 5.17, the pressure measurement does not show absolutely zero but a value close to zero (approximately 1 kPa) for the no-flow period, which implies that there is only a very small liquid column above the inlet pressure transducer. Additionally, we should consider the liquid column not being measured below the inlet pressure transducer. The inlet liquid holdup sensor cannot capture the liquid level because it is positioned a couple of diameters downstream to the first pressure transducer.

Having confirmed from the previous test (high gas rate) the expected no-accumulation of liquid bottomhole between the two no-flow periods, a second test with low gas flow rate was performed. The second test (low gas rate) was carried out for a gas rate considerably below the liquid loading critical gas velocity of Turner and Wallis. Figure 5.19 shows the air and water rate during the entire second test.
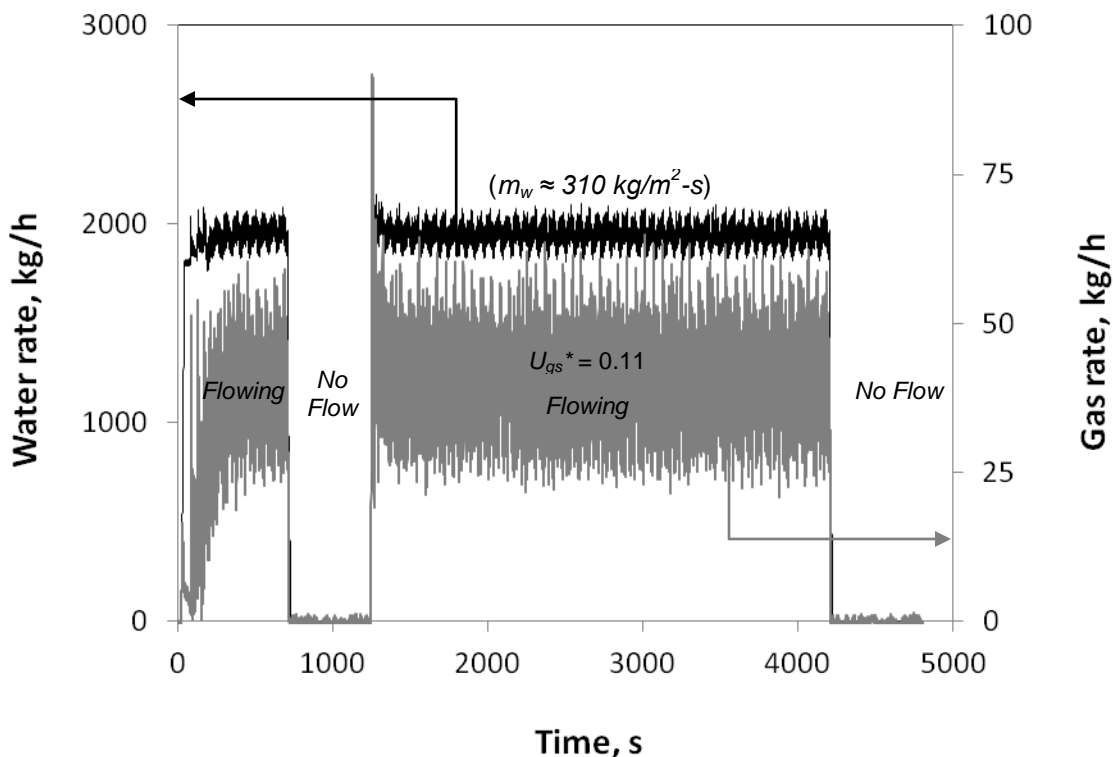
Figure 5.19 – Air and water mass rate for the second test (low gas rate) for start-up/shutdown scenario investigation. The outlet pressure during the stable period is 4.8 bara.

The dimensionless gas velocity during the flowing period of the test was calculated as $U_{gs}^* = 0.08$, which is one order of magnitude lower than $U_{gs}^* = 1$ (Wallis criterion). The outlet superficial gas velocity was calculated as 0.85 m/s, which is also considerably lower than the calculated Turner critical velocity for this test ($U_c = 7.39$ m/s). From the visual observations, the flow regime recognized for this test was slug flow (as described in Figure 5.10). The time-averaged pressure profile for the flowing period is shown in Figure 5.20. The bottom (inlet) gauge pressure is presented in Figure 5.21 for the entire test.
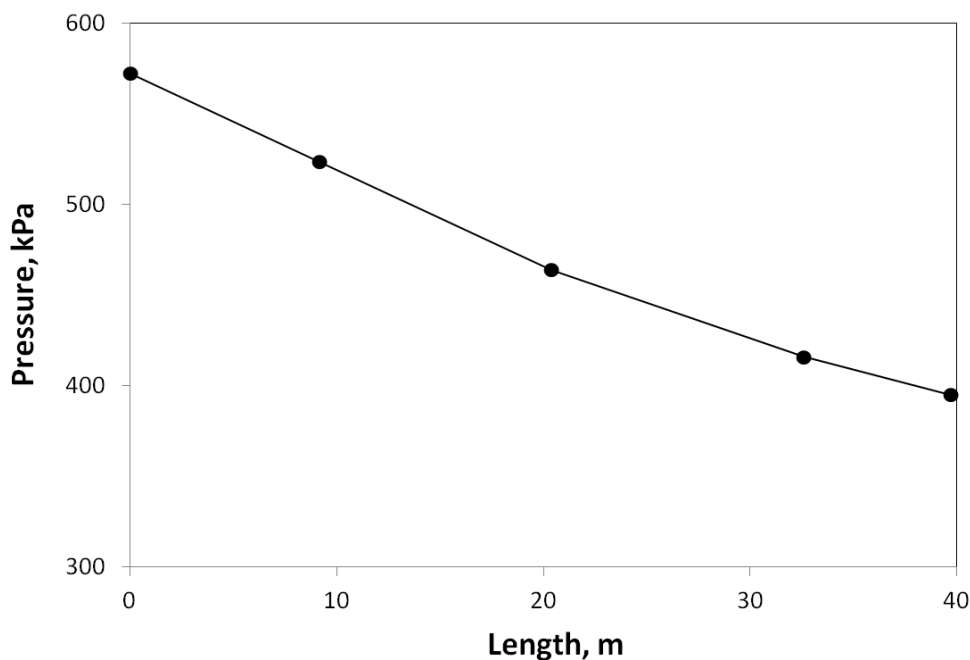
Figure 5.20 – Average pressure profile for the second test (low gas rate) during the flowing period for the start-up/shutdown scenario investigation.

As can be seen from Figure 5.21, during the first no-flow period there is a considerable liquid column above the inlet pressure transducer. Calculating the liquid column using the inlet pressure and a hydrostatic model ($\Delta p = \rho_l \cdot g \cdot \Delta h_l$), we obtain a liquid column of approximately $\Delta h_l = 28.1$ m. Now, if we do the same calculation for the

second no-flow period, we obtain Δh_l = 28.0 m, which is virtually the same as the first one. Thus, no liquid accumulation was observed again between the two shutdown periods, even for a very low gas rate.

To confirm even further the absence of liquid build up in the vertical tube over time, we can also look at the probability density function (PDF) of the liquid holdup for the two flowing periods. The PDF here means the frequency history (histogram) of each particular value of liquid holdup during the first and second flowing period. Figure 5.22 presents the liquid holdup PDF for the inlet sensor (at L/D = 85) and Figure 5.23 shows the PDF for the outlet sensor (at L/D = 800).
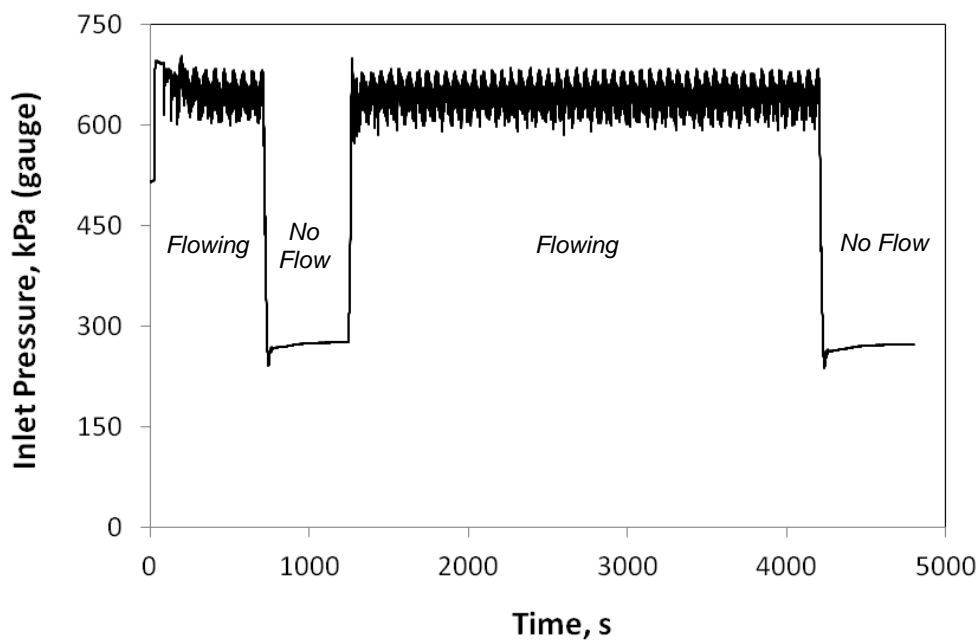
Figure 5.21 – Inlet (bottom) pressure (gauge) for the second test (low gas rate) for start-up/shutdown scenario investigation.
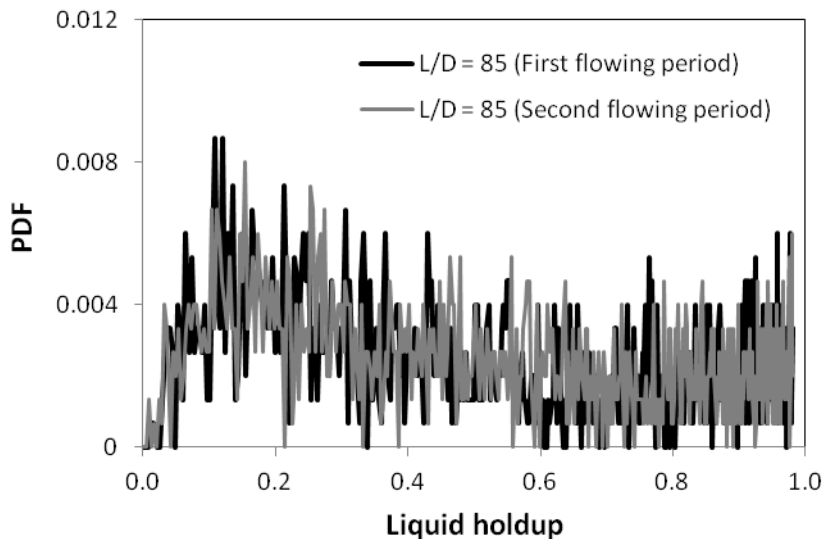
Figure 5.22 – Inlet (bottom) liquid holdup PDF for the second test (low gas rate) during the flowing periods. This liquid holdup sensor is positioned at L/D = 85 from the mixing tee.
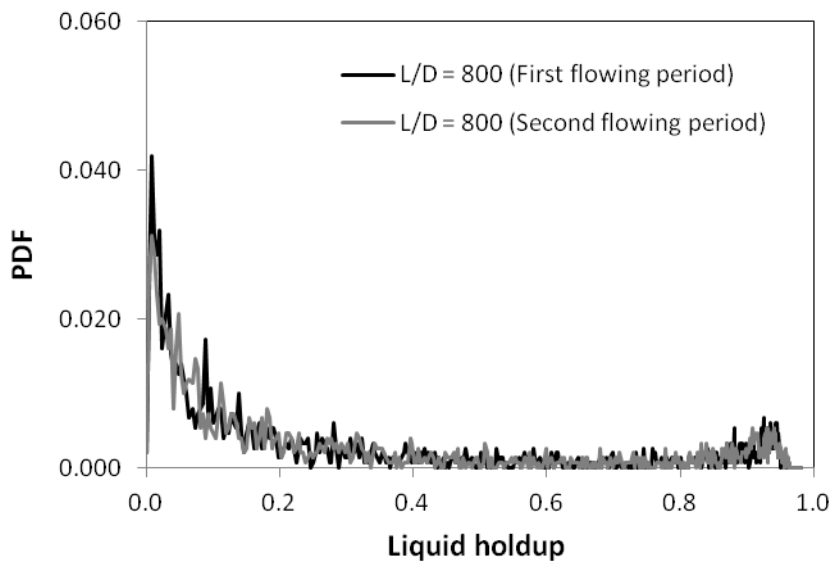
Figure 5.23 – Outlet (top) liquid holdup PDF for the second test (low gas rate) during the flowing periods. This liquid holdup sensor is positioned at L/D = 800 from the mixing tee.

As can be seeing from both figures, there is almost no difference between the liquid holdup PDFs for the first and second flowing periods for both inlet and outlet positions. In other words, even after the first shutdown and keep the flow under liquid

loading conditions regarding the criteria assumed here, the amount of liquid in the vertical tube while it is flowing is the same, not showing any liquid build up when considering the liquid holdup measurements.

5.2.3. *Dynamic behavior of annular–to-churn flow transition*

As presented in the previous sections, a sudden change in liquid holdup (e.g., onset of liquid loading) as the gas velocities decreases was not observed for fixed outlet pressure and liquid rates. However, from the literature review presented in this work, it is possible to conclude that downward flow of liquid in a vertical tube can be strongly related to the transition from annular-to-churn flow, since the main feature of this transition is the liquid flow reversal. Therefore, in order to understand the behavior of the liquid flow during this transition, some experimental runs were carried out to characterize and correlate variations in gas and liquid velocities with the changes in flow regime, liquid holdup and pressure. Transient tests were performed for annular-to-churn flow transitions, for different outlet pressures and liquid rates.

The tests procedure consists of setting up a desired gas and liquid rate, and wait (approximately 3-5 minutes) until the flow conditions reach steady-state in annular flow. Then, the transition to churn flow is created by partially closing the choke valve (outlet valve), which will consequently increase the test section pressure and decrease the inlet gas and liquid rates. Figure 5.24 and Figure 5.25 present the pressure and inlet gas/liquid mass rates variation during this test.
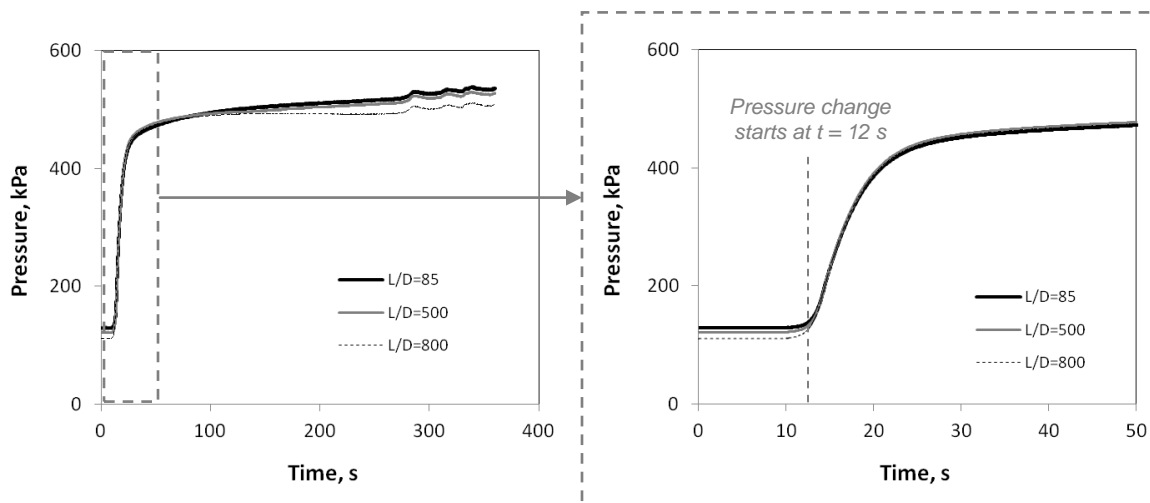
Figure 5.24 – Pressure variation at three axial positions for the first test for annular-to-churn transition investigation. The plot in the left shows the pressure variation for the first 50 seconds.

As can be seen from Figure 5.25, the gas rate is decreased by 20% and the liquid rate by 40%, with the increase in pressure. These variations in the inlet flow rates are a consequence of the performance curves of both air compressor and water pump.

Using the visualization system available in TowerLAB, it is possible to visualize the behavior of the liquid phase at three different axial positions (L/D = 85, 500, 800) simultaneously. Table 5.2 and Table 5.3 present the snapshots of the video recordings of the liquid flow behavior for times varying between 0 and 350 seconds.
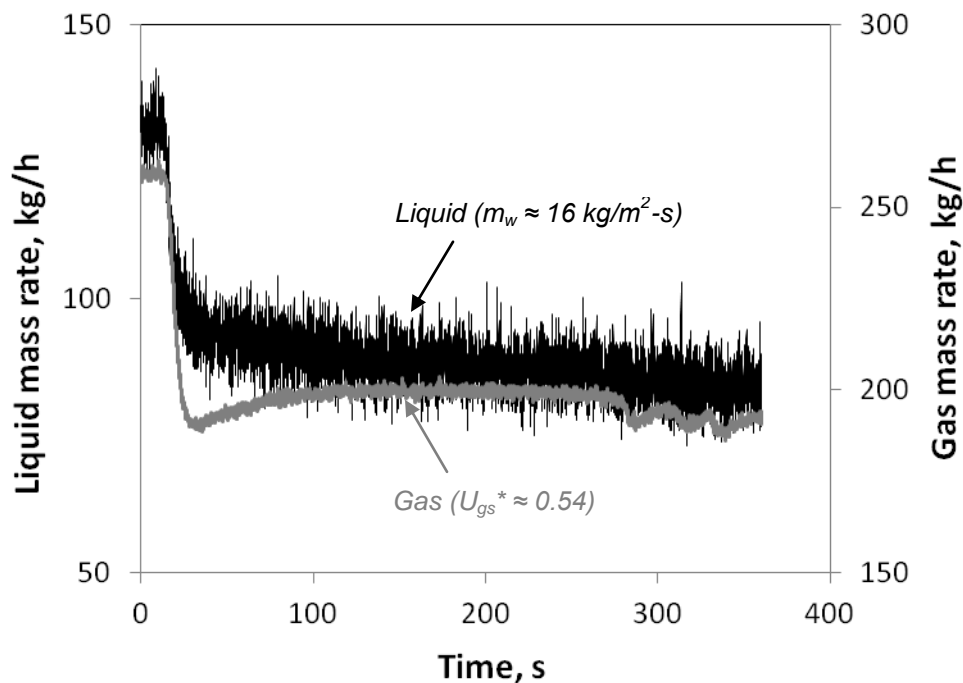
Figure 5.25 – Air and water mass rate for the first test for annular-to-churn transition investigation.

Figure 5.24 shows that the beginning of the pressure change starts at 12 seconds. As can be seen from Table 5.2, the liquid film at L/D = 800 is clearly discontinuous at t = 15 s. At the same time, the liquid film at L/D = 500 starts to show some discontinuity, but at L/D = 85 the film seems to still be continuous and flowing upwards. At time = 45 s, the film breaks-up in all three axial locations. From the video recording it was possible to observe that the liquid filaments attached to the tube wall remain static between t = 30 and 45 s. However, during the same period, entrained droplets seem to travel upward in the gas core and keep depositing in the tube wall. This deposition is followed by the coalescence of the arriving droplets with the liquid already attached to the tube wall. When the attached liquid filament becomes large enough (due to coalescence), it starts to flow downwards. A couple of diameters downstream where it began to flow downwards, the same filaments break up in small droplets, and they become static again. Then, the deposition process starts over again. This cyclic phenomenon seems to keep a zero net

liquid flow. This mechanism was observed at all three axial locations for times between 30 and 45 seconds.

After 45 seconds the liquid film front coming from the bottom reached the location L/D = 85 (since the liquid was being continuously injected at the inlet), and the deposition process just described could not be observed anymore.

Table 5.2- Snapshots of the simultaneous video recording at three different axial locations in the test section for times between 0 and 45 seconds.

L/D	t = 0 s	t = 15 s	t = 30 s	t = 45 s
800				
500				
85				

Table 5.3 - Snapshots of the simultaneous video recording at three different axial locations in the test section for times between 165 and 350 seconds.

L/D	t = 165 s	t = 235 s	t = 240 s	t = 350 s
800				
500				
85				

Another interesting mechanism observed in this test was the visualization of the progression of the liquid film front along the vertical tube.

The snapshots in Table 5.2 and Table 5.3 for times t = 45, 165 and 240 s were taken at times when the liquid film front has just passed the locations L/D = 85, 500 and 800, respectively. With the information of time and distance between the visualization

locations, it is possible to calculate the velocity of the film liquid front. Hence, for a total time difference of 195 s (= 240 – 45 s) and a total distance of 34.4 m (= (800 – 85)*0.048 m), the velocity of the liquid front can be calculates as $v_f = 0.176$ m/s.

The previous calculation is only valid if the film front velocity is constant over time. One way that was found to verify this linearity with time was analyzing the pressure drop between different axial locations. Since the gas and liquid mass rates being injected are nearly constant for times higher than 50 s, the friction component of the total pressure drop should also be nearly constant after the liquid front has passed. Thus, the change in the total pressure drop should be directly related to the variation in the gravitational component. In turn, the gravitational component increases as the liquid film front flows upward in the vertical tube. Figure 5.26 shows the total pressure drop between the outlet pressure ($L/D = 820$) and four different axial positions in the test section. The time when the liquid front passes the first pressure tap is indicated in the figure as $t_{f,0}$.

As can be seem from the figure, for all axial locations the pressure drop changes linearly with time after the film liquid front has passed each corresponding pressure tap. Then, we can calculate the film liquid front velocity, v_f, using Figure 5.26 and the following relation,

$$v_f = \frac{\left(\text{Pressure tap distance from first tap}\right)}{\left(\text{Time when pressure starts incresing linearly} - t_{f,0}\right)} \tag{5.2}$$

The film front velocity for each pressure tap was obtained as $v_f \approx 0.18$ m/s for all four positions in the figure. This result shows an excellent agreement with the calculation based on the video recording observations previously presented ($v_f = 0.176$ m/s).
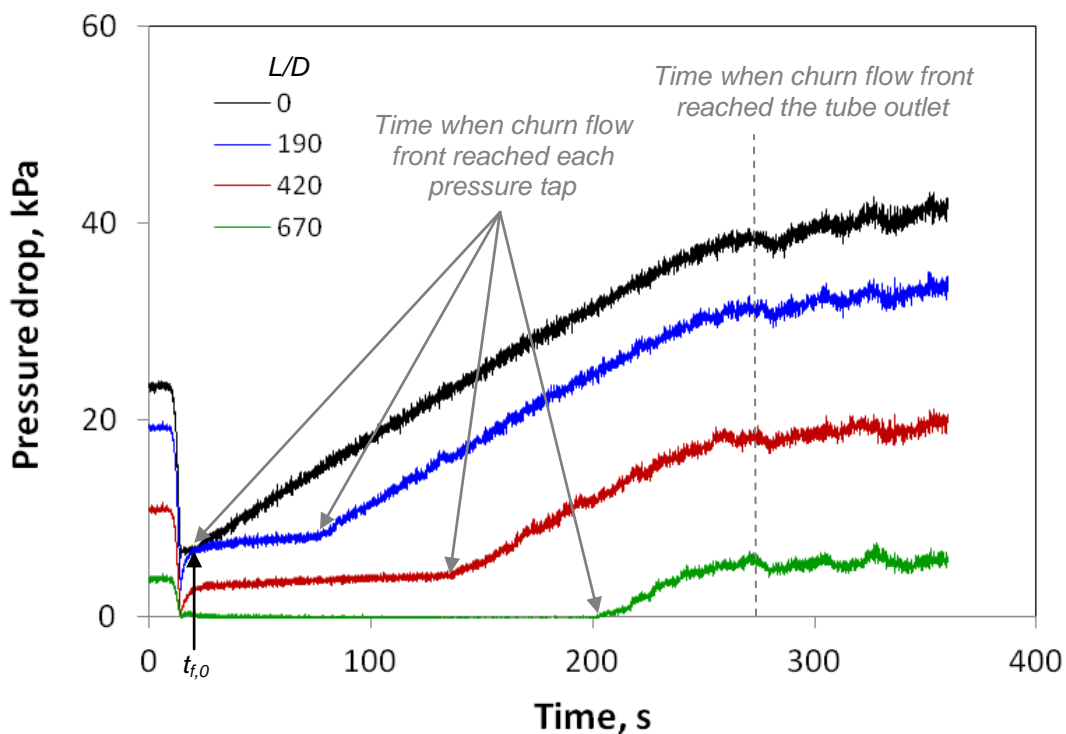
Figure 5.26 – Total pressure drop between the outlet pressure and four axial position in the test section
(L/D = 0, 190, 420, 670).

The information of liquid mass rate being transported in the film and entrained liquid is also important to have a more comprehensive understanding of the liquid flow behavior under transient conditions.

The mass flow rate in the liquid film can be calculated using the film velocity together with the measurement of the liquid film thickness (Figure 5.27). A schematic diagram of the approach used to calculate the film and entrained liquid mass flow rate during the transient tests is illustrated in Figure 5.28.

From Figure 5.27, the time-averaged film thickness for the location L/D = 85 can be calculated as $\delta_{f,85} = 0.66$ mm (for 50 < time > 350). For location L/D = 800 and 250 < time < 350, the time-averaged film thickness is $\delta_{f,800} = 0.51$ mm. If we consider the average between these two locations we obtain $\delta_f = 0.59$ mm (average film thickness of the liquid front). Using the film velocity previous calculated and using δ_f to evaluate the

average cross-sectional area of the film front moving along tube, we can obtain the film mass flow rate as $m_f = 57.2$ kg/h.
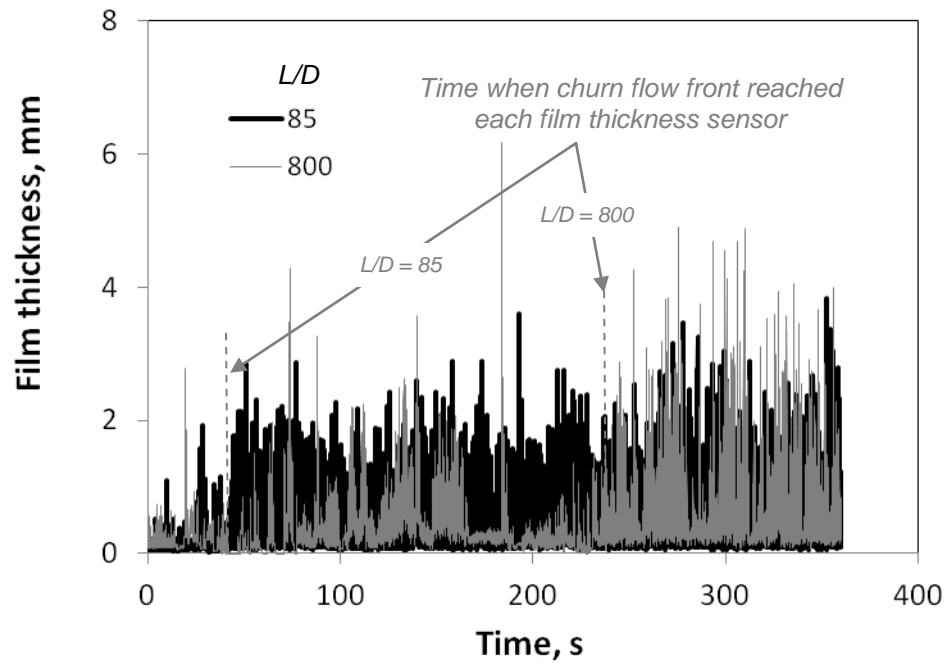
Figure 5.27 – Film thickness measurements for the inlet (L/D = 85) and outlet (L/D = 800) locations in the test section.
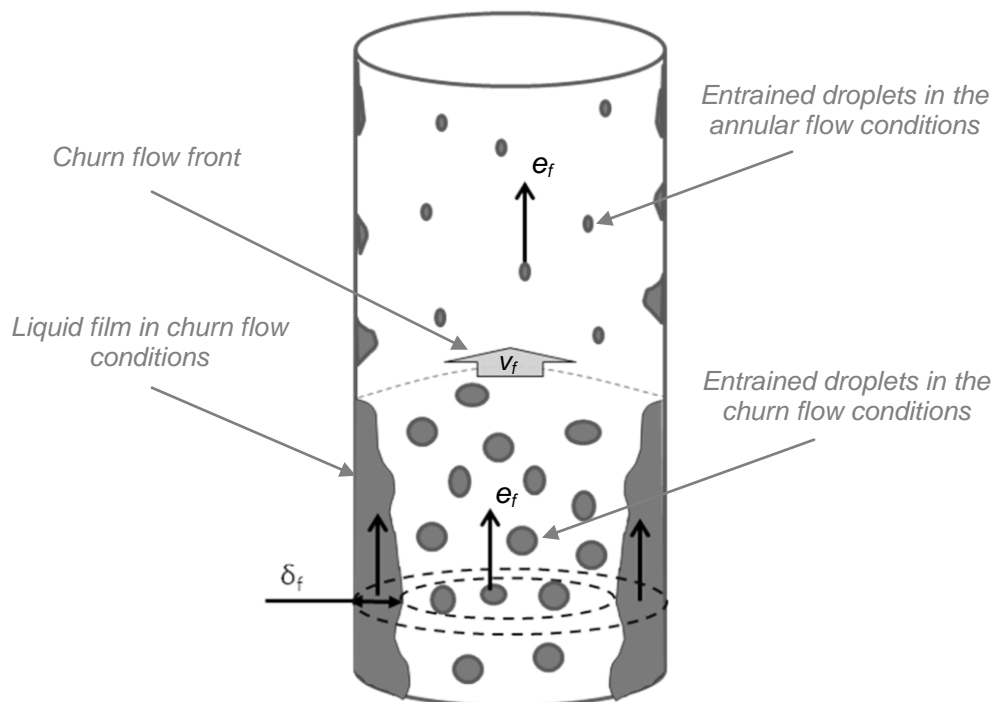
Figure 5.28 – Schematic diagram of the approach used for the calculation of the mass flow rate for the liquid film and entrainment during the annular-to-churn flow transition test.

In Figure 5.25, we can notice that the time-average liquid rate being injected is around 90 kg/h (after the pressure increase or time > 50 s). Thus, the difference between the liquid being injected and the calculated film flow rate could be attributed to the flow of entrained droplets. This difference corresponds to 35% of the total liquid being injected. This result shows a good agreement with the experimental data obtained by Barbosa et al. (2002) for the entrained liquid fraction.

It is important to mention here that some of the measurements presented in Figure 5.27 are not very realistic when compared to the visual observation. Because of the local measurement characteristic of the two-wire liquid holdup sensor, if the liquid film breaks-up some liquid droplets can get trapped between the two wires and create a false measurement of the liquid content surrounding the sensor. After having a close look at the video recordings for this experimental run between 20 and 200 seconds, it was possible to observe the break-up of the liquid film and stagnation of large droplets, as illustrated in Figure 5.29b. However, after 200 seconds, the liquid film coming from

the bottom reaches the top of the tube and a continuous and oscillatory liquid film (which characterizes churn flow) is reestablished. Besides the limitation of the sensor for this specific time range in this test, the assumption of liquid distribution symmetry with respect to the pipe centerline is believed to be maintained in average. The video recordings of all experimental runs were closely analyzed and symmetry seems to be the case whenever a continuous film is present.

Upward continuous liquid film

Break-up of liquid film into static large droplets

Oscillatory continuous liquid film

(a)   (b)   (c)
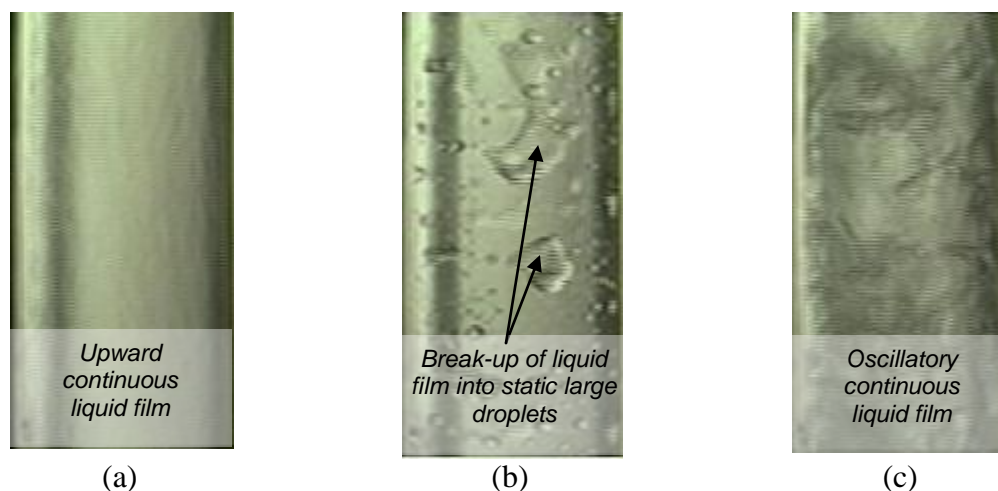
Figure 5.29 – Snapshot of the video recordings of experimental run at location L/D = 800 for times (a) 5 s, (b) 100 s and (c) 250 s.

An estimation of the pressure drop for the transient period for this test can be performed using the entrained fraction levels from the previous calculation. Two axial locations (L/D = 190 and 420) from Figure 5.26 were choose for this estimation, since these positions showed the longest stable period during the transition in the experimental run. As can be seen from Table 5.2 and Table 5.3, the flow downstream to the churn flow front does not exhibit a continuous liquid film. Thus, the pressure drop calculations should only consider the gravitational component and the friction component between the tube wall and the gas core (plus entrained droplets). Therefore, the total pressure drop is obtained by (Shoham 2006),

$$\Delta p = \underbrace{\rho_C f_w \frac{\Delta L}{D} \frac{U_{CS}^2}{2}}_{Friction} + \underbrace{\rho_C g \Delta L}_{gravitational} \tag{5.3}$$

$$U_{CS} = U_{gs} + U_{sl} e_f \tag{5.4}$$

$$\rho_C = \rho_g \alpha_C + \rho_l (1 - \alpha_C) \tag{5.5}$$

$$\alpha_C = \frac{U_{gs}}{U_{gs} + U_{ls} e_f} \tag{5.6}$$

where f_w is the Darcy friction factor, ΔL is the distance between the corresponding tap position and the outlet tap, U_{gs} and U_{ls} are the superficial gas and liquid velocities, g is the acceleration due gravity, and e_f is the liquid entrained fraction. The flow as assumed as turbulent and the tube wall as rough pipe (relative roughness equal to 0.05).

The comparison between the calculated and experimental pressure drop (from Figure 5.26) for both axial locations are presented in Table 5.4. An entrained fraction of 35% (Figure 2.6) was used in the calculation, following the experimental observations obtained by Barbosa et al. (2002) for high pressure (3.6 bara), low liquid mass flux (22 kg/m^2-s) and dimensionless gas velocity U_{gs}* = 0.5. If we consider that the entrainment flows at the same velocity as the gas core, the entrainment levels of churn flow conditions should reach the top of the tube in 4 seconds. This was the main reason to assume high entrainment levels even for the regions that the churn flow front has not passed yet.

The results from the table showed a good agreement between the calculated pressure drop and the experimental data.

Table 5.4- Comparison of the calculated results and experimental data for total pressure drop for the transition period (30 < t < 130 s) between the outlet pressure and two different axial locations (L/D = 190 and 420).

L/D	Calculated Δp, kPa	Experimental Δp, kPa	Error %
420	3.71	3.67	12.1
190	5.86	7.73	-23.2

Similar calculations were also performed for the period after the churn flow front has passed and the flow reached steady state (t > 300 s) in churn flow conditions. However, this calculation considers only a force balance in the gas core and includes the interfacial friction factor as proposed by Jayanti and Brauner (1994). Table 5.5 presents the results for the comparison between calculated and experimental data. An entrained fraction of 35% was used in these calculations as well. The results from Table 5.5 show again a reasonable agreement with the experimental data when using the entrained liquid fraction obtained by Barbosa et al. (2002).

Table 5.5- Comparison of the calculated results and experimental data for total pressure drop for the steady-state churn flow period (t > 300 s) between the outlet pressure and two different axial locations (L/D = 190 and 420).

L/D	Calculated Δp kPa	Experimental Δp, kPa	Error %
420	19.51	18.84	3.5
190	30.79	32.34	-4.8

The exercise here is not to develop a churn flow model to calculate the pressure drop, but to show that the use of the selected entrained fraction (35%) gives a good approximation for a simplified pressure drop calculation for this flow regime.

Similar analysis were also carried out for other liquid mass fluxes (m_w = 150 and 310 kg/m^2-s) and analogous results as presented above were obtained for these higher liquid rate levels as well.

These results indicate that the liquid re-distribution during annular-to-churn flow transitions (created by an increase in pressure and decrease in flow rates) can be simply described using a constant liquid front flowing upward, based on the inflow of liquid rate at the bottom of the vertical tube. The understanding of such mechanism can be used in the prediction of how fast a liquid front will reach a specific point in a vertical well, as a consequence of changes in gas flow rates. In other words, the prediction of the type of transient behavior described here could be obtained without the use of complex transient multiphase flow simulators. Additionally, the use of the current start-of-the-art commercial simulator for transient multiphase flows in pipes (Bendiksen et al. 1991) could not accurately predict the progression of the churn flow front as observed in the experimental runs. These results will be discussed later in Section 6. However, the development of a more comprehensive model is recommended.

It is also important to mention here that even for a gas velocity lower than Tuner and Wallis liquid loading criteria, the liquid in the vertical tube flows steadily upwards during the transition between annular to churn flow. Also, the liquid film that was already present in the tube before the transition have the trend of staying static during the transition and also did not show a significant accumulation in the bottom of the tube. In overall, the transition showed a behavior of a pseudo-steady state flow, or in other words, the flow exhibit a sequence of steady-state churn flow behavior as the liquid flows upward in the vertical tube. This is an important piece of information, which can indicate that steady-state models maybe applicable for this type of transition if deployed in a pseudo-steady state approach.

5.3. Conclusions

The present study investigated the models and techniques available in the literature for prediction of the onset of liquid loading in gas wells. From the literature review, it was found that there is still some inconsistencies on which mechanisms trigger

the onset. After having gathered experimental evidences based on the literature, the main mechanism that the present author believes should be related to the onset of liquid loading is the transition from annular to churn flow, which is indicated by the liquid film flow reversal (Wallis criterion).

However, the most widely used approach to predict liquid loading onset in the oil and gas industry is the so-called Turner critical velocity, which provides a minimum gas velocity as a threshold to avoid liquid loading symptoms. This criterion is based on the gas flow rate and fluid properties only. Therefore, an experimental campaign was carried out to investigate the mechanism of the model proposed by Turner to predict the onset of liquid loading. The experimental investigations consisted of carrying out two-phase flows in a long (42-m long) vertical tube for a wide range of pressure, liquid and gas velocities, which included gas velocities higher and lower than the Turner critical velocity.

From the experimental results for a fixed outlet pressure, liquid and gas rates, and considering the Turner critical velocity, the bottomhole liquid accumulation described by classical definition of the onset of liquid loading was not observed. Another set of similar tests were performed to analyze the relationship between the gas flow rate decline, increase in liquid holdup, and its relation with the Turner criterion. The liquid holdup as a function of the gas flow rate exhibits a continuous and smooth curve, where no sudden change in liquid holdup is observed for a decline in gas flow rate. Thus, because of the continuous and smooth curve behavior, it was found extremely subjective to use Turner critical gas velocity to indicate when the onset of severe liquid build up (or liquid loading) would occur. The proposition here is that the analyses of liquid loading in gas wells should not only consider Turner's or Wallis' criteria to predict the onset, but should take into account the reservoir behavior (as in nodal analysis, for instance) in order to properly investigate liquid loading. From the experimental runs carrier out here and from other author's observations regarding the minimum point in the pressure gradient curve, even for nodal analysis Wallis' criterion seems to be a more objective approach than Turner's to indicate the onset of liquid loading.

Nodal analysis is a steady-state approach, and the behavior of liquid loading is transient in nature. In order to investigate more precisely the fundamentals of liquid loading phenomena, the author here would suggest an experimental set up or a modeling approach where the near-wellbore reservoir is attached to the bottom of the vertical tube, as proposed by Falcone (2006).

Analyses from experimental observations showed that the liquid re-distribution during annular-to-churn flow transitions (created by an increase in pressure and decrease in flow rates) can be simply described using a constant liquid front flowing upward, based on the inflow of liquid rate at the bottom of the vertical tube. This information can be used towards the development of simplified models for annular-to-churn flow transitions, which is believed here to be directly related to liquid loading in gas wells.

6. PERFORMANCE OF VERTICAL TRANSIENT TWO-PHASE FLOW MODELS APPLIED TO LIQUID LOADING*

6.1. Introduction

Recently, several investigations on liquid loading have been carried out (Lea et al. 2003; Belfroid et al. 2008; Veeken et al. 2009; Veeken and Belfroid 2010). However, a detailed understanding of the fluid flow behavior during liquid loading is not yet fully available, and prediction methods of this phenomenon are still rather incipient. A better comprehension of liquid loading fundamentals can lead to the development of more general and reliable models and correlations, which can consequently provide more accurate production forecasts, effective design of flowlines and completions, and remediation of wells under liquid loading conditions.

Liquid loading is a transient phenomenon in nature: after its onset, a sequence of events starts to occur in the wellbore, as presented in Figure 6.1.

The events can be described as follows (Veeken et al., 2003):

1. Both gas and liquid are being produced to surface.

2. The velocity of the gas decreases and it is insufficient to lift liquids to surface. Liquid flow reversal occurs. Liquids begin to accumulate bottom-hole.

3. Due to liquid accumulation, the bottom-hole pressure increases. As pressure keeps increasing, the gas flow rate reduces even further, until the well stops flowing.

_____

4. The liquids that build up bottom-hole are then re-injected back to the formation, once the bottom-hole pressure reaches values higher than the near-wellbore region. During the re-injection, the pressure in the near-wellbore region recharges.

5. The near-wellbore pressure recharges until it is high enough to lift the fluids column (gas + liquids) in the wellbore, and then the well starts flowing again.
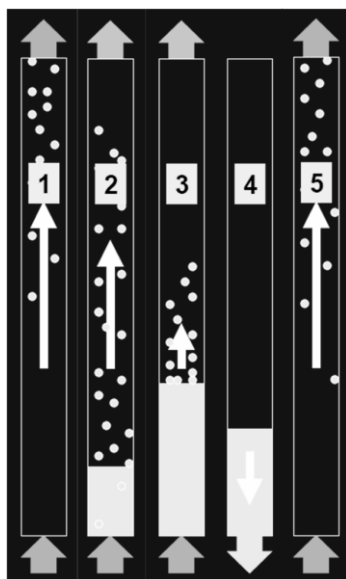
Figure 6.1 – Events sequence for gas wells under liquid loading conditions (Veeken, K. et al. 2003).

This sequence of events keeps repeating until a point when the reservoir is not capable of recharging the pressure to a level high enough to lift the fluids column. At this point the well dies.

Clearly, the liquid loading process is transient in nature, and therefore requires characterization via transient flow models. Understanding the flow features taking place in the well is important not only to properly predict wellbore performance, but also to describe the near-wellbore region of the reservoir. The pressure, temperature, and liquid holdup at bottom-hole are necessary boundary conditions for reservoir modeling. Thus,

if the wellbore parameters is not correctly estimated (or measured), the near-wellbore performance will be incorrectly characterized.

Although liquid loading has a transient nature, standard models still use steady-state analyses to predict and diagnose liquid loading. The most widely accepted concept that is used to predict the onset of liquid loading is the droplet model developed by Turner et al. (1969). Besides the good acceptance of Turner's droplet model in the oil and gas industry, the conclusions of the studies from section 5 have found that it fails to correlate the exact point of the inception of liquid loading.

This section describes the modeling of two-phase flows for a synthetic well using the market-leading software package in the oil and gas industry and two research codes: one for steady-state flow (GRAMP) and one for transient flow (HyTAF). The objective of the present section is to analyze the capabilities and limitations of these simulators for liquid loading flow conditions and discuss the main divergences between results. Based on the literature review, the analyses will be focused on the simulators' ability to capture the features related to the transition between annular and churn flow, pressure drop and liquid holdup profiles.

6.2. Review of Models Main Features

6.2.1. Simulator 1

Simulator 1 is a widely available commercial simulator for transient multiphase flow modeling in the oil and gas industry (Bendiksen et al. 1991). The current version of this simulator consists of a three-fluid (oil, water and gas) model solver. The three-fluid model has been validated against experimental and field data (Nossen et al. 2001).

Five mass conservation equations are solved for the different phases/fields (Yusuf et al. 2010): i) gas phase, ii) water droplets, iii) oil droplets, iv) oil film, and v) water film. Momentum equations are solved for three different fields: i) gas/droplets, ii) oil bulk, and iii) water bulk. One energy equation is solved for the multiphase mixture. Closure laws are used for calculating wetted perimeters and friction factors. These relationships are flow regime-dependent, so transition criteria have to be solved to

determine the prevailing flow regime for a given set of local flow conditions. The existing flow regimes in this simulator are: stratified, annular, slug, and dispersed bubble.

The fluid properties (densities, viscosities, surface tensions, thermal conductivities and heat capacities) are generated via a multicomponent PVT software package, which runs externally before the simulations are performed in Simulator 1. The table generated with the corresponding fluid properties (based on the fluid composition) is then available to Simulator 1 during the flow simulations as a function of pressure and temperature.

6.2.2. GRAMP

GRAMP is a research code for steady-state one-dimensional two-phase flow in vertical ducts. It allows for the prediction of the following flow regimes: bubble, slug, churn, annular and wispy-annular. The code was originally developed at Imperial College London in the mid 1990's, but several versions appeared afterwards that included boiling and condensation of pure fluids and mixtures. A detailed description of the GRAMP code has been presented by Barbosa and Hewitt (2006).

GRAMP solves the mass, momentum and energy equations for the bulk flow. In annular flow, one additional equation is solved to determine the fraction of the liquid flow rate entrained as droplets as a function of distance. The solution method is based on the classical triangular relationship between the film flow rate, the film thickness and the wall shear stress. The model equations are solved via a 4th-order Runge-Kutta method. The required inputs in GRAMP are the inlet pressure and temperature, the liquid and gas mass fluxes, and entrainment fraction (if annular flow exists at the pipe inlet).

Recent modifications in the GRAMP code included Black Oil model subroutines and integration using external compositional PVT packages (Falcone 2006).

6.2.3. HyTAF

HyTAF is a research code for transient, one-dimensional, upward co-current annular flow. This research code is described in more details by Gessner and Barbosa (2010). Eight equations are solved for the three fields (gas, droplets and liquid film – see Figure 2.3): three mass conservation equations, two momentum equations (it is assumed that there is no slip between phases in the gas core), and three energy equations. Closure relationships are needed for the rates of droplet entrainment and deposition, interfacial and wall friction factors. The momentum equations also include the effects of non-viscous forces (virtual mass, interfacial pressure and compressibility).

The system of governing equations in HyTAF is hyperbolic. It is solved via the Split Coefficient Matrix Method (SCMM) using the finite difference method. The SCMM is suitable for dealing with fast transient flows where sharp discontinuities, such as shocks and void waves, can occur. According to Gessner and Barbosa, HyTAF is the first code to employ the SCMM in modeling of non-equilibrium annular flows. Under its current state of development, air and water are the only fluids available in HyTAF.

6.3. Models Set-Up

The simulations were performed for a vertical round tube of 40 m in length and internal diameter of 0.049 m, as described in Figure 6.2. The inlet boundary conditions were: air and water mass flow rates, and temperature of the phases. Pressure was selected as an outlet boundary condition. The flow was considered adiabatic, assuming no heat transfer between the tube and its surroundings.

As Simulator 1 and HyTAF required either pressure or mass flow rate at the inlet of the tube as input parameters, different outlet pressures for these codes were tested (using a trial-and-error approach) so as to match the experimental inlet pressure data. This heuristic approach was not necessary in GRAMP, since it requires inlet pressure and mass flow rates as input parameters.
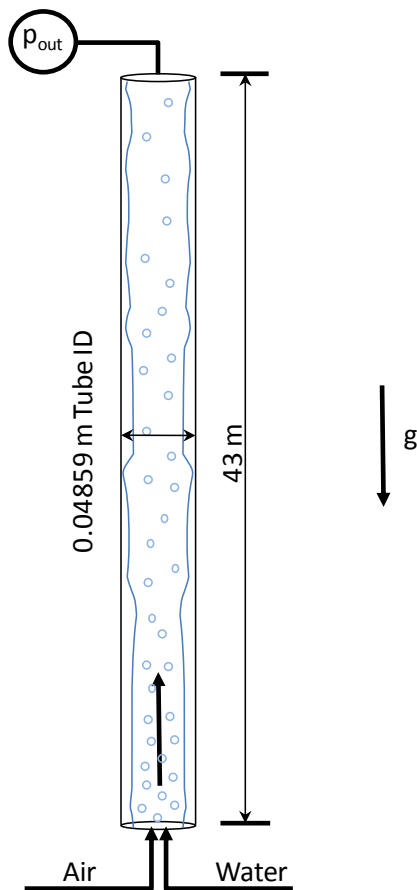
Figure 6.2 – Geometry implemented in the flow models.

6.4. Models Results and Discussion

The present study included an analysis of three different cases for steady-state and five cases for transient conditions. Simulator 1 and GRAMP simulators were also used for quality check of experimental data generated by TowerLAB, since these simulators have been validated against a wide experimental database. HyTAF had not been validated with experimental data yet.

All cases were run at a fluid temperature of around 25 ^{o}C.

For transient conditions, the configuration investigated included annular, churn flow and transition between both flow regimes. For transient conditions, only Simulator

1 and HyTAF were used due to the fact that GRAMP was developed for steady-state only.

6.4.1. Steady-state cases

The comparison included analysis for annular, churn and slug flow. Table 6.1 shows the boundary conditions for all three codes for the steady-state cases. The spatial discretization used was: 50 mm for Simulator 1 and 1mm for HyTAF and GRAMP.

It is important to mention here that HyTAF could not be used for Case 2 and Case 3 (churn and slug flow) because this code was specifically developed for annular flow only.

In what follows, the results and discussions of each of the four cases described above will be presented.

Table 6.1- Boundary conditions used in the simulators for comparison with the experimental data

Case	Flow Regime	Inlet pressure kPa	Air mass flux kg/m^2-s	Water mass flux kg/m^2-s
1	Annular	559	72	51
2	Churn	516	40	51
3	Slug	600	1	339

Case 1 – Annular flow

Figure 6.3a shows good agreement for the pressure between the experimental data and all three simulators. The average discrepancy for the pressure gradient between the experimental data and HyTAF, Simulator 1 and GRAMP was -10%, -2% and 24%, respectively.
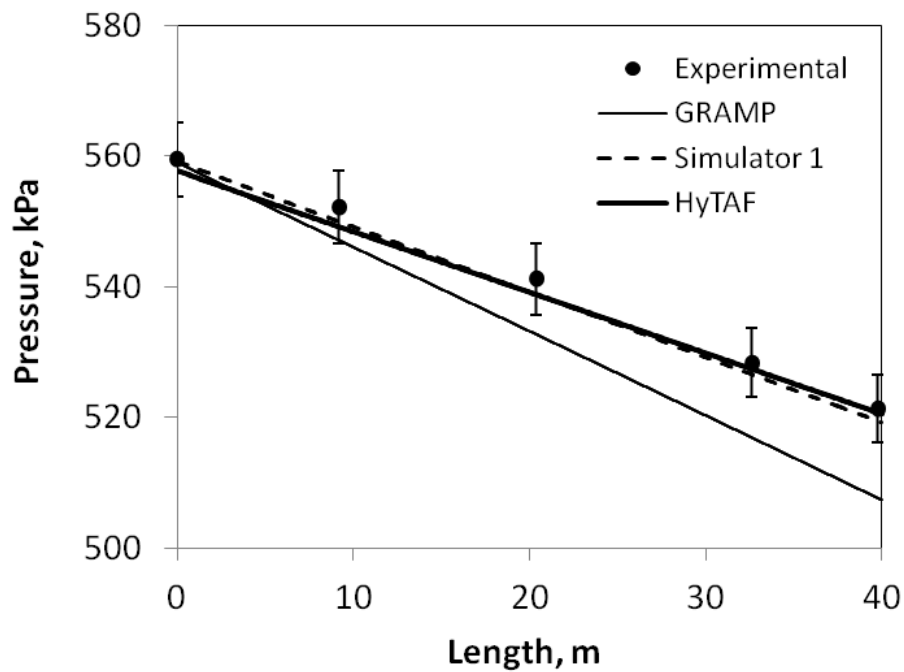
(a)
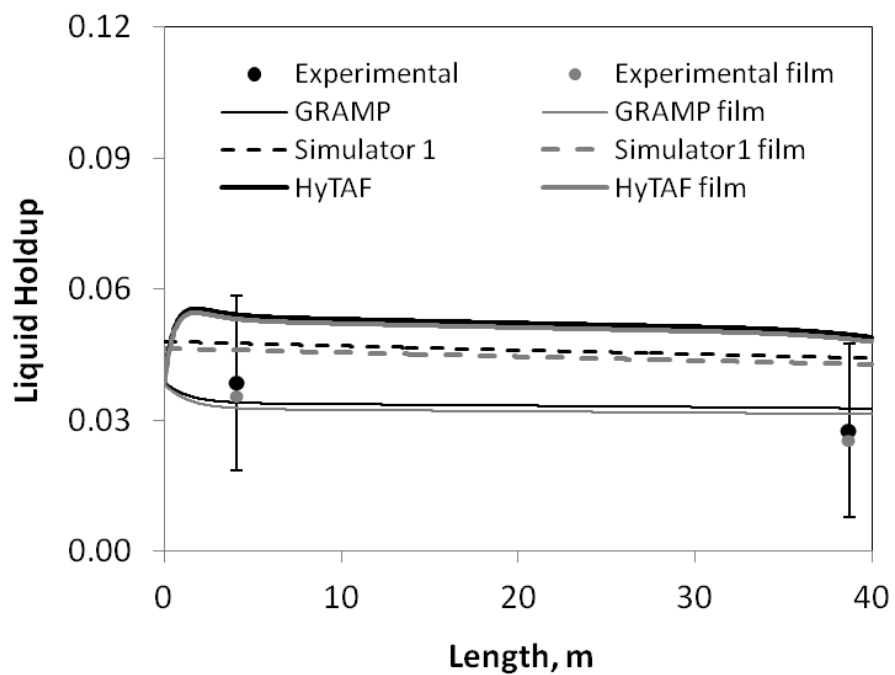
(b)

Figure 6.3 – (a) Pressure and (b) liquid holdup profile: SIMULATOR 1, GRAMP, HyTAF and experimental results for steady-state annular flow.

Once the gravitational component contributes for only around 30% of the total pressure drop, the discrepancies observed for GRAMP should be mainly related to the friction component (however, miscalculation of the holdup also affects the in-situ velocity indirectly). As described by Gessner and Barbosa (2010), the liquid film velocity is higher for GRAMP than for HyTAF, which consequently results in higher values of wall friction. Figure 6.4 presents the liquid film velocity comparison for all three codes and experimental data, which shows that the film velocity for HyTAF, GRAMP and Simulator 1 is significantly lower than that for experimental data. Surprisingly, the liquid film velocity obtained for Simulator 1 is 50% lower than HyTAF; however, both codes still give similar results in terms of pressure gradient. Thus, the relatively small difference observed between HyTAF and Simulator 1 could be related to, for instance, uncertainty in the closure relationships to calculate the friction factors, where such relationships generally carry around 15-20% uncertainty (Fore et al. 2000).

Figure 6.3b presents a comparison of the calculated liquid holdup between the three codes. This flow parameter presented a similar difference as observed for the pressure gradient. This difference was around -29% between GRAMP and Simulator 1, -35% between GRAMP and HyTAF, and only 7% between Simulator 1 and HyTAF. Based on the comparison of pressure profiles showed in Figure 6.3a, one can conclude that the liquid film velocity and holdup predictions by Simulator 1 and HyTAF are the most accurate. In fact, the simulators showed good predictions of the liquid holdup, with a maximum difference of only 0.02 when compared to the experimental data. This difference can be understood as small since the level of measurement of liquid holdup for this case is approximately the same as the uncertainty for this measurement (±0.02).

Case 2 – Churn flow

For the boundary conditions described in Table 6.1 for Case 2, Simulator 1 predicted slug flow throughout the test section, while GRAMP predicted churn flow.

The dimensionless gas velocity calculated for Case 2 based on the imposed inlet conditions was $U_{gs}^* = 0.69$, indicating that churn flow should be expected. For Case 1, the value obtained was $U_{gs}^* = 1.2$, which is in agreement with the annular flow regime predicted by the simulators.
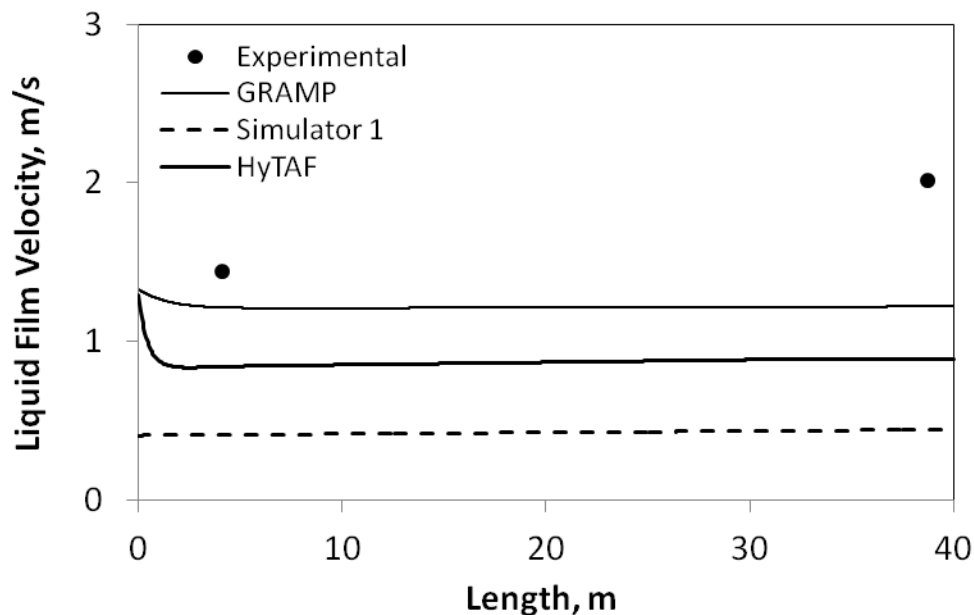
Figure 6.4 – Liquid film velocity: Simulator 1, GRAMP and HyTAF predictions for steady-state annular flow.

Figure 6.5a presents the absolute pressure comparison between the experimental data and GRAMP, showing good agreement with an average error of 7%. However, when the same comparison was performed with Simulator 1, the average error obtained was 38%. Since the gravitational pressure gradient contributes by almost 80% of the total pressure gradient in Case 2, the liquid holdup miscalculation should be the main cause for the discrepancies between experimental data and Simulator 1 predictions.
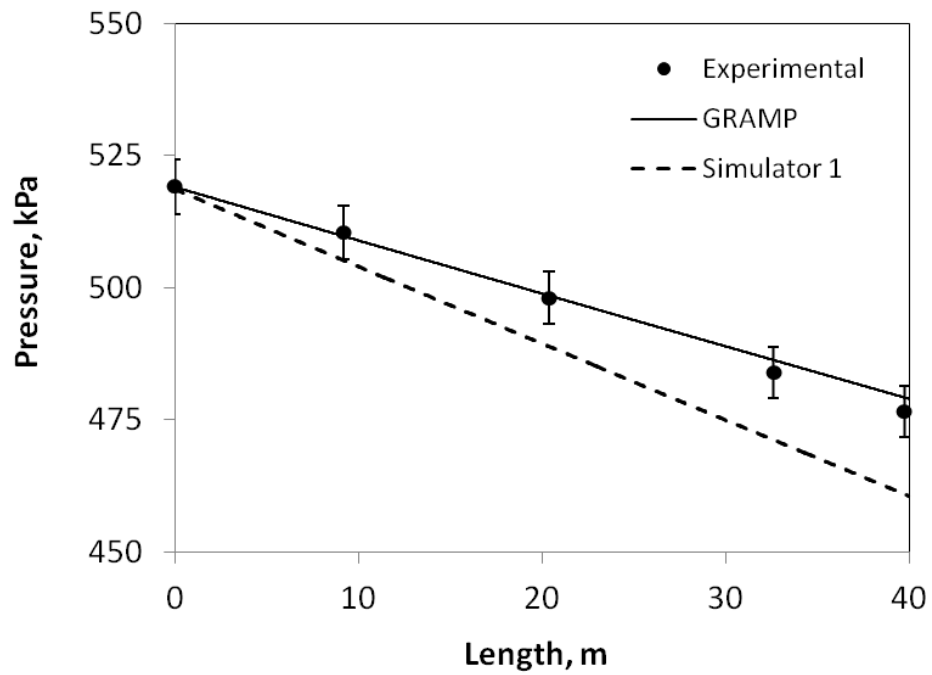
(a)
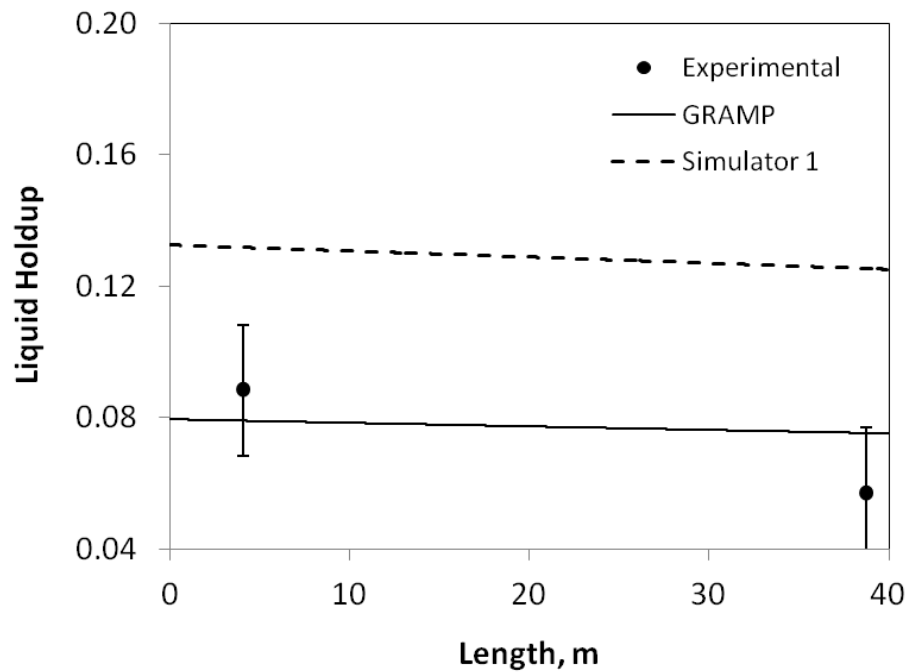
(b)

Figure 6.5 – (a) Pressure and (b) liquid holdup profile: SIMULATOR 1 and GRAMP and experimental results for steady-state churn flow.

A comparison of the simulated liquid holdup for both codes and experimental data is showed in Figure 6.5b. As expected, Simulator 1 model presented a much higher discrepancy (~50%) than GRAMP results, which has a good agreement within the liquid holdup measurement uncertainty range. The discrepancies in Simulator 1 results are believed to be related to the fact that Simulator 1 does not model churn flow. In general, churn flow presents a considerably lower liquid holdup than slug flow (Silva et al. 2010).

For the churn flow case, Simulator 1 predicted slug flow throughout the test section, while GRAMP predicted churn flow. The flow visualization during the experimental run confirmed churn flow regime from bottom to top of the test section in TowerLAB.

Case 3 –Slug flow

For the boundary conditions described in Table 6.1 for Case 3, the flow regimes predicted by the simulators were as presented in Figure 6.6b. Simulator 1 predicted slug flow for the whole 40 m tube length, while GRAMP predicted bubble flow for the first 5 m, and then slug flow for the remainder of the pipe length. From visual observation during the experiments conducted for Case 3, slug flow was detected for almost the entire tube length, and bubble-to-slug flow transition seemed to be occurring in the first meters of the test section. However, it is known that the visual differentiation between slug and bubbly flow (especially during flow transitions) can be difficult to distinguish.

Another important feature that can be observed from Figure 6.6b is related to the axial changes in the liquid holdup predicted by the simulators. GRAMP presented a sharp change in liquid holdup when the transition occurs from bubble to slug flow. This sharp change in liquid holdup is due to the fact the GRAMP calculates all parameters in a marching approach, without any smoothing or interpolation of the calculated parameters.
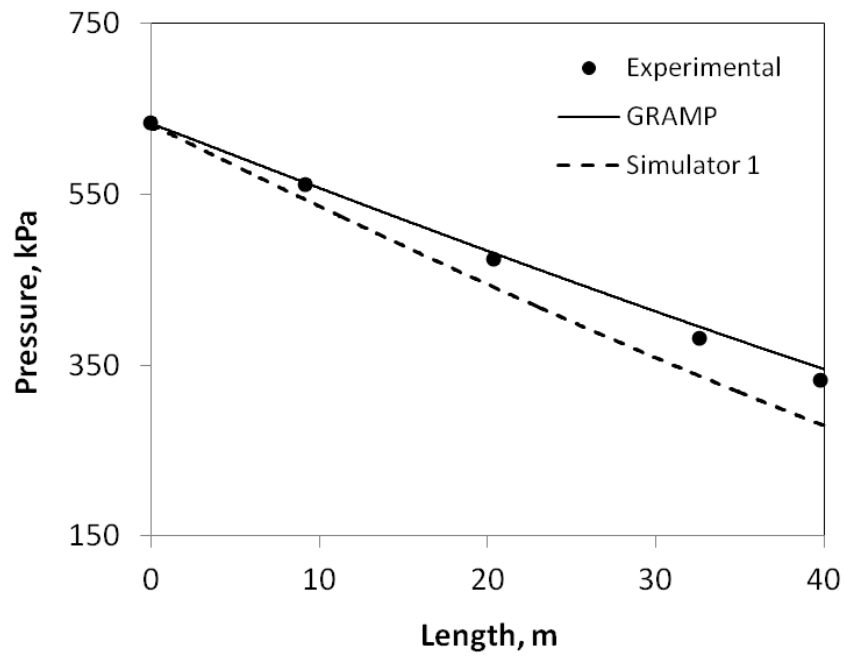
(a)
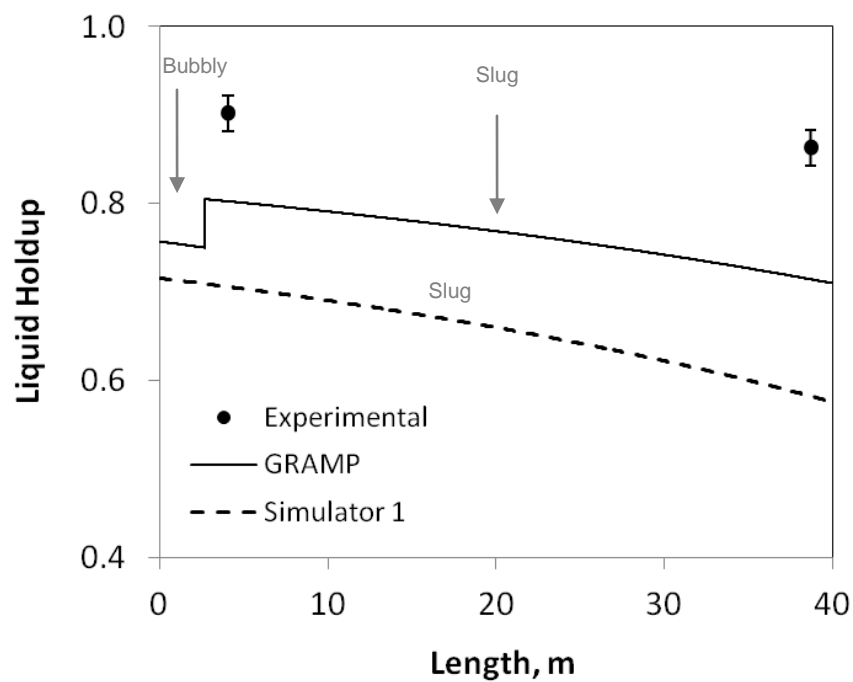
(b)

Figure 6.6 – (a) Pressure and (b) liquid holdup profile: SIMULATOR 1 and GRAMP and experimental results for steady-state slug flow.

In Simulator 1, due to the fact that the solver calculates the parameters of all nodes simultaneously, unrealistic sharp changes can be avoided, even when transitions of flow regimes are present. However, it should be borne in mind that no transitions were predicted with Simulator 1 in the present case.

Figure 6.6a presents the absolute pressure comparison between experimental data, Simulator 1 and GRAMP, showing good agreement with an average error of 16% and 6%, respectively. For this particular Case 3, the gravitational pressure gradient contributes by 90% to the total pressure gradient, which indicates that liquid holdup is the major component of the pressure gradient predictions. Indeed, as can be seen in Figure 6.6a, the discrepancy between Simulator 1 and GRAMP was around 15%. However, even though GRAMP presents a higher value for liquid holdup, the pressure gradient it predicted was lower than with Simulator 1. The difference for the liquid holdup between the experimental data and the simulators was approximately -15% for GRAMP and -55% for Simulator 1.

Although the focus of this work is on churn and annular flows, simulations for slug flow were performed to verify the validity of the experimental data generated by TowerLAB against benchmark simulators that have already been tested against other experimental database, especially for bubbly, slug and annular flows (Barbosa and Hewitt, (2006).

6.4.2. Transient cases

After comparing HyTAF and Simulator 1 simulation results against experimental data for steady-state annular flow, both codes were analyzed for transient conditions.

Case 4 – Fast outlet pressure change

The boundary conditions for each code were selected as follows:
- Spatial discretization: 50 mm for Simulator 1 and HyTAF
- Initial outlet pressure: 500 kPa
- Perturbed outlet pressure: 480 kPa

- Air mass flow rate: 76 kg/m^2-s
- Water mass flux: 299 kg/m^2-s

For this case, both simulators were run for 100 s using the boundary conditions above in order to reach steady-state. Then, after 100 s, the imposed outlet pressure was perturbed, triggering transient flow. Figure 6.7 shows the results comparison between simulators for the pressure profile, from time 0 to 10 s. After 10 s, steady-state was re-established, according to both simulators. No experimental data were included for the comparisons since the experimental facility could not reproduce the fast change in the outlet pressure.
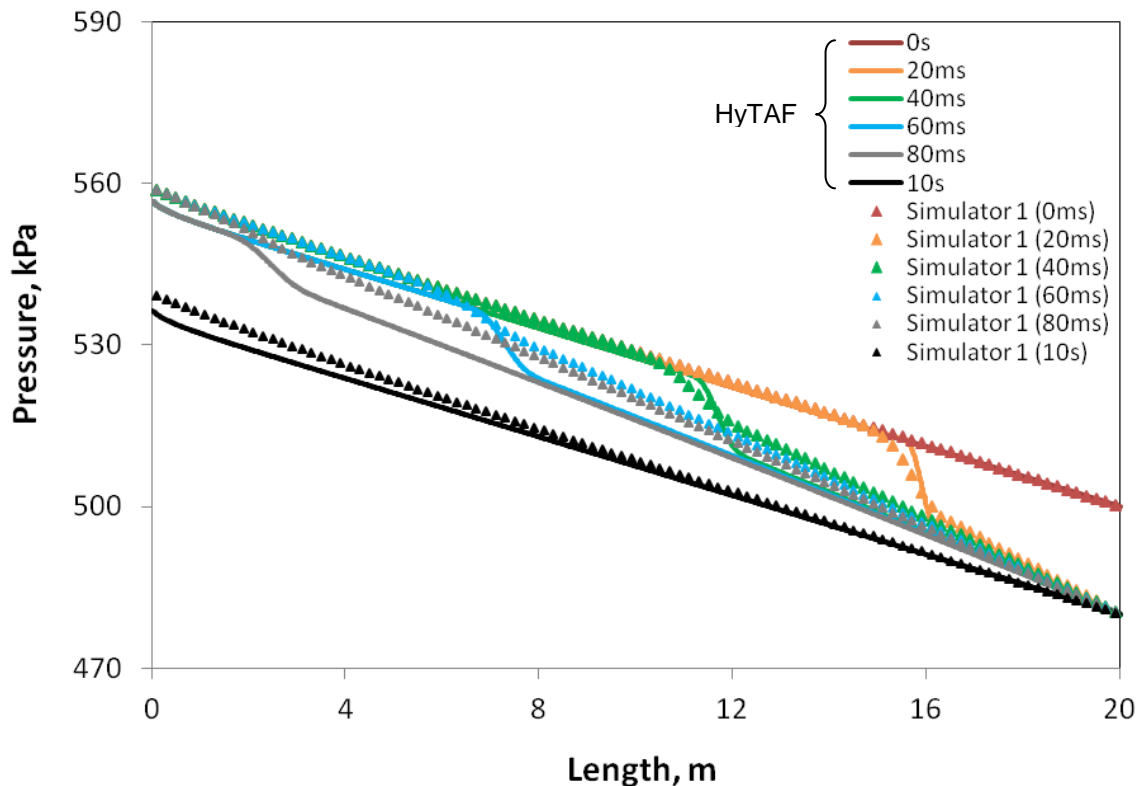
Figure 6.7 – Pressure profile: Simulator 1 and HyTAF predictions for transient annular flow.

As can be seen from the above figure, Simulator 1 and HyTAF were in very good agreement for the initial and final steady-state conditions, as observed previously with

the steady-state analysis (Figure 6.3). However, some divergences can be noted for the transient behavior. Figure 6.7 shows that, especially after 20 ms, the HyTAF results exhibit a sharper change in pressure wave than with Simulator 1. This is probably due to the way HyTAF deals with discontinuities such as shock and void waves. The author believes that Simulator 1 is not capturing the sharper transition because it was originally developed to model slower transients. The importance of capturing these shock waves may be crucial to understand instabilities due to sudden changes in pressure, which can consequently destabilize the liquid film and hence change the flow characteristics. Further improvements in the experimental should be made to measure and verify the validity of these results using experimental data.

Since the experimental facility could not generate the fast changes in the outlet pressure as for the previous case and slower variation in pressure are more common in the oil and gas industry, experimental runs with slower changes were carried out to investigate the performance of Simulator 1. Four parameters were selected for variation during the transient tests: flow regime, gas and liquid flow rates, and pressure. Table 6.2 shows a summary of the tests conditions used in the experimental runs for the transient cases.

Table 6.2- Conditions used in the experimental runs for the transient cases.

Case	Flow Regime (initial/final)	Initial outlet pressure, kPa	Final outlet pressure, kPa	Initial Air mass flux kg/m^2-s	Final Air mass flux kg/m^2-s	Initial Water mass flux kg/m^2-s	Final Water mass flux kg/m^2-s
5	**Annular/Churn**	**110**	**493**	39	27	19	13
6	**Churn/Annular**	**490**	**110**	31	39	15	22
7	Annular/Annular	**236**	**342**	39	37	315	297
8	Churn/Churn	370	237	27	33	**289**	**18**
9	**Churn/Annular**	**420**	**140**	30	52	298	364

The flow regimes included in Table 6.2 were obtained from visual observations during the experiments, using a high-speed camera. For all cases, enough time was

allowed (approximately 5-10 min) for the experimental runs to reach steady-state conditions before the test starts. The simulations were run for 100 s using the initial boundary conditions from Table 6.2 in order to reach steady-state as well. Then, after 100 s, the experimental measurements of outlet pressure, water and air mass flow rates (for every 0.5 seconds) were imposed as boundary conditions for the simulations. The total time for the experimental and simulation runs was 300 seconds.

The results and discussions of each transient case included in Table 6.2 are presented next.

Case 5 - Outlet pressure increase (Annular-to-Churn transition for low liquid rate)

The experimental procedure for this case consists of increasing the test section outlet pressure from 110 to 493 kPa, in order to trigger a transition from annular to churn flow. Additionally, as a consequence of increasing in pressure, the liquid and gas flow rates are also decreased due to the performance curve of the air compressor and centrifugal pump. Initial and final values for the pressure, liquid and gas rates are described in Table 6.2. During the experimental run was also possible to observe the transition from annular to churn flow conditions from bottom to top of the test section.

Figure 6.8 presents the experimental data and simulation results for the inlet (bottom) pressure in the vertical test section for the initial 35 seconds. As can be seen, there is an excellent agreement between Simulator 1 and the experimental data. Simulator 1 predicted transition from annular to slug flow at 20 seconds at the inlet of the tube.

For the total experimental run time, Figure 6.9 shows that the excellent agreement between simulator and experimental results extends until the end of the total run time. Figure 6.10 illustrates the error of Simulator 1 predictions when compared to the experimental data. As can be seen, besides the 15% error of the initial period, there is virtually no error for the simulator predictions for the following time after the pressure starts rising.
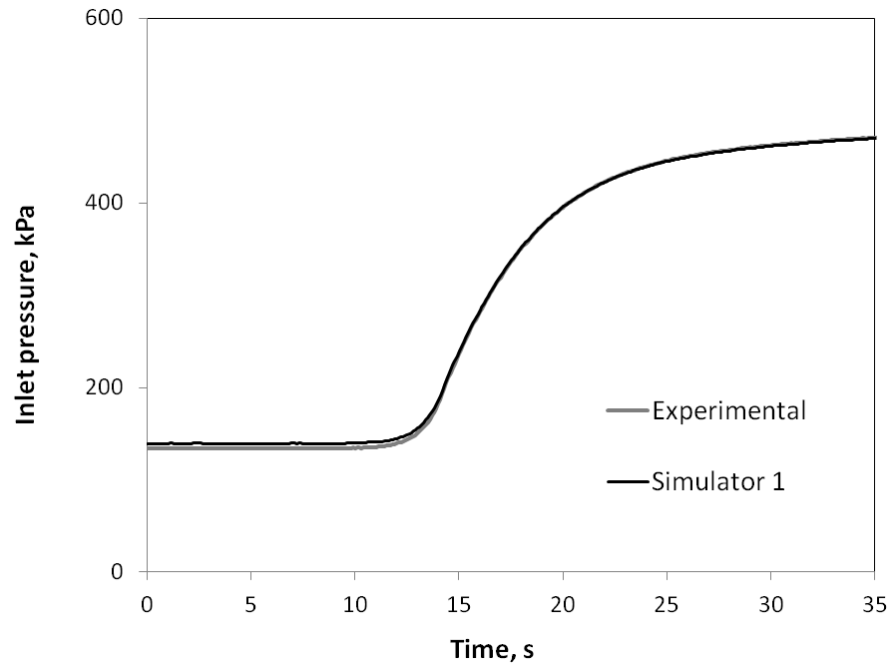
Figure 6.8 – Inlet pressure prediction comparison between Simulator 1 and experimental data for the first 35 seconds of the experimental run for annular-to-churn flow transition.
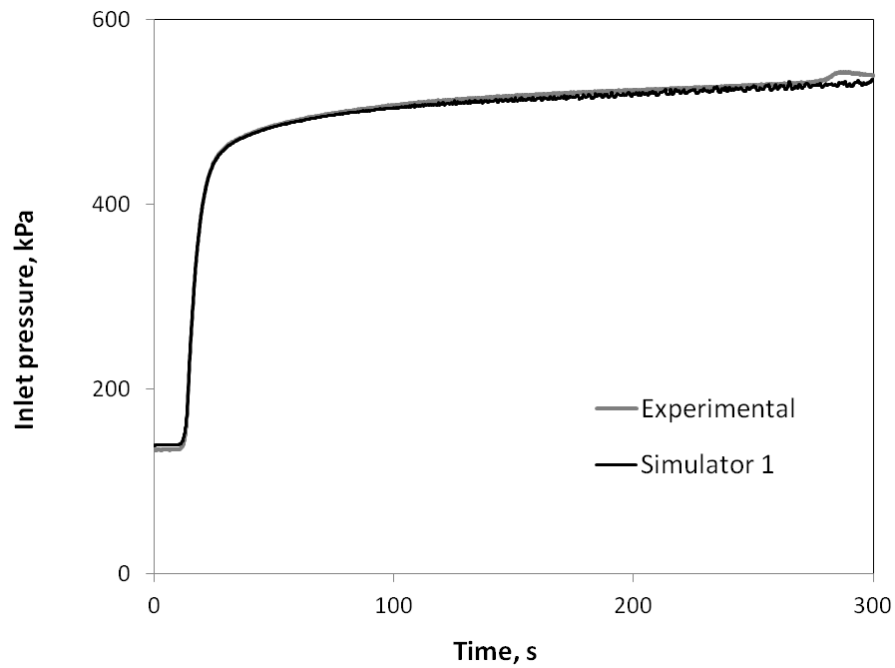
Figure 6.9 – Inlet pressure prediction comparison between Simulator 1 and experimental data for the total experimental run time for annular-to-churn flow transition.
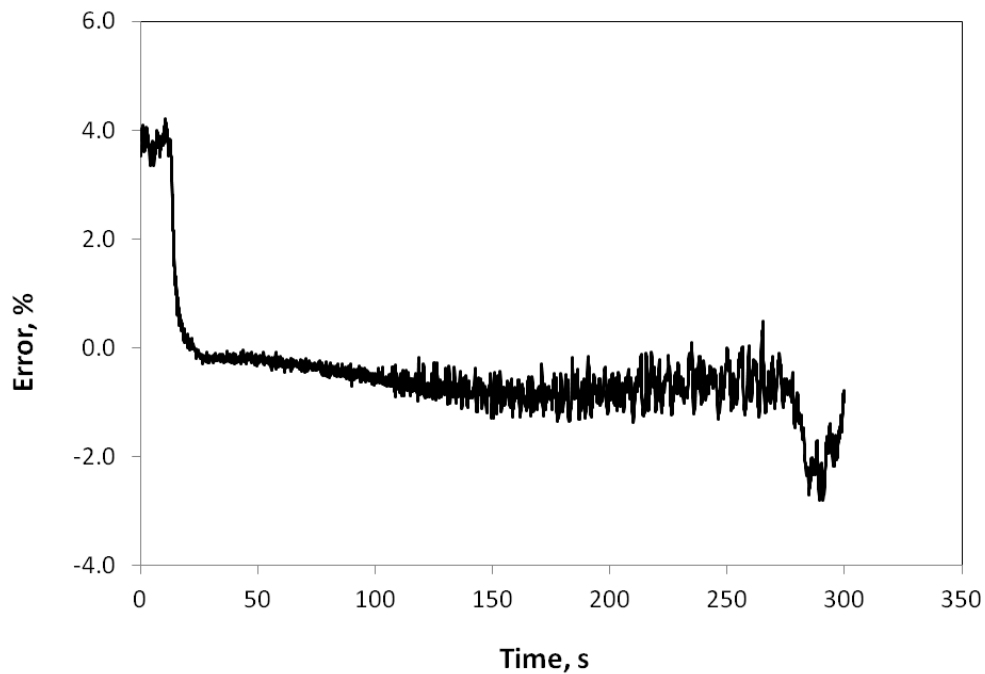
Figure 6.10 – Simulator 1 prediction error for inlet pressure when compared to experimental data for annular-to-churn flow transition.

A comparison with the experimental data was also verified for the pressure profile throughout the vertical test section as presented in Figure 6.11. It is easy to see that Simulator has also an excellent agreement when compared with the experimental data. This comparison was obtained only for the initial 17 seconds. However, since the inlet pressure showed a good match for the total run time, it is expected that the pressure profile should also exhibit the same quality match for the following time steps.
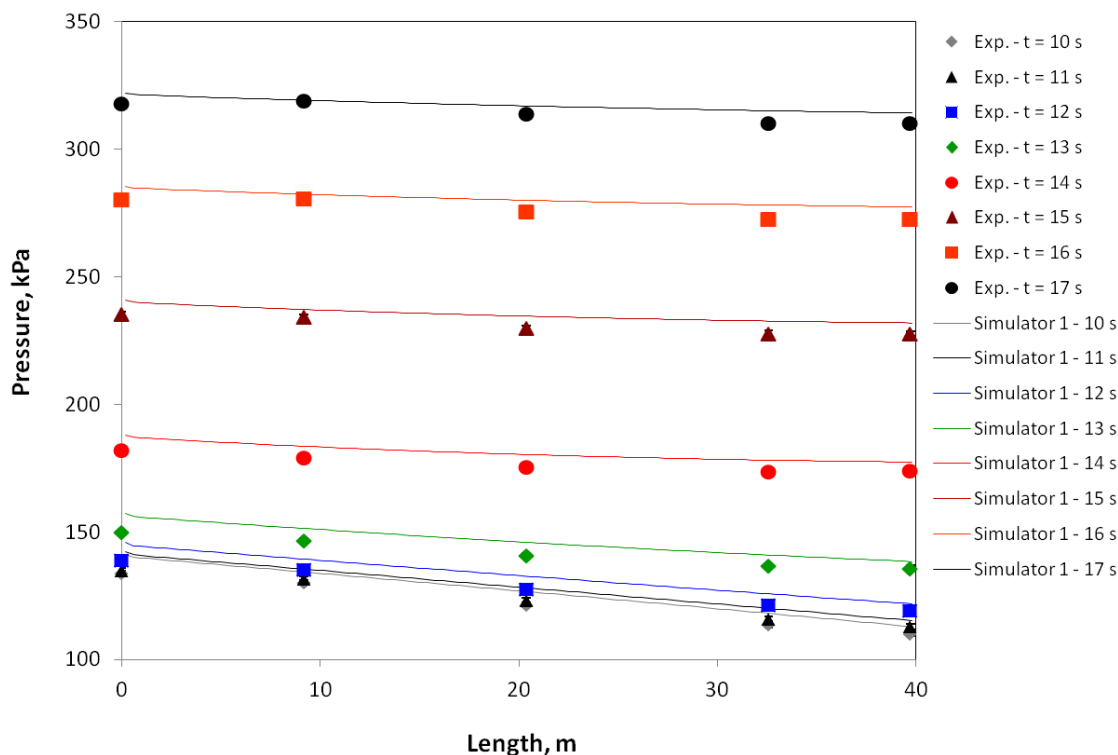
Figure 6.11 – Pressure profile prediction comparison between Simulator 1 and experimental data for the initial 17 second of run time for annular-to-churn flow transition.

The simulator prediction of liquid holdup at the inlet and outlet of the test section were also analyzed, as shown in Figure 6.12 and Figure 6.13. The blue line in both figures is the corrected liquid holdup to include the entrained liquid fraction, since the sensor is not able to capture the liquid entrained present in the gas core for annular and churn flows. The entrained fraction correction was made using a correlation proposed by Barbosa et al. (2002).

Surprisingly, the liquid holdup at the bottom of the vertical tube (see Figure 6.12) did not show as good agreement as in the pressure predictions. In average, the discrepancies in the liquid holdup are as much as 300%. Also, around time = 100 s, Simulator 1 predicts a peak in liquid holdup which is not observed in the experimental measurements.
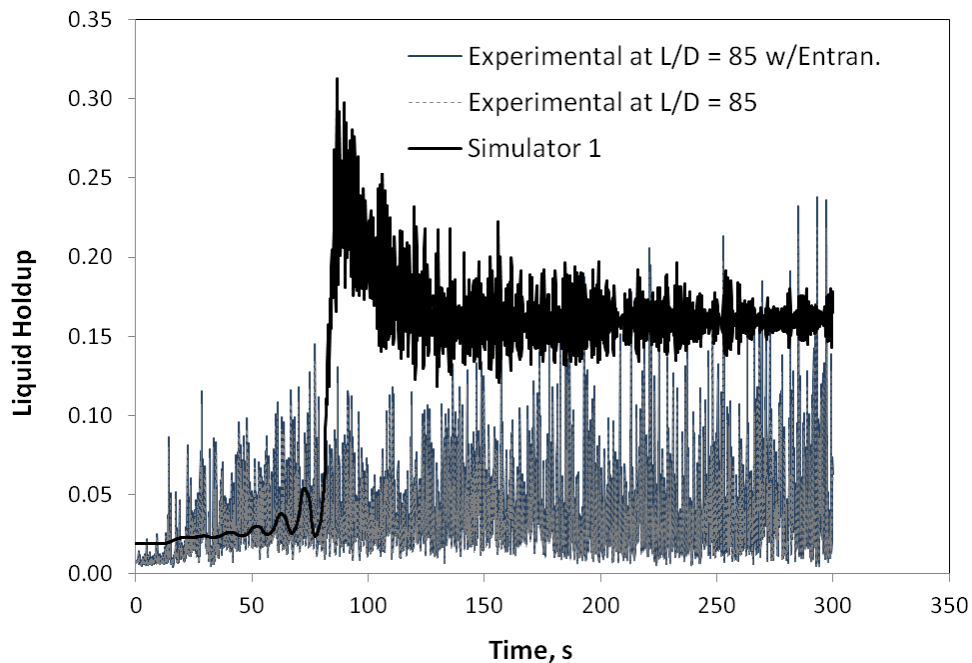
Figure 6.12 – Inlet (L/D = 85) liquid holdup comparison between Simulator 1 and experimental data for annular-to-churn flow transition.
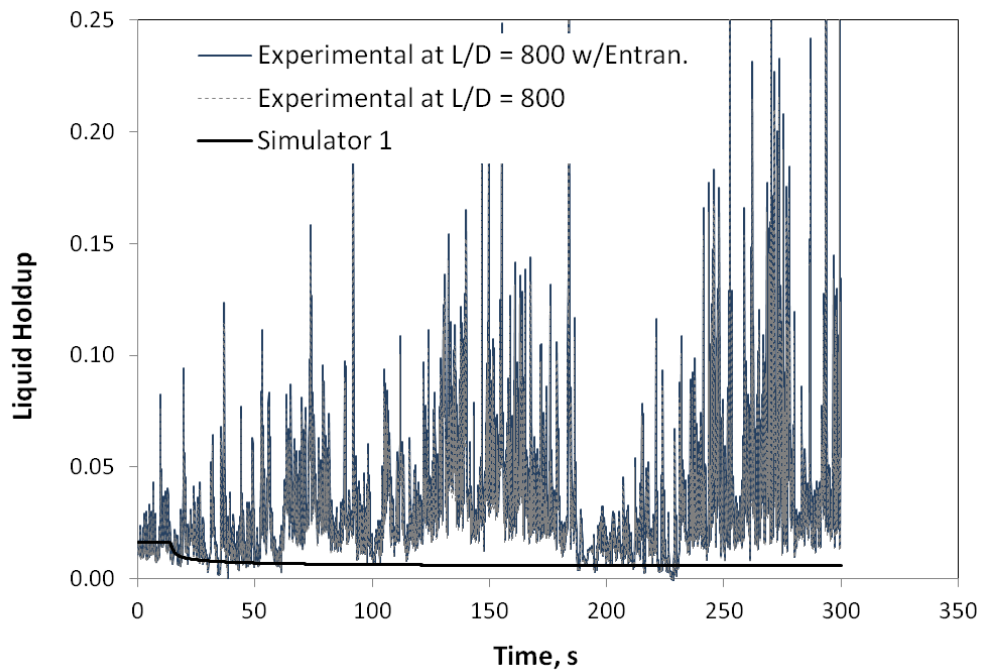
Figure 6.13 – Outlet liquid holdup comparison between Simulator 1 and experimental data for annular-to-churn flow transition.

On the other hand, the outlet liquid holdup (Figure 6.13) for Simulator 1 is considerably lower than the experimental observations. Since the simulation results are higher in the inlet and lower in the outlet than the experimental data, there is a possibility that the overall liquid content in the vertical tube for the simulation can be the same as in the experimental measurements.

To have a better understanding of the predictions of Simulator 1 regarding the tracking of the liquid movement in the vertical tube, a comparison of the liquid front observed in the experimental run and the simulation results was carried out. The experimental data used here is the same as in the analyses discussed in section 5.2.3.

From Table 5.2 and Table 5.3 it is possible to correlate the time when the high liquid holdup front reaches three different axial positions in the vertical tube (L/D = 85, 500 and 800). Table 6.3 presents the time when the liquid front reached each axial location observed from the video recordings for the experimental run used in Case 5.

Table 6.3- Time when the high liquid holdup front reached each corresponding axial location from visual observations for the experimental data in Case 5.

L m	L/D	t_{exp} s
4	85	45
24	500	165
39	800	240

With the information from this table and the simulation results for the liquid holdup profile for the same corresponding time, is possible to compare the simulated movement of the liquid front with the experimental observations, as illustrated in Figure 6.14. The dashed lines shows the locations and time when the liquid front was observed in the experiment. As can be seen, there is a significant discrepancy in the locations between the simulation results and the experimental observations for the high liquid holdup front movement. Again, the reason for this not accurate prediction is believed to be due to the mis-modeling of churn flow by Simulator 1. Slug flow regime was

predicted by Simulator 1 following at the same points where the results exhibited high liquid holdup levels, while churn flow conditions were observed during the experimental run.
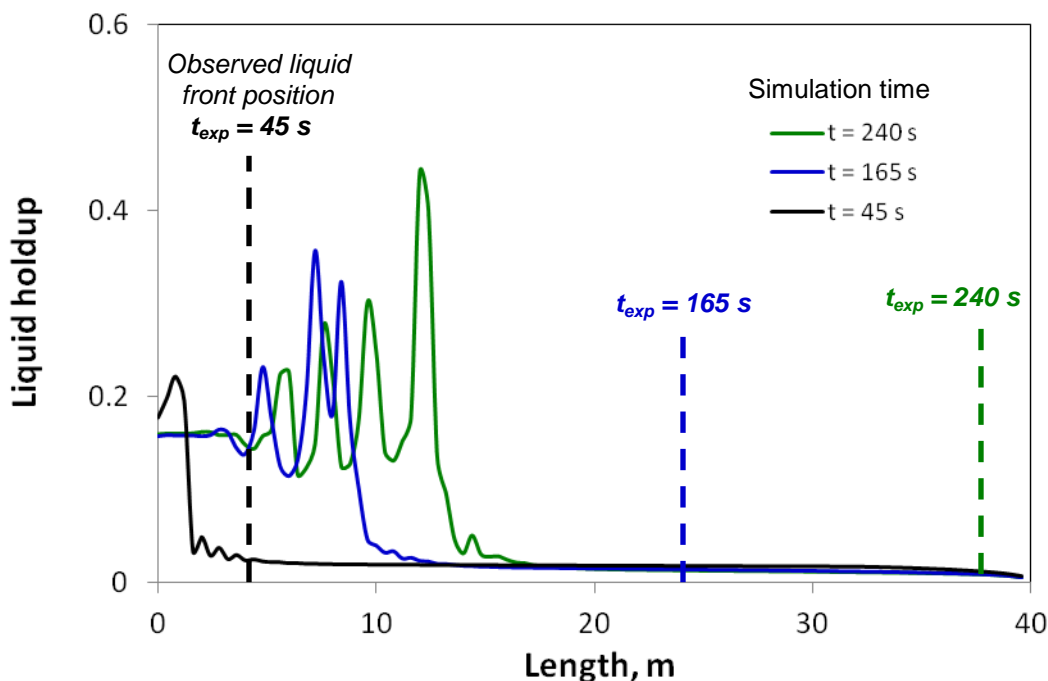
Figure 6.14 – Comparison of the liquid holdup profile between Simulator 1 and experimental observations for Case 5.

A comparison for the total pressure drop (difference between inlet and outlet pressure) is also presented in Figure 6.15. The Simulator 1 results shows a good match for the pressure gradient, especially for the time after the pressure start rising. Figure 6.16 illustrates the error between Simulators 1 predictions and the experimental data. Besides the peak of 50% (which is likely an effect of the peak in liquid holdup as shown in Figure 6.12), error values stayed in the range of ±20%, which is acceptable for multiphase flow predictions.
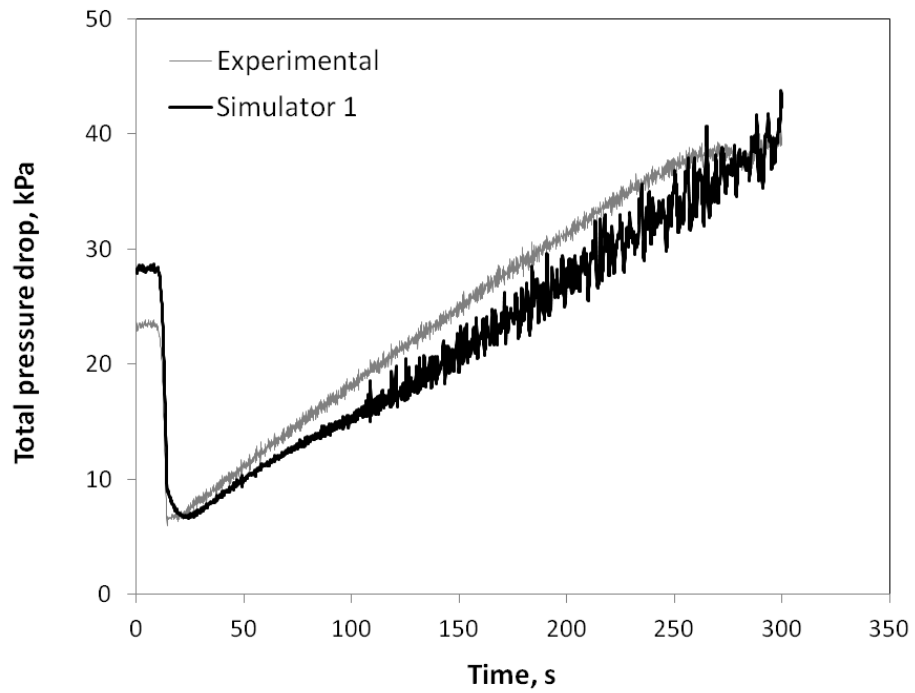
Figure 6.15 – Total pressure drop comparison between Simulator 1 prediction and experimental data for annular-to-churn flow transition.
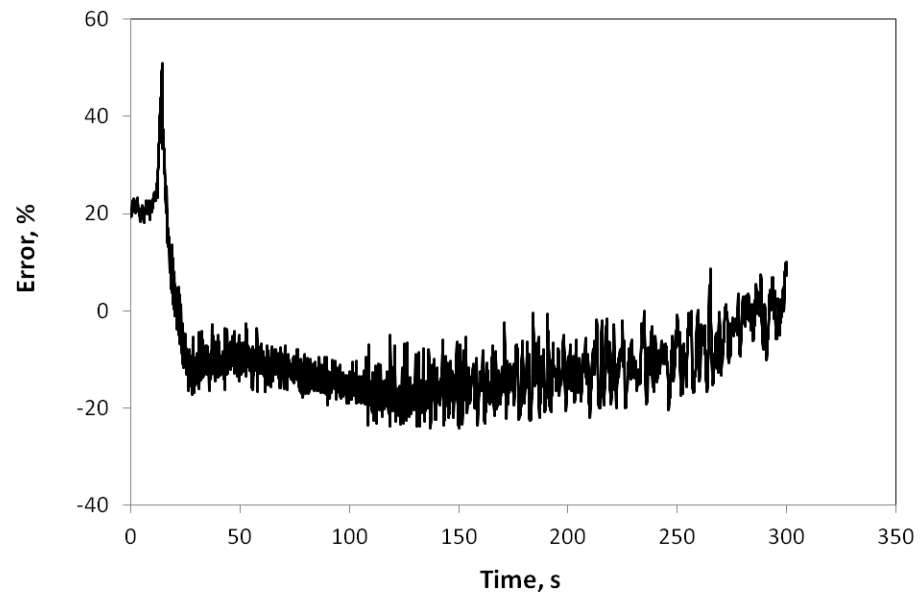
Figure 6.16 – Total pressure gradient error of Simulator 1 prediction compared to experimental data for annular-to-churn flow transition.

Case 6 - Outlet pressure decrease (Churn-to-Annular transition and low liquid rate)

This case was set up to verify the hysteresis of both experimental and simulator performance for annular-to-churn flow transitions. The experimental run procedure was carried out in a similar way to case 5, but for a reversed sequence (e.g., decreasing the outlet pressure instead of increasing).

Figure 6.17 presents the inlet pressure comparison between the experimental data and Simulator 1 results. The discrepancies in the initial period (before pressure decrease) are small and agree well with the final period of case 5 (see Figure 6.10). However, after the pressure starts decreasing, the differences between experimental and simulation results reaches high levels, up to 90% as present in Figure 6.18. For the final period, the discrepancies are lowered to approximately 20%, which agrees again with the initial period differences found for annular-to-churn flow case. Thus, looking at the initial and final stages of the inlet pressure, one can say there is only a small or no hysteresis for the annular-to-churn flow transition for both experimental and simulation runs. However, during the transient period when the pressure starts decreasing, higher error levels are exhibited for the churn-to-annular than annular-to-churn scenario.

Figure 6.17 – Inlet pressure comparison between Simulator 1 and experimental data for churn-to-annular flow transition.
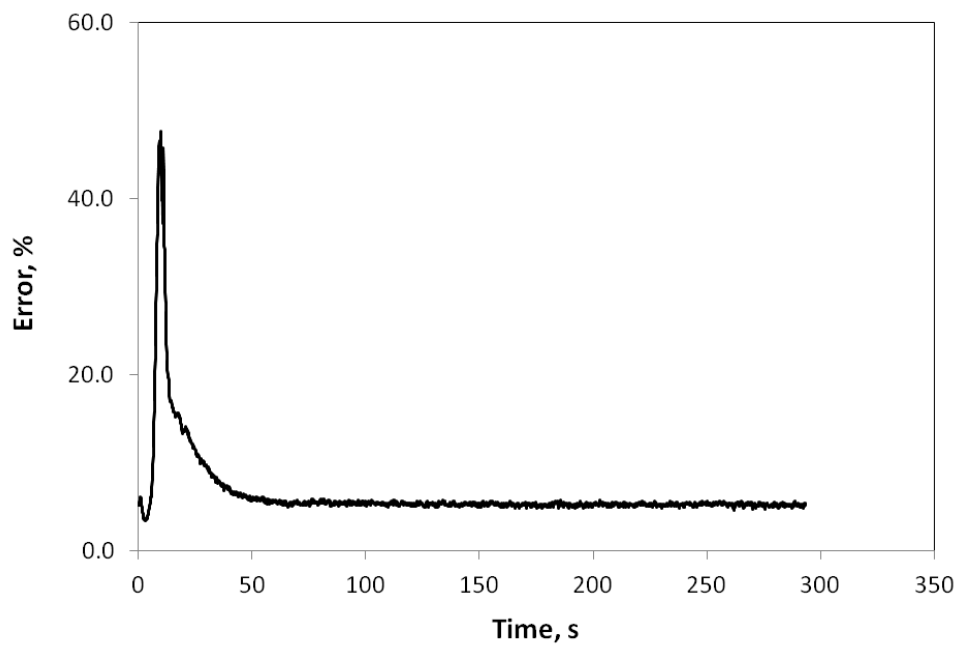
Figure 6.18 – Simulator 1 prediction error for inlet pressure when compared to experimental data for churn-to-annular flow transition.

From Figure 6.19, we can see that the discrepancies between Simulator 1 and experimental results for the total pressure gradient are also considerably higher than for the inlet pressure, especially for the initial 50 seconds.
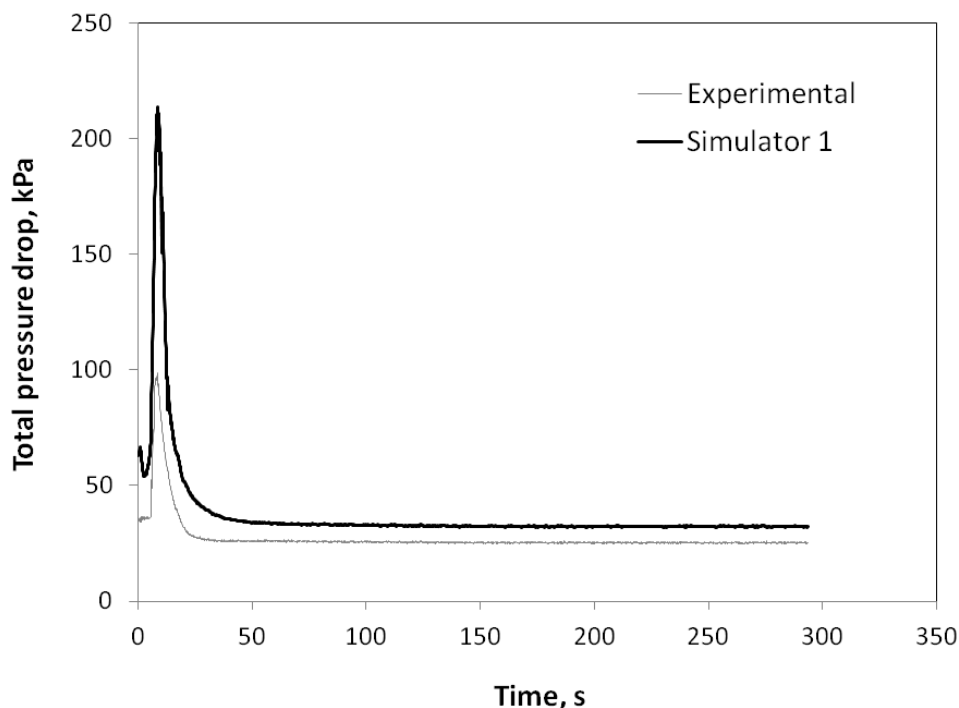
Figure 6.19 – Total pressure drop comparison between Simulator 1 prediction and experimental data for churn-to-annular transition.

Figure 6.20 shows that Simulator 1 error for the total pressure gradient can reach up to 140% for the conditions tested here. However, the error levels are lowered to approximately 20% for the final stable period. One of the reasons that can be attributed for the mismatch in the total pressure is the discrepancies also found in the liquid holdup, as presented in Figure 6.21 and Figure 6.22. As can be seen from both figures, there is a mismatch between the Simulator 1 predictions for the initial 50 seconds, which is also the same trend for the errors found in the total pressure drop. After the initial transient period, the inlet liquid holdup shows a very good agreement with experimental

data. In the other hand, the outlet predictions are considerably higher than the experimental measurements. The combination of both observations can indicate a more elevated total amount of the liquid content in the vertical tube for the simulation results than for the experimental run. Consequently, this would create the overestimation of total pressure drop in the simulation evaluations, as observed in Figure 6.20.
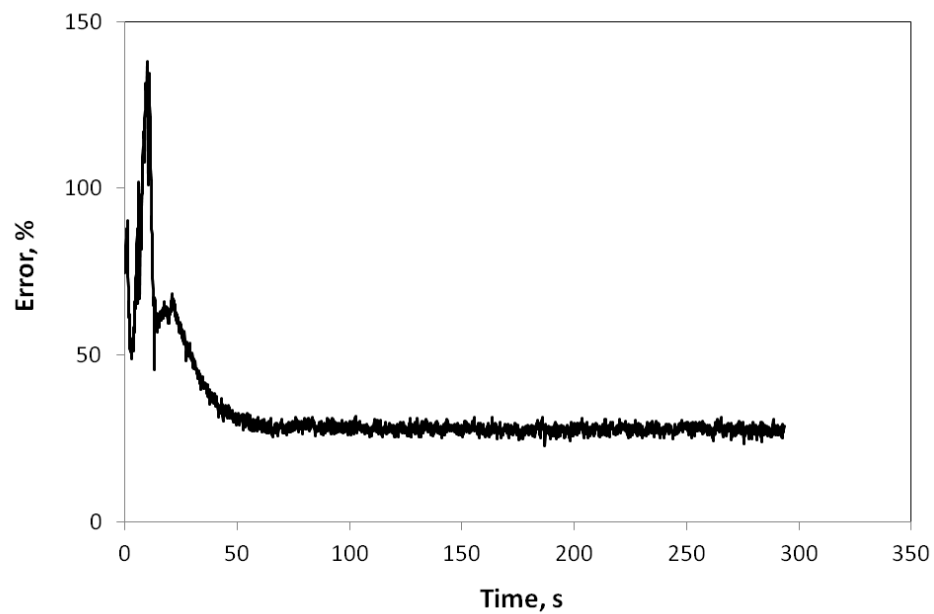
Figure 6.20 – Total pressure gradient error of Simulator 1 prediction compared to experimental data for churn-to-annular flow transition.
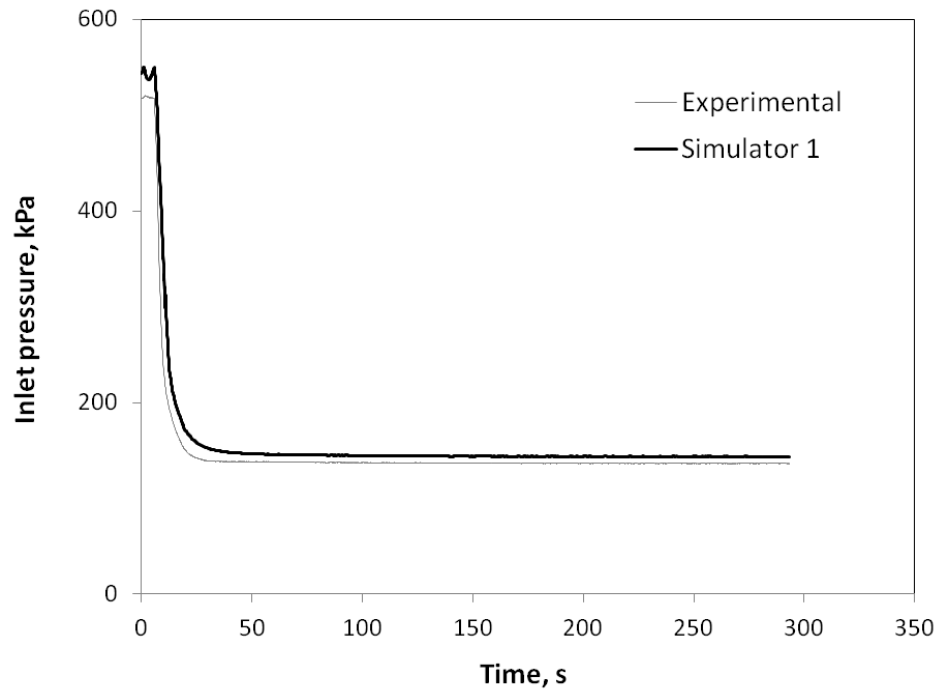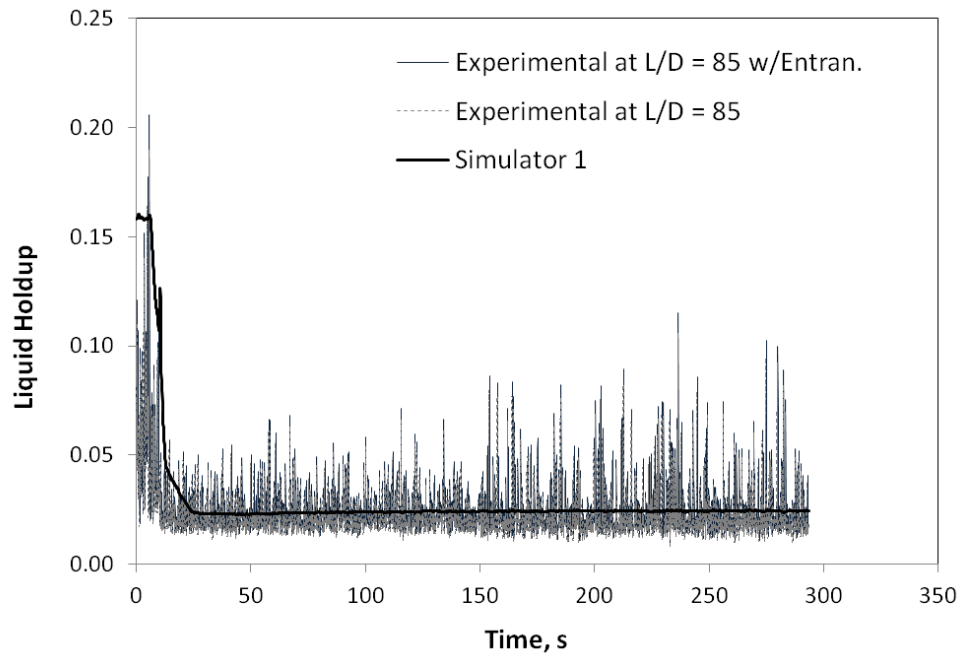
Figure 6.21 – Inlet liquid holdup comparison between Simulator 1 and experimental data for churn-to-annular flow transition.
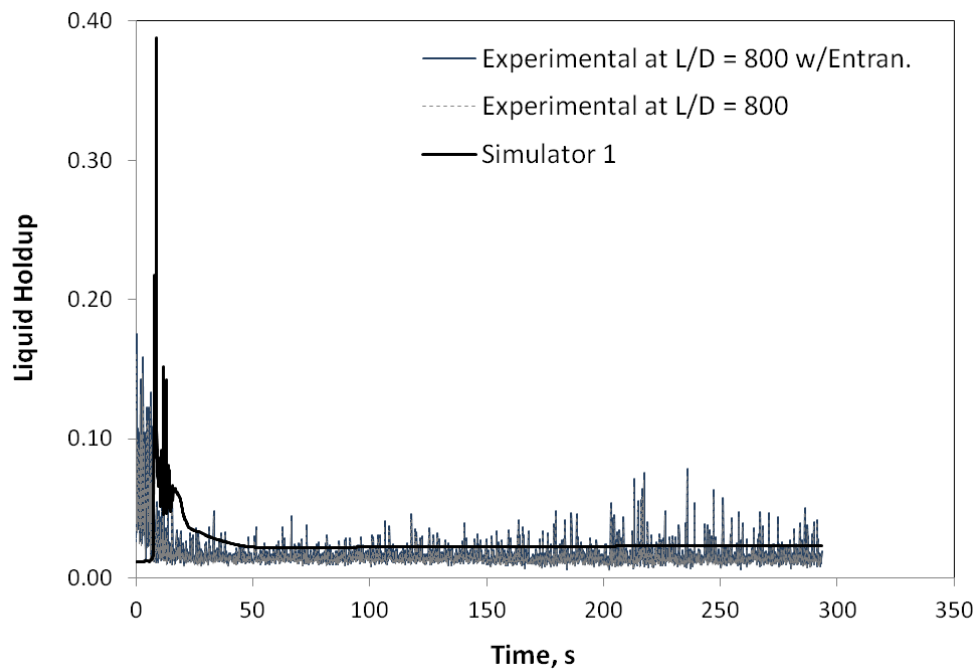
Figure 6.22 – Outlet liquid holdup comparison between Simulator 1 and experimental data for churn-to-annular flow transition.

Case 7 - Outlet pressure increase (Transient annular flow and high liquid rate)

In this case, the experimental run was performed in a way to keep the flow under annular conditions or at least close to the transition to churn flow. The initial and final conditions can be found in Table 6.2.

As can be seen from Figure 6.23, the inlet pressure in the initial period predicted by Simulator 1 (before the pressure change) does not show as good agreement as the cases before. In this case the differences reached up to 70%. However, the simulation results and experimental data become closer as pressure increases and reach the stable final period. The same trend is observed for the total pressure gradient (Figure 6.24 and Figure 6.25), inlet and outlet liquid holdups (Figure 6.26 and Figure 6.27). Thus, it is possible to infer here that the evaluations for Simulator 1 are likely to present lower error levels for conditions closer to churn flow and high liquid rates.

This behavior could be attributed to the flow regime prediction (together with the associated closure relationships) and calibration of the flow model. Since Simulator 1 does not have a churn flow model and high liquid rates can create scenarios closer to conditions in slug than annular flow, Simulator 1 is likely to be calibrated to recognize slug flow conditions for high liquid rate scenarios. For the initial part of the experimental run, it was possible to observe clearly annular flow conditions. For the final period, transition to churn flow behavior started to appear in the bottom of the tube. Simulator 1 predicted slug flow during all simulation time for the bottom part of the tube, even for the initial annular flow period. However, it is not properly evaluating the flow regime experimentally observed. Additionally, a similar behavior is encountered in case 6, where the mismatch of liquid holdup for churn flow in lower liquid rates scenario could be explained by the prediction of slug flow conditions.

The discrepancies found in the initial period for this case should be also related to flow regime prediction and liquid rate level. For low liquid rates scenarios as case 1, Simulator 1 exhibit a excellent match compared to experimental data (where annular flow regime together with most flow parameters were accurately predicted). However, for high liquid rate scenarios as in this case, annular flow was observed from bottom to

top of the vertical test section in the experimental run, but Simulator predicted slug flow during the entire simulation time. The same trend can also be confirmed in case 6, where reasonable match in annular flow conditions is obtained for low liquid rates.
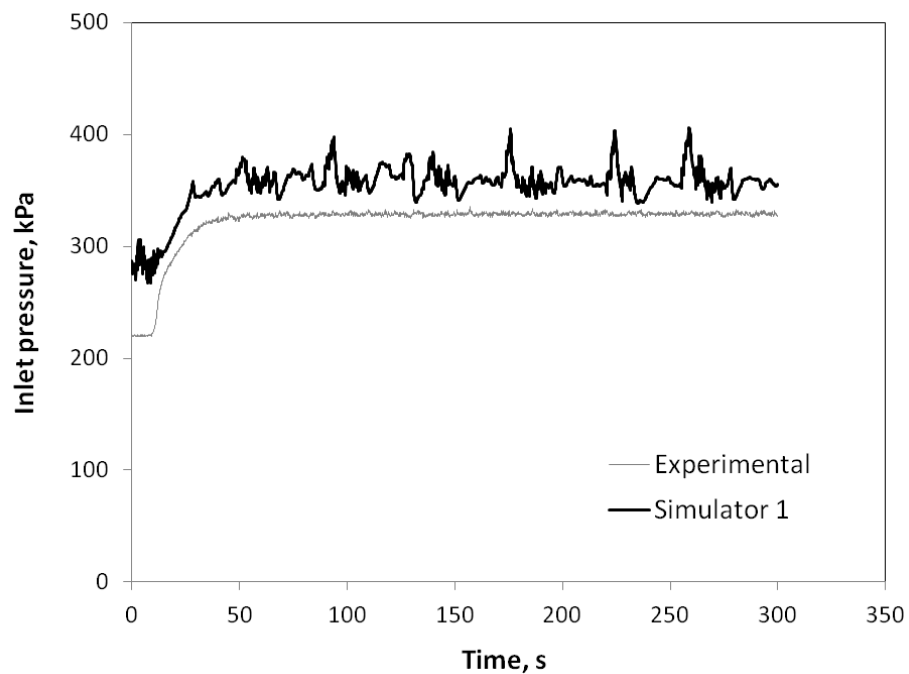
Figure 6.23 – Inlet pressure comparison between Simulator 1 and experimental data for transient annular flow.
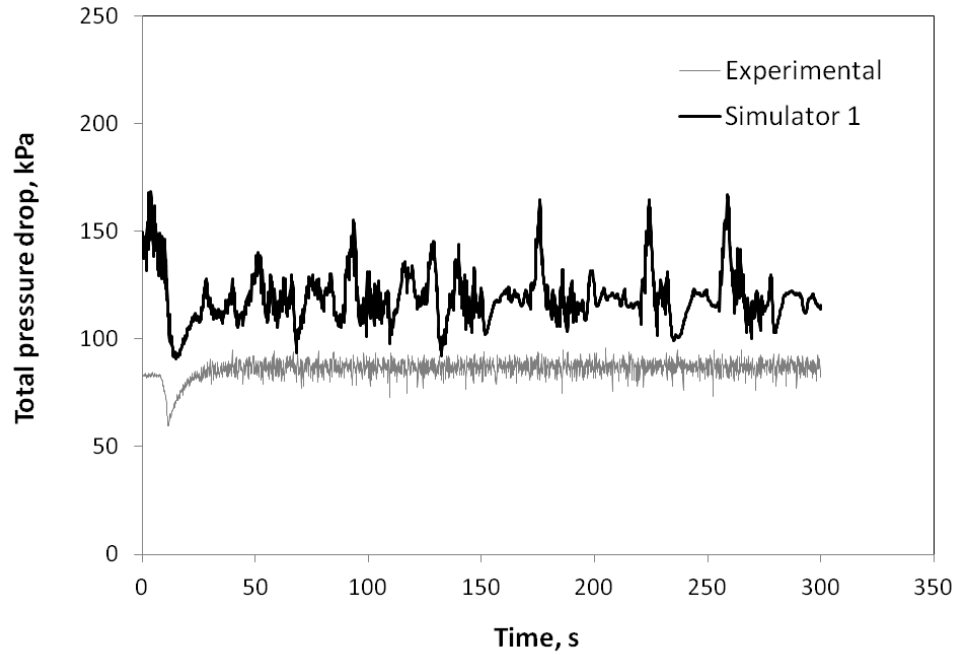
Figure 6.24 – Total pressure drop comparison between Simulator 1 prediction and experimental data for transient annular flow.

Figure 6.25 – Total pressure drop error of Simulator 1 prediction compared to experimental data for transient annular flow and high liquid rate.

Figure 6.26 – Inlet liquid holdup comparison between Simulator 1 and experimental data for transient annular flow and high liquid rate.

Figure 6.27 – Outlet liquid holdup comparison between Simulator 1 and experimental data for transient annular flow and high liquid rate.

Case 8 – Liquid rate decrease (Transient churn flow)

As the liquid rate level seems to play an important role in the quality of the predictions for Simulator 1, this case was performed for churn flow conditions varying the liquid rate from high to low levels, as shown in Figure 6.28. As can be seen in the results for case 1, Simulator 1 have small discrepancies when compared to the experimental data for churn flow conditions and high liquid rate. However, in this case is clear to see that as the gas rate decreases, the mismatch increases for Simulator 1 results as presented in Figure 6.29 to Figure 6.31. The same mismatch trend is observed for the liquid holdup as presented in Figure 6.32 and Figure 6.33. These results seem to confirm the problem about mis-modeling the flow regime. In the experimental runs churn flow was observed from bottom to top of the vertical tube, while Simulator 1 predicted slug flow for the bottom part. However, when the liquid rate is high, conditions closer to slug flow are created, and this should be one of the main reasons why Simulator 1 has a better performance.
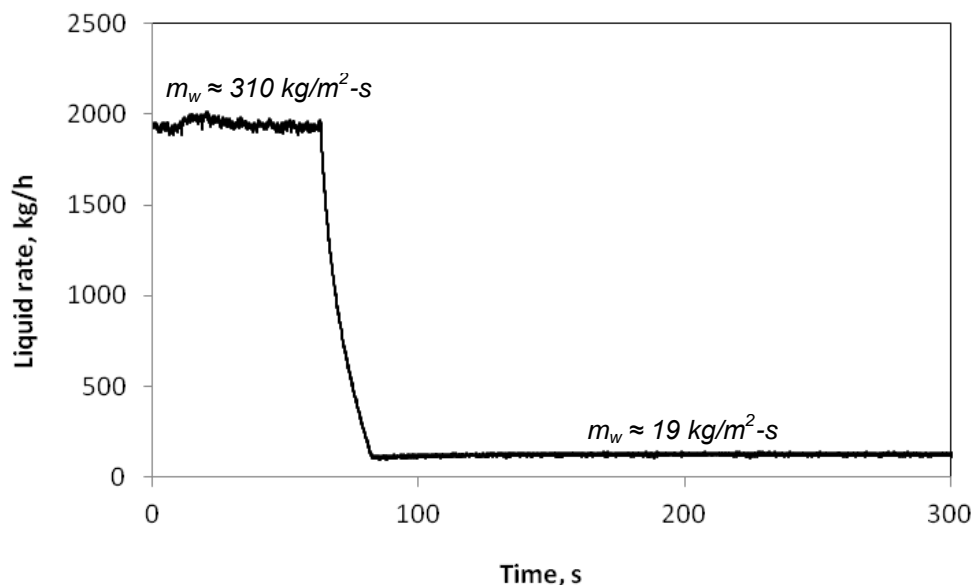
Figure 6.28 – Liquid rate variation imposed during the experimental run for transient churn flow in case 8.
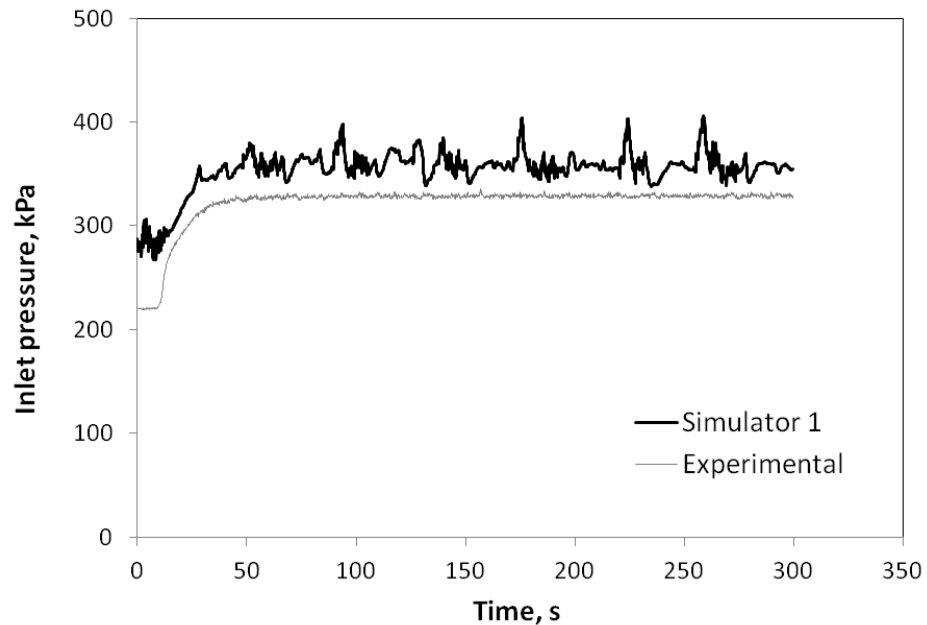
Figure 6.29 – Inlet pressure comparison between Simulator 1 and experimental data for transient churn flow and liquid rate variation.
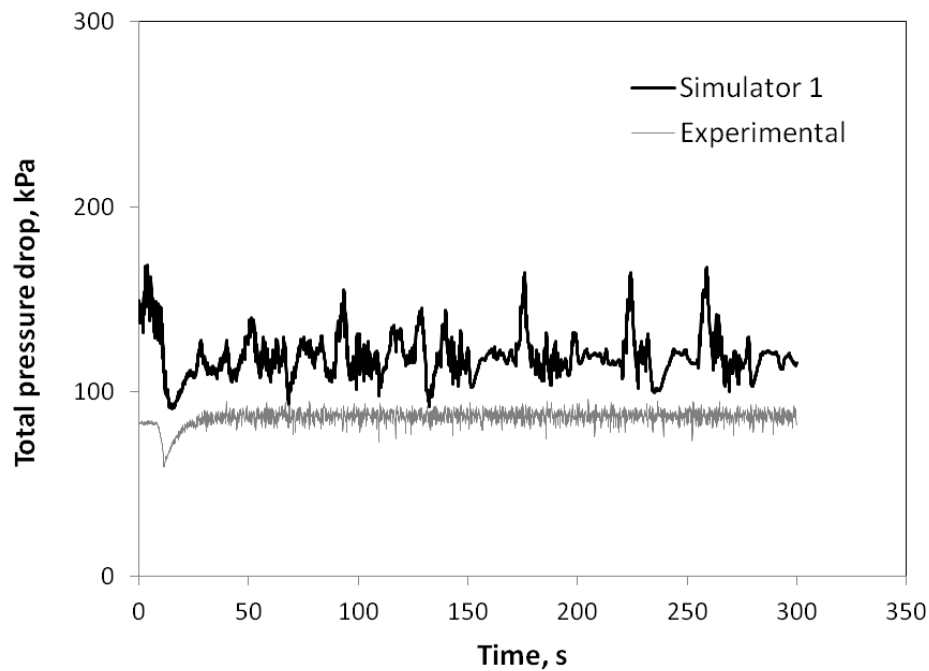
Figure 6.30 – Total pressure drop comparison between Simulator 1 prediction and experimental data for transient churn flow liquid rate variation.
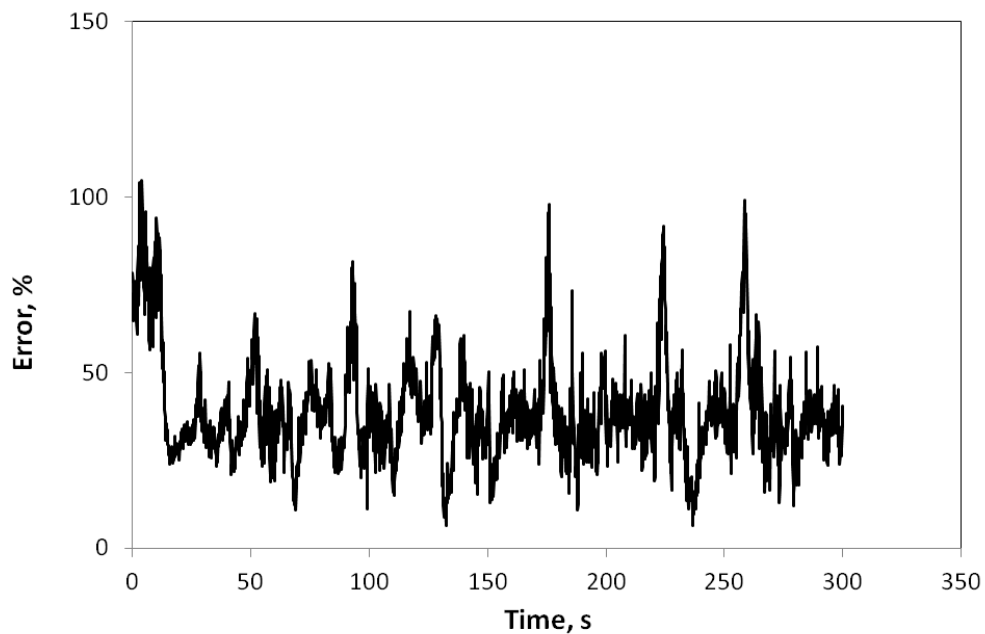
Figure 6.31 – Total pressure drop error of Simulator 1 prediction compared to experimental data for transient churn flow liquid rate variation.
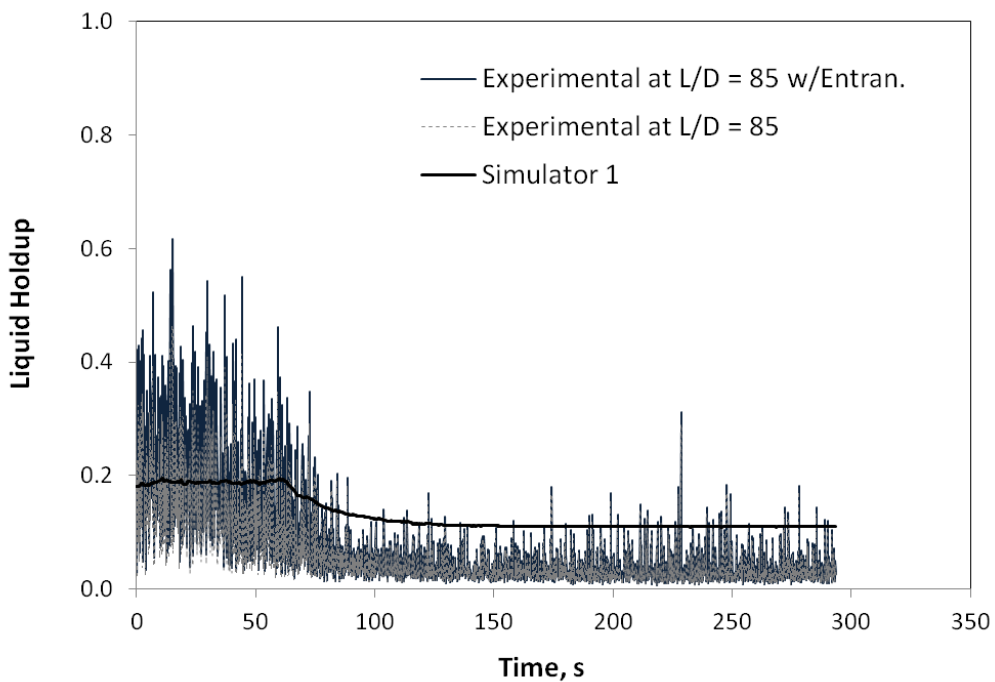
Figure 6.32 – Inlet liquid holdup comparison between Simulator 1 and experimental data for transient churn flow liquid rate variation.
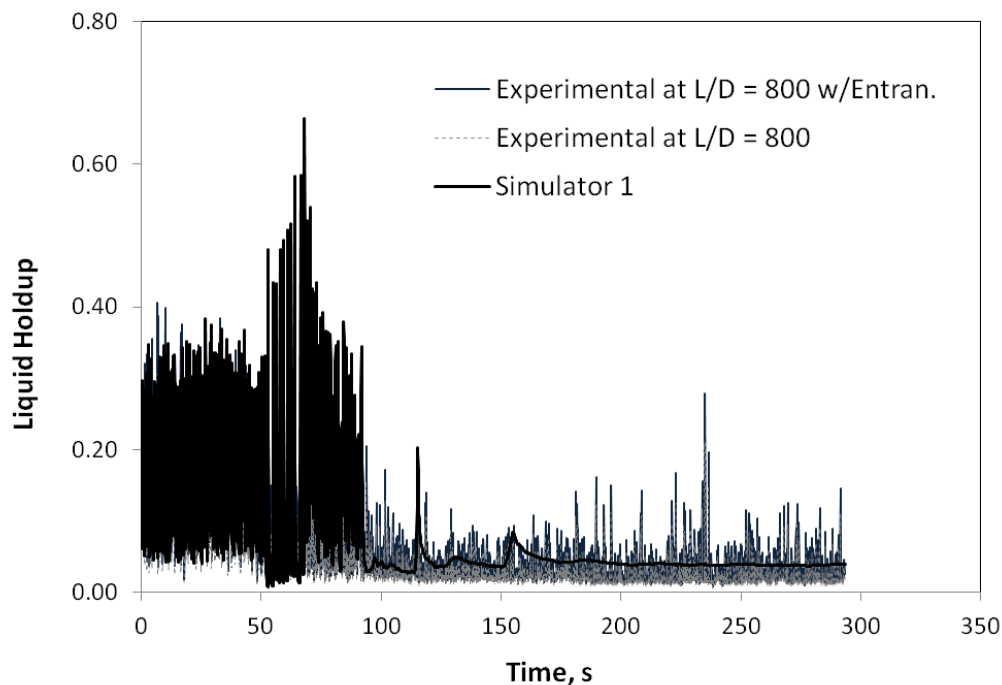
Figure 6.33 – Outlet liquid holdup comparison between Simulator 1 and experimental data for transient churn flow liquid rate variation.

Case 9 – Outlet pressure decrease (Churn-to-annular transition and high liquid rate)

One last case was carried out to confirm the good match of Simulator 1 results with experimental data for churn flow and the mis-modeling for annular flow for high liquid rates. As can be seen from Figure 6.34 to Figure 6.36, this case scenario can confirm most of the previous observation in terms of prediction of the pressures and liquid holdup. From the results for this case it is easy to see that for the initial period (before pressure start decreasing), Simulator 1 exhibits an excellent match for churn flow (flow regime observed during the experiments) and high liquid rates. In the other hand, as pressure decreases and the experimental observations indicate annular flow conditions, the results show a significant mismatch between the simulator and experimental data.
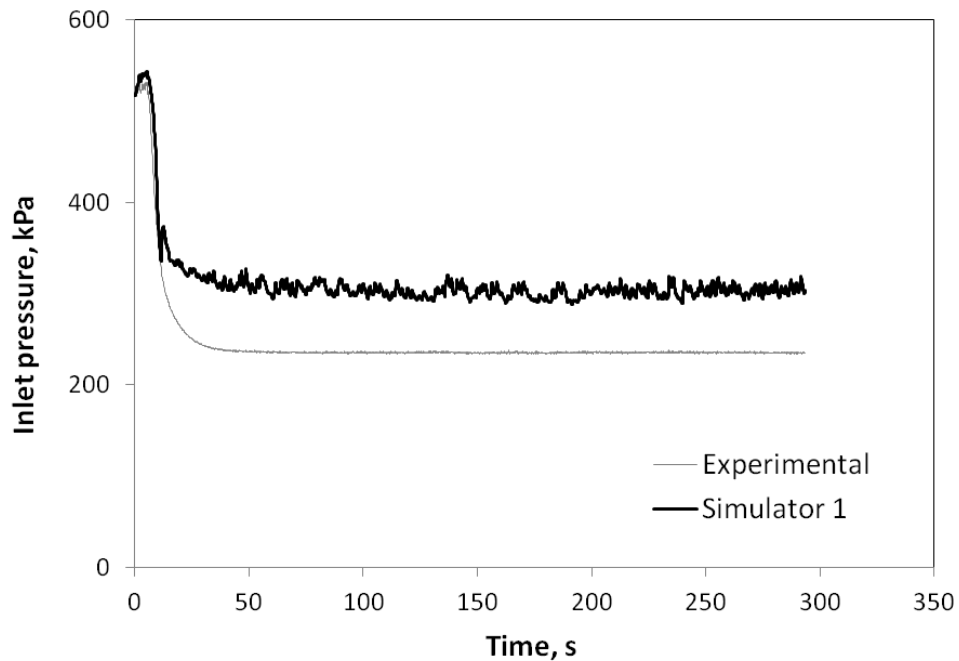
Figure 6.34 – Inlet pressure comparison between Simulator 1 and experimental data for transient churn-to-annular transition and high liquid rate.
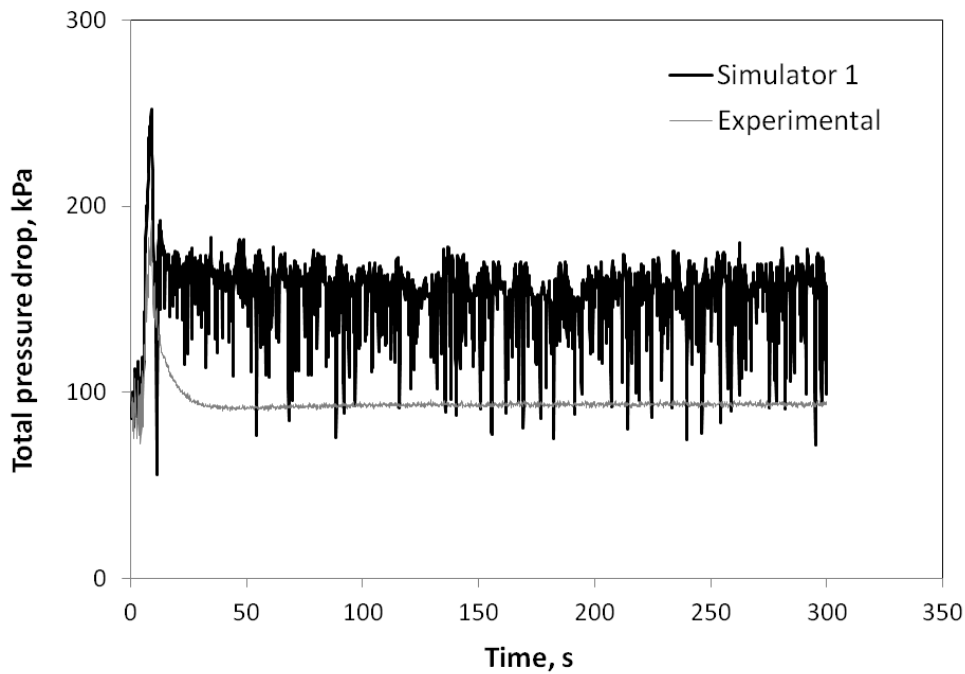
Figure 6.35 – Total pressure gradient comparison between Simulator 1 and experimental data for transient churn-to-annular transition and high liquid rate.

A similar trend is observed for the outlet liquid holdup (Figure 6.37), but surprisingly, an excellent match is verified for the inlet (Figure 6.38). However, as the liquid holdup is virtually the same in the inlet but considerably higher for the outlet, the total liquid content in the simulation is larger than the experimental data, and this would be the reason for the elevated total pressure gradient predictions during the final period of the simulation. Since the gravitational pressure gradient contributes by approximately 80% of the total pressure gradient in slug flows (which was the flow regimes predicted for almost the entire tube in the simulations), the liquid holdup miscalculation should be the main cause for the discrepancies between experimental data and Simulator 1 results.
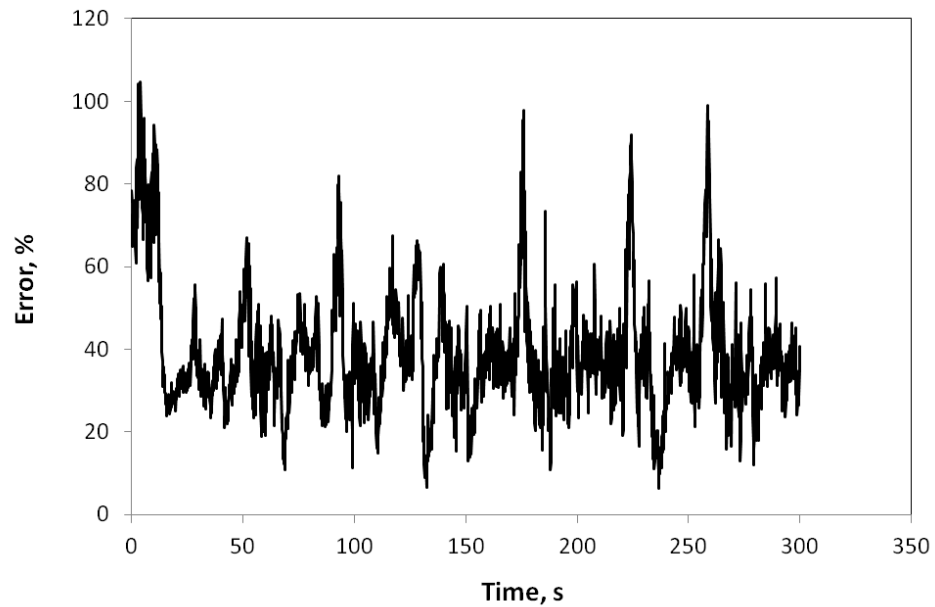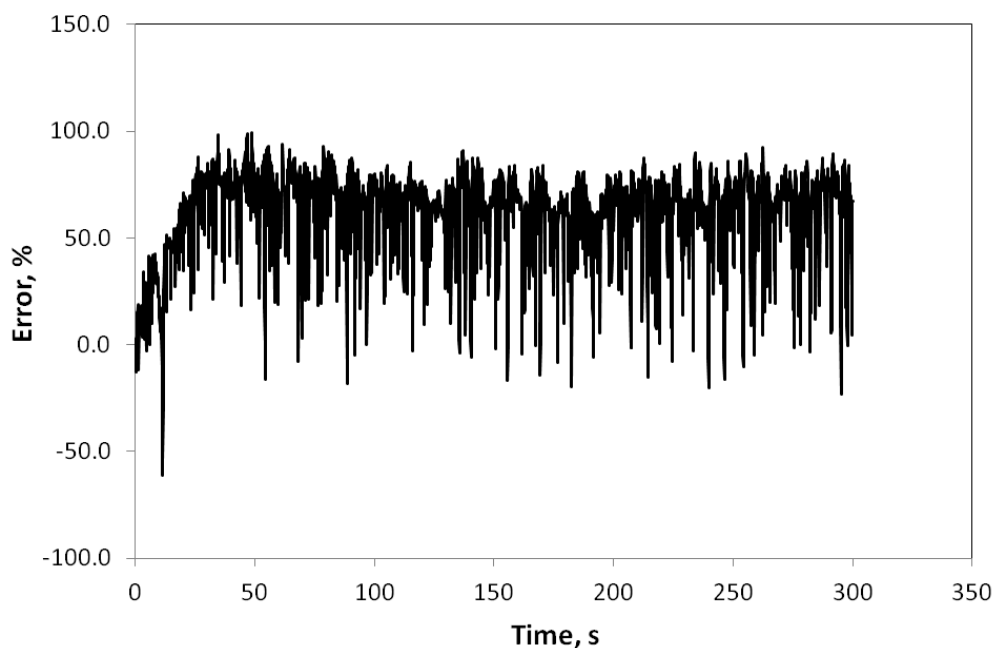

Figure 6.36 – Total pressure drop error of Simulator 1 prediction compared to experimental data for transient churn-to-annular transition and high liquid rate.
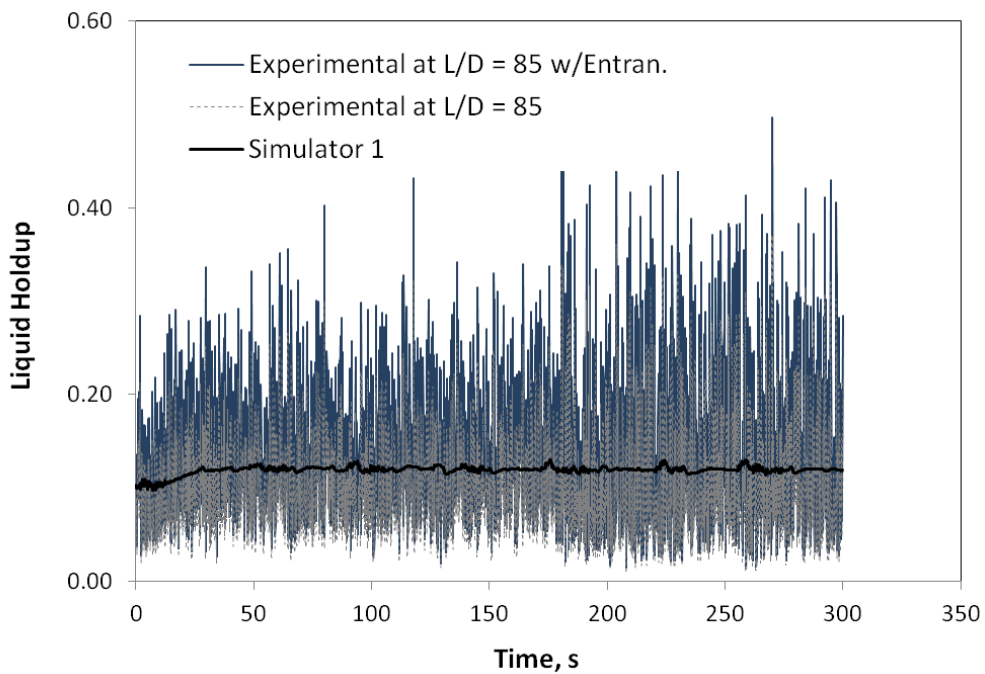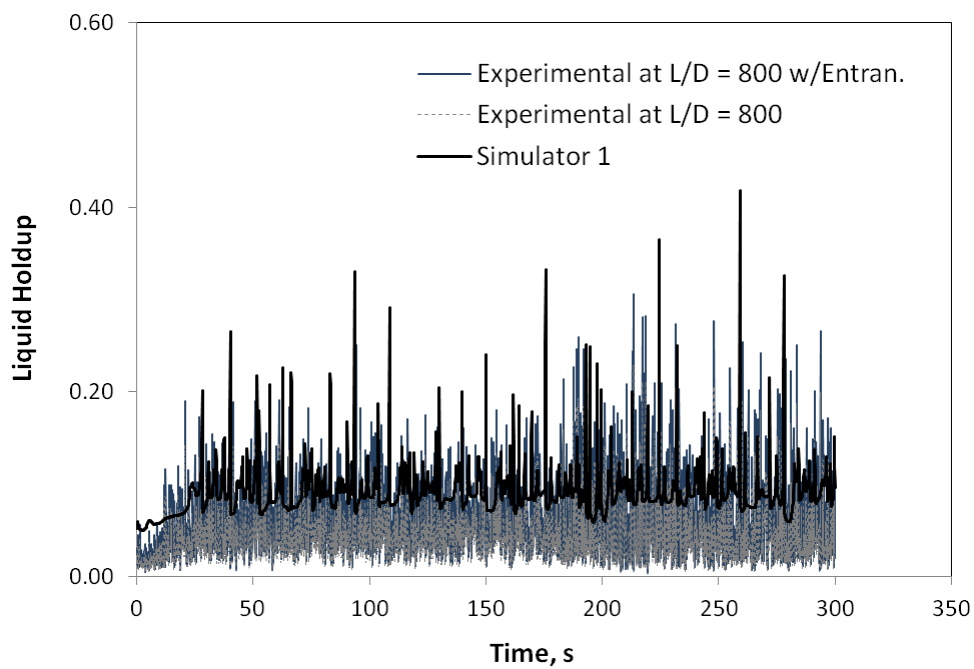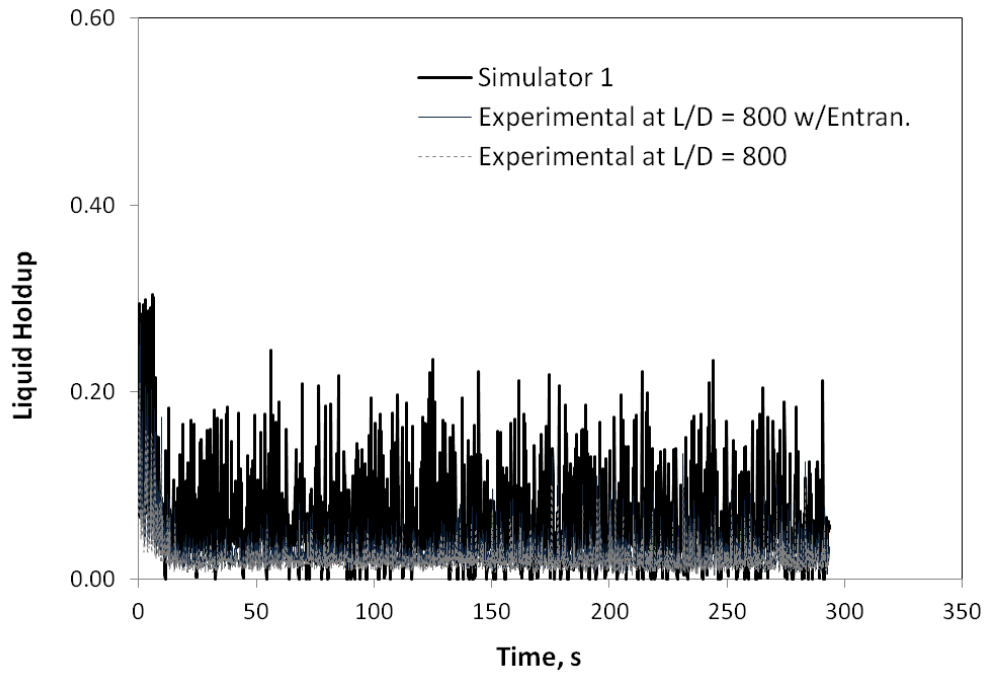
Figure 6.37 – Outlet liquid holdup comparison between Simulator 1 and experimental data for transient churn-to-annular transition and high liquid rate.
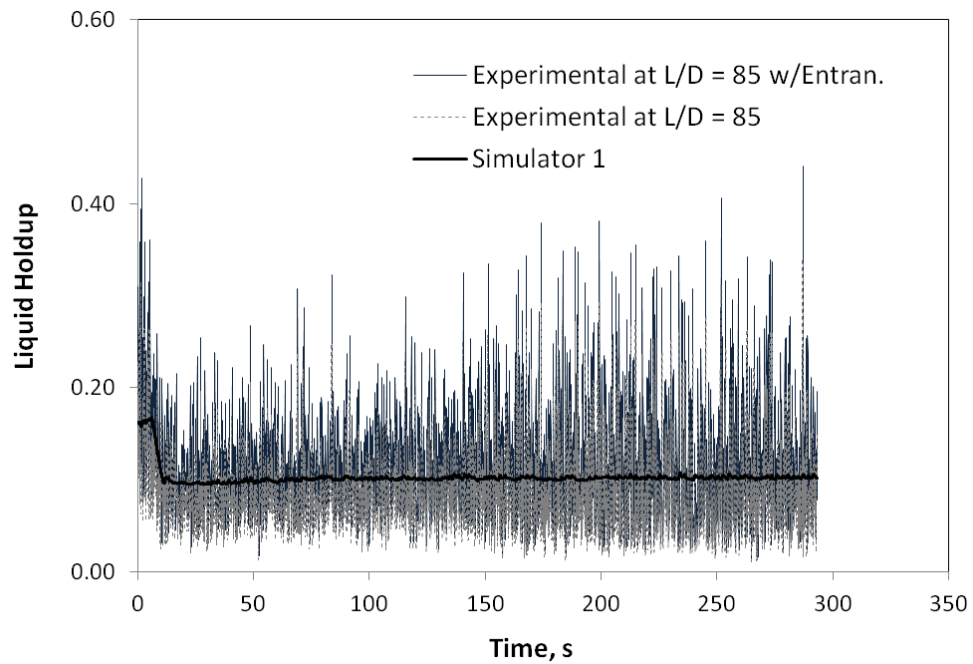
Figure 6.38 – Inlet liquid holdup comparison between Simulator 1 and experimental data for transient churn-to-annular transition and high liquid rate.

6.5. Conclusions

Comparisons for steady state conditions between a benchmark code for multiphase flow in pipes (Simulator 1), experimental data and two research codes (GRAMP and HyTAF) for vertical two-phase flow were conducted. After having validated Simulator 1 and HyTAF for steady-state annular flow, analyses were also performed for transient conditions for both codes. The following conclusions were obtained from the steady-state and transient analysis:

- All three codes showed a good agreement (with a maximum of 24% difference) against experimental pressure gradient for steady state annular flow. Some divergences were found in the liquid holdup and film velocities.

- An excellent match (7% difference) was observed for churn flow conditions using GRAMP code when compared with experimental pressure gradient. However, for the same input conditions for Simulator 1, slug flow was predicted, and the results presented 38% divergence against experimental pressure gradient. The mis-modeling of churn flow is believed to be the main reason for the divergence in pressure gradient prediction for Simulator.

- Investigation on slug flow was carried out and a good match was obtained for Simulator 1 and GRAMP when compared with experimental pressure gradient. This analysis in a certain extent validates the quality of the experimental data, once these simulators were calibrated and validated against a more extensive experimental database.

- HyTAF and Simulator 1 presented a reasonable agreement for pressure profiles for transient annular flow under a sudden outlet pressure change. However, Simulator 1 was not able to capture the sharp pressure waves. Pressure waves maybe important for the stability of annular flow especially in the liquid film. Nevertheless, further investigations are needed regarding these instabilities.

- Based on all experimental runs and transient simulation results described here, a summary of the comparison analyses is presented in Table 6.4. The main conclusion which can be extracted from the table is that Simulator 1 exhibited an excellent prediction for annular flows and low liquid rates and churn flows for high liquid rates. It is important to mention that these conclusions were based on the conditions of the experimental runs tested here. In order to have a more comprehensive understanding of the prediction behavior regarding Simulator 1, different fluids (such as oil and natural gas) and higher pressure should be also tested.

Table 6.4 - Summary of the comparison between Simulator 1 predictions and experimental data.

Reference Cases	Inlet pressure, kPa	Gas mass flux, kg/m2-s	Flow Regime	Liquid mass flux level, kg/m2-s	Overall predictions quality	Max inlet pressure error, %	Max Δp/ΔL error, %	Max liq. holdup error %
5,6	110-150	39	**Annular**	**15**	**Good**	20	30	50
7,9	110-150	37-52	Annular	300	Poor	70	80	100
6,8	200-500	31-33	Churn	15	Poor	85	150	250
8,9	200-500	27-33	**Churn**	**300**	**Good**	5	10	50

The proper evaluation of the multiphase flow behavior is crucial for the understanding and predictions of liquid loading in gas wells. Since the transition from annular to churn flow is believed here to be one of the roots of liquid loading, the summary presented in the table above can guide in the improvement of the simulators in order to use them in liquid loading studies.

7. CONCLUSIONS AND FUTURE WORK

This section presents the major conclusions of the investigations performed during this study.

One of the main outcomes from the experimental investigation carried out here is that liquid loading should not be characterized based on onset criteria alone. It may not be a wellbore-only problem, as the reservoir also plays a key role in determining if/when/how liquid loading manifests itself. Several tests were performed in steady state, pseudo-steady state and transient conditions. These tests had the objective of triggering and observing the onset and subsequent phenomena of liquid loading. However, using a long vertical tube (42-m long or L/D = 840), the liquid loading symptoms as observed in the field, such as donwhole liquid accumulation, were not observed in any of these tests. Instead, the liquid holdup increased along the entire vertical tube, and not only at the bottom, with the decrease in the gas velocity.

The onset criteria available in the literature to predict liquid loading in gas wells were also investigated. When compared with the experimental data, it is possible to conclude that the use of these criteria is very subjective to evaluate liquid loading onset. The experimental results did not show any point of sudden increase in liquid content in the vertical tube with the decrease in gas velocity. The liquid content in the vertical tube increased smoothly and continuously for all axial locations as the gas velocity decreased. Hence, the determination of the onset of liquid build up in the tube was found to be very subjective.

Next are presented the other conclusions about the detailed tests and comparisons which support the majors conclusions described above. Recommendations for future work are also made in order to stimulate new ideas for further research in the area of transient two-phase flow and its application to liquid loading in gas wells.

7.1. Axial Development of Churn and Slug Flows

Section 4 presented an experimental investigation of the axial development of churn and slug flows using a long vertical tube. Based on the results, the following conclusions were drawn:

- It was possible to show the similarities between the slug flow entrance region of Dukler and Taitel (1986) and churn flow, which had previously generated some confusion in the literature concerning the existence of churn flow as a separate flow regime. Additionally, the video recordings and PDF results also confirmed churn flow for all three axial positions (L/D = 85, 500 and 800).

- A comparison of the experimental observations and flow regime models showed a good prediction for the transition from annular-to-churn flow when using Wallis' criterion ($U_{gs}* \approx 1$). For the churn-to-slug flow transition, Brauner and Barnea (1986) model along with that of Jayanti and Hewitt (1992) presented a good prediction for lower pressure levels (1.4 bara), while Hewitt and Roberts (1969) model showed a better prediction for higher pressure (4.2 bara).

- The liquid holdup showed significant axial variation at all monitoring locations for higher liquid mass fluxes (310 kg/m^2-s), while it appeared that developed flow was reached at L/D = 500 for lower mass fluxes (19 kg/m^2-s).

- The disturbance wave frequency did not exhibit significant axial variation for dimensionless gas velocity between 0.2 and 1.6.

7.1.1. Future Work

The main objective of the experimental investigation carried out in Section 4 was to characterize some parameters of churn flow in the axial direction. Some of the data obtained, such as axial variation of liquid holdup and wave frequency, can be used to better understand two-phase flow behavior during liquid loading. However, extra parameters seem to be needed to provide a more comprehensive understanding of the phenomenon. Therefore, the following recommendations for future work can be made:

- Utilization of shear stress probes to axially characterize the initiation of the liquid film flow reversal. This information is essential to better understand the behavior of the liquid film in churn flow conditions, which is believed to characterize this flow regime.

- Development and implementation of liquid film probes in vertical flow, which would allow measuring liquid velocity and estimating the volume of the waves in churn flow. This information can provide a better quantification of the liquid volumes being carried via the liquid film. These measurements could be performed by means of optical techniques, such as Particle Imaging Velocimetry (PIV), or intrusive probes, such as consecutive conductivity two-wire sensors.

7.2. Onset of Liquid Loading in Gas Wells

Section 5 described an experimental campaign that consisted of carrying out two-phase flows in a 42-m long vertical tube for a wide range of pressure, liquid velocity and gas velocity. These gas velocities were greater than and lower than the Turner critical velocity. Turner's model is the most widely used criterion in the oil and gas industry. The experimental runs here had the main objective of investigating the onset models currently available in the literature. Based on the literature review and the experimental results presented in Section 5, the following conclusions were made:

- For fixed outlet pressure, liquid rate and gas velocity (lower than the Turner critical velocity), the bottomhole liquid accumulation depicted by classical definitions of the onset of liquid loading was not observed.

- The liquid holdup as a function of the gas flow rate exhibits a continuous and smooth curve, with no sudden change being observed for a decline in gas flow rate. Thus, using the Turner (or derived) critical gas velocity criterion to predict the onset of severe liquid build up in a vertical tube is extremely subjective, based on the observations and test conditions evaluated in this work.

One of the main conclusions is that the analyses of liquid loading in gas wells should not only consider Turner or Wallis' criteria to predict the onset, but that the reservoir behavior has also to be taken into account in order to properly investigate liquid loading.

Analyses based on the experimental observations showed that the liquid re-distribution during annular-to-churn flow transitions (created by an increase in pressure and decrease in flow rates) can be described using a pseudo-steady approach. Steady-state churn flow conditions were observed along the vertical tube after the churn flow front has reached each corresponding axial location, during the transition from annular to churn flow. These experimental observations can be used towards the development of simplified models for annular-to-churn flow transitions, which can consider pseudo-state approach to simulate transitions between annular and churn flow. As previously described in section 2, the transition between annular to churn flow can be related to liquid loading onset.

7.2.1. Future Work

As presented in Section 5 and in the conclusions above, the current available methods (Turner, Wallis and nodal analysis) are not able to accurately capture the onset of liquid loading under the conditions tested during this study. For further investigation on the development of more accurate models to predict liquid loading conditions, the following future work is proposed:

- An experimental facility which includes a reservoir at the bottom of the wellbore, as already proposed by Falcone (2006). This set up would be able to mimic the dynamics of reservoir inflow performance and the behavior of the multiphase flow in the vertical tube. If the reservoir cannot be physically attached to the vertical test section, another idea would be to create an integrated system where the fluids inflow in the bottom of the tube is controlled by a simulation reservoir model, which uses the bottomhole pressure as input. Figure 7.1 shows a schematic workflow of this integrated experimental set up. The integrated wellbore-reservoir model could still be

used if only a small piece of porous medium is possible to be attached to the vertical tube (to mimic the near-wellbore reservoir region). The reservoir simulator can provide the fluids inflow, or in other words, the inflow performance relationship (IPR) curve for the far region of the reservoir. The flow loop boosting system can artificially create an IPR for the fluid inflow, following the simulator model. Although the simulated IPR cannot completely simulate the fluid flow in a actual porous medium due to the limitation and assumption of the mathematical model, at least it can generate a scenario where the parameters of the reservoir (such as relative permeability and porosity) can be varied and their impact in liquid loading phenomena can be better understood using a coupled wellbore-reservoir approach. To minimize the differences between the simulated and porous medium IPRs, the simulated IPR response should be first calibrated with experimental data obtained from an experiment involving an actual porous medium (core) alone, measuring gas and water rates as a function of the inlet and outlet pressures on the core.

- All the tests carried out in this work used a vertical test section. Slight inclination can change the flow behavior considerably, especially in terms of counter-current liquid flow. Previous works have included inclined vertical tube (Belt (2007); Belfroid et al. (2008)). However, these works used only short tubes (L/D < 300), and they usually correlated the experimental results with Turner critical velocity.

- Fluid properties also play an important role in the flow behavior. As fluid properties are affected by pressure and temperature, it is suggested that experiments be performed at pressures closer to those in the field (e.g. in the order of 100 bara). Additionally, different fluids with different viscosities and surface tensions should be considered in future experimental campaigns, to assess the role of interfacial friction factors and phase distributions in two-phase flows.
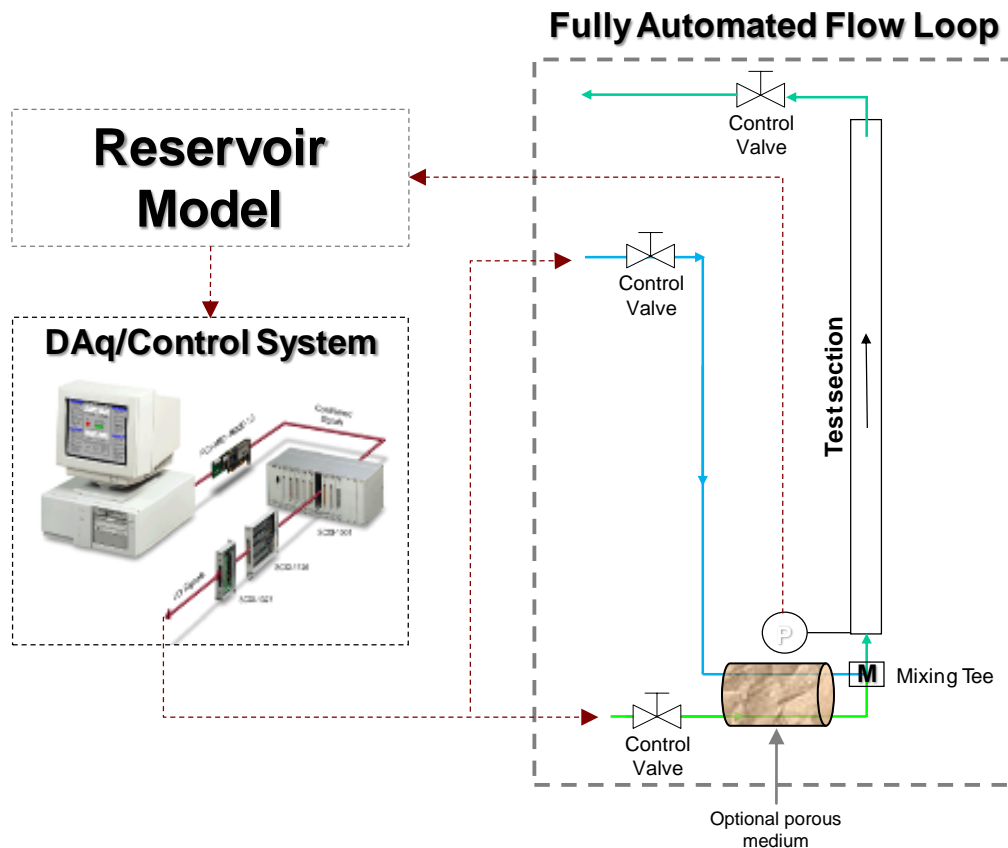
Figure 7.1 – Schematic workflow of the proposed experimental set up for an integrated wellbore-reservoir model.

7.3. Performance of Vertical Two-Phase Models Applied to Liquid Loading

Section 7 presented comparisons for steady state and transient flow conditions between a benchmark code for multiphase flow in pipes (Simulator 1), experimental data and two research codes (GRAMP and HyTAF). The main conclusions from the comparisons were as follows:

- All three codes showed good agreement with the experimental data for annular flow and low liquid rates (< 500 kg/h) in steady -state.
- A good match (7% difference) was observed for churn flow in steady-state conditions using GRAMP code when compared with the experimental pressure gradient, while Simulator 1 presented some divergences for this flow regime, especially for low liquid rates.

- For transient conditions, Simulator 1 exhibited excellent prediction capabilities for annular flow at low liquid rates and for churn flows at high liquid rates.

7.3.1. *Future Work*

The comparisons with the experimental data, as presented in Section 7, gave some insights into where the codes should be improved. The following recommendations can be made:

- GRAMP presented the best overall performance among all three codes analyzed. GRAMP is the only code (among those tested in this study) that includes a churn flow model. Therefore, it is recommended that churn flow models be also implemented in the other simulators for better prediction of liquid loading.
- In order to have a better understanding of the capability of Simulator 1 to predict liquid loading, different fluids (e.g. oil and natural gas) and higher pressures should be also tested.
- Further experimental characterization of churn flow is encouraged to fill in the gaps currently existing in the literature. A more detailed understanding of this flow regime, which is considerably complex and far from being well characterized, would significantly enhance the understanding of liquid loading in gas wells.

REFERENCES

Al-Saidi, L.F., Mortensen, K., and Almdal, K. 2003. Environmental Stress Cracking Resistance. Behaviour of Polycarbonate in Different Chemicals by Determination of the Time-Dependence of Stress at Constant Strains. *Polymer Degradation and Stability* **82** (3): 451-461. DOI: 10.1016/s0141-3910(03)00199-x

Azzopardi, B.J. 1997. Drops in Annular Two-Phase Flow. *International Journal of Multiphase Flow* **23** (7): 1-53.

Azzopardi, B.J. and Wren, E. 2004. What Is Entrainment in Vertical Two-Phase Churn Flow? *International Journal of Multiphase Flow* **30** (1): 89-103.

Barbosa, J.R. 2001. Phase Change of Single Component Fluids and Mixtures in Annular Flow. PhD thesis, Department of Chemical Engineering and Chemical Technology, Imperial College of Science, London, UK.

Barbosa, J.R., Govan, A.H., and Hewitt, G.F. 2001. Visualisation and Modelling Studies of Churn Flow in a Vertical Pipe. *International Journal of Multiphase Flow* **27** (12): 2105-2127.

Barbosa, J.R. and Hewitt, G.F. 2006. *Gas-Liquid Two-Phase Flow in Vertical Pipes - a Description of Models Used in the Gramp 2 Programme*. Internal Report, Department of Chemical Engineering, Imperial College, London, UK.

Barbosa, J.R., Hewitt, G.F., König, G., and Richardson, S.M. 2002. Liquid Entrainment, Droplet Concentration and Pressure Gradient at the Onset of Annular Flow in a Vertical Pipe. *International Journal of Multiphase Flow* **28** (6): 943-961.

Belfroid, S., Schiferli, W., Alberts, G., Veeken, C.a.M., and Biezen, E. 2008. Predicting Onset and Dynamic Behaviour of Liquid Loading Gas Wells. Paper presented at the SPE Annual Technical Conference and Exhibition, Denver, 21-24 September.

Belt, R.J. 2007. On the Liquid Film in Inclined Annular Flow. PhD thesis, Department of Petroleum Engineering, Delft Univesrity of Technology, Delft, Netherlands.

Bendiksen, K.H., Maines, D., Moe, R., and Nuland, S. 1991. The Dynamic Two-Fluid Model Olga: Theory and Application. *SPE Production Engineering* **6** (2): 171-180. DOI: 10.2118/19451-pa

Brauner, N. and Barnea, D. 1986. Slug/Churn Transition in Upward Gas-Liquid Flow. *Chemical Engineering Science* **41** (1): 159-163.

Brown, D.J., Jensen, A., and Whalley, P.B. 1975. Non-Equilibrium Effects in Heated and Unheated Annular Two-Phase Flow. *ASME Paper* **75** (7): 754-757.

Chue, S.H. 1975. Pressure Probes for Fluid Measurement. *Progress in Aerospace Sciences* **16** (2): 147-223. DOI: 10.1016/0376-0421(75)90014-7

Chun, M.H. and Sung, C.K. 1986. Parametric Effects on the Void Fraction Measurement by Capacitance Transducers. *International Journal of Multiphase Flow* **12** (4): 627-640.

Coleman, S.B., Clay, H.B., Mccurdy, D.G., and Norris Iii, L.H. 1991a. A New Look at Predicting Gas-Well Load-Up. *SPE Journal of Petroleum Technology* **43** (3): 329-333. DOI: 10.2118/20280-pa

Coleman, S.B., Clay, H.B., Mccurdy, D.G., and Norris Iii, L.H. 1991b. Understanding Gas-Well Load-up Behavior. *SPE Journal of Petroleum Technology* (3): 334-338. DOI: 10.2118/20281-pa

Coney, M.W.E. 1973. The Theory and Application of Conductance Probes for the Measurement of Liquid Film Thickness in Two-Phase Flow. *Journal of Physics E: Scientific Instruments* **6** (9): 903-911.

Da Riva, E. and Del Col, D. 2009. Numerical Simulation of Churn Flow in a Vertical Pipe. *Chemical Engineering Science* **64** (17): 3753-3765.

Dukler, A.E. and Taitel, Y. 1986. *Flow Pattern Transition in Gas-Liquid Systems: Measurement and Modeling*. New York: Hemisphere Publishing Co.

Falcone, G. 2006. Modelling of Flows in Vertical Pipes and Its Application to Multiphase Flow Metering at High Gas Content and to the Prediction of Well Performance. PhD Dissertation, Department of Chemical Engineering and Chemical Technology, Imperial College London, London, UK.

Falcone, G., Hewitt, G.F., and Alimonti, C. 2009. *Multiphase Flow Metering*. Amsterdam: Elsevier.

Farias, P.S.C., Martins, F.J.W.A., Sampaio, L.E.B., Serfaty, R., and Azevedo, L.F.A. 2012. Liquid Film Characterization in Horizontal, Annular, Two-Phase, Gas-Liquid Flow Using Time-Resolved Laser-Induced Fluorescence. *Experiments in Fluids* **52**: 633-645.

Fernandez, J.J., Falcone, G., and Teodoriu, C. 2010. Design of a High-Pressure Research Flow Loop for the Experimental Investigation of Liquid Loading in Gas Wells. *SPE Projects, Facilities & Construction* **5** (2): 76-88. DOI: 10.2118/122786-pa

Fore, L.B., Beus, S.G., and Bauer, R.C. 2000. Interfacial Friction in Gas–Liquid Annular Flow: Analogies to Full and Transition Roughness. *International Journal of Multiphase Flow* **26** (11): 1755-1769. DOI: 10.1016/s0301-9322(99)00114-7

Gamio, J.C., Castro, J., Rivera, L., Alamilla, J., Garcia-Nocetti, F. et al. 2005. Visualisation of Gas-Oil Two-Phase Flows in Pressurised Pipes Using Electrical Capacitance Tomography. *Flow Measurement and Instrumentation* **16** (2-3): 129-134.

Gessner, T.R. and Barbosa, J.R. 2010. A Three-Field Model for Transient Annular Two-Phase Flow in a Vertical Tube. Paper presented at the 2nd Brazilian Conference of Boiling, Condensation and Multiphase Flow , Sao Carlos, Brazil, 3-4 May.

Govan, A.H. 1990. Modelling of Vertical Annular and Dispersed Two-Phase Flows. PhD thesis, Department of Chemical Engineering, Univeristy of London, Imperial College of Science, London, UK.

Govan, A.H., Hewitt, G.F., Richter, H.J., and Scott, A. 1991. Flooding and Churn Flow in Vertical Pipes. *International Journal of Multiphase Flow* **17** (1): 27-44.

Guo, B., Ghalambor, A., and Xu, C. 2006. A Systematic Approach to Predicting Liquid Loading in Gas Wells. *SPE Production & Operations* **21** (1): 81-88. DOI: 10.2118/94081-pa

Hazuku, T., Takamasa, T., and Matsumoto, Y. 2008. Experimental Study on Axial Development of Liquid Film in Vertical Upward Annular Two-Phase Flow. *International Journal of Multiphase Flow* **34** (2): 111-127.

Hewitt, G.F. 1982. *Handbook of Multiphase Flow Systems*. New York: Hemisphere Publishing Corporation.

Hewitt, G.F. and Jayanti, S. 1993. To Churn or Not to Churn. *International Journal of Multiphase Flow* **19** (3): 527-529.

Hewitt, G.F., Martin, C.J., and Wilkes, N.S. 1985. Experimental and Modelling Studies of Annular Flow in the Region between Flow Reversal and the Pressure Drop Minimum. *PCH, PhysicoChemical Hydrodynamics* **6** (1-2): 69-86.

Hewitt, G.F. and Roberts, D.N. 1969. *Study of Two-Phase Flows Patterns by Simulataneous X-Ray and Flash Photography*. UKAEFA Report AERE- M 2159, Atomic Energy Research Establishment, Berkshire, UK.

Hu, B., Veeken, C.a.M., Yusuf, R., and Holmås, H. 2010. Use of Wellbore-Reservoir Coupled Dynamic Simulation to Evaluate the Cycling Capability of Liquid-Loaded Gas Wells. Paper presented at the SPE Annual Technical Conference and Exhibition, Florence, Italy, 19-22 September DOI: 10.2118/134948-ms.

ISO/IEC Guide 98, Guide to the Expression of Uncertainty in Measurement, 1998. Geneva, Switzerland: Iso.

Jayanti, S. and Brauner, N. 1994. Churn Flow. *Multiphase Science and Technology* **8** (1-4): 471-521

Jayanti, S. and Hewitt, G.F. 1992. Prediction of the Slug-to-Churn Flow Transition in Vertical Two-Phase Flow. *International Journal of Multiphase Flow* **18** (6): 847-860.

Jayanti, S., Hewitt, G.F., Low, D.E.F., and Hervieu, E. 1993. Observation of Flooding in the Taylor Bubble of Co-Current Upwards Slug Flow. *International Journal of Multiphase Flow* **19** (3): 531-534.

Julia, J.E., Ozar, B., Dixit, A., Jeong, J.J., Hibiki, T. et al. 2009. Axial Development of Flow Regime in Adiabatic Upward Two-Phase Flow in a Vertical Annulus. *Journal of Fluids Engineering, Transactions of the ASME* **131** (2): 0213021-02130211.

Kaichiro, M. and Ishii, M. 1984. Flow Regime Transition Criteria for Upward Two-Phase Flow in Vertical Tubes. *International Journal of Heat and Mass Transfer* **27** (5): 723-737.

Labview. version 7.1. Texas: National Instruments.

Lea, J.F. and Nickens, H.V. 2004. Solving Gas-Well Liquid-Loading Problems. *SPE Journal of Petroleum Technology* (04): 30-36. DOI: 10.2118/72092-ms

Lea, J.F., Nickens, H.V., and Wells, M.R. 2003. *Gas Well Deliquification*. Amsterdam: Elsevier.

Li, J., Chen, Q., Dong, X., and Liu, S. 2005. Electrical Capacitance Tomography Measurement of Flow Patterns and Film Thickness in a Thermosyphon. *Journal of Thermal Science* **14** (1): 81-86.

Mao, Z.S. and Dukler, A.E. 1993. The Myth of Churn Flow? *International Journal of Multiphase Flow* **19** (2): 377-383.

Marashdeh, Q. 2006. Advances in Electrical Capacitance Tomography. PhD thesis, Department of Electrical Engineering, The Ohio State University, Columbus, OH.

Nosseir, M.A., Darwich, T.A., Sayyouh, M.H., and Sallaly, M.E. 2000. A New Approach for Accurate Prediction of Loading in Gas Wells under Different Flowing Conditions. *SPE Production & Operations* **15** (4): 241-246. DOI: 10.2118/66540-pa

Nossen, J., Shea, R.H., and Rasmussen, J. 2001. New Developments in Multiphase Flow Modelling and Field Data Verification. Paper presented at the Engineering Technology Conference on Energy, Houston, 5-7 February.

Owen, D.G. 1986. An Experimental and Theoretical Analysis of Equilibrium Annular Flow. PhD thesis, Departament of Chemical Engineering, University of Birmingham, Birmingham, UK.

Photron Fastcam Viewer for High Speed Digital Imaging. version 3.28.2. California: Photron.

Prasser, H.M. 2008. Novel Experimental Measuring Techniques Required to Provide Data for Cfd Validation. *Nuclear Engineering and Design* **238** (3): 744-770.

Prasser, H.M., Böttger, A., and Zschau, J. 1998. A New Electrode-Mesh Tomograph for Gas-Liquid Flows. *Flow Measurement and Instrumentation* **9** (2): 111-119.

Rodríguez, D.J. and Shedd, T.A. 2004. Entrainment of Gas in the Liquid Film of Horizontal, Annular, Two-Phase Flow. *International Journal of Multiphase Flow* **30** (6): 565-583.

Sagen, J., Ostenstad, M., Hu, B., Henanger, K.E.I., Lien, S.K. et al. 2011. A Dynamic Model for Simulation of Integrated Reservoir, Well and Pipeline System. Paper presented at the SPE Annual Technical Conference and Exhibition, Denver, 30 October-2 November DOI: 10.2118/147053-ms.

Sagen, J., Sira, T., Ek, A., Selberg, S., Chaib, M. et al. 2007. A Coupled Dynamic Reservoir and Pipeline Model - Development and Initial Experience. Paper presented at the 13th International Conference on Multiphase Production Technology, Edinburgh, UK, 13-17June.

Schubring, D., Ashwood, A.C., Shedd, T.A., and Hurlburt, E.T. 2010. Planar Laser-Induced Fluorescence (Plif) Measurements of Liquid Film Thickness in Annular Flow. Part I: Methods and Data. *International Journal of Multiphase Flow* **36** (10): 815-824.

Shaw, R. 1960. The Influence of Hole Dimensions on Static Pressure Measurements. *Journal of Fluid Mechanics* **7** (04): 550-564.

Shoham, O. 2006. *Mechanistic Modeling of Gas-Liquid Two-Phase Flow in Pipes*. New York: Society of Petroleum Engineers.

Silva, M.J., Thiele, S., Abdulkareem, L., Azzopardi, B.J., and Hampel, U. 2010. High-Resolution Gas-Oil Two-Phase Flow Visualization with a Capacitance Wire-Mesh Sensor. *Flow Measurement and Instrumentation* **21** (3): 191-197.

Silva, M.J.D. 2008. Impedance Sensors for Fast Multiphase Flow Measurement and Imaging. PhD thesis, Department of Electrical Engineering, Technische Universität Dresden, Dresden, Germany.

Solomon, F.A., Falcone, G., and Teodoriu, C. 2008. Critical Review of Existing Solutions to Predict and Model Liquid Loading in Gas Wells. Paper presented at

the SPE Annual Technical Conference and Exhibition, Denver, 21-24 September. DOI: 10.2118/115933-ms.

Sutton, R.P., Cox, S.A., E. Glynn Williams, J., Stoltz, R.P., and Gilbert, J.V. 2003. Gas Well Performance at Subcritical Rates. Paper presented at the SPE Production and Operations Symposium, Oklahoma City, 22-25 March. DOI: 10.2118/80887-ms.

Sutton, R.P., Cox, S.A., Lea, J.F., and Rowlan, O.L. 2009. Guidelines for the Proper Application of Critical Velocity Calculations. Paper presented at the SPE Production and Operations Symposium, Oklahoma City, 4-8 April.

Taitel, Y., Bornea, D., and Dukler, A.E. 1980. Modelling Flow Pattern Transitions for Steady Upward Gas-Liquid Flow in Vertical Tubes. *AICHE. J.* **26** (3 , May 1980): 345-354.

Turner, R.G., Hubbard, M.G., and Dukler, A.E. 1969. Analysis and Prediction of Minimum Flow Rate for the Continuous Removal of Liquids from Gas Wells. *SPE Journal of Petroleum Technology* **21** (11): 1475-1482. DOI: 10.2118/2198-pa

Veeken, C.a.M. and Belfroid, S. 2010. New Perspective on Gas-Well Liquid Loading and Unloading. Paper presented at the SPE Annual Technical Conference and Exhibition, Florence, Italy, 19-22 September

Veeken, C.a.M., Hu, B., and Schiferli, W. 2009. Transient Multiphase Flow Modeling of Gas Well Liquid Loading. Paper presented at the Offshore Europe, Aberdeen, UK, 8-11 September.

Veeken, K., Bakker, E., and Dousi, N. 2003. Liquid Loading in Gas Wells Symptoms and Cures. Paper presented at the SPE Annual Technical Conference and Exhibition, Denver, 16-17 June.

Wallis, G.B. 1969. *One-Dimensional Two-Phase Flow*. New York: McGraw-Hill.

Westende, J.M.C.V.T., Kemp, H.K., Belt, R.J., Portela, L.M., Mudde, R.F. et al. 2007. On the Role of Droplets in Cocurrent Annular and Churn-Annular Pipe Flow. *International Journal of Multiphase Flow* **33** (6): 595-615.

Wolf, A., Jayanti, S., and Hewitt, G.F. 2001. Flow Development in Vertical Annular Flow. *Chemical Engineering Science* **56** (10): 3221-3235.

Yusuf, R., Veeken, C.a.M., and Hu, B. 2010. Investigation of Gas Well Liquid Loading with a Transient Multiphase Flow Model. Paper presented at the SPE Oil and Gas India Conference and Exhibition, Mumbai, India, 20-22 January. DOI: 10.2118/128470-ms.

Zabaras, G., Dukler, A.E., and Moalem-Maron, D. 1986. Vertical Upward Cocurrent Gas-Liquid Annular Flow. *AIChE Journal* **32** (5): 829-843. DOI: 10.1002/aic.690320513

Zhang, H., Falcone, G., and Teodoriu, C. 2010. Modeling Fully Transient Two-Phase Flow in the near-Wellbore Region During Liquid Loading in Gas Wells. *Journal of Natural Gas Science and Engineering* **2** (2–3): 122-131. DOI: 10.1016/j.jngse.2010.04.005

Zhou, D. and Yuan, H. 2010. A New Model for Predicting Gas-Well Liquid Loading. *SPE Production and Operations* **25** (2): 172-181.

VITA

Name: Paulo Jose Waltrich

Address: 3116 TAMU, 602 Richardson Building,
           College Station, TX 77843-3116

Email Address: paulinhowaltrich@gmail.com

Education: B.S., Mechanical Engineering, Federal University of Santa Catarina, 2006
           M.S., Mechanical Engineering, Federal University of Santa Catarina, 2008